UNIVERSITY OF ADELAIDE LIBRARY
19·4·94

APPLICATION OF MONTE CARLO METHODS TO SOME PROBLEMS IN HIGH ENERGY ASTROPHYSICS

Anthony A. Lee

Thesis submitted for the degree of
Doctor of Philosophy
in
The University of Adelaide
(Faculty of Science)

December, 1993

Awarded 1994

Contents

This thesis contains neither material which has been accepted for the award of any other degree or diploma in any university or other tertiary institution and, to the best of the author's knowledge and belief, contains no material previously published or written by any other person, except where due reference is made.
I give consent to this copy of my thesis, when deposited in the University Library, being available for loan and photocopying.

Signed:

Anthony Lee

Acknowledgements

I would like to thank my supervisors Roger Clay and Raymond Protheroe for there guidance and support. I would also like to thank my unofficial supervisors Apostolos Mastichiadis and Bruce Dawson who also have provided large amounts of their time in support of my candidature. I would like to thank my fellow postgraduate students Michael Roberts, Rishi Meyhandan, Gary Hill, Janice Reid, Anthony Szabo, Gavin Rowell, Andrew Smith and Petar Atanackovic for their friendship and advice. The members of the High Energy Astrophysics Group including Phil Edwards, Greg Thornton, Neville Wild, Paul Johnson and Alan Gregory, I thank for their good physics advice and stimulating conversation.

My thanks to Mark Ferraretto for his invaluable computing advice and also to the general staff of the Physics and Mathematical Physics department including Arlene Shaw, Sharon Frencken, Deidree Simpson and Janet Hobbs for their time and assistance when needed. This work would not have been possible without the financial assistance of an Australian Postgraduate Research Award and I acknowledge their support. I would like to thank my family and family in-law for their support and encouragement. Without their continuing support throughout my candidature it would have been impossible to complete my Ph.D

Finally I would like to thank my wife Michelle and our son Matthew for their love, support and patience especially towards the concluding stages of my candidature.

Abstract

This thesis describes the methodology and results from the investigation of three areas of interest in High Energy Astrophysics. These areas are, firstly the structure of the ejecta of SN 1987A, secondly the propagation of cosmic rays through our galaxy with energies greater than 1×10^{18} eV, and thirdly the detection of these same extremely energetic cosmic rays. The method used to investigate each of these areas is by computer simulation using Monte Carlo methods.

The principle of the Monte Carlo approach is to trace out a large number of special cases for the problem being investigated and from the analysis of these infer a general solution. The problem being treated may have many possible branchings and the decision to follow a certain path is made by sampling from the appropriate probability distribution. The iterative approach of this method makes it an ideal application for high speed computers (for a review of Monte Carlo theory see James (1980)) and the first use of Monte Carlo methods was in the simulation of neutron scattering for the design of the first nuclear reactors in the 1950's using the first primitive computers.

Chapter 1 provides an introduction to SN 1987A. It describes the generation of radioactive isotopes within the supernova ejecta, their subsequent decay and production of γ-rays. Chapter 2 details the Monte Carlo code used to treat the propagation and energy degradation of γ-rays throughout the supernova ejecta. Chapter 3 introduces the treatment of clumping of the elements within the supernova ejecta and examines the effects on the X-ray and γ-ray lightcurves of SN 1987A. The results of the simulations are then compared with experimental data (Syunyaev *et al.*, 1990), theoretical calculations (Arnett, Fryxell and Muller, 1989) and another simulation also investigating the structure of the ejecta of SN 1987A (Kumagai *et al.*, 1989).

A general summary of cosmic rays is contained within Chapter 4. This serves as an introduction to Chapter 5 which investigates the propagation of cosmic rays with energies greater than 1×10^{18} eV. In Chapter 5 the method for simulating cosmic ray propagation is outlined including the effects of galactic magnetic field turbulence. From

these simulations predictions for cosmic ray anisotropy can be calculated. These results are compared with experimental results (e.g. Fichtel and Linsley (1986)) and other treatments of the same problem (e.g. Giller *et al.* (1993) and Berezinsky *et al.* (1991)).

As an introduction to Chapter 7, Chapter 6 outlines the theory of Extensive Air Showers (EAS) which are generated when cosmic rays interact with the earth's atmosphere. Chapter 7 investigates different detector designs for the detection of cosmic rays with energies greater than 1×10^{18} eV. The method used to investigate each of the detector designs is by the use of Monte Carlo methods and these are outlined in some detail. Results from these simulations are then used to decide on an optimum detector configuration.

Chapter 8 summarises the work presented in this thesis and discusses how the work presented here could be further extended in the future.

UNIVERSITY OF ADELAIDE LIBRARY

Chapter 1

Supernova 1987A

1.1 Introduction

Supernova 1987A (hereafter SN 1987A) was discovered by Ian Shelton in the Large Magellanic Cloud (LMC) using a 10 inch astrograph at the Las Campanas Observatory in Chile at February 24.23UT 1987 (IAU Circular No. 4316). From the detection of neutrinos (Bionta *et al.*, 1987; Hirata *et al.*, 1987) resulting from the formation of a neutron star, the core collapse can be timed at February 23.316UT 1987. The observation of neutrinos from the direction of SN 1987A represented the first detection of extra-galactic neutrinos.

Supernova 1987A was defined as a Type II supernova by the presence of hydrogen lines in its emission spectra with associated velocities ranging up to 0.1c (IAU Circulars No. 4316 and 4317). The position of SN 1987A is at (White and Malin, 1987)

$$\mathrm{RA} = 5^h 35^m 49.95s \pm 0.039s\ (0.21'')\ ,$$

$$\mathrm{dec} = -69^\circ 17' 57.9'' \pm 0.27''\ ,$$

for equinox (B1950.0)

1.2 Progenitor.

The stellar population in the LMC had been analysed in detail by virtue of its relative closeness ($\sim$ 55 kpc). This made possible the identification of the progenitor of SN 1987A. The position given for SN 1987A coincided with a known B3I supergiant which is called for convenience SK -69 202 (short for star number 202 at dec -69° in the Sanduleak catalogue) (Walborn *et al.*, 1987).

SK -69 202 was an unusual progenitor for a Type II supernova in that it was a blue giant (Rousseau *et al.*, 1978) and not a red supergiant when it exploded. A red supergiant is a star of luminosity of $\sim 1000\ L_{\odot}$ and a radius of $\sim 1000\ R_{\odot}$ with an extremely diffuse hydrogen envelope which may be undergoing mass loss. This extremely high luminosity results from the expansion and cooling of the star late in its evolution.

A more compact star, of a similar luminosity but with a smaller radius ($\sim 10\ R_{\odot}$) is called a blue giant. Generally the progenitor for a Type II supernova is expected to be a red supergiant with a large distended envelope as opposed to a more compact blue giant such as SK -69 202. This is because the shockwave resulting from the collapse of the progenitor (see Section 1.3) is expected to lose a significant proportion of its energy within the large envelope of a red supergiant, providing energy for the ensuing lightcurve. For the smaller blue giant, the shockwave couples more efficiently with the envelope, and its energy is converted into the kinetic energy of the ejecta.

The theories that give reasons as to why SK -69 202, a blue giant and hence a compact star, exploded to form a Type II supernova are divided into two areas (Arnett *et al.*, 1989). One suggestion is that the progenitor was a massive red giant which after having lost most of its hydrogen envelope evolved into a blue supergiant. A blue supergiant formed by this method is characterised by having no hydrogen envelope or a very small envelope with a high helium concentration. This explanation for the progenitor of SN 1987A was invoked by Chevalier and Fransson (1987a), Chevalier and Fransson (1987b), Shigeyama *et al.* (1987), Woosley *et al.* (1987).

However there are some weaknesses to this argument. Stellar evolution models (Saio, Kato and Nomoto, 1988; Woosley, Pinto and Ensman, 1988) suggest that the assumed mass and radius of SK -69 202 before explosion allows only two classes of evolution. One is a star which has lost a little mass, the other is a star which has lost its entire hydrogen envelope. Levels of mass loss between these two limits still produce red supergiants. In this case the progenitor was a blue supergiant with a great deal of evidence indicating that it also had a substantial hydrogen envelope at the time of core collapse. If it didn't have a substantial hydrogen envelope X-rays and γ-rays would have escaped at a much earlier epoch after core collapse and their fluxes would have been much greater. Also the spectrum of SK -69 202 was more abundant in hydrogen than helium, again pointing to a substantial hydrogen envelope.

The other theory constructed to account for the compactness of SK -69 202 is the low metallicity of the LMC. Metal deficient stellar models which evolve to blue super giants have been calculated (Saio, Kato and Nomoto, 1988; Woosley, Pinto and Ensman, 1988).

The detection of a circumstellar shell, overabundant in nitrogen, surrounding SN 1987A (Kirshner, 1987) implies that SK -69 202 had spent some time as a red supergiant with this circumstellar material the result of preprocessing in the progenitor, followed by mass loss (Fransson *et al.*, 1989). This has led to models (e.g. Hillebrandt *et al.* (1987), Saio, Nomoto and Kato (1988), Woosley, Pinto and Weaver (1988)) which combine both low metallicity plus mass loss to explain the evolution of the progenitor. In these models SK -69 202 burns hydrogen as a blue supergiant ($\sim 1 \times 10^7$ years), then spends time as a red supergiant when burning helium ($\sim 1 \times 10^6$ years) before undergoing mass loss and evolving once again to a blue supergiant before it explodes. In general the results obtained are still very dependent on model parameters.

The following represent the most likely physical characteristics for the progenitor:

1. A helium core 5–7 $M_\odot$. This is determined by the luminosity of SK -69 202 since the energy generated in the helium core contributes almost wholly to the luminosity (Woosley *et al.*, 1987).

2. Prior to mass loss the mass was $\sim$ 16–22 $M_\odot$. This is calculated using the most likely stellar evolution models (Hillebrandt *et al.*, 1987; Saio, Kato and Nomoto, 1988; Saio, Nomoto and Kato, 1988; Woosley, 1988).

3. By knowing the distance from the LMC and the luminosity of SK -69 202, the

surface temperature can be inferred as being between 15,000–18,000 K by assuming a black body radiator.

4. The radius of the progenitor can be inferred from the time delay between neutrino detection and the optical outburst. This has been determined to be $(3\pm1) \times 10^{12}$ cm (Shigeyama, Nomoto and Hashimoto, 1988; Shigeyama *et al.*, 1987; Woosley, Pinto and Ensman, 1988).

5. The fact that SN 1987A was subluminous by a factor of 10 compared to a "normal" Type II supernova also suggests that the progenitor was compact.

1.3 Type II Explosion Mechanism.

Stars initially evolve from large gas clouds which accrete due to gravity, producing energy from the loss of potential energy and generating heat. When the temperature reaches $\sim 10^7$ K, protons overcome their Coulombic repulsion and fusion occurs. As stars evolve the lighter elements fuse to form heavier elements, as in

$$H \longrightarrow He \longrightarrow Li \longrightarrow Be \longrightarrow \cdots .$$

Stars with masses greater than ~ 8 $M_\odot$ can ignite the advanced burning stages of carbon, neon, oxygen and silicon which will ultimately lead to the formation of an iron core. For a 20 $M_\odot$ star, these last burning stages occur in the last 1000 years of the stars life, which is an extremely short time compared to the $\sim 1 \times 10^7$ years when hydrogen and helium are the foremost energy sources (Woosley and Weaver, 1988). Thus the structure of a typical Type II pre-supernova star with a mass M, $8\ M_\odot < M < 40\ M_\odot$ resembles an onion. That is, the star is composed of different layers with different elemental abundances progressing from iron in the core to an at least partially intact hydrogen envelope, with pressure and temperature reducing as the distance from the core increases. A star of this type is usually a red supergiant. As mentioned previously, SK -69 202 was different in being a blue giant, but the explosion mechanism is essentially the same.

The progenitor in its last stages of evolution reaches the endpoint of energy generation once iron has been formed. Thus no energy is available to prevent the progenitor from collapsing under its own gravitational pull. Electron degeneracy pressure is overcome and relativistic electrons combine with core nuclei producing neutrinos by inverse beta decay:

$$p^+ + e^- \longrightarrow n + \nu_e \; . \tag{1.1}$$

In fact all flavours of neutrinos and anti-neutrinos are produced. The intensities of each type of neutrino are governed by many different processes such as their individual hydrodynamic, weak interaction and radiative properties. These neutrinos are trapped within the core as the core reaches nuclear density, but diffuse out when the star turns supernova. Without any thermonuclear pressure from fusion, or from relativistic electrons, the iron core begins to collapse. Three main possibilities can occur here. One is that the star may continue collapsing, thus forming a black hole. The second possibility is that the dynamics of the collapse will produce a shock blowing the outer layer of the star off. The remaining portion of the star whose mass is above the Chandrasekhar limit (the Chandrasekhar limit is the mass above which a star cannot support itself by electron degeneracy pressure ~ 1.4 $M_\odot$) remains as a neutron star which supports itself by virtue of neutron degeneracy pressure. The third possibility is that the remaining core mass, after a Type II supernova event, is above ~ 2.5 $M_\odot$. The gravitational force from this mass is sufficient to overcome the neutron degeneracy pressure and the star collapses to a black hole.

A Type II supernova is an example of the second possibility noted above. It must be said at the outset that the manner in which a Type II supernova occurs is not completely understood. Simulations of Type II supernova explosions require as initial parameters, conditions which may seem artificial (Arnett *et al.*, 1989; Wilson *et al.*, 1986; Woosley and Weaver, 1986). This applies to SN 1987A as well, however the basic physical details are understood. There are two main models. These are the "Prompt Hydrodynamical Explosion Model" and the "Delayed Explosion Mechanism Model".

1.3.1 Prompt Hydrodynamical Explosion Model

In this theory of the origin of Type II supernovae, the collapse of the iron core proceeds in two stages. The inner iron core, with a mass of typically 0.6–0.8 $M_\odot$ and a temperature of typically $kT \sim$ 10–15 MeV (Woosley and Weaver, 1986) collapses homologously (i.e. $v \propto r$ where v is the velocity of the collapsing core at radius r). The inner part of the iron core collapses with a velocity of $\sim$ 70,000 km s^{-1}. The outer iron core and outer regions of the progenitor do not participate in the homologous collapse of the core since the information that a collapse is proceeding can only propagate at the speed of sound.

When the inner core reaches a density of $\sim 3\rho_{nuc} \simeq 8 \times 10^{14}$ g cm^{-3}, where ρ_{nuc} is the density of an atomic nucleus, the nuclear force, which is usually attractive changes sign and becomes repulsive. Thus the inner core "stiffens". This pressure, acting in an opposite direction to the infalling supersonic matter, generates a shockwave. The energy from the "stiffening" of the inner iron core, plus the rebound energy, as the infalling matter rebounds off of the inner iron core, propagates the shock out of the total iron core with enough energy to eject the rest of the star ($\sim 1 \times 10^{51}$ ergs).

In this model, the shock has been generated and the explosion is underway in $\sim$ 20 ms, hence its name. The critical problem with this model is that as the shock moves through the outer regions of the iron core, photodisintegration and losses from neutrino diffusion reduce the shockwave energy. This implies that the likelihood of the shockwave exiting the iron core will depend on the total iron core mass.

1.3.2 Delayed Explosion Mechanism

The "Delayed Explosion Mechanism" employs the vast amount of energy released from the collapsing core in the first seconds of collapse by neutrinos to assist the propagation of the shockwave. Approximately 99% of the gravitational binding energy of the neutron star formed is released as neutrinos. The vast majority of these neutrinos do not result from the dynamics of the collapse but result from the cooling of the neutron star on a timescale of seconds. This energy is $\sim$ 100 times that needed for a Type II supernova. For example, if the hydrodynamical shock is stalled, neutrinos diffusing from the newly formed neutron star may couple their energy to the matter behind the shock, thus restarting it. The main problem with this scenario is the coupling of the energy of the neutrinos to the matter behind the shock. Theoretically (see Wilson *et al.* (1986)) the "Delayed Explosion Mechanism" method could be the mechanism occurring for supernovae whose progenitors are large stars of mass M, where $45\ \mathrm{M}_\odot < M < 50\ \mathrm{M}_\odot$. As yet there is no consensus as to the explosion mechanism responsible for SN 1987A.

1.4 Nucleosynthesis in Supernova Shock Waves

Fusion of the lighter elements within a star does not continue to the iron group outside of the iron core. At large temperatures ($> 10^9$ K) the energy losses from neutrino emission dominate the pre-supernova element formation occurring in the inner regions of the star. These energy losses make heavier element burning impossible on a large scale. This implies that the last effective energy generation process for a star is ^{16}O burning to ^{24}Si and to a lesser extent ^{32}S, this occurring ~ 1 year before core collapse and a possible supernova event.

Bodansky, Clayton and Fowler (1968) and Truran, Arnett and Cameron (1967) showed that as the shock wave from a supernova passed through the regions of ^{16}O, ^{24}Si, ^{32}S and ^{12}C within the progenitor, the iron group elements could be formed. What follows is a brief qualitative review of these theories.

The temperature T and density ρ of the stellar environment immediately following the passage of the supernova shock is

$$T \geq 5 \times 10^9\ \mathrm{K} \qquad \rho \sim 1.3 \times 10^7\ \mathrm{g\ cm^{-3}}\ . \tag{1.2}$$

At this temperature and density photodisintegration occurs. The most resistant element to this process is ^{24}Si, this being relatively stable to α-decay in these conditions. This implies that the most abundant element is ^{24}Si at one thousandth of a second after the shock wave has passed. The details of the calculations also show that there will be limited quantities of ^{12}C, ^{16}O and ^{32}S. New elements will be created when ^{12}C, ^{16}O and ^{32}S combine with free α-particles and protons resulting from photodisintegration following the shock. Bodansky, Clayton and Fowler (1968) and

Truran, Arnett and Cameron (1967) have shown that the most abundant elements produced by this mechanism are the iron group elements, in particular ^{56}Ni.

It is important to remember that this process does not occur throughout the stellar environment, but primarily inside the silicon shell of the pre-supernova star which is located in the inner regions of the star. The radius to which this occurs can be estimated using (Woosley and Weaver, 1986) an approximate expression for the temperature behind the shock T. This is found by equating the radiation density aT^4 (where a is the radiation density constant) multiplied by the volume behind the shock $\frac{4}{3}\pi R^3$ to the explosion energy E_0 ($\sim 10^{51}$ ergs) resulting in

$$T \simeq \left(\frac{3E_0}{4\pi R^3 a}\right)^{\frac{1}{4}} . \tag{1.3}$$

This implies, assuming shock nucleosynthesis for $T \geq 10^9$ K, that all of the material interior to $R = 3500$ km should be processed mainly to the iron group elements. This process is responsible for the abundances of elements with atomic weights $28 \leq A \leq 57$. It was pointed out by Clayton, Colgate and Fishman (1969) that γ-ray lines produced from the decay of ^{56}Ni to its daughter products may be of sufficient strength to be detected in Type II supernovae of distances less than 1 Mpc away. The extent to which this energy source is important for the evolution of the supernova and the prospects for detection of X-ray and γ-ray from SN 1987A will be considered in the next section.

1.5 Radioactive Decay of ^{56}Ni.

The amount of ^{56}Ni produced in SN 1987A can be determined by calculating the energy resulting from its decay i.e.

$$^{56}\mathrm{Ni} \xrightarrow{6.1\mathrm{days}} {}^{56}\mathrm{Co} \xrightarrow{77\mathrm{days}} {}^{56}\mathrm{Fe} ,$$

where the quantities above the arrows are the respective half lives for decay to the daughter product. The ^{56}Ni produced at the core regions of SN 1987A decays rapidly to ^{56}Co ($t_{1/2} = 6.1$ days). The γ-rays produced by each decay of cobalt to ^{56}Fe have a spectrum given by Table 1.1. The total energy per decay is ~ 3.5 MeV typically in the

Decay	Energy (keV)	Probability of emission for a line per decay
1	511	0.3800
2	734	0.0021
3	788	0.0030
4	847	0.9998
5	978	0.0144
6	1038	0.1408
7	1140	0.0015
8	1175	0.0224
9	1238	0.6758
10	1360	0.0428
11	1443	0.0020
12	1772	0.1600
13	1811	0.0048
14	1964	0.0072
15	2015	0.0309
16	2035	0.0795
17	2213	0.0063
18	2598	0.1672
19	3010	0.0100
20	3202	0.0303
21	3254	0.0743
22	3273	0.0176
23	3452	0.0086

Table 1.1: Table of γ-ray emission probabilities for the decay of ^{56}Co $\longrightarrow$ ^{56}Fe from Ambwani and Sutherland (1988).

form of three photons.

Thus the total γ-ray photon generation rate of the core $K_\gamma(t)$, is

$$K_\gamma(t) \simeq 6.4 \times 10^{48} M_{\rm Ni} \exp\left(-t/113.7 \text{ days}\right) \text{ photons s}^{-1} , \tag{1.4}$$

where $M_{\rm Ni}$ is the mass of ^{56}Ni in units of solar masses.

From this, the total gamma ray luminosity $L_\gamma(t)$ of the core can be calculated by multiplying $K_\gamma(t)$ by the mean energy of each decay photon $\overline{E}_\gamma$ ($\sim$ 1.2 MeV)

$$L_\gamma(t) = K_\gamma(t) \times \overline{E}_\gamma . \tag{1.5}$$

Therefore, a lower limit of the amount of nickel needed to account for the bolometric lightcurve can be calculated, assuming the energy comes from the decay of nickel followed by cobalt. This can apply at times after 100 days from the core collapse, when the energy powering the supernova comes directly from the radioactive input and not from the initial supernova shock wave. γ-rays interact within the ejecta, thermalising their energy, which is then released in the optical, UV and infrared wavelengths contributing to the bolometric lightcurve. For times greater than $\sim$ 400 days, a significant proportion of the X-rays and γ-rays will leak directly from the ejecta, not contributing to the bolometric lightcurve. The mass of cobalt needed to power the SN 1987A bolometric lightcurve has been investigated by Woosley, Pinto and Hartman (1989) who found that 0.075 $M_\odot$ of ^{56}Co and ^{57}Co can account for experimental observations. This can be seen in Figure 1-1. The abundance by mass of ^{57}Ni and hence ^{57}Co is very small compared to ^{56}Co, with the ratio of ^{57}Co to ^{56}Co $\sim$ 0.025. Also the half life of ^{57}Co is 271 days, which implies that the energy by decay will be small in the 100–400 day interval after core collapse. This implies that the inclusion of ^{57}Co makes a very small difference to the calculation. At later times past core collapse (700 days), ^{57}Co, ^{44}Ti and ^{22}Na will take over the radioactive input of energy to the supernova ejecta.

1.5.1 Calculation of γ-ray line flux

Not all of the γ-ray energy is trapped in the ejecta. There remains a possibility of detecting characteristic emission lines from the ^{56}Co decay. As an introduction to the full radiative transfer problem covered in Chapter 2, the expected γ-ray line flux is calculated for the most prominent line emission using a simple envelope model.

A simple assumption for the expanding envelope is to assume spherically symmetric homologous expansion (Mastichiadis, Kylafis and Ventura, 1988; Mastichiadis, Ogelman and Kirk, 1988; McCray, Shull and Sutherland, 1987). The ejecta will have a velocity profile $v(r,t)$

$$v(r,t) = V_{exp} \times \left(\frac{r}{R(t)}\right) , \tag{1.6}$$

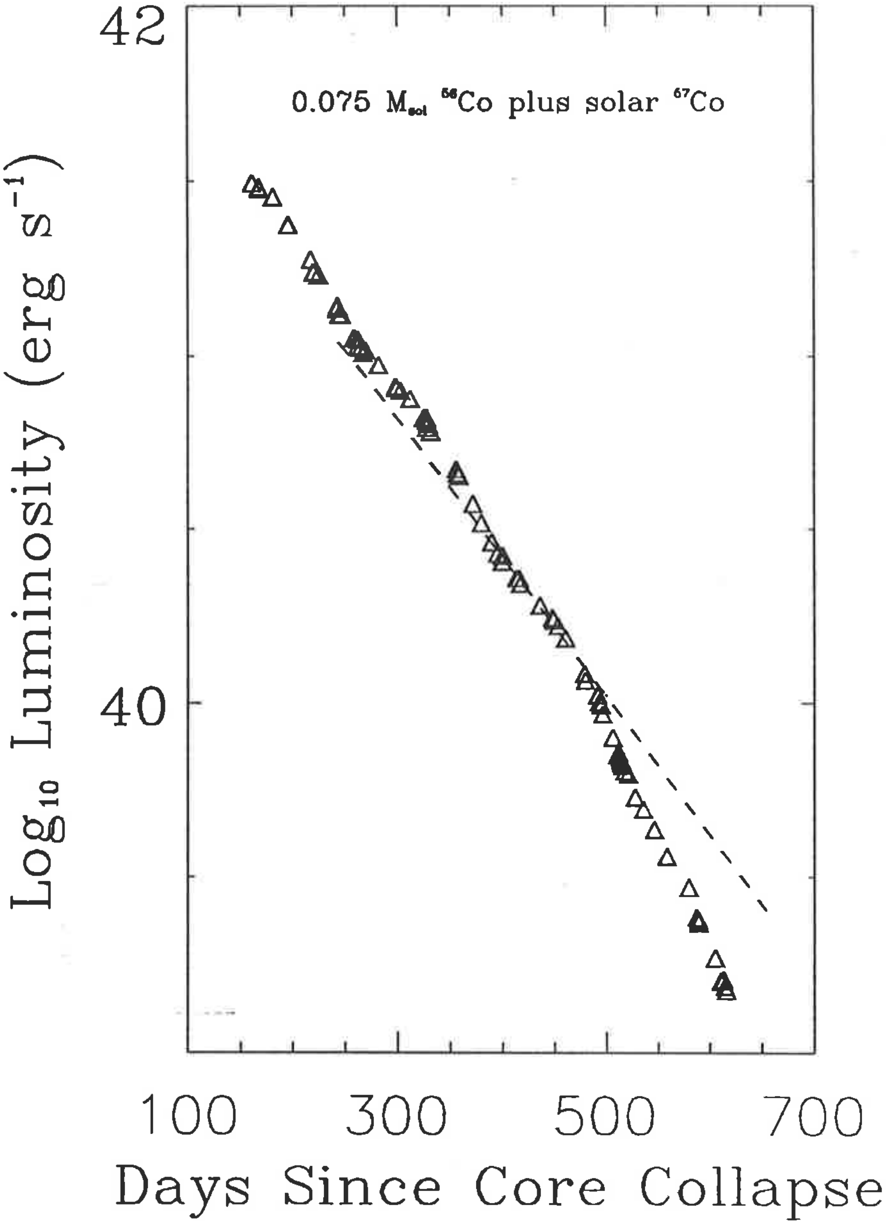

Figure 1-1: Comparison of predicted bolometric flux from cobalt decay and observations (adapted from Woosley, Pinto and Hartman (1989)). Data is from SAAO. The dashed line assumes 100% deposition of all γ-rays.

where r is the radius, t is the time, V_{exp} is the expansion velocity of the outer edge of the envelope, $R(t) = V_{exp}t$ and uniform density is assumed. The optical depth and hence the escape probability of photons can be calculated in this model quite simply. Photons scatter off from electrons in the supernova ejecta, so the Thomson optical depth τ_T is used. This is defined as

$$\tau_T(t) = n_e \sigma_T R(t) \ , \tag{1.7}$$

where n_e is the number density of electrons and σ_T is the Thomson cross section and describes classically the scattering of photons and electrons. σ_T is equal to 6.65×10^{-29} m^2.

Relation 1.7 can be rewritten to obtain

$$\tau_T = \frac{3N_e\sigma_T}{4\pi(R(t))^2} \ , \tag{1.8}$$

where N_e is the number of electrons within the envelope. If we assume, as an approximation, solar abundances for the envelope (in reality, abundances may be heavier due to the advanced stage of nuclear burning, or lighter due to SN 1987A being in the metal poor LMC) then

$$\tau_T(t) \sim 24\frac{M_{env}}{(V_4 t_m)^2} \ , \tag{1.9}$$

where V_4 is velocity in units of 10^4 m s^{-1}, M_{env} is the mass of the envelope in solar masses and t_m is time in months.

Thus the optical depth scales as $1/t^2$ and as time goes on it would be expected that the γ-ray lines will be detected. However the decay of cobalt must also be taken into account. Therefore the total γ- ray line flux detected at earth would be expected to evolve as

$$F_\gamma(t) = \frac{K_\gamma(t)\exp(-0.3\tau_T(t))}{4\pi D^2} \ \text{photons cm}^{-2}\ \text{s}^{-1} \ , \tag{1.10}$$

where D is the distance from earth to the LMC. τ_T is multiplied by 0.3 to take into account that the Klein-Nishina cross section (which accurately describes scattering of photons at high energies) is lower than the Thomson cross section at 1 MeV. Thus the approximate time that γ-ray lines will be detected can be calculated using known detector thresholds. Equation 1.10 can be rewritten as

$$F_\gamma(t) \simeq 1.5 \times \exp\left(-\left(\frac{t_m}{3.8} + \frac{110}{t_m^2}\right)\right) \text{ photons cm}^{-2}\text{ s}^{-1} \ . \tag{1.11}$$

To obtain the flux at a certain time for a given line, $F_\gamma(t)$ must be multiplied by the probability of that line being emitted (see Table 1.1). If the flux for the 847 keV line is calculated using this method, then at four months a flux of $\sim 5 \times 10^{-4}$ photons cm^{-2} s^{-1} is obtained. This suggests that at four months the 847 keV line should be detectable with detector sensitivities at a few times 10^{-4} photons cm^{-2} s^{-1} (e.g. Share *et al.* (1988)).

However, with the homologous model a constant density is assumed throughout the envelope. This is too simplistic. In reality, the envelope consists of shells of varying metallicity. If the Thomson optical depth at six months is calculated for the helium core (i.e. all of the material interior to and including the helium shell) using a radius of 2×10^{15} cm, a mass of 4.5 M$_\odot$ (i.e. ignoring the degenerate core) and taking into account the enhanced metallicity of this region then $\tau_T \sim 70$ is obtained. Clearly this will dominate the exponential term in Equation 1.11. Gehrels, MacCullum and Leventhal (1987) perform a more detailed calculation for a 15 M$_\odot$ progenitor with a 4.5 M$_\odot$ He core. They obtain a peak flux for the for the 847 keV line of $\sim 3 \times 10^{-4}$ photons cm^{-2} s^{-1} at 580 days and a slightly higher flux for the 1238 keV line 30 days earlier. Ebisuzaki and Shibazaki (1988b), Grebenev and Syunyaev (1987a), Itoh *et al.* (1987), McCray, Shull and Sutherland (1987), Pinto and Woosley (1988b) and Xu, Sutherland and McCray (1988) also obtained similar results.

The calculations presented here are approximate, as the distribution of cobalt within the envelope mass is assumed to be concentrated at the centre. As for the X-rays resulting from the comptonisation of the γ-ray lines, this is a more complicated calculation. A Monte Carlo method for solving this problem is described in Chapter 2.

Chapter 2

Modelling of X-ray Emission from SN 1987A

2.1 Introduction

The evolution of the X-ray emission from SN 1987A results from the Compton scattering and consequent photoabsorption of energy degraded γ-rays. These γ-rays result from the radioactive decay of elements produced by supernova shock nucleosynthesis. The details of these physical processes will be described here. The structure and elemental abundances within the supernova ejecta will also determine the evolution and spectral characteristics of the X-ray emission. A multi-zoned model of the ejecta is used, with concentric cells of varying elemental abundance. The particular model used is adapted from an already published model of the ejecta. The details of this adaptation are discussed. The computational procedure that models the propagation of photons through the multi-zoned ejecta is then analysed.

2.2 Photon-Electron Interactions

2.2.1 Comptonisation.

Compton scattering of photons occur when a photon interacts with a free electron. This may also occur with electrons bound to an atom, provided that the photon energy is large compared with the binding energy of the electron. There are two types of

Compton scattering. Compton-down scattering occurs when the energy is transferred from the photon to the electron, thus resulting in photon energy loss. This is the case for γ-rays interacting with electrons in the supernova ejecta. Compton-up scattering (known also as inverse Compton scattering) is the reverse case, where relativistic electrons transfer energy to low energy photons, thus raising their energy. For the supernova ejecta, the electrons can be considered to be stationary since the velocities associated with their thermal and expansion energies are negligible compared with c the speed of light.

The expression for the frequency change for Compton scattering of a photon of frequency ν to ν' is derived (see for example Pozdnyakov, Sobol' and Syunyaev (1983)) as

$$\frac{\nu'}{\nu} = \frac{1 - \frac{\mu v}{c}}{1 - \frac{\mu' v}{c} + \frac{h\nu}{\gamma m_e c^2}(1 - \cos\theta)} \,, \tag{2.1}$$

where

$v = |\vec{v}|$ the electron's initial velocity.

c is the velocity of light.

γ is the Lorentz factor equal to $\sqrt{1 - \frac{v^2}{c^2}}$.

m_e is the electron mass $\sim 511\ \frac{eV}{c^2}$.

$\mu = \hat{k} \cdot \hat{v}$, where $\hat{k}$ is the photon's initial direction and $\hat{v}$ is the electron's initial velocity unit vector.

$\mu' = \hat{k}' \cdot \hat{v}$ and $\hat{k}'$ is the photon's final direction.

$\cos\theta = \hat{k} \cdot \hat{k}'$. See Figure 2-1.

The differential cross section for Compton scattering (see, for example, Akhiezer and Berestetskii (1965)) is given by

$$\frac{d\sigma}{d\Omega} = \frac{r_e^2}{2\gamma^2} \frac{X}{\left(1 - \frac{\mu v}{c}\right)^2} \left(\frac{\nu'}{\nu}\right) \,, \tag{2.2}$$

where

$X = \frac{x_f}{x_i} + \frac{x_i}{x_f} + 4\left(\frac{1}{x_i} - \frac{1}{x_f}\right) + 4\left(\frac{1}{x_i} - \frac{1}{x_f}\right)^2$,

$x_i = \frac{2h\nu}{m_e c^2}\gamma\left(1 - \frac{\mu v}{c}\right)$,

$x_f = \frac{2h\nu'}{m_e c^2}\gamma\left(1 - \frac{\mu' v}{c}\right)$ and

$r_e = \frac{e^2}{4\pi\epsilon_0 m_e c^2}$, the classical electron radius.

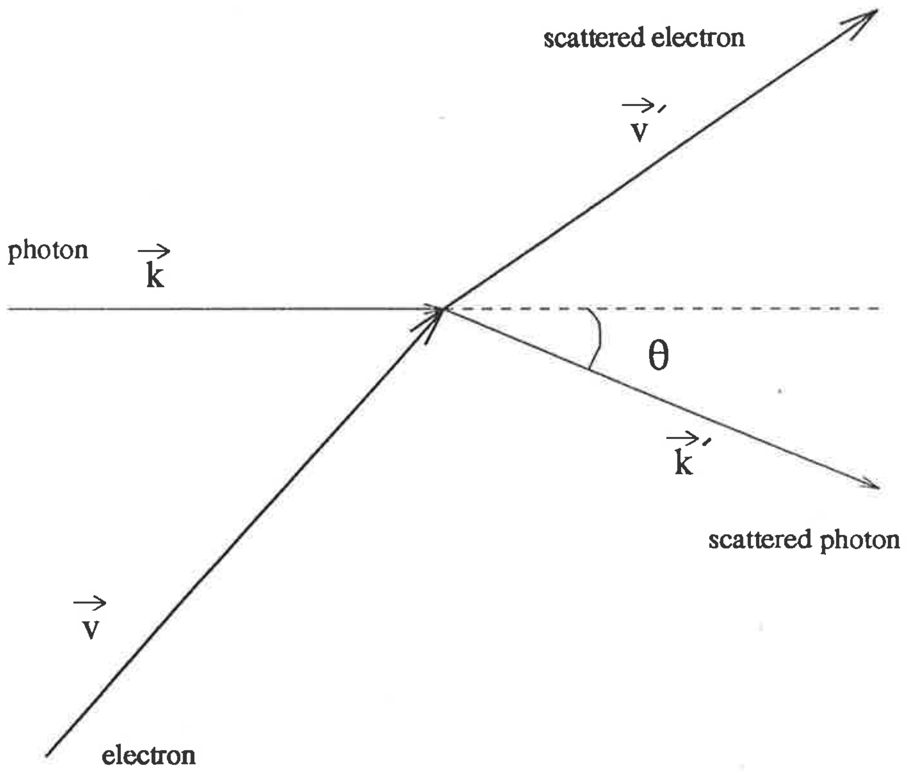

Figure 2-1: Compton scattering: $\hat{k}$ initial photon direction, $\hat{k}'$ final photon direction, $\hat{v}$ initial electron direction and $\hat{v}'$ is the final electron direction.

e is the charge of an electron $\sim 1.6 \times 10^{-19}$ C.

h is Planck's constant $\sim 6.63 \times 10^{-34}$ J s.

ϵ_0 is the permittivity of free space $\sim 8.85 \times 10^{12}$ F m^{-1}.

The energy change a photon undergoes on scattering with an electron can be readily obtained from Equation 2.1 i.e.

$$\frac{E'-E}{E} = \frac{\Delta E}{E} = \frac{\frac{\mu' v}{c} - \frac{\mu v}{c} - \frac{E}{\gamma m_e c^2}(1-\cos\theta)}{1 - \frac{\mu' v}{c} + \frac{E}{\gamma m_e c^2}(1-\cos\theta)} \ . \tag{2.3}$$

The total cross section for this interaction is called the Klein-Nishina cross section

$$\sigma_{KN} = \frac{2\pi r_e^2}{x_i}\left[\left(1 - \frac{4}{x_i} - \frac{8}{x_i^2}\right) ln(1+x_i) + 0.5 + \frac{8}{x_i} - \frac{1}{2(1+x_i^2)}\right] \ . \tag{2.4}$$

The Case of Stationary Electrons.

Simplification of the differential cross section, the energy transfer and the total cross section is obtained by assuming stationary electrons. As noted previously the velocities of electrons are small within the ejecta so $v/c \longrightarrow 0$ and $\gamma \longrightarrow 1$.

Therefore the differential cross section reduces to

$$\frac{d\sigma}{d\Omega} = \frac{r_e^2}{2}\left[1 + \cos^2\theta + \frac{h^2\nu^2(1-\cos\theta)^2}{(m_e c^2)^2\left(1 + \frac{h\nu}{m_e c^2}(1-\cos\theta)\right)}\right]\left(\frac{1}{1 + \frac{h\nu}{m_e c^2}(1-\cos\theta)}\right)^2 , \tag{2.5}$$

and Equation 2.3 simplifies to

$$\frac{\Delta E}{E} = \frac{-\frac{E}{m_e c^2}(1-\cos\theta)}{1 + \frac{E}{m_e c^2}(1-\cos\theta)} \ . \tag{2.6}$$

From this it is easier to see the dependence of energy transfer on the initial energy of the photon. For example if the original photon energy $E \ll m_e c^2$ then

$$\frac{\Delta E}{E} \sim \frac{-E}{m_e c^2}(1-\cos\theta) \ll 1 \ ,$$

and for $E \gg m_e c^2$

$$\frac{\Delta E}{E} \longrightarrow 1 \ .$$

Therefore higher energy photons will lose a greater proportion of their energy per scattering event. Thus high energy photons will lose their energy very quickly when scattering with a cloud of stationary electrons. Lower energy photons will need to scatter many times to lower their initial energy significantly.

The modified Klein-Nishina cross section is identical to Equation 2.4 except that $x_i = \frac{2h\nu}{m_e c^2}$. The Klein-Nishina cross section for electrons at rest is shown in Figure 2-2.

2.2.2 Photoabsorption.

Photoabsorption is the process in which an atom absorbs a photon, resulting in an electron being either ionised or being raised to a higher energy level within the atom. The lifetime of an electron in an excited state is typically $\sim 10^{-7}$ to 10^{-9} sec, after which the excited electron returns to the original energy level, emitting a photon of energy equal to the energy difference of the atomic levels.

Different elements have different cross sections for photoabsorption because of each element's unique atomic structure. The heavy elements are the most important with regard to the photoelectric opacity of the supernova ejecta. These elements have cross sections many orders of magnitude higher than, for example, hydrogen. The cross-sections used are linear approximations. These are listed in Table 2.1. These were checked by comparison with experimentally measured photoabsorption cross sections (Veigele, 1973) and found to be very accurate ($\sim$ 99%).

The total overall photoabsorption cross section for a zone within SN 1987A will depend on the elemental abundances of that zone. Since the supernova model we use is multi-zoned, it is necessary to define an average photoabsorption cross section for each zone. The number of atoms N_i of type i can be determined by

$$N_i = \frac{M_{zone} X_i N_a}{A_i} , \qquad (2.7)$$

where

M_{zone} is the mass of the zone of interest,

X_i is the abundance by weight of element i for the zone of interest,

N_a is Avogadro's number and

A_i is the atomic weight of element i

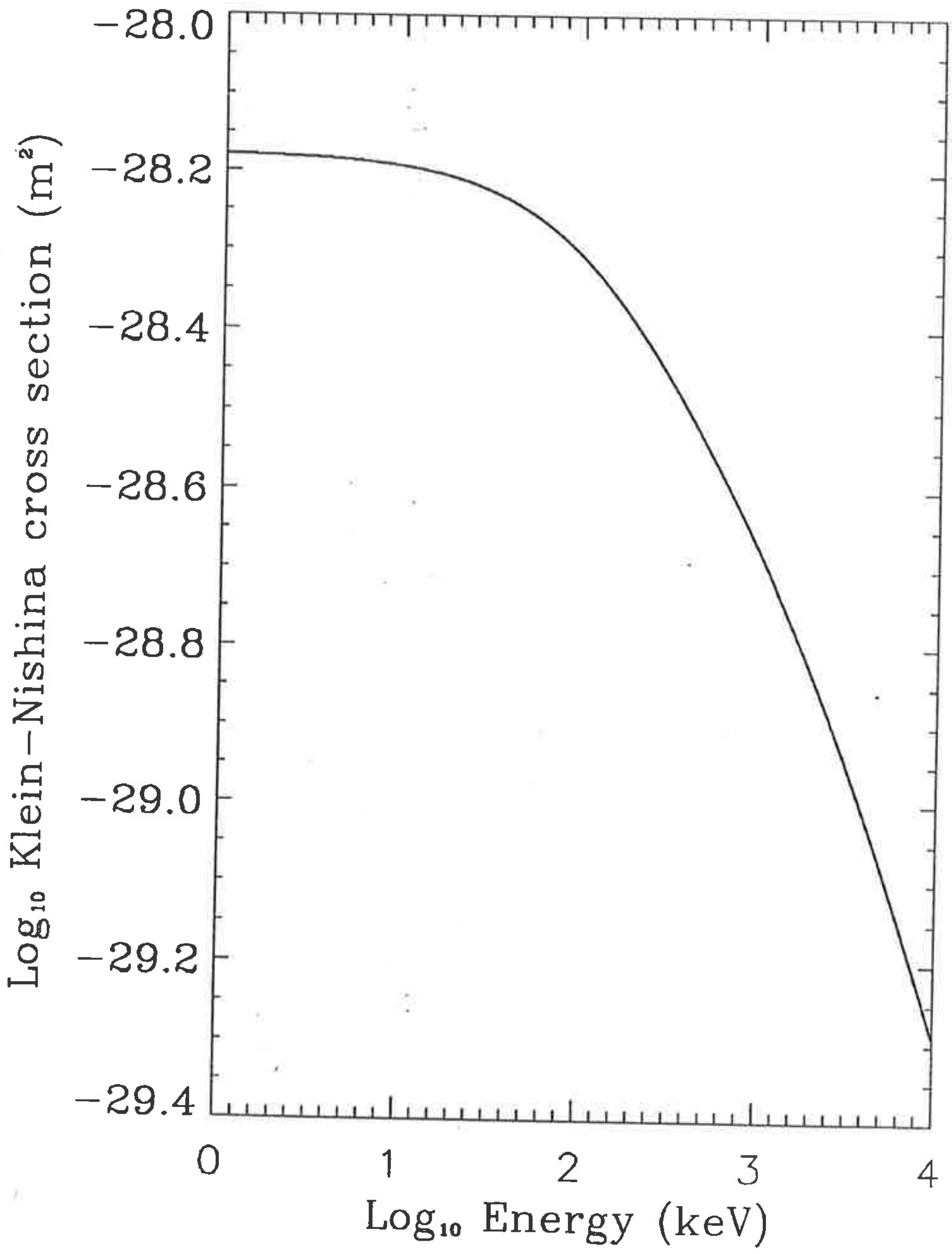

Figure 2-2: Klein-Nishina cross section for electrons at rest.

Element	Atomic No.	Cross section $\sigma_p(E)$ (m^2) $\times \left(\frac{1000\ \mathrm{keV}}{E}\right)^3 \times 10^{-28}$
hydrogen	1	$10^{-9.25}$
helium	2	$10^{-7.56}$
carbon	6	$10^{-4.94}$
nitrogen	7	$10^{-4.62}$
oxygen	8	$10^{-4.31}$
neon	10	$10^{-3.82}$
magnesium	12	$10^{-3.41}$
silicon	14	$10^{-3.06}$
sulphur	16	$10^{-2.77}$
argon	18	$10^{-2.58}$
calcium	20	$10^{-2.37}$
titanium	22	$10^{-2.13}$
chromium	24	$10^{-1.88}$
iron	26	$10^{-1.73}$
cobalt	27	$10^{-1.60}$
nickel	28	$10^{-1.47}$

Table 2.1: Table of photoabsorption cross sections used.

Define the average photoabsorption cross section for a zone as

$$\overline{\sigma}_P(E) = \frac{\sum_i N_i \sigma_{p_i}(E)}{\sum_i N_i} , \tag{2.8}$$

where σ_{p_i} is the individual photoabsorption cross section for each element i.

Figure 2-3 shows the total average photoabsorption cross section for solar metallicity. Comparing this with Figure 2-2, one can see that the photoabsorption cross section dominates at energies less than $\sim$ 10 keV. For higher than solar metallicity, the larger heavy element photoabsorption cross sections will dominate. This will increase the photoabsorption cross section at all energies and thus increase the energy at which photoabsorption dominates over Compton scattering.

An important effect altering the cross section for ^{56}Fe is the K-α line absorption edge. This is taken into account by putting a discontinuity in the cross section at the absorption edge. A comparison between this procedure and the experimentally determined cross section (Veigele, 1973) for ^{56}Fe can be seen in Figure 2-4. In this figure a sharp discontinuity can be seen in the measured photoabsorption cross section for iron at 7.1 keV. Absorption of a photon at this energy results in the almost instantaneous emission of a photon of 6.4 keV. A similar process occurs for ^{56}Co, however the yield is much smaller and not taken into account here. This process also occurs at lower energies for the other elements and at lower yields and so these emission lines were not considered.

2.3 Numerical Model of SN 1987A.

In order to calculate the γ-ray line flux, the continuum emission fluxes, the lightcurve and the spectral characteristics in the energy range considered, a detailed model of the envelope must be constructed. This model must incorporate how quantities such as elemental abundances, velocity and mass vary with respect to their position in the supernova ejecta. Each of these factors will directly determine the optical depth of the ejecta and hence the escape probability of radiation from the envelope. No attempt is made here to derive such a model from first principles, but rather a widely accepted model is used in a simplified form.

2.3.1 Previous Models.

The original model used here is Model 10HMM (Pinto and Woosley, 1988a). This model has been used largely because of its availability. Also it has been very successful in reproducing known characteristics of SN 1987A (Woosley, Pinto and Hartman, 1989). Other models can be found in Arnett, Fryxell and Muller (1989), Arnett and Fu (1989), Grebenev and Syunyaev (1987b), Itoh *et al.* (1987), Saio, Kato and Nomoto (1988), Saio, Nomoto and Kato (1988), Shigeyama, Nomoto and Hashimoto (1988), Shigeyama *et al.* (1987), Woosley (1988), Woosley *et al.* (1987) and Woosley, Pinto and Ensman (1988).

2.3.2 Model 10HMM

Model 10HMM, which models the post-supernova ejecta, was developed from computational models of stellar evolution. The initial step in modelling the supernova ejecta was to take results from simulations of already pre-evolved cores of 15, 20 and

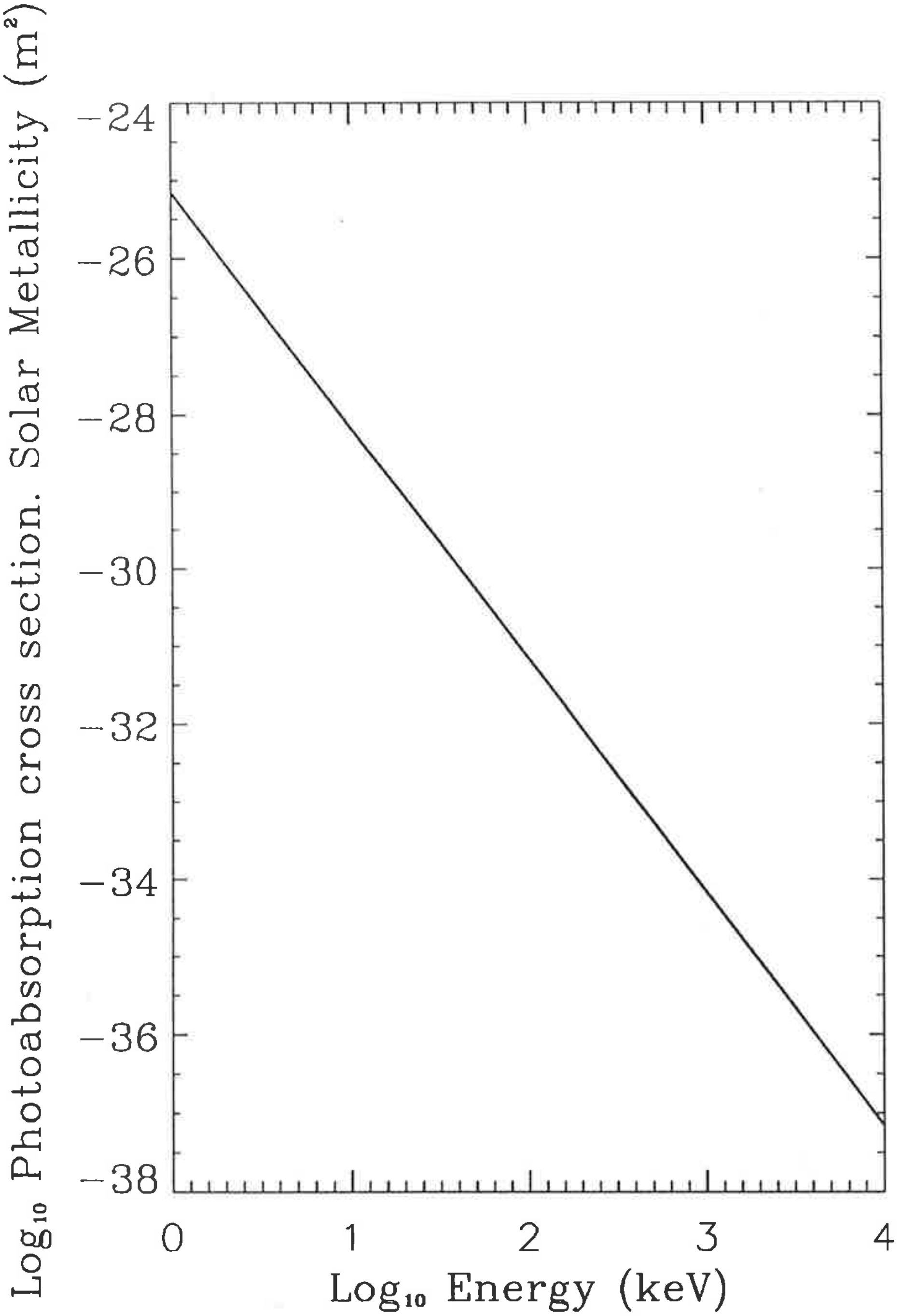

Figure 2-3: Total photoabsorption cross section for solar metallicity, using linear approximation for each individual element's photoabsorption cross section (see Table 2.1).

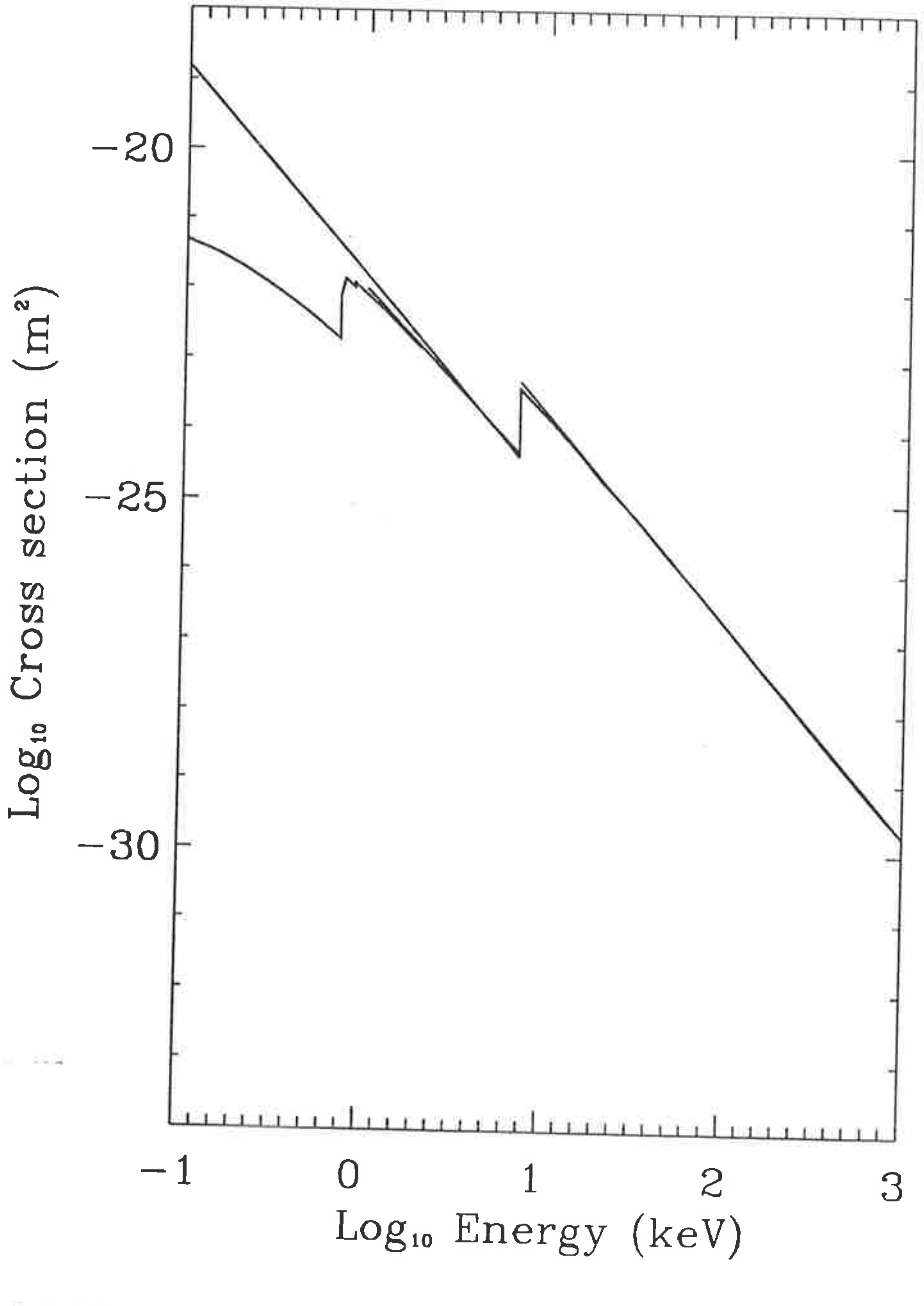

Figure 2-4: Photoabsorption cross section ^{56}Fe, showing the absorption edge at 7.1 keV. The absorption edge below 1 keV is not in the energy range considered. Only the discontinuity at 7.1 keV was modelled as this was the only one occurring above the threshold for the simulation.

Parameters	A	B	C	D	E	F	G	H	I
Main Sequence Mass ($M_\odot$)	15	15	15	15	15	20	20	20	35
He core mass ($M_\odot$)	4.1	4.1	4.1	4.1	4.1	6.2	6.2	6.2	14.3
H envelope ($M_\odot$)	5	10	5	10	5	5	5	10	3
$\log L/L_\odot$	4.5	4.7	4.5	4.7	4.6	5.1	5.1	5.1	5.6
Radius/10^{12} cm	2.5	2.9	2.3	2.8	5.8	5.8	2.3	5.5	3.5
$T_{eff} 10^4$ K	14	14	14	14	9	12	19	12	25
Explosive KE (10^{51} ergs)	0.52	0.52	3.2	3.2	0.52	1.44	2.73	1.44	1.19
$M(^{56}\mathrm{Ni})(M_\odot)$	0.06	0.06	0.08	0.08	0.06	0.44	0.16	0.44	0.26

Table 2.2: Different Progenitor Models (Woosley, Pinto and Ensman, 1988).

35 $M_\odot$ pre-supernova stars which had evolved without mass loss (Wilson *et al.*, 1986). Attached to these cores were hydrogen envelopes of different masses and radii (Woosley, Pinto and Ensman, 1988). With this model of the progenitor, a shock in the form of a supersonic piston was initiated in the central regions of the core. The actual position is determined by the density gradient near the iron core. A shock wave is formed and this propagates outward through the progenitor. Shock nucleosynthesis occurs as the shock moves through the progenitor and the elemental abundances change accordingly. Some of the various stellar initial conditions tested can be seen in Table 2.2.

Initially, there was some doubt that SK -69 202 had in fact exploded. It is interesting to note however, that the progenitor characteristics inferred from the supernova closely matched those of SK -69 202. At early times past core collapse, the main observational parameter with which model predictions could be compared was the bolometric lightcurve of SN 1987A. The detection of the 847 and 1238 keV γ-ray line emission (Dotani *et al.*, 1987; Matz *et al.*, 1988) in August 1987 provided a much more stringent test of envelope models. The detection of the hard X-ray continuum (Syunyaev *et al.*, 1987a; Syunyaev *et al.*, 1987b) resulting from the comptonisation of the cobalt emission lines, also detected at approximately the same time, provided spectral information to which simulations could be compared.

Model 10H (see Table 2.2), where the 10 refers to the mass of the hydrogen envelope, was one of the preferred choices as a model of the likely supernova progenitor (Woosley, 1988), except for its inability to describe the early appearance of the hard

X-ray continuum and the γ-ray lines. The amount of ^{56}Co needed to power the lightcurve is ~ 0.075 $M_{\odot}$ (see Section 1.5). For this mass of ^{56}Co, the expected appearance of the γ-ray line flux at 847 keV is ~ 1.5 years (see Section 1.5.1). As with Arnett and Fu (1989), Bussard, Burrows and The (1989), Ebisuzaki and Shibazaki (1988a), Fu and Arnett (1989), Kumagai *et al.* (1989), Leising (1988), Pinto and Woosley (1988a), Woosley, Pinto and Ensman (1988) and Yamada, Kasahara and Nakamura (1989), the suggested mechanism to explain the early appearance of the 847 keV flux was to invoke mixing of the cobalt from the core of the ejecta to the outer layers. Model 10H incorporated this mechanism (Woosley, 1987) yielding model 10HM. The overall density-velocity profile of model 10H was maintained, but the elemental composition altered to simulate cobalt mixed to the upper layers and hence greater velocities. This lowers the column depth to the cobalt and consequently γ-rays and X-rays can escape the ejecta at earlier times. Model 10HMM (Pinto and Woosley, 1988a; Woosley, Pinto and Hartman, 1989) has the cobalt mixed even more, in order to further increase the agreement with observations. The mixing of cobalt is done in such a manner as to preserve spherical symmetry. No attempt is made to simulate any possible anisotropies in the distribution of cobalt.

2.3.3 Model Used for Simulation

The model used in this report is a variation upon model 10HMM. In order to reduce computational time, the original 69 zone model was reduced to an 18 zone model, model 10HMM (ave).

Comparisons of abundances of each element from 10HMM and the new 18 zone model 10HMM (ave), showed that approximating model 10HMM using 18 zone is adequate. Table 2.3 shows how this procedure is carried out. Less averaging over zones is carried out for the hydrogen envelope to ensure that the metallicity is not enhanced in this region by averaging over high and low metallicity zones. Simulations showed that the metallicity of the envelope is the most important factor in determining the spectral shape of the X-ray data, particularly in the energy range 5–50 keV where the effects of photoabsorption are the most important. Parameters such as the zone's energy, luminosity, entropy, pressure and nuclear entropy are not directly needed by

Zone	Radius (cm)	Mass ($M_\odot$)	Expansion velocity (cm s^{-1})	Equivalent zones in Mod. 10HMM
1	6.734×10^{14}	1.714	4.863×10^{7}	1,2
2	1.011×10^{15}	2.076	7.091×10^{7}	3,4,5,6,7
3	1.311×10^{15}	2.709	9.199×10^{7}	8,9,10,11,12
4	1.562×10^{15}	3.639	1.105×10^{8}	13,14,15,16,17
5	1.810×10^{15}	4.819	1.274×10^{8}	18,19,20,21,22
6	2.235×10^{15}	6.196	1.568×10^{8}	23,24,25,26,27
7	3.244×10^{15}	7.468	2.273×10^{8}	28,29,30,31,32
8	3.693×10^{15}	8.719	2.589×10^{8}	33,34,35,36,37
9	4.090×10^{15}	9.975	2.866×10^{8}	38,39,40,41,42
10	4.500×10^{15}	11.232	3.153×10^{8}	43,44,45,46,47
11	4.980×10^{15}	12.489	3.490×10^{8}	48,49,50,51,52
12	5.628×10^{15}	13.745	3.944×10^{8}	53,54,55,56,57
13	6.143×10^{15}	14.513	4.303×10^{8}	58,59,60
14	6.647×10^{15}	15.029	4.655×10^{8}	61,62
15	7.553×10^{15}	15.641	5.267×10^{8}	63,64
16	1.127×10^{16}	16.202	7.802×10^{8}	65,66
17	1.634×10^{16}	16.253	1.145×10^{9}	67,68
18	2.096×10^{16}	16.257	1.397×10^{9}	69

Table 2.3: Model 10 HMM (ave) parameters at 180 days past core collapse. The radius given is the outer radius of the zone. The mass is the mass interior to the radius. The expansion velocity is the velocity of the ejecta at the outer edge of the zone. The last column shows the equivalent zones between model 10HMM (ave) and the 69 zone model 10HMM.

the X-ray and γ-ray propagation simulation. The abundances by mass of each element in model 10HMM (ave) are contained in Appendix A.

2.4 Computational Procedure

The method of simulating the interaction of cobalt emission γ-rays with the supernova ejecta uses Monte Carlo techniques. The particular technique used is the method of weights (for a general review of Monte Carlo techniques as applied to Comptonisation problems see Pozdnyakov, Sobol' and Syunyaev (1983)). The assumptions made in this model in order to simplify computations are

1. The temperature of the ejecta is assumed to be zero i.e. the effects of ejecta temperature are negligible when dealing with the production of X-rays in the

energy range considered.

2. The only radioactive source used is ^{56}Co. Considering the time period (180–800 days after core collapse) all other radioactive elements contribute negligibly to the X-ray flux.

3. Any effects due to Doppler shifting from the expansion of the ejecta are ignored.

4. No other interaction effects, such as pair-production, are taken into account in the models. The cross section for these various processes are negligible compared to Compton and photoabsorption cross-sections for the energy range considered.

2.4.1 Cobalt line emission.

A γ-ray will be emitted with an energy determined by the probability of emission of that line in the decay $^{56}\mathrm{Co} \rightarrow {}^{56}\mathrm{Fe}$ (see Table 1.1). The six most probable emission lines are used. The ejecta is divided into 18 zones, each having their own individual elemental abundances. The zone of emission is chosen by the proportion of the mass of ^{56}Co in that zone relative to the total mass of ^{56}Co in the ejecta. The position of emission within the chosen zone is determined by sampling a random number $x \in (0,1)$ and choosing the radius r of emission to be

$$r = [r_{in}^3 + x(r_{out}^3 - r_{in}^3)]^{\frac{1}{3}} , \tag{2.9}$$

where r_{in} is the inner radius of the zone and r_{out} is the outer radius of the zone.

At this position the photon is emitted isotropically. The photon is assigned with an initial weight of $w_0 = 1.0$. This weight will be modified according to the particular processes the photon undergoes.

2.4.2 Escape Probability

The direction of propagation will determine how many zones that photon will need to travel through in order to escape the ejecta. The zones have different elemental composition and so the particular zone crossed will have different attenuation properties for the emitted photon. The method used to describe the interaction probabilities of the photon is the optical depth τ. The optical depth for a medium of size l and with a number density of scatterers n_s is defined as

$$\tau = \int_0^l n_s(x)\sigma(E,x)\,dx \ , \tag{2.10}$$

where $\sigma(E,x)$ is the interaction cross section which generally depends on the energy E of the photon. Since photoabsorption and Compton scattering are both occurring, individual optical depths are defined

$$\tau_P(E) = \sum_{j=1}^{n} n_{\mathrm{n}\,ij}\overline{\sigma}_{P\,ij}(E)\Delta l_j \ , \tag{2.11}$$

$$\tau_C(E) = \sum_{j=1}^{n} n_{\mathrm{e}\,ij}\sigma_{KN}(E)\Delta l_j \ . \tag{2.12}$$

Referring to Figure 2-5 which shows a simplified three zone model of the supernova ejecta, it can be seen that the index i refers to the zone number, whereas the index j refers to the j^{th} zone being crossed starting from the point of emission or point of scattering to the edge of the ejecta. Thus the summation is over the number n of zones crossed. It is quite possible for a given path that a zone may be crossed more than once. The quantities defined in Equations 2.11 and 2.12 are $\tau_P(E)$ the optical depth due to photoabsorption and $\tau_C(E)$ the optical depth due to Compton scattering, each for a photon of energy E. $\overline{\sigma}_{P\,i}(E)$ is the photoabsorption cross section for zone i for photon energy E. This cross section will vary according to the elemental makeup of the zone (see Equation 2.8). $\sigma_{KN}(E)$ is the Klein-Nishina cross section (see Equation 2.4), Δl_j is the distance travelled through the j^{th} zone intersection, $n_{\mathrm{n}\,i}$ is the number density of nucleons in zone i and $n_{\mathrm{e}\,i}$ is the number density of electrons in zone i.

Defining the total optical depth $\tau_{Tot} = \tau_P + \tau_C$, the probability of a photon escaping P_{esc} with this trajectory is then

$$P_{esc} = \exp(-\tau_{Tot}) \ . \tag{2.13}$$

Now the initial weight is multiplied by P_{esc} and stored. This portion is considered to have escaped the ejecta. The remaining weight $w_{i+1} = w_i(1 - P_{esc})$ will continue

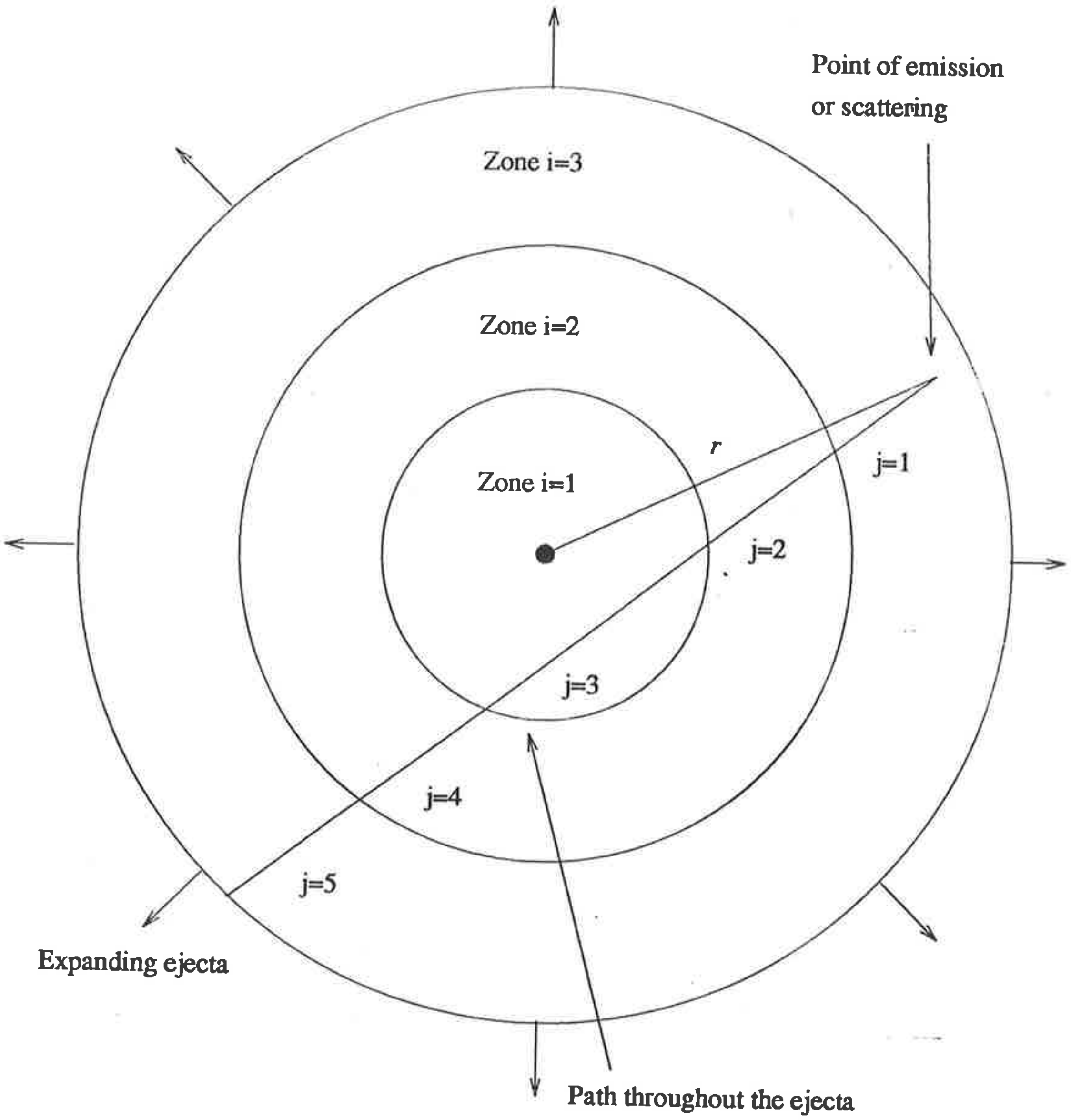

Figure 2-5: A simplified three zone model of the supernova ejecta showing the labelling scheme.

interacting within the ejecta.

2.4.3 Path Length.

The distance travelled along the given trajectory before an interaction occurs is calculated by random selection. Starting from the point of emission (or from the point of last scattering) the optical depth is calculated discretely for each zone crossed. A cumulative escape probability P^k_{esc} can then be calculated

$$P^k_{esc} = \exp(-\sum_{j=1}^{k} \tau_{Tot\,j}) \qquad k = 1, \ldots, n \ , \tag{2.14}$$

where $\tau_{Tot} = \sum_{j=1}^{n} \tau_{Tot\,j}$. This sum is from the initial zone of emission (or scattering) to the final zone at the edge of the ejecta. As k increases P^k_{esc} will become smaller. The maximum value of k is the number of zones the photon path will cross between the interaction point and the edge of the ejecta.

To select a path length, P_l, a random number $x \in (0, 1)$ is chosen. From the sampled x the shell of interaction is found by checking the condition $P^{k-1}_{esc} > x \geq P^k_{esc}$ for $k = 2, \ldots, n$. If for all pairs of P^{k-1}_{esc} and P^k_{esc} the x chosen does not satisfy the above inequality, then another random number is chosen until the above criterion is satisfied. This value of x will define uniquely a pathlength along the trajectory. It has already been determined that the photon interacts in zone k. It is just necessary to determine at what point along the trajectory in zone k the interaction occurs. Note that the sampled value of the random number x defines a particular optical depth τ, which is a function of P_l, by

$$x = P_{esc} = \exp(-\tau) \ , \tag{2.15}$$

where

$$\tau = \sum_{j=1}^{k-1} \tau_{Tot\,j} + \tau_{Tot\,k} \frac{\Delta l}{\Delta l_k} \ ,$$

and $\Delta l = P_l - \sum_{j=1}^{k-1} \Delta l_j$. Solving for the path length P_l it is found that

$$P_l = -\frac{\Delta l_k}{\tau_{Tot\,k}} (\log(x \exp(\sum_{j=1}^{k-1} \tau_{Tot\,j})) + \sum_{j=1}^{k-1} \Delta l_j \ . \tag{2.16}$$

2.4.4 Selection of Photoabsorption and Compton Scattering

Now that the point of interaction has been determined, it is necessary to determine the photon interaction process. Using the weighting technique, a proportional weight is applied according to the probability of each process. For example, the probability of photoabsorption P_{phot} is calculated as

$$P_{phot} = \frac{\tau_{P\,k}}{\tau_{Tot\,k}} , \tag{2.17}$$

where $\tau_{P\,k}$ is the photoabsorption optical depth calculated for zone k where this is the zone of interaction. $\tau_{Tot\,k}$ is the total optical depth for zone k.

Accordingly, the probability for Compton scattering P_{Com} is

$$P_{Com} = 1 - P_{phot} . \tag{2.18}$$

Therefore the proportional weights for photoabsorption and Compton scattering are

$$w_{phot} = w_i P_{phot} \qquad w_{Com} = w_i(1 - P_{phot}) . \tag{2.19}$$

2.4.5 Photoabsorption

When photoabsorption occurs, the photon is lost to the system unless it is absorbed by iron, in which case there is photoemission of the K_α line. This has an energy of 6.4 keV which is high enough to be included, since the energy range of interest here is 5 keV–4 MeV. The photoemission of the lower Z elements is in the optical and UV regions. Using the method of weights, the weight w_{phot} is multiplied by the probability of photoabsorption by iron P_{Fe}. This is defined as

$$P_{Fe} = \frac{N_{Fe}\sigma_{P_{Fe}}(E)}{\sum_i N_i \sigma_{P_i}(E)} , \tag{2.20}$$

where n_{Fe} is the number of iron atoms (which will depend on the zone) and $\sigma_{P_{Fe}}(E)$ is the photoabsorption cross section of iron. The denominator represents a summing over all the photoabsorption cross sections for the zone in question. Thus P_{Fe} will change for individual zones. For zones with high iron content, P_{Fe} will be large compared to the hydrogen rich envelope zones. The energy of the absorbed photon must be greater than 7.1 keV in order to be emitted in the line. Thus the energy of the absorbed photon must be tested using this criterion. If the energy is less than 7.1 keV, the photon (and hence its weight) is lost to the system (i.e. it will contribute to the optical and UV emission). Otherwise, the weight must also be further multiplied by the yield Y_{K_α} of the K_α line where $Y_{K_\alpha} = 0.347$ (Robinson, 1974). Thus the iron line is emitted at the point of absorption with weight $w_{Fe} = w_{phot} P_{Fe} Y_{K_\alpha}$.

2.4.6 Compton Scattering

The weight proportion that is Compton scattered is treated in the following way. The scattering of the photon will cause the photon to lose energy due to the recoil effect. The amount depends on the initial energy and the direction of scattering (see Equation 2.6). To select the angle of scattering, the rejection technique is used. A random direction is selected and the differential cross section $\frac{d\sigma}{d\Omega}$ (see Equation 2.5) calculated. A random number $x \in (0,1)$ is selected and compared with

$$\Phi = \frac{\frac{d\sigma}{d\Omega}}{\left(\frac{d\sigma}{d\Omega}\right)_{max}} . \tag{2.21}$$

where $\left(\frac{d\sigma}{d\Omega}\right)_{max}$ corresponds to the most probable scattering angle. If $x \leq \Phi$, then the angle corresponding to $\frac{d\sigma}{d\Omega}$ is used. If not, the process is repeated until a direction is chosen. This particular Monte Carlo process is not efficient in terms of CPU time. The direction of scattering chosen will determine the new energy and direction of the photon.

The direction and energy of the photon will determine the optical depth to the edge of the ejecta. If the weight of the photon falls below some cutoff value ϵ, where ϵ is typically $\sim 10^{-9}$, then this photon is terminated and takes no more part in the simulation. The lower the value of ϵ, the better the statistical result, however computational time increases. Clearly, within the operation of a computer the two paths of evolution cannot be followed simultaneously. Instead, the proportion of weight pertaining to photoabsorption is stored, along with information about position in the ejecta and time of storing. When the proportional weight that has been Compton scattered falls below ϵ, then an iron line with w_{Fe} is emitted at the position and time of absorption and interacts within the ejecta. This procedure is followed until the value of the weight falls below ϵ. The process is repeated until all of the stored photoabsorbed photons are emitted. The proportional weight which escapes the ejecta is binned according to its energy and the time at which it escapes. A logical flow chart of the whole computational procedure is shown in Figures 2-6, 2-7 and 2-8.

It must be remembered that the supernova ejecta is expanding so that the zone boundaries are in fact expanding. Figure 2-9 shows the reduction of the Thomson optical depth, defined in Section 1.5.1 by Equation 1.7, measured from the centre to the boundary of the ejecta as it expands. Thus the computational procedure outlined occurs within the context of an expanding envelope and the subsequent increasing of zone boundaries and lowering of overall ejecta density.

It is assumed that the ejecta is stationary for the time between photon interactions in the ejecta (i.e. Compton scattering and photoabsorption). This is since the expansion velocity of the outer envelope is $\sim 1/10$ the velocity of a photon and therefore the ejecta density will not alter appreciably between interactions. This implies that τ_P and τ_C will remain approximately constant for the time between interactions. After each photon interaction, the ejecta is expanded by the amount it would have if it had been expanding continuously during the time between the previous photon interaction and the present one. This implies new zone boundaries and densities which are then used to calculate the next path length in the ejecta according to Section 2.4.3. Thus the ejecta expands in small discrete steps, the size of which depends on the individual path lengths between photon interactions.

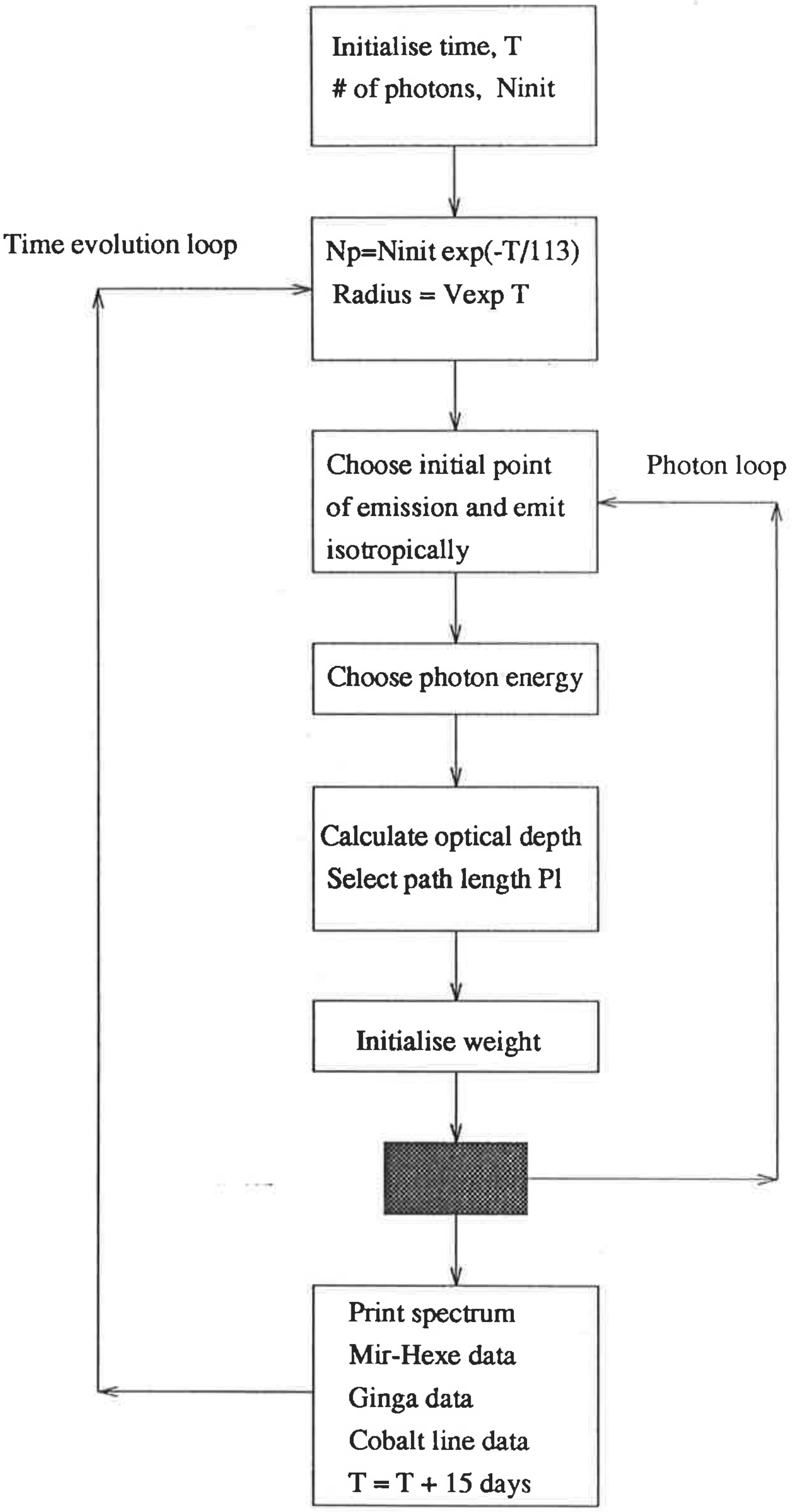

Figure 2-6: Logical flow chart of the simulation of X-ray and γ-ray transmission through SN 1987A ejecta. Main program body.

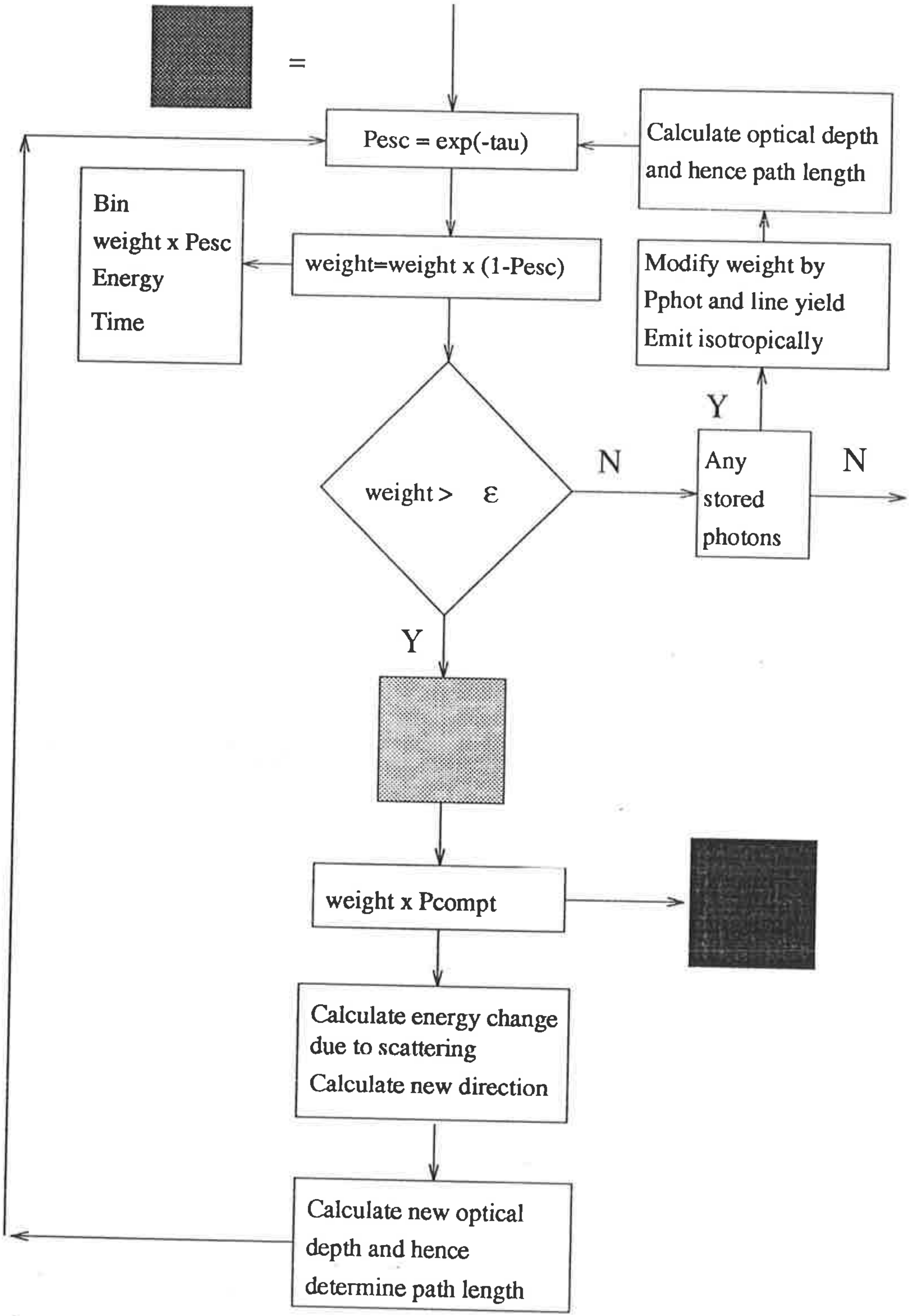

Figure 2-7: Logical flow chart of the simulation of X-ray and γ-ray transmission through SN 1987A ejecta. Selection between photoabsorption and Compton scattering.

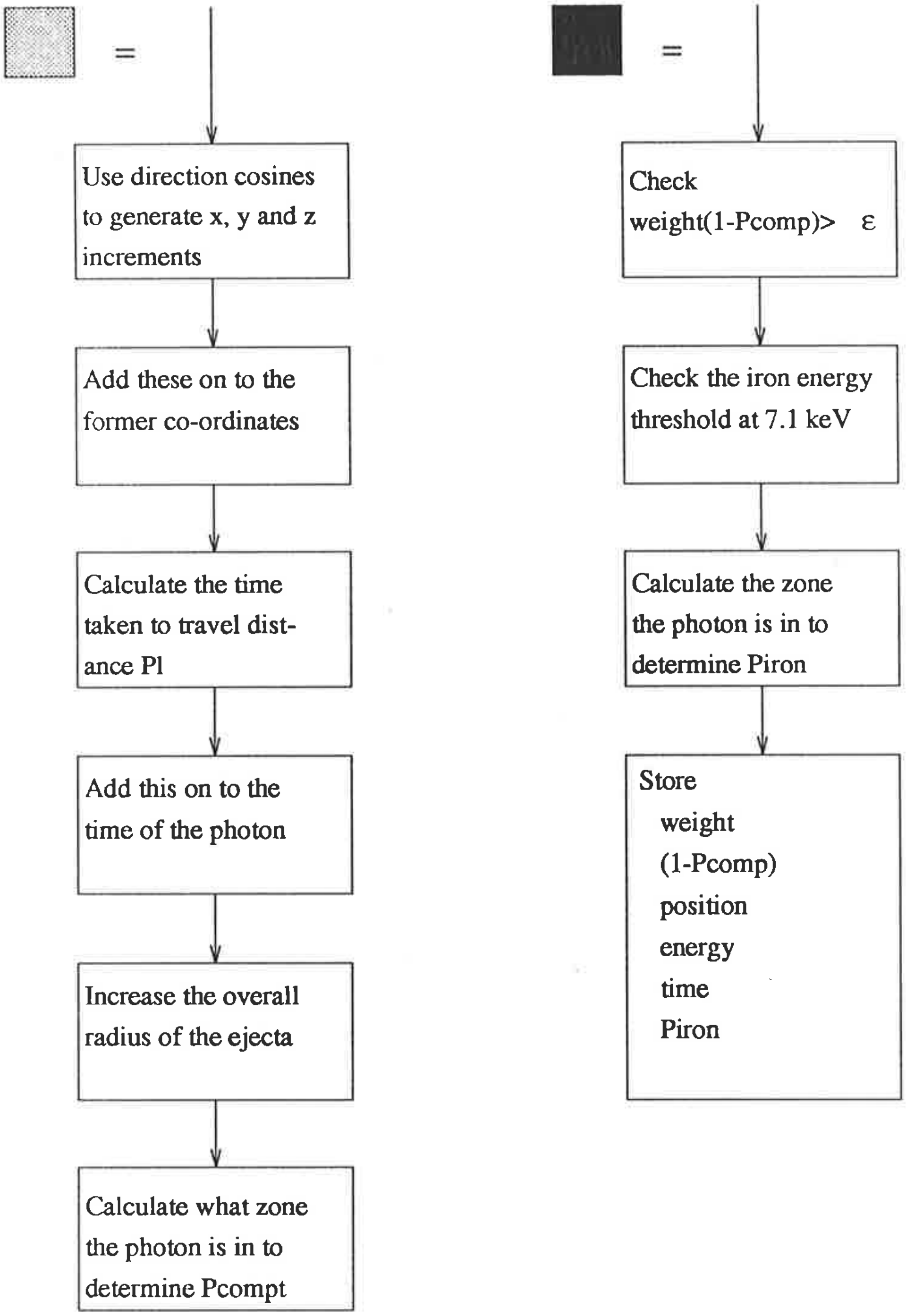

Figure 2-8: Logical flow chart of the simulation of X-ray and γ-ray transmission through SN 1987A ejecta. Shaded box: propagation of photon throughout the ejecta. Solid box: iron line storing procedure.

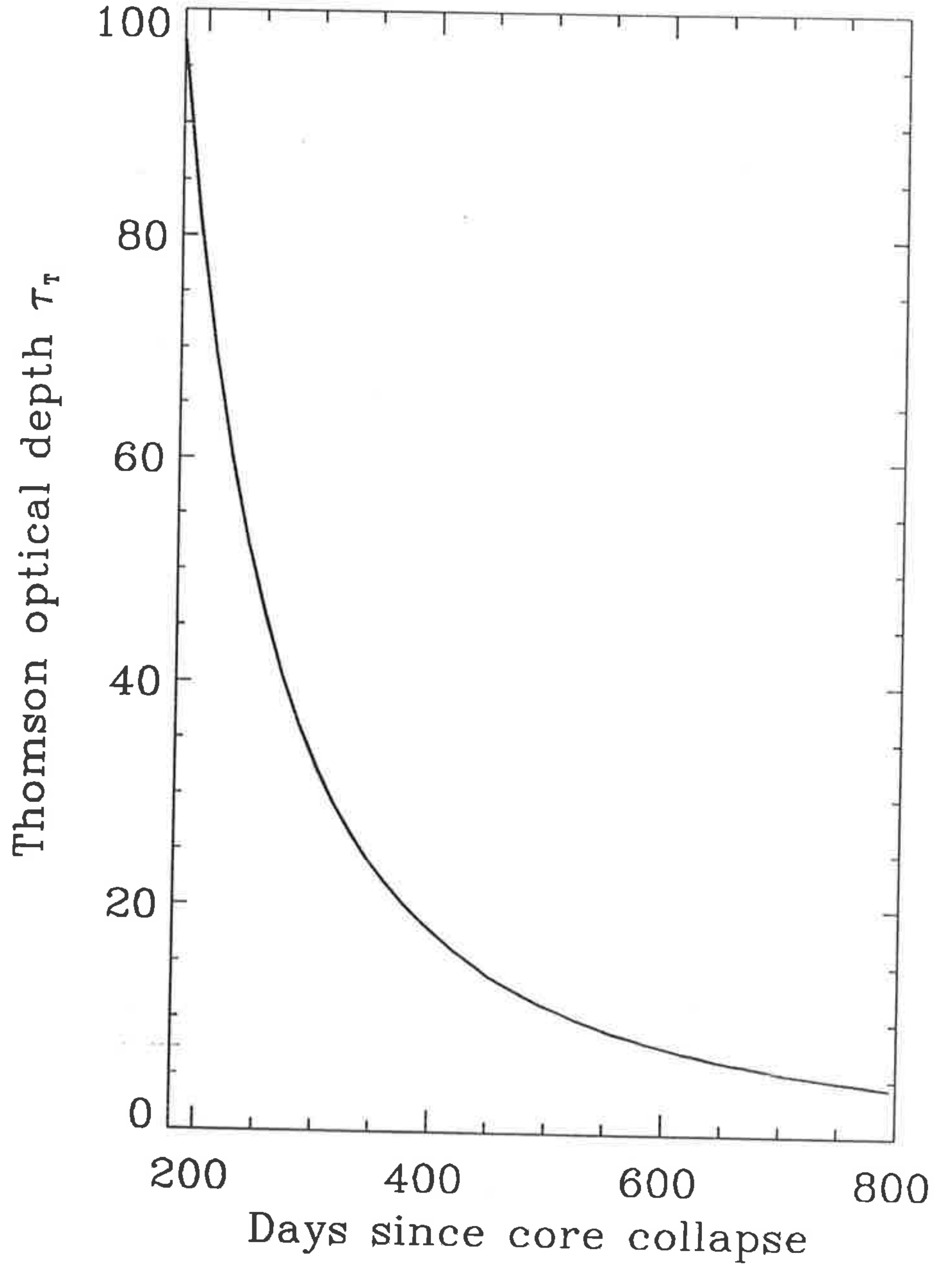

Figure 2-9: Thomson cross section for model 10HMM (ave) calculated according to Equation 2.10 with the Thomson cross section substituted for the Klein-Nishina cross section.

Chapter 3

Effects on X-ray Emission from SN 1987A of Fragmented Ejecta

3.1 Introduction

The results from simulations of X-ray and γ-ray emissions using model 10HMM (ave) are presented here. Some discrepancies with observations are noted. Likely causes for these are discussed, the main cause being the fragmentation of the supernova ejecta. The evidence for this is presented and a method for simulating the effect on X-ray and γ-ray lightcurves is developed. It is shown that some "clumpiness" within the supernova ejecta can ensure that the simulations better agree with observations. Further, the positioning and extent of this fragmentation agrees with theoretical constraints on the instabilities which evolve in the supernova ejecta.

3.2 Results from Initial Simulations

Figures 3-1, 3-2 and 3-3 display the results of the simulation discussed in Chapter 2. This does not incorporate any simulation of clumping. The simulation was begun at 180 days after core collapse. The number of photons used at this epoch was ten thousand. The γ-ray line results (Figure 3-1) are compared with measurements from the gamma-ray spectrometer (GRS) aboard the Solar Maximum Mission (SMM) (Leising and Share, 1990). This instrument was launched in 1980 to observe the Sun.

The GRS consists of seven 3" × 3" NaI detectors and is sensitive to γ-rays in the energy range of 0.3–8.5 MeV with an energy resolution of 6.4% FWHM at 1.0 MeV (for a further review of the detector see Share *et al.* (1988)). As can be seen, the experimental observations are reproduced by the simulation results. The exponential decay is well modelled.

The X-ray lightcurves and spectra are compared with results from the Mir-Hexe (High Energy X-ray Experiment) telescope, which on August 10^{th} 1987 detected hard X-ray radiation at the 10σ level from the neighbourhood of SN 1987A in the Large Magellanic Cloud (LMC) (Syunyaev *et al.*, 1987a; Syunyaev *et al.*, 1987b). The Mir-Hexe telescope is located as part of the International Roentgen Observatory, aboard the *Kvant* module attached to the *Mir* space station. The telescope is sensitive to the 15–200 keV energy range and consists of NaI/CsI phoswich scintillators. There are three other detectors which form part of the Roentgen Observatory. They are the TTM (coded-mask imaging spectrometer), GSPC (gas scintillation proportional counter) and the Russian detector Pulsar X-1.

Pulsar X-1 provides information on the harder section of the X-ray spectrum of SN 1987A. This detector is optimised to the 50–1000 keV energy range. Both Pulsar X-1 and the Mir-Hexe detector provide the spectral data with which the simulations will be compared. The spectral data is well modelled by the Monte Carlo simulation (see Figure 3-2). The spectrum resulting from Compton scattering of the γ-ray emission gives the correct spectral index. A feature of the X-ray spectrum, unfortunately not measured, is the Iron K-α emission line at 6.4 keV. The simulated X-ray lightcurve in the energy range 15–45 keV is too low after 270 days (Figure 3-3). This is not exhibited in the 45–200 keV energy range, where results from the simulation agree well with the experimental observations. The fact that this discrepancy occurs at low energies implies that this low flux could be related to the degree of photoabsorption occurring within the ejecta.

To increase the simulated flux, the metallicity of the ejecta could be lowered. This would reduce the overall photoabsorption at low energies (< 30 keV) and possibly account for the discrepancy between the simulation and observations. However, to increase the flux in the 15–45 keV energy band by a factor of two at 400 days past core collapse, implies a substantial lowering of ejecta metallicity (Mastichiadis, Kylafis and Ventura, 1988). Another possibility is that the heavy elements may not be distributed homogeneously in the ejecta, but instead are clumped together. This would imply that the heavy elements would be distributed in pockets and that, on average, photons would have less chance of interacting within these regions, thus reducing the overall amount of photoabsorption. The evidence for such clumping of heavy elements is discussed in the next section.

3.3 Evidence For Heavy Element Clumping in SN 1987A

Direct evidence for fragmentation of the ejecta of SN 1987A comes from high resolution spectroscopy of emission lines in the far-infrared energy range. The velocity structure of the Doppler broadened lines can identify the position of the emitting material, because the supernova expansion is homologous (i.e. velocity of material is proportional to radius in the ejecta). This is the case for low optical depths in the emission regions. Far-infrared spectroscopy is very useful in determining abundances of heavy elements such as Fe, Co, Si and O, since all of these elements emit in this energy range.

3.3.1 Observation of Infrared Emission From iron

Moseley *et al.* (1989) observed the many fine structure lines in the 16–30 μm region emitted by Fe I, Fe II and Fe III at 270 days past core collapse. These are expected to be the main ionisation states of iron in the supernova ejecta. As mentioned previously the line width velocity will determine the position of the emitting material within the ejecta. The presence of forbidden transition lines will also give an indication as to the temperature of the emitting region. Thus the mass of iron within the ejecta $M(\mathrm{Fe})$ can be calculated by adding the mass derived from the emissivity of the three ionisation stages i.e.

$$M(\mathrm{Fe}) = M(\mathrm{Fe\ I}) + M(\mathrm{Fe\ II}) + M(\mathrm{Fe\ III})\ . \qquad (3.1)$$

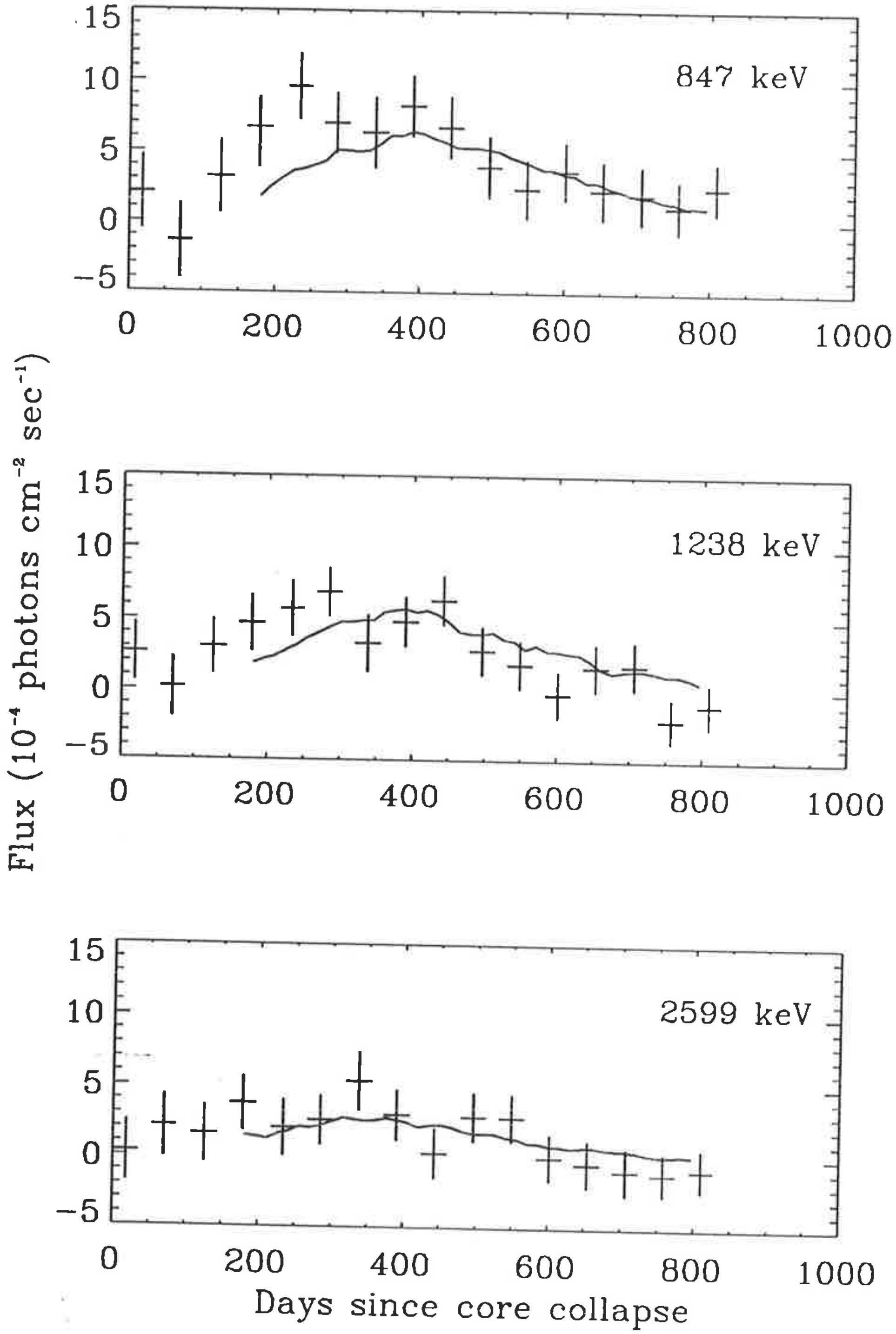

Figure 3-1: Simulation results for the γ-ray lightcurves at 847, 1238 and 2599 keV from SN 1987A. The experimental results are from Leising and Share (1990) and are shown by the discrete points. Errors in the experimental data are indicated at the 1σ level.

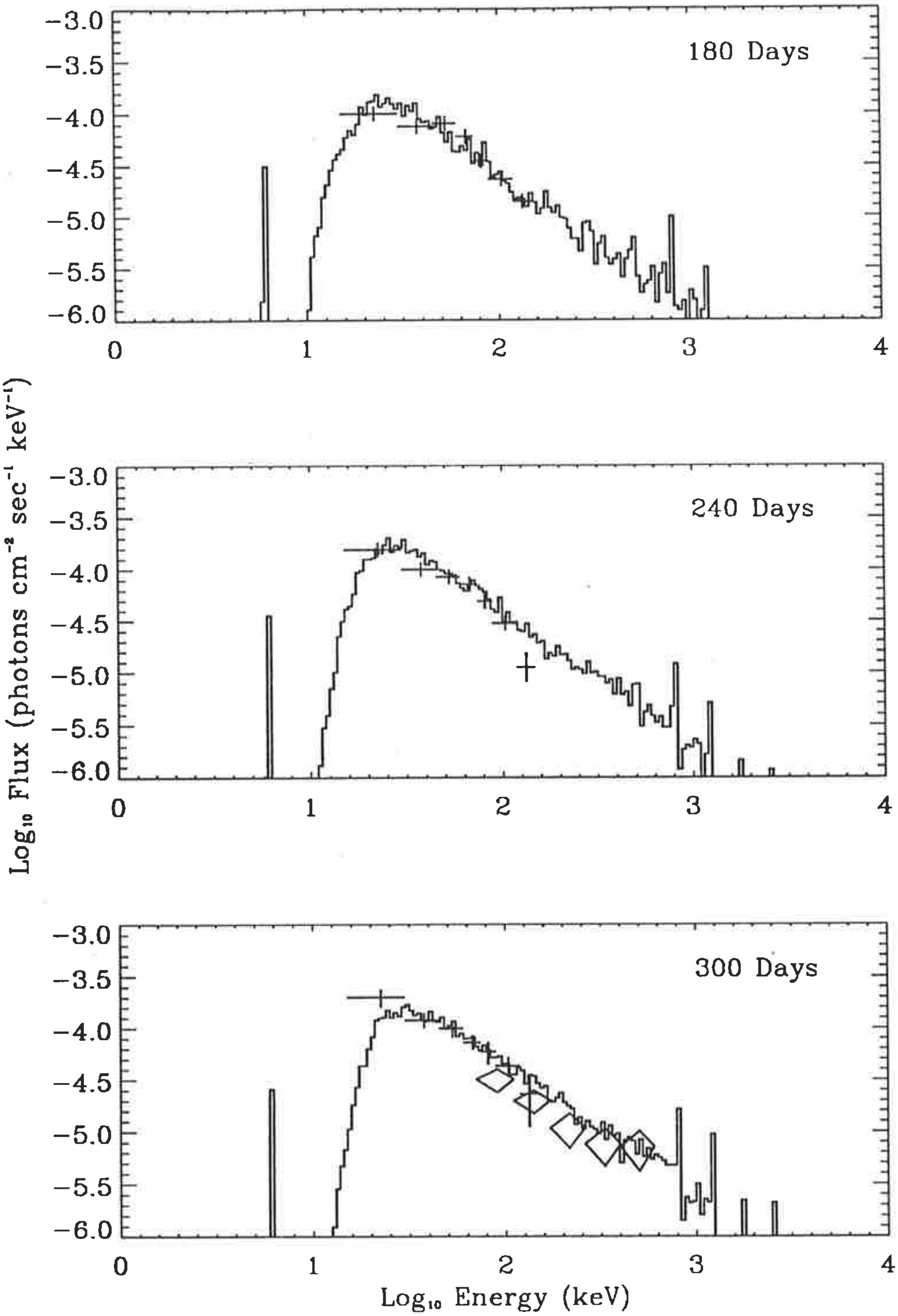

Figure 3-2: Simulation results for the X-ray spectra at three different epochs of 180, 240 and 300 days from SN 1987A. The experimental results are from Syunyaev *et al.* (1988). The crosses are results from the Hexe telescope and the rhomboids are from Pulsar X-1 measurements. Errors in the experimental data are indicated at the 1σ level.

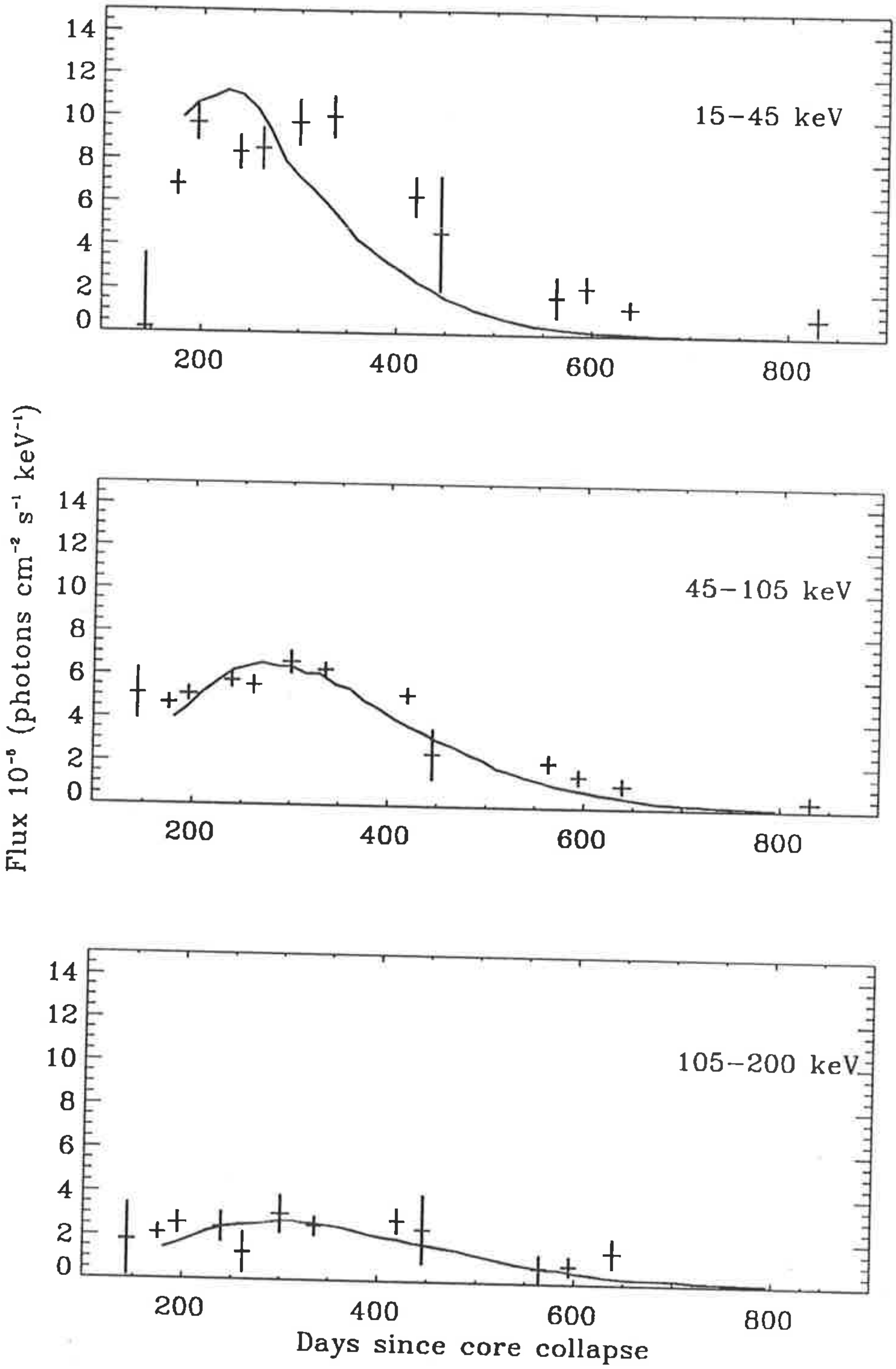

Figure 3-3: Simulation results for the X-ray lightcurves in 15–200 keV range from SN 1987A. Experimental results are taken from Syunyaev *et al.* (1990). The measurements are taken by the Hexe telescope and errors in the experimental data are indicated at the 1σ level.

Moseley *et al.* (1989) report a result for $M(\mathrm{Fe})$ of $0.021 \pm 0.0015 M_{\odot}$ at 270 days. This is lower by a factor of three than the amount of Fe expected from the decay of ^{56}Co. Possible reasons for the lower amount of Fe emission is that the temperature of the ejecta may be too hot or cold. This has been determined to be unlikely (Moseley *et al.*, 1989). Another possibility is that the optical depth at the wavelength of one or all of the Fe far infra-red emission lines is high, thus reducing the flux and hence the derived mass. This was shown not to be the fact in normal circumstances by considering a homogeneous distribution of mass in a homologously expanding environment and calculating the line optical depths at 270 days. These were found to be small, implying that the inferred mass should be close to that calculated from the decay of ^{56}Co. The fact that a homogeneous distribution of iron cannot explain the reduced infrared emission implies that the Fe is distributed non-uniformly throughout the emitting region. One possibility is that 2/3 of the iron is centrally condensed within the emission region at high optical depth and the remaining 1/3 is distributed uniformly throughout the emission region. The other possibility is that the iron may be located in clumps and that the iron flux observed comes from the outer regions of these clumps, where the optical depth to the boundary of the clump is small, and also from the interclump regions.

3.3.2 Evidence for Clumping of Iron

Further measurements of the 17.9 and 26.0 μm emission lines of Fe II at 400 days (Haas *et al.*, 1990) showed that the absence of the iron emission was more than likely to be due to the formation of clumps. The small change in the 26 μm flux at day 400, as compared to day 270, implies that the missing iron emission could come from clumps of high optical depth which still have not become transparent i.e. high optical depth clumps were not emitting at day 270 and were still not emitting at day 400. Haas *et al.* (1990) and Spyromilio, Miekle and Allen (1990) found the emission profiles for 26, 17.9 and 1.26 μm to be very similar. These emission profiles show characteristics thought to be due to the fragmentation of the nickel bubble and mixing of this into the outer regions of the ejecta.

The optical depth for the 1.26 μm emission should be small throughout the ejecta. If the missing iron was concentrated in the core, this would ensure that the velocity profile for the 1.26 μm emission would be peaked at low velocities (by the homologous assumption). This velocity profile would be different to the 17.9 and 26 μm emissions which show evidence of iron being mixed out to the outer regions of the ejecta. However this is not the case, they are similar. This once again implies that the missing iron is due to heavy element clumping.

3.4 Modelling the Fragmentation of the Ejecta

Modelling the clumping or fragmentation of the ejecta could be handled in one of two ways. Firstly, the expansion of the ejecta could be simulated, yielding a density profile for the ejecta and this could be used explicitly within the simulation (e.g. Yamada, Kasahara and Nakamura (1989)). Using this method, a fully three dimensional model would have to be developed. The difficulties associated with this first option and also the expected time needed to perform the simulations make the next method more attractive.

Using the second method, parameters such as optical depths and cross sections already calculated according to the methods described in Section 2.4 can be used. These are modified according to relations derived analytically to describe clumping and thus incur little penalty in computing time. Also a 3-dimensional code need not be developed. This second method adopted in modelling the clumpiness within the ejecta has been used by Kumagai *et al.* (1989) to investigate the effects clumping had on the X-rays in the Ginga detection range of 16–28 keV. This method was originally proposed by Bowyer and Field (1969) in order to model the effects of clumpiness within the interstellar medium on soft X-ray fluxes. Here it is applied to the propagation of X-rays through the supernova ejecta.

3.4.1 Analytic Description of Clumping

Consider propagation through the supernova ejecta, which is simplified as a sphere with uniform composition and density. In the ejecta, there exists clumps of material which will vary in size and hence optical depth. Consider i different sizes of clumps.

There is defined to be n_i clumps of type i, each having an optical depth due to photoabsorption of τ_{Pi} and radius a_i. If the passage of X-rays of energy E through the ejecta is considered, then the X-ray transmission through the ejecta averaged over many trajectories will be

$$\langle T \rangle = \frac{\langle I \rangle}{I_0} = \left\langle \exp\left(-\sum_i n_i \tau_{Pi}\right)\right\rangle \; , \tag{3.2}$$

where

$$\tau_{Pi} = \frac{4}{3} a_i n_a \overline{\sigma}_P(E) \; . \tag{3.3}$$

n_a is the number density of nucleons in a clump (assumed constant) and $\overline{\sigma}_P(E)$ is defined as the average photoabsorption cross section for the clump (see Equation 2.8).

The term $\langle T \rangle$ can also be identified with the average column density of the ejecta $\langle N_a \rangle$ by

$$\langle T \rangle = \exp(-\overline{\sigma}_{Pobs}(E)\langle N_a \rangle) \; , \tag{3.4}$$

where

$$\langle N_a \rangle = \left\langle \sum_i n_i \frac{4}{3} a_i n_a \right\rangle \; . \tag{3.5}$$

$\overline{\sigma}_{Pobs}(E)$ is the cross section that would be deduced from assuming a homogeneous ejecta.

The different types of clumps, of number n_i, are assumed to be distributed about a mean value m_i by a Poisson distribution $P(n_i)$. The overall distribution of all of these clumps will be $\prod_i P(n_i)$, since they are independent. This implies that Equation 3.2 can be rewritten as (see Bowyer and Field (1969))

$$\begin{aligned} \langle T \rangle &= \prod_i \sum_{n_i} \exp(-n_i \tau_{Pi}) \\ &= \exp[-\sum_i m_i (1 - \exp(-\tau_{Pi}))] \; . \end{aligned} \tag{3.6}$$

Equation 3.5 can be rewritten as

$$\begin{aligned} \langle N_a \rangle &= \sum_i m_i \frac{4}{3} a_i n_a \\ &= \frac{1}{\overline{\sigma}_P(E)} \sum_i m_i \tau_{Pi} \; . \end{aligned} \tag{3.7}$$

Comparing Equations 3.4 and 3.6 the following relationship is obtained.

$$\frac{\overline{\sigma}_{Pobs}(E)}{\overline{\sigma}_P(E)} = \frac{\sum_i m_i(1 - \exp(-\tau_{Pi}))}{\sum_i m_i \tau_{Pi}} \; . \tag{3.8}$$

Now assuming clumps of only one type with an optical depth of τ_c then

$$\tau_{Pobs} = \left(\frac{1 - \exp(-\tau_c)}{\tau_c} \right) \tau_P \; . \tag{3.9}$$

Therefore to model the clumpiness of the ejecta, the calculated optical depth for photoabsorption is modified according to Equation 3.9 for clumps of optical depth τ_c. The new optical depth τ_{Pobs} is then used to calculate the path length as in Equation 2.16.

At the energies being considered (< 50 keV), the optical depth for photoabsorption is much greater than that for Compton scattering. Because of this, the optical depth calculated due to Compton scattering is not modified by clumping. Physically, this can be thought of as the clumps being of high metallicity, so that a photon interacting with a clump is by far more likely to be photoabsorbed rather than Compton scattered. It should be emphasised that this model does not simulate the effect of the density variations within the ejecta, but rather the effect of concentrating the metallicity of zones within the clumps. This is considered to be possible since the clumps are thought to be of high metallicity and is supported by the observation of infrared emission from iron within the supernova ejecta (see Section 3.3.2). These concentrations could be created by a Rayleigh-Taylor instability created by the shock passing through the pre-supernova envelope as first suggested by Chevalier (1976) and also suggested for SN 1987A by Arnett, Fryxell and Muller (1989), Benz and Thielemann (1990), Müller *et al.* (1989), Nagasawa, Nakamura and Miyama (1988) and Woosley (1988). Another mechanism suggested by Woosley (1988) is that the heat generated by the radioactive decay of ^{56}Ni and ^{56}Co will boil off bubbles of heavy elements from the inner regions of the ejecta, where the concentration of these elements is high.

3.4.2 Computational Procedure

At the beginning of the simulation ($t = 180$ days after core collapse) a value was chosen for the optical depth of the clump τ_c. In this case the values chosen were 75, 25, and 8.33, which are equivalent to the values chosen in Kumagai *et al.* (1989). As the ejecta expands homologously, then τ_c will scale as $1/(\text{time})^2$ as with the rest of the ejecta. The zone to which clumping occurs was chosen as the free parameter in order to test the effect of changing the radius out to which clumping extends. As part of later simulations the inner boundary of fragmentation was also varied. As previously, the energy and time at which photons escape the envelope are stored.

3.5 Results.

The results presented here show the dependence of the X-ray and γ-ray emission from SN 1987A on the value chosen for the optical depth of the clump and the zone out to which clumping occurs. To determine the position of zones within the supernova ejecta, refer back to Table 2.3. The lightcurves for the 847, 1238 and 2599 keV lines were identical to those in Figure 3-1 and so plots of these are not shown. This is to be expected, since at these energies photoabsorption is negligible. Most of the interest lies in the Mir-Hexe lightcurves, particularly in the 15–45 keV energy range.

3.5.1 Variation of the Outer Boundary of Clumping

The results for extending clumping out to zones 4, 6, 8 and 10 are shown in Figs 3-4, 3-5, 3-6 and 3-7. No effect at all is shown for clumping out to zone 4. When clumping extends out to zone 6, there is some difference with varying τ_c. At clumping to zone 8, the effect of modifying the optical depth can be plainly seen. Clumping out to zone 8 with an optical depth $\tau_c = 75$ provides a much better fit than the original simulation. For clumping extending out to zone 10, the peak flux in the 15–45 keV range is significantly higher than that observed. In the 45–200 keV energy range, no significant changes can be seen with variation in the free parameters in the simulation. Table 3.1 shows the associated χ^2 statistics for the 15–200 keV energy range, which confirms the results evidenced by the plots.

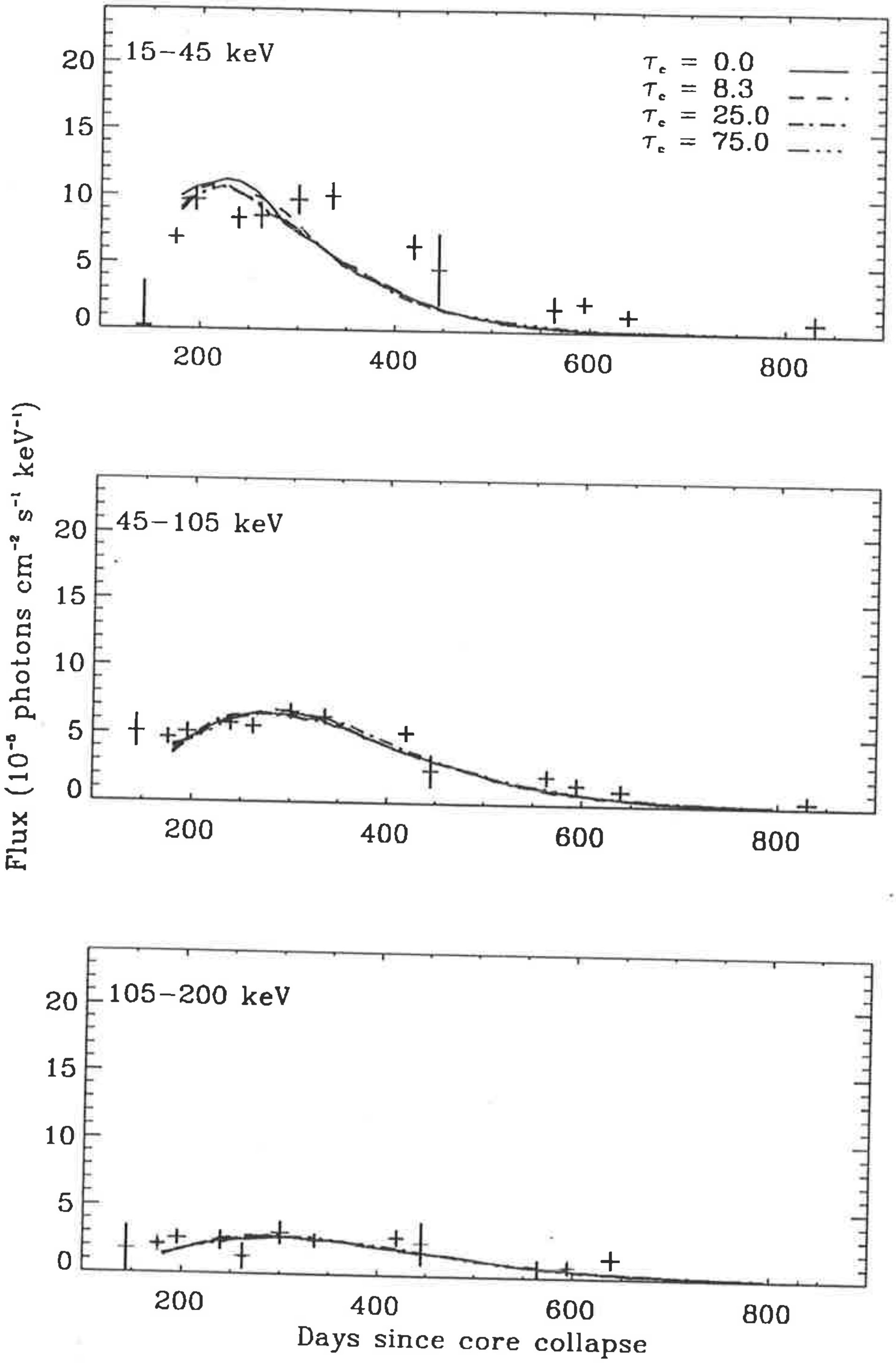

Figure 3-4: Simulation results for X-ray lightcurves in the energy range 15–205 keV energy range with the inclusion of clumping of the ejecta to zone 4 (equivalent to ∼ 8% of the radius of the ejecta). The solid line corresponds to no clumping, –– to $\tau_c = 8.3$, – · – to $\tau_c = 25.0$ and – · ·· to $\tau_c = 75.0$.

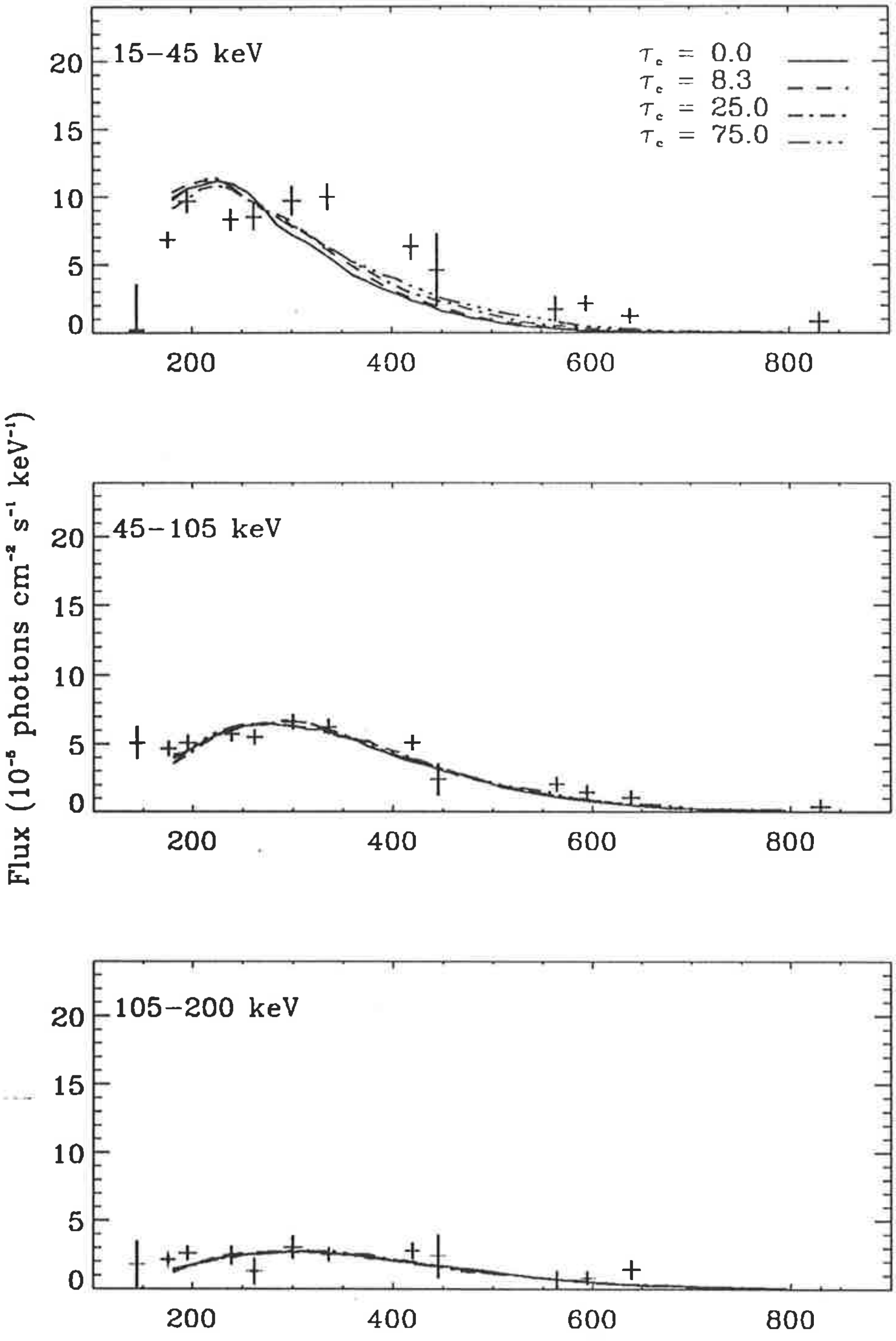

Figure 3-5: Simulation results for X-ray lightcurves in the energy range 15–205 keV energy range with the inclusion of clumping of the ejecta to zone 6 (equivalent to $\sim 11\%$ of the radius of the ejecta). The solid line corresponds to no clumping, —— to $\tau_c = 8.3$, — · — to $\tau_c = 25.0$ and — · ·· to $\tau_c = 75.0$.

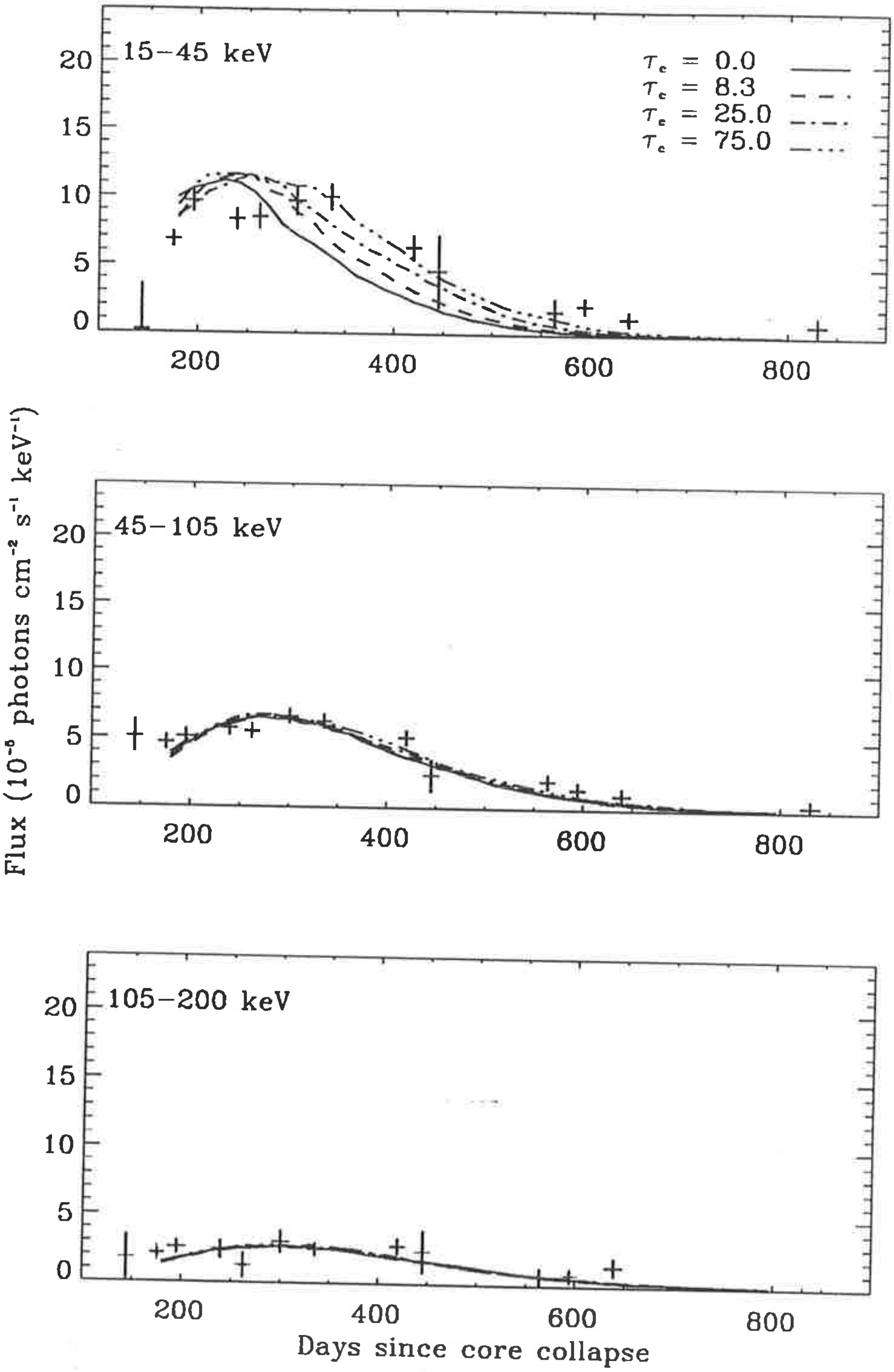

Figure 3-6: Simulation results for X-ray lightcurves in the energy range 15–205 keV energy range with the inclusion of clumping of the ejecta to zone 8 (equivalent to ∼ 19% of the radius of the ejecta). The solid line corresponds to no clumping, −− to $\tau_c = 8.3$, − · − to $\tau_c = 25.0$ and − · ·· to $\tau_c = 75.0$.

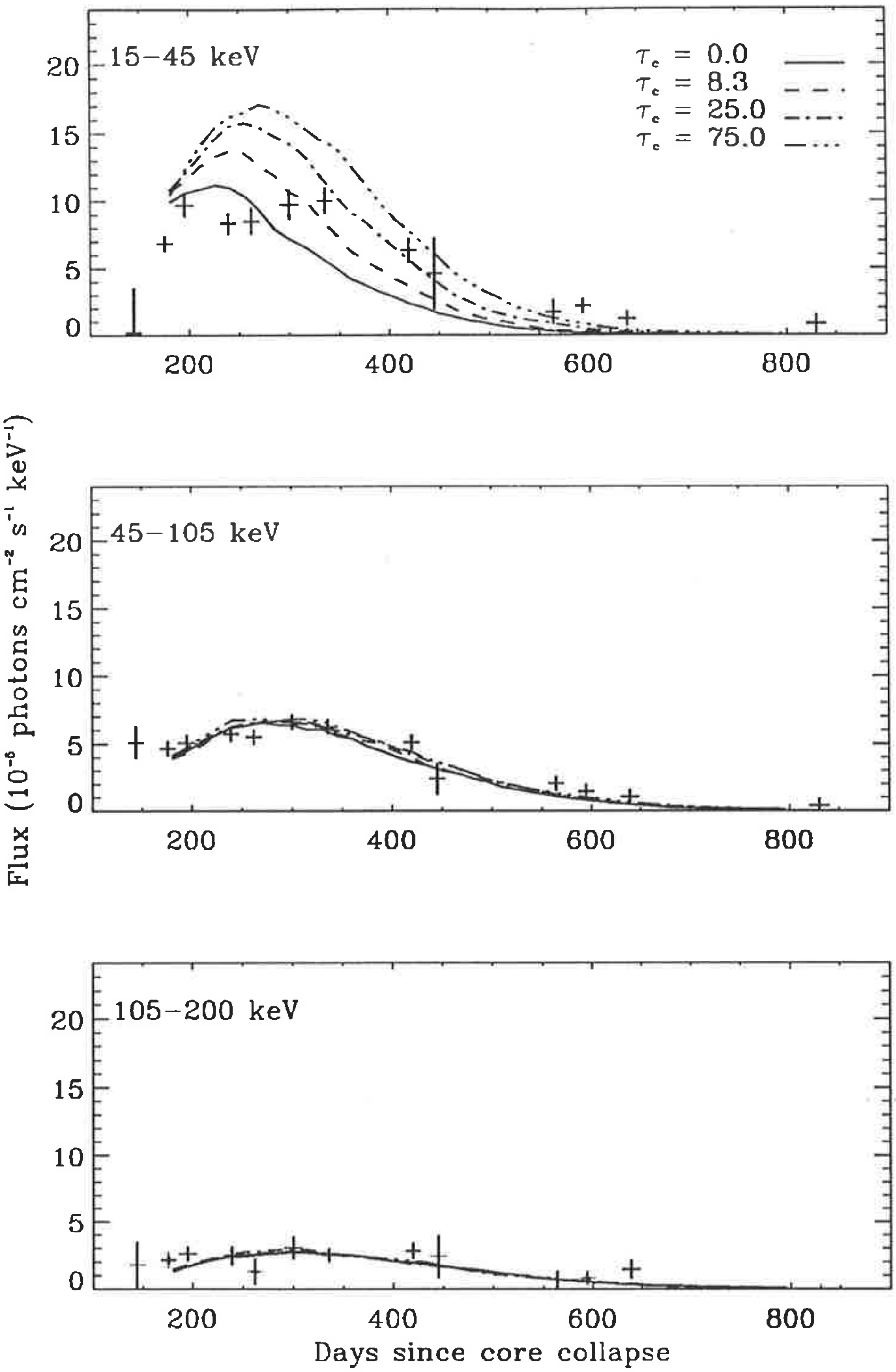

Figure 3-7: Simulation results for X-ray lightcurves in the energy range 15–205 keV energy range with the inclusion of clumping of the ejecta to zone 10 (equivalent to $\sim 23\%$ of the radius of the ejecta). The solid line corresponds to no clumping, –– to $\tau_c = 8.3$, $- \cdot -$ to $\tau_c = 25.0$ and $- \cdot \cdot$ to $\tau_c = 75.0$.

Zones	τ_c	15–45 (keV)	45–105 (keV)	105–200 (keV)
0-4	8.33	66	38	10
	25	67	34	10
	75	65	35	10
0-6	8.33	61	35	10
	25	53	32	11
	75	49	30	11
0-8	8.33	62	39	11
	25	43	33	9
	75	37	20	9
0-10	8.33	96	36	9
	25	168	28	11
	75	236	33	9

Table 3.1: χ^2 statistic with 10 degrees of freedom for each energy range showing the effect of changing the zone out to which clumping extends.

3.5.2 Variation of the Inner Boundary of Clumping

Following on from the previous simulations, the dependence on the inner boundary of clumping was investigated. Since clumping out to zone 8 provided the best fit with experimental observation, the effect of changing the inner boundary of fragmentation with that parameter fixed was investigated. As with the previous results, there is excellent agreement in the energy range 45–200 keV, so only results in the 15–45 keV are presented in Figure 3-8.

It is observed from these results that the effect of clumping is largely maintained, even if it only occurs between zones 6–8. Table 3.2 shows the χ^2 statistics for these plots, implying that clumping only in this region is responsible for the change observed in the simulated 15–45 keV X-ray lightcurve.

3.6 Conclusions

3.6.1 Theoretical Predictions for Clumping

The results presented here provide evidence for fragmentation of the supernova ejecta between $\sim .1R_{ejecta}$ (3.5 $M_\odot$) and $\sim .2R_{ejecta}$ (8.5 $M_\odot$), where R_{ejecta} is the outer

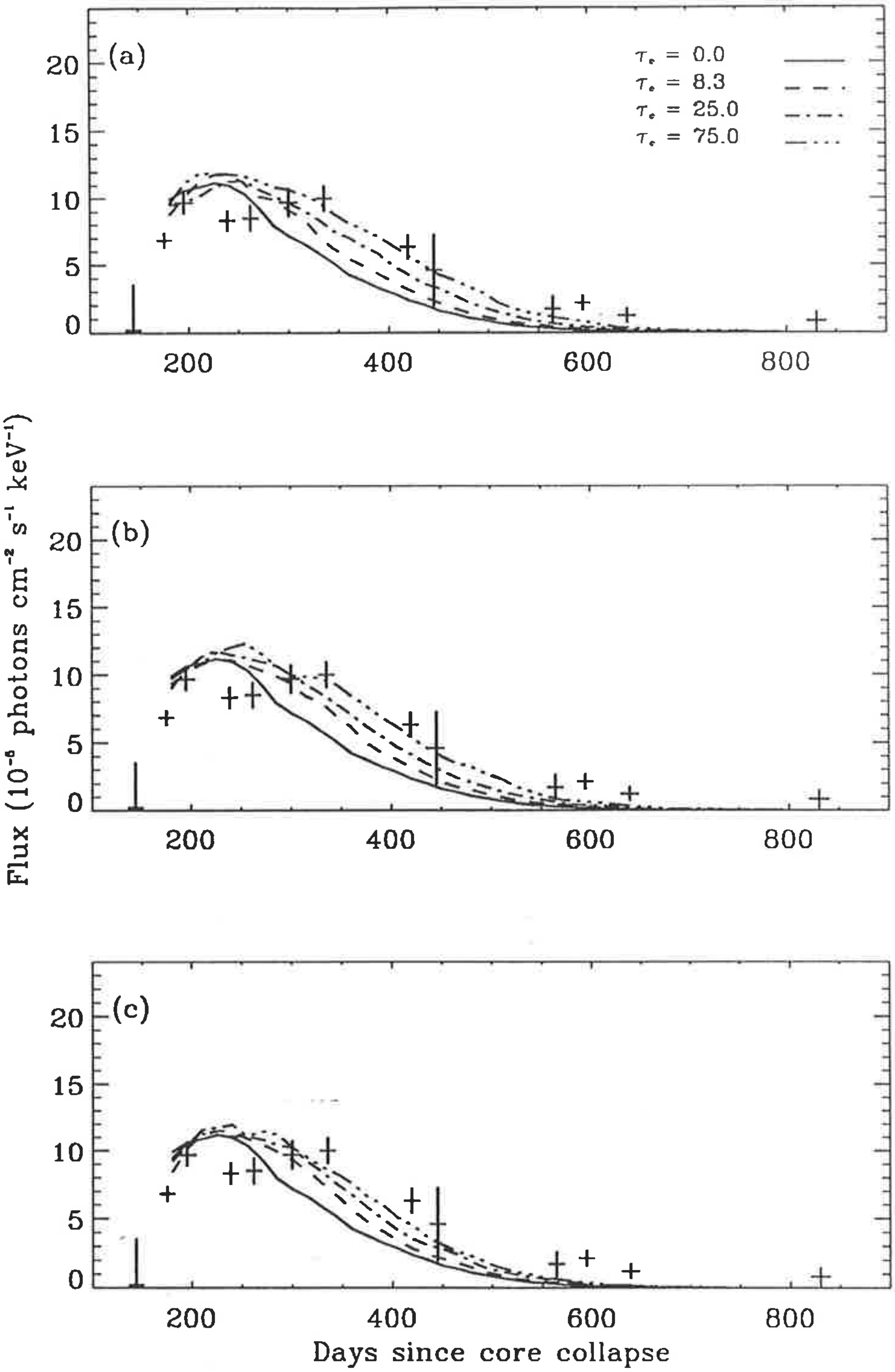

Figure 3-8: Simulation results for X-ray lightcurves in the energy range 15–45 keV energy range with the inclusion of clumping of the ejecta between zones 2-8 (a), 4-8 (b) and 6-8 (c). The solid line corresponds to no clumping, $--$ to $\tau_c = 8.3$, $- \cdot -$ to $\tau_c = 25.0$ and $- \cdot \cdot\cdot$ to $\tau_c = 75.0$.

Zones	τ_c	15–45 (keV)	45–105 (keV)	105–200 (keV)
2-8	8.33	61	30	11
	25	42	34	10
	75	41	22	10
4-8	8.33	49	34	10
	25	45	33	10
	75	45	27	11
6-8	8.33	58	38	10
	25	54	34	10
	75	40	27	10

Table 3.2: χ^2 statistic with 10 degrees of freedom for each energy region showing the effect of changing the inner zone of fragmentation.

radius of the expanding supernova. Clumping extending beyond this radius results in peak X-ray fluxes which are larger than experimental results in the 15–45 keV energy band. This implies that large scale fragmentation, of the type predicted by Nagasawa, Nakamura and Miyama (1988), throughout the envelope is not supported. The above authors investigated the explosion of a 10 $M_\odot$ n=3 polytrope. They found that there is a large degree of clumpiness resulting from the Rayleigh-Taylor instability, extending out to $\sim .8R_{ejecta}$ (14 $M_\odot$), with large explosion energies.

These results were largely refuted, firstly by Benz and Thielemann (1990) who repeated the same calculations and found that an initial 2% density perturbation resulted in only 15–20% density fluctuations, compared to the 400% fluctuations obtained by Nagasawa, Nakamura and Miyama (1988). These results were also confirmed by Müller *et al.* (1989), who concluded that it was unlikely that a shock wave of the type of SN 1987A in a n=3 polytrope would lead to the Rayleigh-Taylor instability on the timescale of the shock propagation through the ejecta. These results implied that a more realistic stellar model should be used, and have subsequently been supported by Yamada, Yoshida and Den (1992) and Yamada, Nakamura and Nomoto (1990), who also find that for a n=3 polytrope no significant Rayleigh-Taylor instability occurs for realistic initial conditions.

It is important to establish whether the results presented here agree with predictions of fragmentation and clumping for realistic supernova models. As the shock wave propagates out through the ejecta the expansion of the inner core is decelerated by the low density envelope. This sets up a reverse shock wave, resulting in a pressure inversion between it and the blast wave. Thus a Rayleigh-Taylor instability sets in at possibly the H/He or He/C+O interface. Arnett, Fryxell and Muller (1989) examine the evidence for the Rayleigh-Taylor instability in a realistic progenitor model of 16 $M_\odot$ and an explosion energy of 2×10^{51} ergs (from Arnett (1987)). Their results for an initial random perturbation of 10%, positioned at random in the ejecta, show a pronounced Rayleigh-Taylor instability (see Figure 3-9), which begins at the trailing edge of the dense mass shell and mixes heavy elements through the hydrogen envelope and hydrogen down to the lower regions of the ejecta. This effectively concentrates the heavy elements. From Figure 3-9 the region of the Rayleigh-Taylor instability can be estimated at the time shown. Using the homologous assumption and assuming an expansion velocity of 1.3×10^7 m.s^{-1} and an initial radius for the progenitor of 3×10^{12} cm, the region of instability is found to be between $\sim .1R_{ejecta}$ and $\sim .2R_{ejecta}$. This agrees well with the results presented in this report.

Other simulations have been carried out (Den, Yoshida and Yamada, 1990; Yamada and Sato, 1991; Yamada, Nakamura and Nomoto, 1990; Yamada, Yoshida and Den, 1992) which also use realistic presupernova models. In this case the models used are M11 and M14 (Itoh *et al.*, 1987; Shigeyama and Nomoto, 1990) These consist of a 6 $M_\odot$ helium core and a 6.7 $M_\odot$ hydrogen rich envelope for model M11, and a 10.3 $M_\odot$ hydrogen rich envelope for M14[1]. The general method of simulation is to propagate the shock in a spherically symmetric manner until it either reaches the He/C+O interface at a Lagrangian mass coordinate of 2.3 $M_\odot$, or the H/He interface which occurs at 4.4 $M_\odot$ and then map the results to a 2 dimensional or 3 dimensional grid. Perturbations of velocity or density are introduced at the interface chosen. Den, Yoshida and Yamada (1990) investigate the effect of introducing perturbations before the H/He or He/C+O interface and find that these die very quickly unless the perturbations are of the order of 30% even with aspherical expansion considered (Yamada and Sato, 1991).

In order for non linear instabilities to evolve at the He/C+O interface, large seed perturbations ($\sim$ 20%) must be assumed. It is found that initial perturbations of 5%

---

[1] The 11 and 14 refer to the mass of the ejecta i.e. helium core + hydrogen envelope - 1.4 $M_\odot$

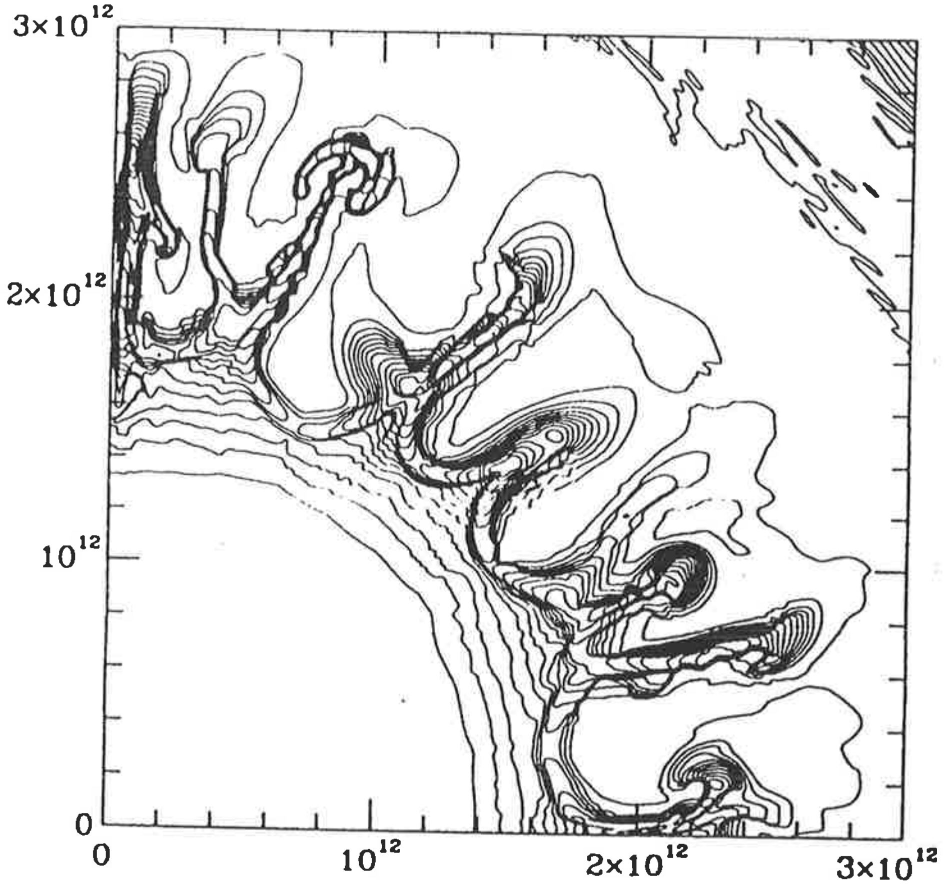

Figure 3-9: Density contours (5% spacing) at 9814 s after explosion. The progenitor model used is a 15 $M_\odot$ B3 supergiant with a radius of 3×10^{12} cm. The Rayleigh-Taylor instability mixes heavier elements into the helium mantle and the hydrogen envelope. Variations in density have already reached a factor of two at this early stage and this will increase with the added effect of heating from ^{56}Ni decay (from Arnett, Fryxell and Muller (1989)). Axis scales are in cm.

at the H/He interface, which could be due to asymmetries in the shock wave or some pockets of thermonuclear activity, lead to the Rayleigh-Taylor instability. This agrees with the results presented here which suggest clumping occurring between 4–9 $M_{\odot}$. It must be remembered that the hydrodynamical simulations reviewed here do not look at the structure of the ejecta at 180 days past core collapse, which is the time at which the results presented in this report begin. At this time initial instabilities will have grown, and possibly be enhanced by the expansion resulting from ^{56}Ni decay. Woosley (1988) suggested that the energy released by the radioactive decay of ^{56}Ni in the inner dense regions heats this region and drives a pressure wave into the overlaying one. This boiling off of the nickel would be expected to occur at times of approximately the decay constant of ^{56}Ni (8.8 days) after the core collapse. This instability due to radioactive decay occurs on much larger time scales than the hydrodynamic instability, which occurs on the order of 1000 seconds after core bounce, and could thus add to any initial instability.

3.6.2 Chevalier's Condition

It is interesting to apply Chevalier's condition (Chevalier, 1976) for the stability of a one-dimensional hydrodynamic flow, namely

$$\left(\frac{\partial P}{\partial r}\right)\left(\frac{\partial \rho}{\partial r}\right) < 0, \tag{3.10}$$

where P is the pressure, r is the radius and ρ is the density, to the published model 10HMM on which the model in this report is based. Between zones 29 and 35 of model 10HMM, the Chevalier criterion for instability is satisfied. This region corresponds to zones 6 to 8 in model 10HMM (ave). Therefore the region of instability indicated is the same region as that arrived at from investigating the effects of fragmentation on the X-ray lightcurve.

3.6.3 Comparison with other Simulations and Data

The results from model 10HMM (ave) are now compared with the Ginga X-ray results in the 16–26 keV energy band. Figure 3-10 shows the X-ray lightcurve for clumping out to zones 6, 8 and 10, compared with no clumping. The results are essentially the same as those obtained for the Mir-Hexe energy band of 15–45 keV. Fragmentation to zone 8 gives the best fit. However, the late time evolution (past 500 days) is not well modelled by the simulation results. Figure 3-11 shows how the dependence on the inner boundary of fragmentation is also the same as that for the Mir-Hexe results.

Kumagai *et al.* (1989) have done a similar simulation using model M11. They find that fragmentation out to 6 $M_\odot$ and with $\tau_c = 75$ at 180 days gave the best result. This discrepancy between their result and that presented here can be understood by realising that the hydrogen envelope of model M11 is ~ 2.5 $M_\odot$ less than of model 10HMM (ave). This implies an overall lower optical depth, which in turn reduces the extent out to which clumping occurs. Kumagai *et al.* (1989) find that there exists a contribution to the 16–26 keV energy band from the decay of ^{57}Co during this time. However no contribution from ^{57}Co was found when it was included in the present simulations and consequently it wasn't considered. The non-contribution of ^{57}Co decay photons in this period is also due to the larger size of the hydrogen envelope used in model 10HMM (ave) compared to M11.

3.6.4 Conclusion

In conclusion, it is found that large scale fragmentation of the type predicted by Nagasawa, Nakamura and Miyama (1988) is ruled out by these results. The X-ray flux in the 15–45 keV energy range can be used to set a limit on the fragmentation. It is found that fragmentation out to greater than .2 of the ejecta radius results in fluxes in the 15–45 keV band being higher than those observed. Concentration of the heavier elements into clumps is favoured, rather than fragmentation of the ejecta as a whole. If the Compton optical depth were reduced by virtue of all elements being clumped together, the results obtained for the X-ray spectra would be softer, and the overall γ-ray line emission fluxes would be higher. This is not borne out in the results, which show that the high energy spectra and γ-ray line emission are reproduced by the original simulation without the introduction of clumping.

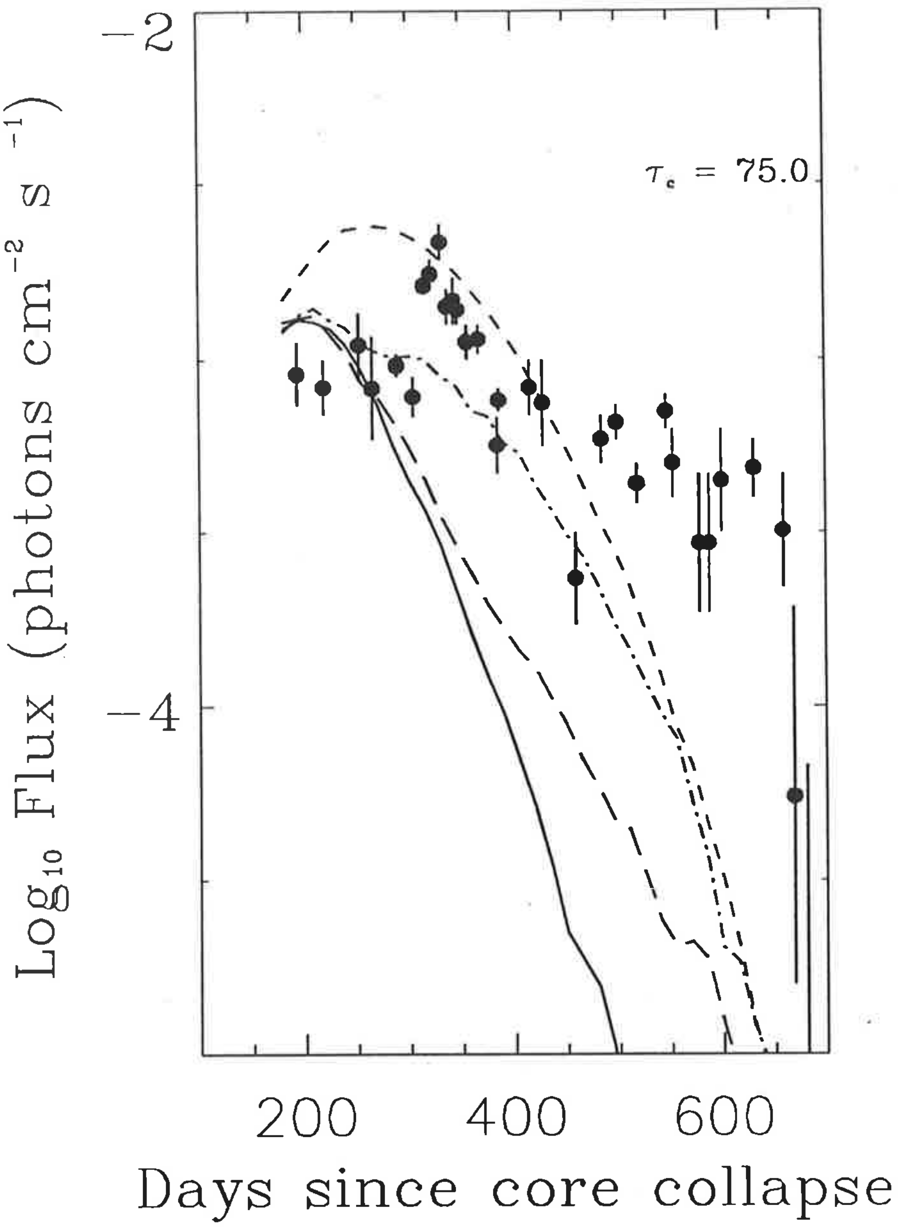

Figure 3-10: Simulation results for X-ray lightcurves in the energy range 16–26 keV energy range. Experimental results are from the Ginga satellite (Kumagai *et al.*, 1989) and errors are indicated at the 1σ level. The solid line corresponds to no clumping, – – to clumping out to zone 6, — · — clumping out to to zone 8 and - - clumping out to zone 10.

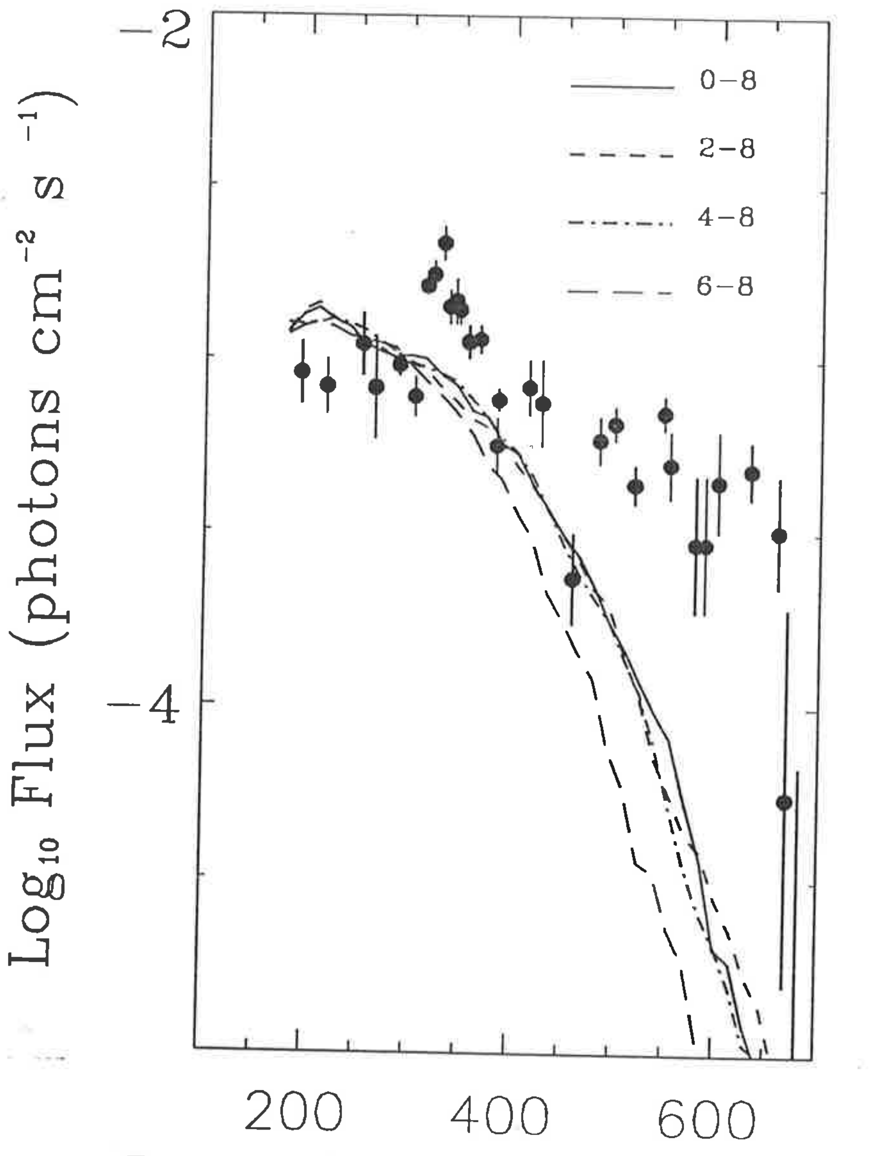

Figure 3-11: Simulation results for X-ray lightcurves in the energy range 16–26 keV energy range. Experimental results are from the Ginga satellite (Kumagai *et al.*, 1989) and errors are indicated at the 1σ level. The solid line corresponds to clumping out to zone 8, - - to clumping between zones 2 and 8, — · — between zones 4 and 8 and — — to clumping between zones 6 and 8.

Chapter 4

An Overview of Cosmic Rays

4.1 Introduction

Cosmic rays consist of high energy nuclei, subatomic particles and photons which are of extraterrestrial origin. These cosmic rays are thought to originate in our galaxy excepting possibly those of energy greater than $\sim 10^{19}$ eV. They propagate from their sources and travel throughout the galaxy, possibly undergoing acceleration along the way. Those that reach earth are detected by a variety of methods ranging from satellite detection to the measuring of subatomic showers formed when high energy cosmic rays interact with the earth's atmosphere.

Cosmic rays have been detected with energies between 10^9–10^{20} eV. This makes cosmic rays the source of the most energetic particles known thus far. For example the Super-conducting Super Collider has been designed to accelerate particles to 40 TeV in the centre of mass frame ($E_{lab} = 8 \times 10^{17}$ eV), still a factor of at least 100 below the energy of the highest energy cosmic rays. Many properties of the cosmic ray flux are still not known. Details regarding their origin, acceleration, propagation and composition are all areas of active research. The following is a brief review of some of the important results from cosmic ray research.

4.2 History of Cosmic Ray Research

In 1912, Victor Hess investigated the variation of the atmosphere's ionisation level with height. This ionisation was thought to be caused by some ambient radiation and was measured by an electroscope. Using a balloon, he noted that whilst the degree of ionisation decreased for the first 700 metres of the ascent, it then increased rapidly at higher altitudes. Hess assumed that this ionisation was due to some extra-terrestrial radiation bombarding the earth (Giacconi *et al.*, 1962). At this time the three known types of ionising radiation were α, β and γ. Of these, γ-radiation was known to be the most penetrating. Thus it was assumed that the extraterrestrial radiation was a type of "ultra γ-radiation". These were termed cosmic rays by Millikan in 1926.

When Clay (1927) investigated the variation of the cosmic radiation with latitude, he found that there was a decrease in the equatorial regions, relative to measurements at higher latitudes. This effect had been predicted by Störmer in 1914, who investigated the passage of charged particles in the geomagnetic field. Further observations (Alvarez and Compton, 1933; Johnson, 1933) showed that there existed an excess of cosmic rays west of zenith, as compared to the east. This effect is expected if cosmic rays are positively charged.

The nature of the cosmic radiation was investigated, using a cloud chamber, by Skobelzyn (1929). He found that cosmic ray particles arrive in individual swarms or showers. Anderson (1933) found that these showers contained both positive and negative electrons. Work by Rossi (1933) confirmed the existence of these showers, by observing coincidences between three Geiger-Muller counters arranged in a triangle. Later in 1938, Kolhörster, Matthes and Webber (1938) and Auger, Maze and Grivet-Mayer (1938), observed air showers which extended over distances of 300 metres. This implied a primary cosmic ray particle energy of $\sim 10^{15}$ eV, which was much larger than thought possible at the time. At these large energies exotic particles were discovered such as κ-mesons and λ particles. Protons (Powell, Fowler and Perkin, 1959), γ-rays (Clark, Garmire and Kraushaar, 1968), heavy elements , positrons, electrons (Giacconi *et al.*, 1962), and nuclei heavier than iron (Fowler *et al.*, 1967) have all been now discovered in the primary cosmic ray flux.

4.3 Properties of the Cosmic Ray Flux

Cosmic rays of energies between 10^9 and 10^{15} eV are detected using both balloon and satellite borne detectors. Above an energy of 10^{15} eV, the low flux of cosmic rays requires detection by indirect methods. This involves the observation of Extensive Air Showers (hereafter EAS) formed when a cosmic ray interacts with the earth's atmosphere (see Chapter 6). Whilst below $\sim 10^{15}$ eV measurements of the properties of cosmic rays are well defined, above 10^{15} eV properties of the primary flux are less well known. This is primarily because of the indirect method of detection.

4.3.1 Energy Spectrum

The cosmic ray energy spectrum is usually expressed as either a differential or integral energy spectrum. Figure 4-1 shows the integral energy spectrum $N(>E)$, for cosmic rays with energy in the range 10^{12}–10^{20} eV. $N(>E)$ is defined as the number of cosmic rays greater than energy E, in units of $\mathrm{m^{-2}\ s^{-1}\ sr^{-1}}$. Expressed in terms of a differential spectrum (in units of $\mathrm{m^{-2}\ s^{-1}\ sr^{-1}\ eV^{-1}}$), the cosmic ray energy spectrum peaks at ~ 1 GeV (Simpson, 1983a) and continues to $\sim 3 \times 10^{15}$ eV with a slope of -2.7. At $\sim$ 3–5 $\times 10^{15}$ eV, the differential energy spectrum steepens with a change in differential slope to $\sim$ -3.0. This is termed the "knee" of the cosmic ray energy spectrum. Between the energies of 10^{16} and 10^{18} eV, experimental results agree with a uniform spectrum with a differential slope of $\sim$ -3.0 (Baltrusaitis *et al.*, 1988; Lawrence, Reid and Watson, 1991; Nagano *et al.*, 1992). Above 10^{19} eV the energy spectrum is much well less known. As can be appreciated by inspecting Figure 4-1, the approximate cosmic ray flux above 10^{19} eV corresponds to $\sim 1\ \mathrm{km^{-2}\ sr^{-1}\ year^{-1}}$. Initial experimental results found a steepening above 4×10^{19} eV (Krasilnikov *et al.*, 1983). In contradiction to this, results from Haverah Park (Lawrence, Reid and Watson, 1991), the Fly's Eye experiment (Cooper *et al.*, 1991a), the Yakutsk array (Efimov *et al.*, 1991) and Akeno (Nagano *et al.*, 1992) imply a flatter differential spectrum above $\sim 6 \times 10^{18}$ eV, with a measured slope between $\sim$ -2.65 and -2.90. This has been termed the "ankle" of the cosmic ray energy spectrum. Analysis of high quality "stereo events" by the Fly's Eye collaboration has also found significant

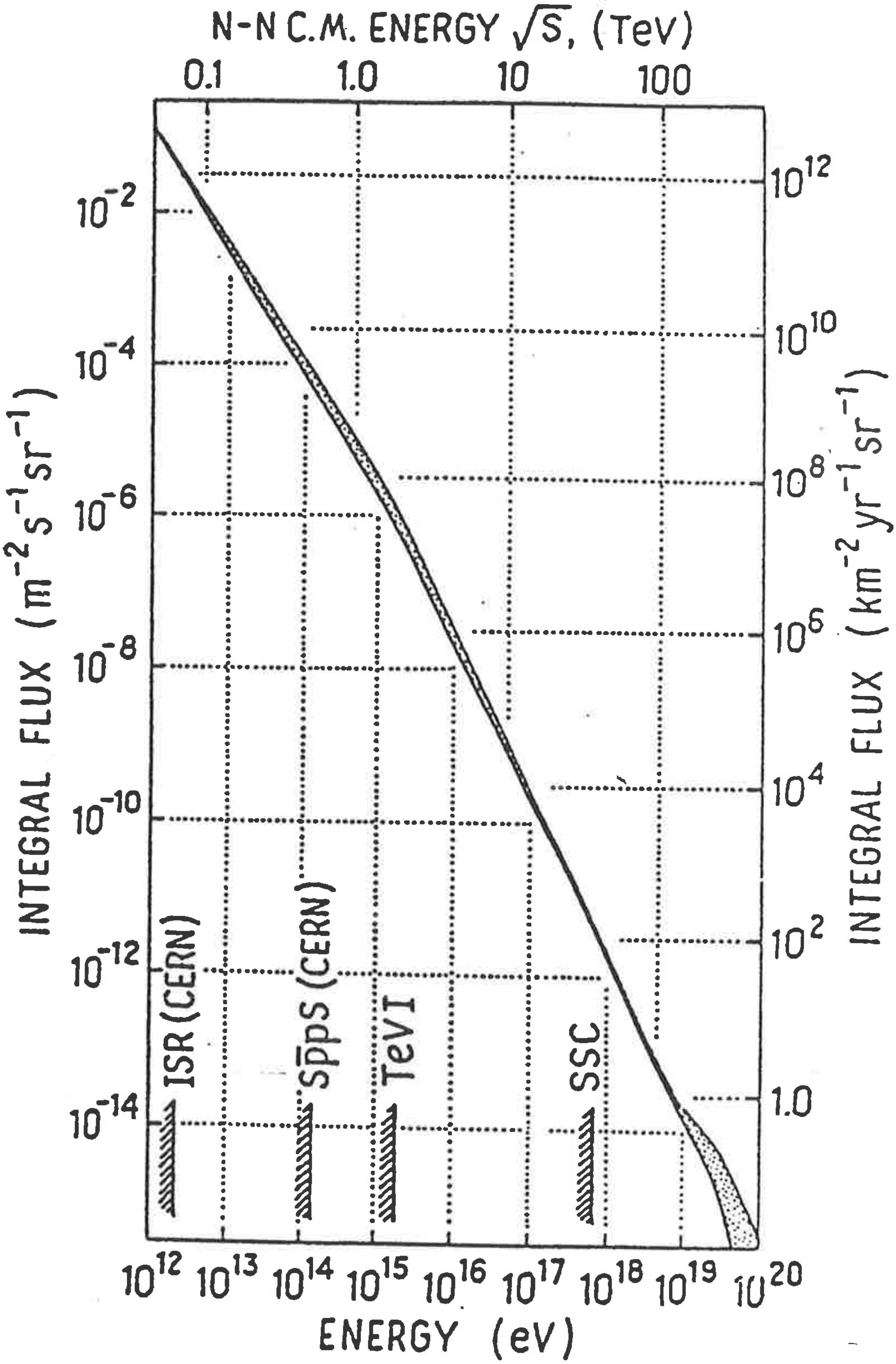

Figure 4-1: The primary cosmic ray particle flux (all particle) as measured at the top of the atmosphere, shown in its integral form. The stippled regions indicate experimental uncertainties. The maximum attainable energies of existing and proposed accelerators are also indicated (from Jones (1985)).

evidence for a dip (or steepening with a spectral index of -3.27) in the spectrum before the "ankle" (Bird *et al.*, 1993c). In this analysis the "ankle" starts at 3×10^{18} eV with the dip occurring between 4×10^{17} eV and the "ankle". There is some evidence for a cutoff in the spectrum just below 10^{20} eV (Baltrusaitis *et al.*, 1985a). However, the paucity of events at this energy make this result inconclusive. To date there has been no further evidence of a cutoff below 10^{20} eV.

Implications of the "knee"

The "knee" of the cosmic ray energy spectrum may be related to a source effect, propagation effect or may be due to some change in the nuclear physics (see Section 6.2.3) which determines the evolution of EAS in this energy region. Some combination of all of these factors cannot be ruled out either. The knee is in the region of the energy spectrum where measurements are made by detecting EAS using ground based particle detectors.

Clay (1985) pointed out that this type of detector would preferentially detect proton initiated showers which have a larger depth of first interaction. These proton initiated showers can fluctuate in such a way as to mimic higher energy events. One effect of this bias is that the measured change in the air shower particle size spectrum of ~ 0.5, which would normally imply the same change in the primary energy spectrum, could actually correspond to a change in the primary energy spectrum of ~ 1.5. This assumes a significant proton flux.

A possible source effect accounting for such a change is that discussed by Protheroe (1984). The discovery of binary system Ultra-High Energy (UHE) γ-ray sources, Cygnus X-3 (Lloyd-Evans *et al.*, 1983; Samorski and Stamm, 1983b) and Vela X-1 (Protheroe, Clay and Gerhardy, 1984), implied that cosmic ray nuclei were being produced with energies up to $\sim 10^{17}$ eV. Protheroe (1984) has shown that if these cosmic ray nuclei can escape the source region (expected to be surrounding the neutron star) they will then be severely attenuated by photo-pion production on the starlight field of the more massive companion. This produces a strong energy absorption feature in the energy spectrum of cosmic rays in the energy range 10^{15}–10^{16} eV.

An alternative source explanation for the "knee" adopts the model of pulsar acceleration of cosmic rays (Ostriker and Gunn, 1969). If the proposed cosmic ray energy spectrum from pulsars is extrapolated to above 10^{14} eV, then particles of these higher energies dominate in the region of the "knee" (Karakula, Osborne and Wdowczyk, 1974; Strong, Wdowczyk and Wolfendale, 1974).

One of the earliest theories to explain the "knee" was to postulate that the propagation or source mechanism for cosmic rays is rigidity dependent (Peters, 1961). The rigidity R, of a cosmic ray is defined as

$$R = \frac{pc}{Ze} \,, \tag{4.1}$$

where p = momentum of cosmic ray

c = velocity of light

Ze = charge of cosmic ray.

Two cosmic rays of different energy, but the same rigidity, have the same gyroradius r_G in a magnetic field. Consider, for example, cosmic rays propagating in some confinement region. The leakage of cosmic rays out of this confinement region would be expected to depend on r_G. Given a population of nuclei, one would expect the protons to leak out first at some energy E where r_G is greater than the confinement region, and progress to iron at $26 \times E$. This stepwise leakage would manifest itself as a sequence of knees over a range of $\sim 30 \times E$. Unfortunately the break in the spectrum at 3×10^{15} eV does seem to be sharper than that predicted by this rigidity dependent theory (Hillas, 1984).

Implications of the "ankle"

If the position of the ankle is accepted at $\sim 2 \times 10^{19}$ eV, this has strong implications for the origins of Extra High Energy (EHE) cosmic rays. After the discovery of the 2.7 K relic microwave background by Penzias and Wilson (1965), Greisen (1966) and Zatsepin and Kuz'min (1966) independently proposed that for protons with energies above 5×10^{19} eV, the dominant energy loss mechanism would be pion photoproduction:

$$p + \gamma \longrightarrow p + \pi^0 \,,$$

$$p + \gamma \longrightarrow n + \pi^+ \ .$$

This would imply a spectrum cutoff (GZK cutoff) between 5 $\times 10^{19}$ eV for cosmic rays which have travelled greater than several interaction lengths (i.e. $\sim$ 50 Mpc).

Hill and Schramm (1985) showed that if a component of the cosmic ray flux was produced by quasi-local extragalactic sources ($d \lesssim$ 50 Mpc), then the energy losses suffered by the high energy cosmic rays from pion photoproduction and pair production would produce a spectral enhancement just below the expected cutoff. This is one possible explanation for the ankle. In subsequent calculations, Hill, Schramm and Walker (1986) concluded from the Fly's Eye data that the spectral enhancement seen above 2×10^{19} eV was not due to a recoil proton pileup resulting from an E^{-3} injection spectrum. They gave two other alternatives for the "ankle": (a) the flattening results from an extragalactic component with a flatter energy spectrum which crosses over the steeper lower energy spectrum or (b) there exists some arbitrary object with an injection spectrum at above 10^{20} eV located at a suitable distance, which after interaction with the microwave background radiation, would give the observed features of the "ankle" (see also Stecker (1989) and Hill, Schramm and Walker (1987)).

The most popular explanation (see Hillas (1981)) for the cosmic ray ankle is the dominance of an extragalactic flux beginning at the position of the ankle. At these energies the rarity of cosmic ray detections makes it difficult to substantiate any claims. If there exists a cutoff in the cosmic ray energy spectrum at $\sim 5 \times 10^{19}$ eV, then one possible conclusion is that the majority of sources for these EHE cosmic rays are extragalactic. An example of such a suggested quasi-local extragalactic source is the Virgo Cluster (Shapiro and Silberberg, 1983), located $\sim$ 20 Mpc from our galaxy. The non existence of a cutoff would imply a galactic origin to EHE cosmic rays.

The measurement of the cosmic ray energy spectrum is only one part of determining the origin of EHE cosmic rays. The EHE cosmic ray composition and anisotropy must also be determined to further narrow theories speculating about EHE cosmic ray origin. This is also true for lower energy cosmic rays.

4.3.2 Composition

The determination of the cosmic ray flux's elemental composition is essential in establishing answers to the origin and propagation of cosmic rays. This discussion of cosmic ray propagation is divided into "Low Energy Composition", for cosmic rays with energies $< 10^{14}$ eV/nucleon where good direct measurement of the primary flux is possible, and "High Energy Composition" where measurements of composition are inferred from the development of EAS.

Low Energy Composition

The general composition of cosmic rays in the energy region 10^{9}–10^{11} eV, where direct measurements can be made, is $\sim$ 98% nuclei and 2% electrons and positrons. The elemental breakup of the nuclear component is $\sim$ 87% hydrogen, 12% helium and 1% heavier nuclei (Simpson, 1983b). Figure 4-2 depicts the cosmic ray elemental abundances for elements with $Z \leq 29$. Elements with $30 < Z < 90$ have been detected (Fowler *et al.*, 1987), but they have abundances of $\sim 10^{-4}$ that of iron. The large abundances of Li, Be and B as compared to their respective solar abundances, are taken as evidence of spallation. These nuclei result from the interaction of C, N and O with the interstellar medium. The enhancement of the elements Sc–Mn is also thought to be due to spallation of iron primaries.

Elemental energy spectra have been measured by both satellite and balloon borne detectors. It has been found that the ratio of secondary spallation products to primary nuclei is approximately energy independent below $\sim 2 \times 10^{9}$ eV/nucleon and then decreases with increasing energy. By assuming a certain energy spectrum at the source and taking into account nuclear spallation, ionisation and nuclear decay, models for cosmic ray propagation can be solved to give the mean escape length from the galaxy λ_e (e.g Protheroe, Ormes and Comstock (1981)). One estimate of λ_e is given by

$$\lambda_e = 14.0\beta \text{ g cm}^{-2} \quad 3 < R \leq 5.5 \text{ GV} ,$$

$$\lambda_e = 34.1\beta R^{-0.60} \text{ g cm}^{-2} \quad R > 5.5 \text{ GV} ,$$

(Engelmann *et al.*, 1990) where $\beta = v/c$. Clearly the rigidity (energy) dependence at

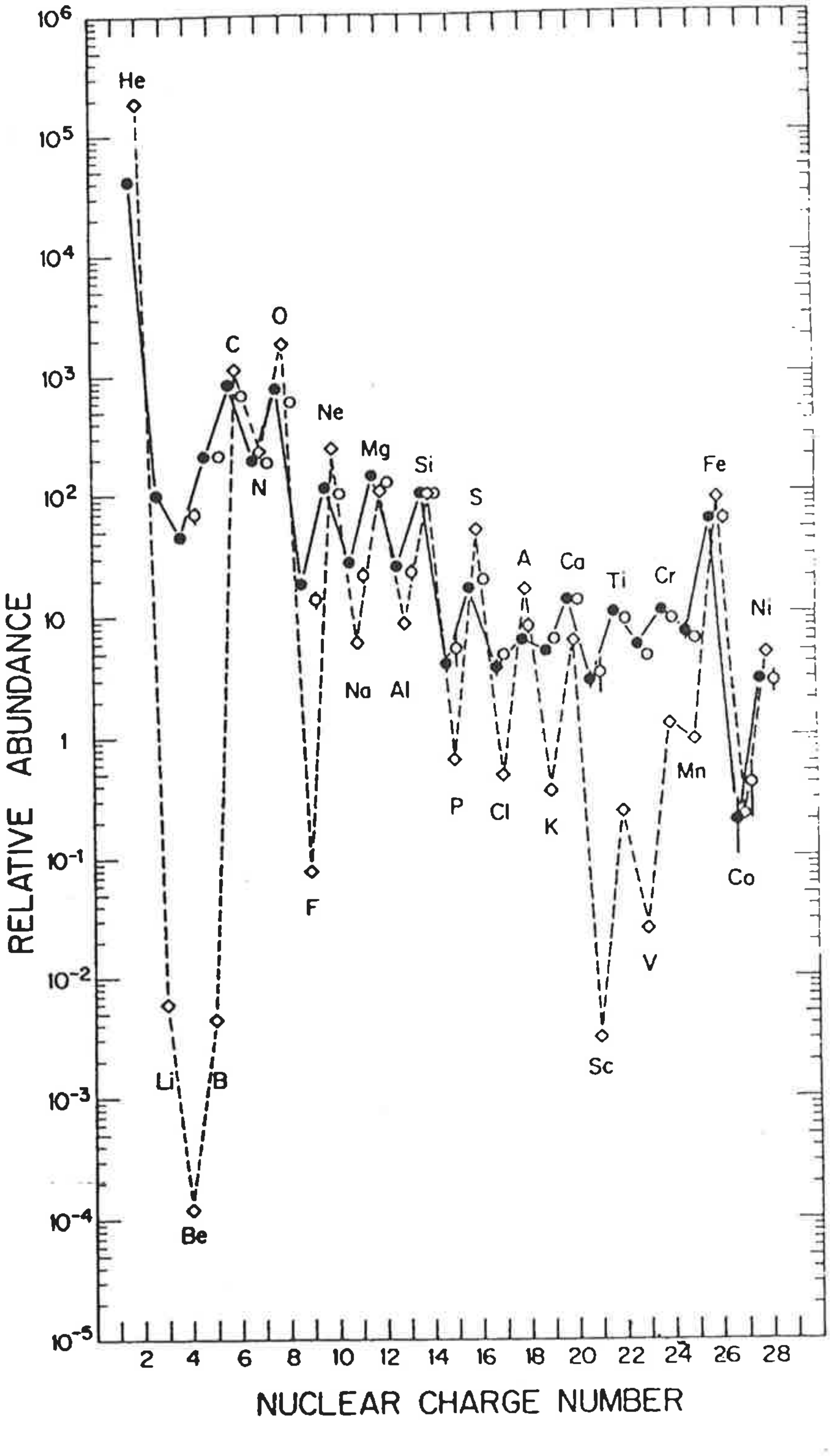

Figure 4-2: The cosmic ray elemental abundances measured at the earth compared with solar system abundances. All abundances are relative to Silicon which is arbitrarily set to 100. Filled circles are lower energy data (70–280 MeV/nucleon), while open circles correspond to higher energy data (1–2 GeV/nucleon). Diamonds represent the solar system abundances (from Simpson (1983b)).

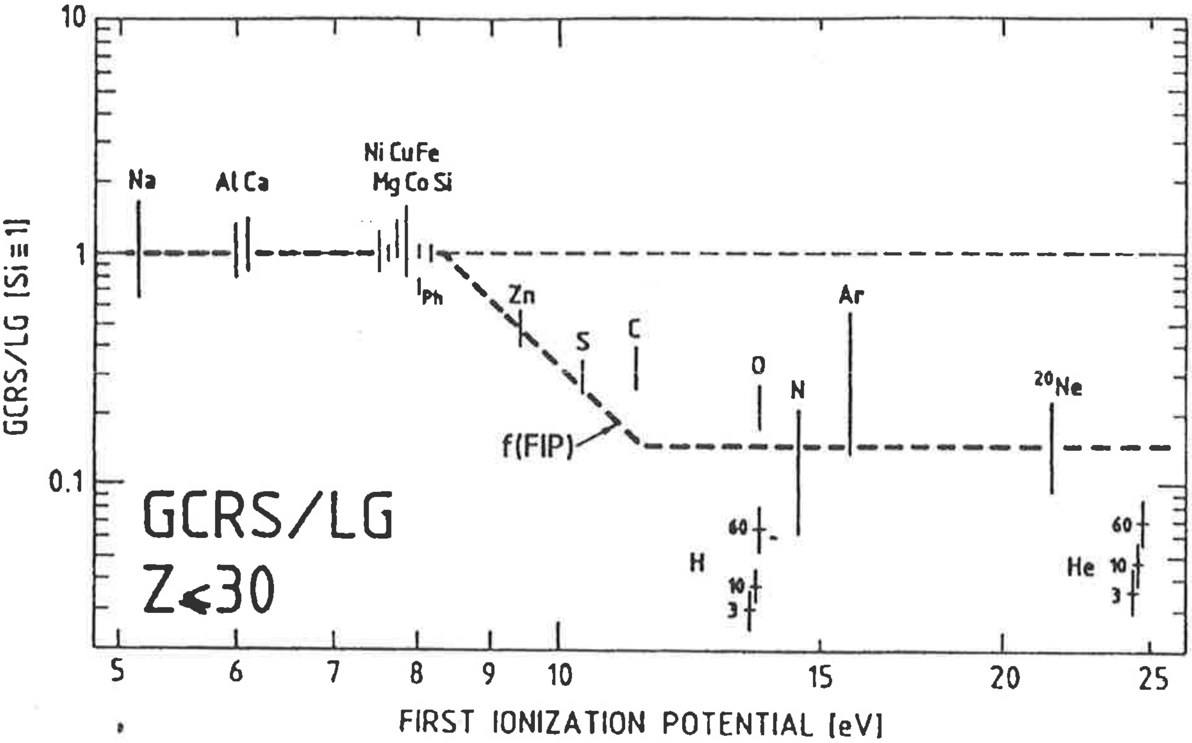

Figure 4-3: Galactic cosmic ray source (GCRS) to local galactic (LG) ratios plotted against first ionisation potential. Hydrogen and helium ratios are shown for measurements at 3, 10 and 60 GeV/nucleon. The bold line corresponds to an adopted function of correlation between the GCRS/LG ratio and the first ionisation potential (from Meyer (1985a)).

higher energies is important in determining the original acceleration energy spectrum (Morfill, Meyer and Lust, 1985; Ormes and Protheroe, 1983).

By taking into account propagation effects and working backwards from observed cosmic ray abundances, the elemental abundances at the sources of cosmic rays can be derived (Meyer, 1985a). It is interesting to note (see Figure 4-3) that the ratio of galactic cosmic ray source (GCRS) abundances and local galactic (LG) abundances, shows a depletion for those elements with a high first ionisation potential (FIP). A similar effect is noted for solar energetic particles (SEP) (Meyer, 1985b) associated with acceleration due to solar phenomena. This implies that there may be some effect at the electron volt level which affects acceleration to higher energies.

The accurate measurement of Be isotope abundances allows an estimate of the age of cosmic rays with energies of ~ 1 GeV to be calculated. ^{10}Be has a half life of 1.5×10^6 years, whereas the other isotopes of Be are stable. Since Be is a secondary particle formed by the interaction of primary cosmic rays with interstellar matter, the

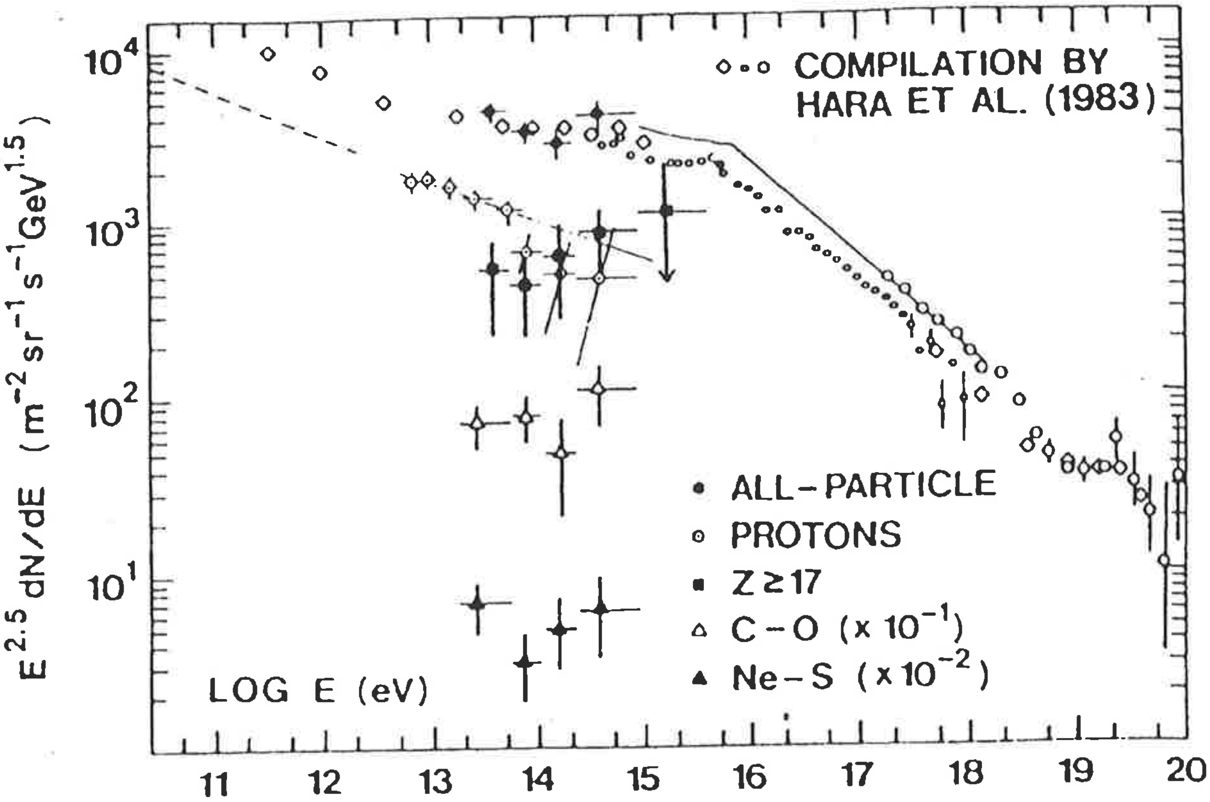

Figure 4-4: The total energy spectra as measured using balloon borne detectors by the JACEE Collaboration. Enhanced intensities of medium to heavier nuclei can be seen from 200 TeV to 930 TeV. The average lnA (mass) of detected cosmic rays at ~ 400 TeV is 2.33 ± 0.27 (from Asakimori *et al.* (1991a)).

theoretical ratio of unstable to stable isotopes of Be can be calculated. Any decay of ^{10}Be will lower this ratio. This results in an estimate for the lower limit for the age of cosmic rays with energies ~ 1 GeV of 1–2 $\times 10^7$ years (Simpson, 1983b). This age gives an indication of the containment time for such cosmic rays. Since the amount of matter traversed by cosmic rays can be found by the degree of spallation observed, the average interstellar density that cosmic rays encounter can be calculated. This is found to be ~ 0.1–0.3 atoms cm^{-3} (Simpson, 1983b). Since the galactic density is ~ 1 atom cm^{-3}, this implies that the cosmic rays must spend significant time in regions of lower than galactic density. One example of such a region is a galactic halo.

The JACEE Collaboration (Japanese-American-Emulsion-Chamber-Experiment) uses balloon borne emulsion chambers with long exposure times to measure cosmic ray composition up to ~ 10^{15} eV. Recent results (Asakimori *et al.*, 1991a; Asakimori *et al.*, 1991b) report that the spectra of medium to heavy nuclei are flatter than the spectra obtained for both H and He (see Figure 4-4). This agrees with other recent measurements of the composition of cosmic rays greater than 10^{10} eV. At $\sim 10^{14}$ eV the primary cosmic ray flux can be represented as the sum of five components (H, He, C–O, Ne–S, A>17) each of equal abundance, with the overall cosmic ray flux becoming progressively heavier as energy increases.

High Energy Composition

At energies greater than 1×10^{15} eV direct measurement of the composition of primary cosmic rays is presently impossible. Thus inferences must be drawn from the detections of cosmic ray air showers. Unfortunately there is as yet no agreement on the composition of primary cosmic rays. Heavy cosmic rays are expected to interact earlier within the atmosphere than protons and consequently the depth in the atmosphere at which the shower size is at its largest, X_{max}, is less than that for a proton. Also the intrinsic fluctuations in the position of X_{max} for individual showers are expected to be less for iron as compared to proton primaries.

Measurements of composition in the energy range 10^{15}–10^{16} eV inferred by observing high energy muons in cosmic ray showers (Yodh *et al.*, 1984), air Čerenkov emission (Dawson, 1985), observation of high energy gamma families (Ren *et al.*, 1988), hadronic analysis of the cores of cosmic ray showers (Freudenreich *et al.*, 1990) and N_μ/N_e (muon to electron) ratios (Châtelet *et al.*, 1991), favour an increase in the proportion of heavy cosmic rays as energy increases. Many analyses (Châtelet *et al.*, 1991; Freudenreich *et al.*, 1990; Ren *et al.*, 1988; Yodh *et al.*, 1984) compare predictions based on theoretical proton-nucleon cross sections which have not been measured but are obtained by extrapolation from low energy accelerator data.

On the other hand, studies of composition based upon muon multiplicities between 3×10^{13}–3×10^{15} eV, using an energy independent two component model, find 83% protons and 17% iron (Cebula *et al.*, 1990). This does seem to be in contradiction with the JACEE results (Asakimori *et al.*, 1991a; Asakimori *et al.*, 1991b). Fichtel and Linsley (1986) suggest that the observed increase in the elongation rate with increasing energy, where the elongation rate (ER) is defined as

$$ER = \frac{d(\langle X_{max} \rangle)}{d \ln E}, \tag{4.2}$$

points to a composition which is becoming increasingly proton enriched between 10^{15}–10^{17} eV. Observations of Čerenkov light parameters reported by Chantler *et al.* (1982), related to X_{max} and fluctuations in X_{max}, found proportions of 60–70% protons and 30–40% iron in the energy region 10^{17}–10^{18} eV. Kifune, Wdowczyk and Wolfendale (1986) found by analysing muon rich events, thought to be produced by showers initiated by heavy nuclei, that the fraction of heavy nuclei ranges from 10% at 10^{15} eV to 3% at 10^{17} eV.

Recent reports have been made by the Fly's Eye group, e.g. (Bird *et al.*, 1993d; Gaisser *et al.*, 1993), using the atmospheric fluorescence technique (Baltrusaitis *et al.*, 1985b) which detects the scintillation light produced by nitrogen molecules in the atmosphere excited by the passage of air shower particles. As opposed to other techniques, the development of the shower can be observed directly and the energy calculated by observing all of the energy deposited in the atmosphere through ionisation. To determine the composition, measured X_{max} distributions are compared with those obtained from modelling the evolution of an air shower and the detector response. Once again this is an indirect indicator of composition, but somewhat less indirect than techniques which rely on measurements sampled at only one point in the shower development. Results from the Fly's Eye group indicate that for a two component fit, iron nuclei make up $\sim 80\%$ of the cosmic-ray flux at 5×10^{17} eV, lowering to $\sim 60\%$ at 10^{18} eV, the rest of the flux being made up of protons (Bird *et al.*, 1993d).

At this stage it would be fair to say that the composition of cosmic rays above 10^{15} eV is not known unequivocally. However the development of more sophisticated cosmic ray shower simulations, actual measurements of interaction cross section by accelerators and the advent of new experiments, such as the HiRes Fly's Eye, will help to answer this important question.

4.3.3 Anisotropy

Chapter 5 deals in detail with the anisotropy of EHE cosmic rays, investigating the effects of magnetic field turbulence and the inclusion of a halo magnetic field. Presented here is a brief review of the experimental measurements to date and methods of analysis.

Cosmic rays are charged particles which propagate in the galactic magnetic field $\vec{B}$ (in μG) with a gyroradius r_G (in pc) defined as

$$r_G = \frac{1.08 E_{\mathrm{PeV}}}{Z \left|\vec{B}\right|} ,$$

where E_{PeV} is energy in units of 10^{15} eV and Z is the atomic charge. Recent measurements of the galactic magnetic field, obtained by analysis of pulsar rotation measures (Chi and Wolfendale, 1990; Rand and Kulkarni, 1989) suggest a magnetic field directed along the spiral arm with a regular component $\left|\vec{B}_{\mathbf{reg}}\right| \sim 2\ \mu$G. Associated with this regular field is a randomly orientated magnetic field $\left|\vec{B}_{\mathbf{ran}}\right|$ with a field strength of $\sim 5\ \mu$G and a typical length scale of ~ 100 pc.

The anisotropy of cosmic rays is directly related to the configuration of the galactic magnetic field. Cosmic rays of low energy (i.e. gyroradii $<< 100$ pc) will be scattered by turbulence in the galactic magnetic field between source and observer. At higher energies ($E \geq 10^{18}$ eV), the gyroradii for protons become greater than the half thickness of the galactic disk. At even higher energies ($E > 10^{20}$ eV), cosmic ray protons from sources within the galaxy would travel in virtually a straight line from their source to the observer. Thus the study of the anisotropy of cosmic rays is important in establishing their origin.

The degree of cosmic ray anisotropy, δ is defined as

$$\delta = \frac{I_{max} - I_{min}}{I_{max} + I_{min}} , \tag{4.3}$$

where I_{max} is the maximum intensity of cosmic rays observed and I_{min} is the minimum. The conventional method for expressing cosmic ray anisotropy is to conduct an harmonic analysis of Right Ascension (RA) for incident cosmic ray showers (Linsley, 1975; Linsley, 1975). This approach is taken because ground based arrays, which are continuously operating, have relatively uniform exposure in RA. Anisotropy is normally quoted as the amplitude of the first and second harmonic with an accompanying phase. The amplitude r of the n^{th} harmonic is defined as

$$r = (a^2 + b^2)^{1/2} , \tag{4.4}$$

where

$$\begin{aligned} a &= \frac{2}{N} \sum_{i=1}^{N} \cos n\alpha_i , \\ b &= \frac{2}{N} \sum_{i=1}^{N} \sin n\alpha_i , \end{aligned}$$

and α_i are the values of RA for N cosmic ray showers. The resultant phase Ψ is defined as

$$\Psi = \begin{cases} \Psi' & \text{if } b > 0,\ a > 0 \\ \Psi' + \pi & \text{if } a < 0 \\ \Psi' + 2\pi & \text{if } b < 0,\ a > 0 \end{cases}$$

for $\Psi' = \arctan(\frac{b}{a})$, $-\frac{\pi}{2} \leq \Psi' \leq \frac{\pi}{2}$.

Figure 4-5 shows the measured first harmonics and associated phases of the cosmic ray flux. At energies below 10^6 GeV the cosmic ray anisotropy is $\sim 0.05\%$ with a relatively constant phase. Above 10^6 GeV, the amplitude of the first harmonic appears to increase as $\sim E^{0.5}$ up to 10^{20} eV and the phase varies rapidly. This change occurs at the approximate position of the "knee" of the cosmic ray energy spectrum. This suggest that the cause of the knee may also be responsible for the observed change in anisotropy. Clay (1987) in his review of cosmic ray anisotropies above 10^{15} eV finds no statistically significant indication of anisotropy. The increase in amplitude of the first harmonic is largely due to the decrease in the number of events analysed at higher energies.

The detection of UHE γ-rays from Cygnus X-3 (Lloyd-Evans *et al.*, 1983; Samorski and Stamm, 1983b) led Wdowczyk and Wolfendale (1984a) to suggest that UHE γ-rays may be contributing to the measured anisotropy below 10^{18} eV. However, a cutoff must be introduced above 10^{17} eV so that the γ-ray flux does not dominate

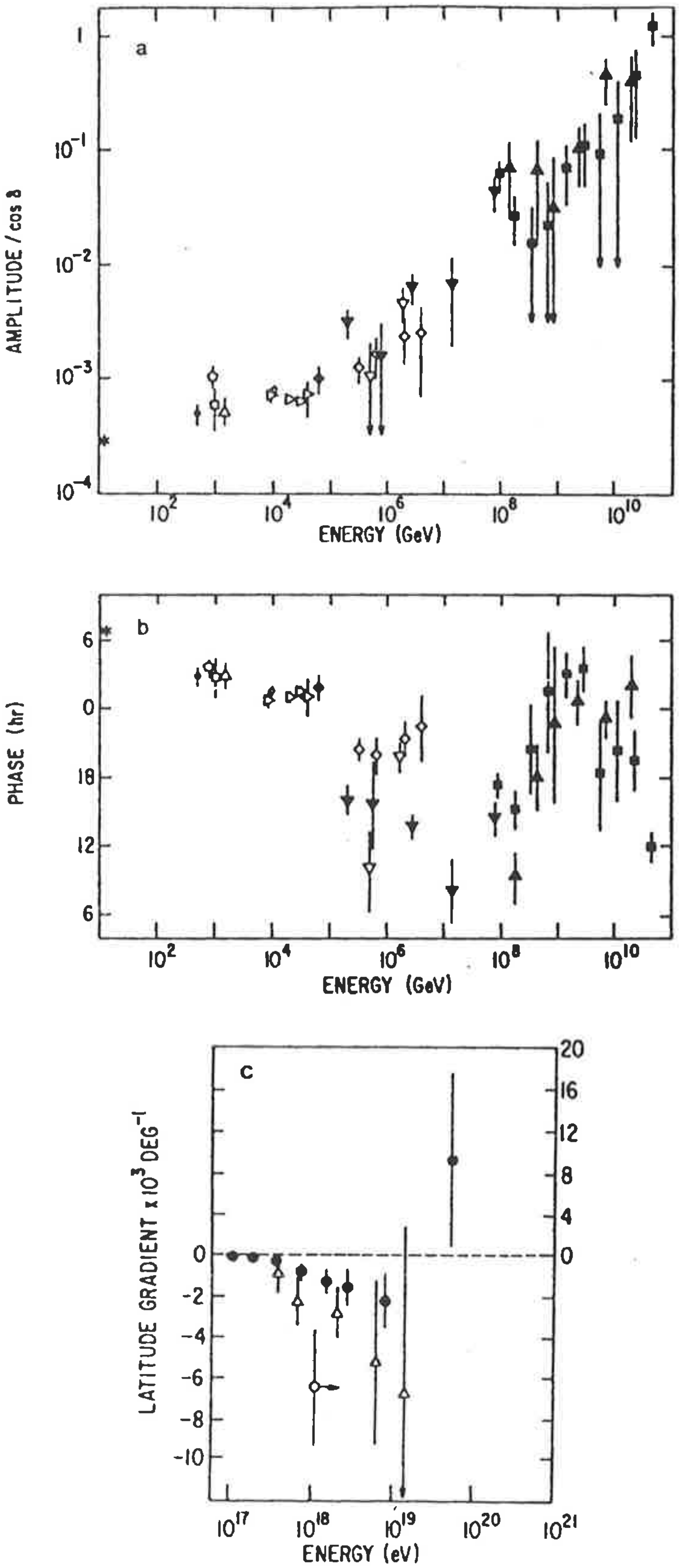

Figure 4-5: Summary of the results of cosmic ray anisotropy in terms of (a) the amplitude and (b) the phase of the first fourier component of a harmonic analysis in Right Ascension (RA). Also shown is the latitude gradient (c) of the cosmic ray flux (from Fichtel and Linsley (1986)).

anisotropy measurements in a way not observed. At EHE energies ($E > 10^{18}$ eV) Haverah Park (Astley *et al.*, 1981) and Yatkutsk (Efimov, Mikhailov and Pravdin, 1983) have found evidence for an increase in the flux of cosmic rays south of the galactic plane with energy up to 3×10^{19} eV. It has been suggested (Szabelski, Wdowczyk and Wolfendale, 1986; Wdowczyk and Wolfendale, 1984b) that this effect is due to northern hemisphere detectors, which have a poor exposure to south galactic latitudes, misinterpreting a galactic equatorial excess. However analyses of Sydney data (Winn *et al.*, 1986a) and Fly's Eye data (Cooper *et al.*, 1991a) show no significant galactic plane excess.

It has been suggested that cosmic rays with $E \geq 3 \times 10^{19}$ eV are of extragalactic origin. Referring to Figure 4-5, above $\sim 3 \times 10^{19}$ eV there is an abrupt change from what appears to be a southern hemisphere excess to a northern hemisphere excess. Using a cluster analysis of these high energy showers, Chi *et al.* (1992a) and Chi, Wdowczyk and Wolfendale (1992) argue that this effect is due to a deficiency of cosmic rays arriving from the inner galaxy. Using this style of analysis they claim that there is evidence for a significant galactic plane excess which increases with energy past 3×10^{19} eV, with the cosmic rays originating from nearby sources with distances ≤ 1 kpc. This analysis is also applied to finding the sources of EHE cosmic rays (Chi *et al.*, 1992b), with evidence showing clustering of cosmic showers in the direction of the Virgo cluster and one cluster close to a pulsar PSR 0157+6212, which has the strongest magnetic field observed. The validity of grouping showers into clusters has been tested by Monte Carlo methods which indicate that the probability of chance clusterings such as that observed is quite high (Lloyd-Evans, 1991).

In conclusion no significant anisotropy has been detected for EHE cosmic rays (Sokolsky, Sommers and Dawson, 1992).

4.4 Acceleration of Cosmic Rays

The acceleration of cosmic rays up to energies of $\sim 1 \times 10^{20}$ eV is still not a fully understood process. The most likely method for the acceleration of cosmic rays is through the shock acceleration of low energy cosmic rays. A precursor to the theory of shock acceleration was the theory of Fermi (1949) which suggested that cosmic rays could gain energy by collisions with randomly moving magnetic fields in the interstellar medium (ISM). This is a relatively inefficient process, where the fractional energy gain per interaction is $\propto \beta^2$ (where $\beta = v/c$) and is termed second order Fermi acceleration.

The most widely accepted theory for the acceleration of cosmic rays up to energies of $\sim 10^{14}$ eV is diffusive shock acceleration by supernova remnants (SNR) (Axford, Leer and Skadron, 1977; Bell, 1978a; Bell, 1978b; Blandford and Ostriker, 1978; Krymskii, 1977). In this theory, particles are scattered by turbulence in the magnetic field either side of a shockwave created by the supernova blastwave sweeping into the ISM. This is a first order acceleration process, since the fractional energy gain per shock crossing is $\propto \beta$. This theory is popular since the combined energy from SNR, assuming an efficiency of 10%, is enough to account for the acceleration of the bulk of the cosmic ray flux. Also, a power law spectrum results naturally from the assumption of first order shock acceleration. For the case of a strong shock, the spectral index is -2. Diffusive shock acceleration of solar wind ions has also been observed *in situ* in the heliospheric bow shock (Ellison and Möbius, 1987).

The lifetime of the supernova shock limits the maximum energy a cosmic ray can attain to $\sim 10^{14-15}$ eV (Lagage and Cesarsky, 1983). Jokipii (1987) suggests that the upper energy limit for cosmic ray acceleration in all types of shocks can be increased by two orders of magnitude by assuming quasi-normal shocks where the orientation of the average magnetic field is along the shock. Another theory suggests that supernova shocks expanding into a stellar wind may accelerate cosmic rays up to energies of $E_{max} = Z \times 10^{17}$ eV (Völk and Biermann, 1988). In this case the cosmic ray composition would reflect the elemental abundances of the pre-supernova wind rather than the ISM (Silberberg *et al.*, 1990). Another type of shock that may accelerate cosmic rays to energies past the knee are those associated with the stellar winds emanating from young stars (Cassé and Paul, 1980).

Observations of UHE γ-rays from X-ray binary systems (e.g. Cyg X-3 Lloyd-Evans *et al.* (1983), Samorski and Stamm (1983b)) point to the presence there of cosmic rays of energies $\geq 10^{16}$ eV. There are several models employed to explain the acceleration of cosmic rays at these sources, all of which use the accretion energy or rotation energy of the pulsar to power the acceleration (e.g. see Nagle, Gaisser and

Protheroe (1988)).

A further proposed acceleration mechanism for EHE cosmic rays is by acceleration at a galactic wind termination shock (Jokipii and Morfill, 1985; Jokipii and Morfill, 1987). This could in part explain the smooth spectrum of energies obtained over many decades, since it invokes the same acceleration mechanism that is used at lower energies. The energy deposited by supernovae may provide energy for a galactic wind with a speed of ~ 500 km s^{-1}, resulting in a termination shock at a radius of ~ 100 kpc. Because of the size and timescale of the shock region, cosmic rays may be accelerated up to $\sim 10^{20}$ eV. Unfortunately there is no evidence to suggest our galaxy possesses a galactic wind.

Another model proposed for the acceleration of cosmic rays of energies past the knee, uses the centres of Active Galactic Nuclei (AGN) as the acceleration sites (Protheroe and Szabo, 1992; Szabo, 1992). Protons which are accelerated at the accretion shock located at the centre of the AGN interact in the intense radiative environment to produce neutrons. These neutrons escape and eventually decay, resulting in a purely proton beam.

Generally it is accepted that cosmic rays with energies $\geq 10^{19}$ eV are extragalactic. A good illustration of the problems encountered in accelerating cosmic rays to energies greater than 10^{19} eV via stochastic mechanisms such as shock acceleration is given by Hillas (1984). Cosmic rays contained within a stochastic system will gain energy continuously by interacting with scattering centres at a rate given by $\frac{dE}{dt} = \frac{E}{t_A}$ where t_A is some characteristic acceleration time. Cosmic rays will be lost to the system and this can be represented by some mean escape time t_E. Cosmic rays leaving this system will have an energy spectrum $J \propto E^{-\gamma}$ where $\gamma = 1 + t_A/t_E$. The mean pathlength λ between scatterings can be defined in terms of the gyroradius r_G in the average magnetic field, as $\lambda = \eta r_G$. It is usually assumed that $\eta = 10$.

As well as gaining energy within the scattering environment, energy losses will occur. In a strong magnetic field synchrotron losses will dominate. In a weak magnetic field cosmic ray interactions with low energy photons, including the background 2.7 K photons, will be the main source of energy loss. Figure 4-6 shows how different possible extragalactic source regions satisfy the criteria for the acceleration of cosmic rays up to

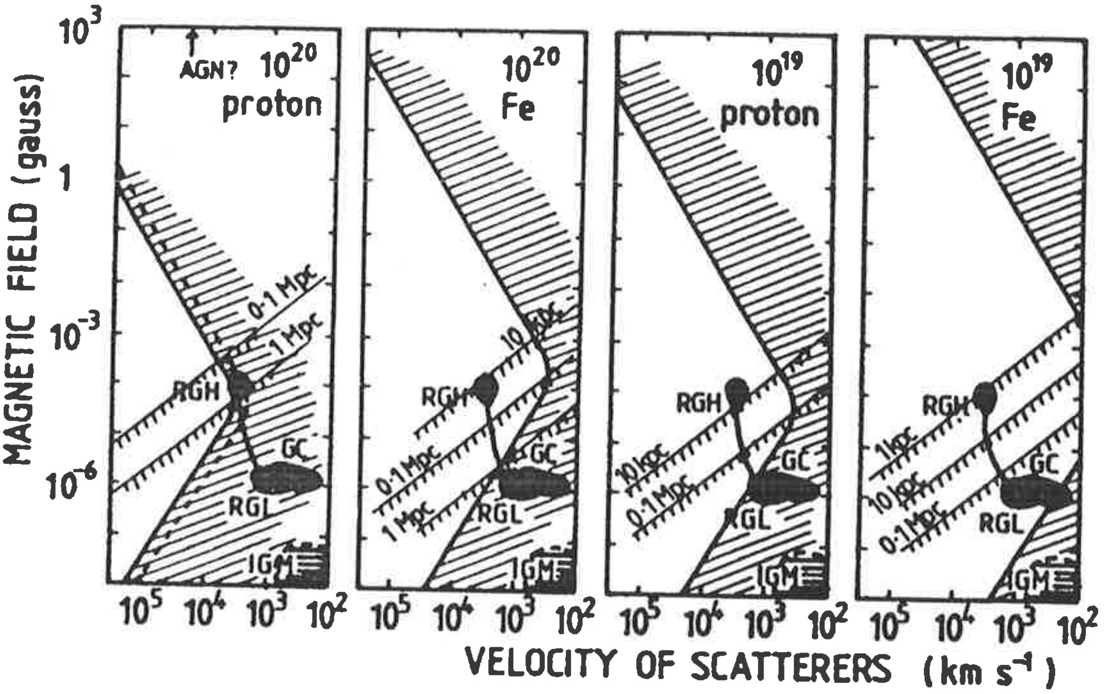

Figure 4-6: Combinations of magnetic field strength and velocity of scattering centres that allow Fermi acceleration to reach 10^{20} or 10^{19} eV for protons or iron nuclei. Only the unshaded triangular at the left in each diagram beats synchrotron losses (above the upper leg of the triangle) and photoreactions (below the lower leg). Any candidates must also lie above the diagonal line appropriate to their radius or diffusive escape will be two rapid. Positions of galactic clusters (GC), radio galaxy lobes (RGL), radio galaxy hotspots (RGH), and the intergalactic medium are indicated. The dashed line in the first figure shows the effect of reducing η to 4 (after Hillas (1984)).

10^{20} eV. One of the most promising sources for these cosmic rays are "radio hot spots" where jets originating from AGN terminate, forming galactic scale shocks (Begelman, Blandford and Rees, 1984; Bridle and Perley, 1984).

In conclusion, shock acceleration in SNR is thought to be able to explain acceleration of cosmic rays up to 10^{14} eV. Above this energy many models exist and no preference for any single model has emerged.

Chapter 5

Propagation of Cosmic Rays with Energies of 10^{18} eV and above

5.1 Introduction

In this chapter the anisotropy of Extremely High Energy (EHE) cosmic rays is investigated. These cosmic rays of energies 10^{18} eV or greater show a remarkable degree of isotropy. At 10^{18} eV the gyroradius of a proton in the Galactic Magnetic Field (GMF) is ~ 300 pc which is approximately equal to the half thickness of the Milky Way galaxy. If the sources of these cosmic rays lie within the galactic disc then this would imply that a significant excess of cosmic rays would come from the direction of the galactic plane. The purpose of this chapter is to investigate the effects of GMF turbulence on the propagation of EHE cosmic rays and its implications regarding their lifetime and anisotropy.

Firstly, methods of measuring the GMF are described. Theoretical explanations for the presence of a GMF are reviewed, the two main theories being the relic field model and the galactic dynamo model. Two mathematical models which have been used to describe the GMF are then discussed, these being the quasi-longitudinal model of Thielheim and Langhoff (1968) and the axisymmetric concentric ring model of Rand and Kulkarni (1989). The method of simulating cosmic ray propagation in the galaxy, including a model for incorporating the random component of the GMF, is then derived. Simulations of the expected anisotropy and lifetime of EHE cosmic rays are then presented. The second half of this chapter investigates the effect of including a galactic halo with its own magnetic field, both random and non-random, on EHE cosmic ray propagation. The chapter concludes with a discussion on the implications of the results presented.

5.2 Galactic Magnetic Field

The first evidence for the existence of a galactic magnetic field was from the observation of linear polarisation of starlight (Hiltner, 1949). The galactic magnetic field appears to have an ordered structure, at least in the region within 3 kpc of our solar system. This is the region where the strength and direction of the galactic magnetic field can be determined by observations of Faraday rotation. It is expected however that the ordered magnetic field encompasses the entire galactic disk as this is observed in external galaxies (Sofue, Fujimoto and Wielebinski, 1986). The strength of the ordered magnetic field is estimated to be $\sim 2\ \mu$G. Associated with this ordered field is a non-ordered field with a magnitude 1–3 times greater than the ordered component. This random field appears to have a length scale in the range 50–150 pc (Chi and Wolfendale, 1990; Rand and Kulkarni, 1989). For a general discussion of interstellar magnetic fields see Heiles (1976) and Heiles (1987).

It is thought that a galactic halo exists with possibly its own magnetic field outside of the galactic plane. However, any observation of this halo magnetic field is complicated by the observers position being located in the galactic plane with its own magnetic field. As a result, the nature of the halo magnetic field is speculative.

5.2.1 Measurements

Faraday Rotation

Faraday Rotation is the rotation of the plane of polarisation when radiation which is plane polarised travels through a magnetised plasma. The angle of rotation $\delta\theta$ over a distance l (in pc) is given by

$$\delta\theta \quad = \quad \frac{\lambda^2 e^3}{8\pi^2 c^3 \epsilon_0 m_e^2} \int_0^l n_e B_{||}\, dl$$

$$= \quad 8.1 \times 10^5 \lambda^2 \text{ RM} , \tag{5.1}$$

where n_e is the thermal electron density in cm^{-3}, $B_{||}$ is the component of $\vec{B}$ parallel to the line of sight, λ is the wavelength of the radiation in metres and RM is the rotation measure, defined as $\int n_e B_{||}\, dl$. Measurements at different wavelengths are necessary since $\delta\theta$ may be greater than 2π for one wavelength. Pulsars are the ideal candidates for measuring Faraday rotation since they emit linearly polarised radiowaves over a range of frequencies.

The different frequency components travel through a plasma at different velocities since the time T taken for a component of frequency ν to travel a distance l is given by

$$T = \frac{l}{c} + \frac{e^2}{8\pi^2 \epsilon_0 m_e c \nu^2} \text{ DM} , \tag{5.2}$$

where the Dispersion Measure (DM) is defined as $\int n_e dl$.

A value for the average magnetic field $B_{||}$ along the line of sight is given by

$$\begin{aligned} < B_{||} > &= 1.232 \frac{\int n_e B_{||} dl}{\int n_e dl} \mu\text{G} \\ &= 1.232 \frac{\text{RM}}{\text{DM}} \mu\text{G} . \end{aligned} \tag{5.3}$$

By measuring radio emissions from pulsars the structure of the local magnetic field can be discerned.

Zeeman Splitting

The presence of an atom or molecule in an external magnetic field results in splitting of the atomic energy levels. This is termed Zeeman splitting. In the case of the hydrogen atom the galactic magnetic field splits the upper level of the 21 cm (1.42 GHz) line into three levels. The frequency difference $\Delta\nu$, between the upper and lower of these levels is given by $2.8 B_{\text{tot}}$ Hz, where B_{tot} is the total strength in μG. When the external field is parallel to the line of sight, the atom radiates two circularly-polarised components with frequencies $\Delta\nu$ apart. The hydrogen atom also radiates three linearly polarised components with maximum amplitudes perpendicular to the magnetic field.

In almost all cases the frequency splitting is much less than the intrinsic line width so that only the change of sign of circular polarisation across the line can be observed. The amplitude A of the circularly polarised component is proportional only to the parallel component of the magnetic field (i.e. $A \propto \frac{B_{\parallel}}{\Delta\nu}$). Zeeman splitting of the 21 cm line was first detected by observing HI clouds against strong extragalactic radio sources. Zeeman splitting of the OH 18 cm line has also been observed in molecular clouds. By its nature the Zeeman splitting method detects the magnetic field in clouds with large HI(OH) column densities and narrow line widths i.e. cold dense HI(OH) clouds. This leads to estimates of the galactic magnetic field usually an order of magnitude greater than that obtained from observations of Faraday rotation which are biased to warm ionised regions of the ISM (Heiles, 1976; Heiles, 1987).

Polarisation of Starlight

This method for observing the galactic magnetic field is different from the two previously discussed methods. The polarisation of starlight measures the direction of the component lying perpendicular to the line of sight $B_{\perp}$ and not the strength of the component parallel to the line of sight $B_{\parallel}$. The observation of linear polarisation of starlight provided the first evidence for the existence of an interstellar magnetic field (Hiltner, 1949).

For an elongated dust grain in the ISM, the preferred axis of rotation is that with the largest angular momentum. If the energy associated with the dust grain's rotation is apportioned equally about all three principal axes, then the preferred axis of rotation is perpendicular to the longest dimension of the dust grain. Energy considerations ensure that over time the dust grains align themselves so that they experience a time independent magnetic field. This aligns the spin axis parallel to the magnetic field (Spitzer, 1978). The spinning grains polarise the lightwave in the direction perpendicular to their spin axes, linearly polarising light in the direction of $B_{\perp}$.

5.2.2 Origin of the Galactic Magnetic Field

The galactic magnetic field $\vec{B}$ has an energy density, defined as $\frac{B^2}{8\pi}$, equal to ~ 1 eV cm^{-3}. This value is comparable to the thermal energy density of the ISM (nkT where $n \sim 1$ cm^{-3}, $k =$ Boltzman's constant and $T \sim 10^4$ K), the energy density of interstellar turbulence ($nm_pv^2/2$ where m_p = proton mass and $v \sim 10$ km s^{-1}) and the cosmic ray energy density. This implies that whilst the galactic magnetic field is weak, in the order of a few μG, its large scale has made it an integral part of the galaxy's evolution. As to the question of the origin of the field, there are two main theories. These are the relic field theory, which suggests that the field resulted from a primordial universal field being wound up as the galaxy formed, and the galactic dynamo theory which suggests that the large scale ordered field is the result of small turbulent helical motions which can combine and grow to form the galactic magnetic field.

Relic Field Model

The relic field model assumes that the present day galactic magnetic field originates from an primordial intergalactic field. According to this theory, galaxies are formed from intergalactic clouds which themselves are embedded in a weak ($\sim \frac{1}{100}$ μG) large scale ($\sim$ 100 Mpc) magnetic field (Piddington, 1964). Thus the question of the origin of the galactic magnetic field becomes a question of the origin of the pregalactic magnetic field. The magnetic field configuration expected from the relic field theory is a spiral configuration. This is caused by the non-uniform rotation of the galactic field winding up the primordial magnetic field.

The most significant problem with the relic field theory is that interstellar turbulence is expected to dissipate the field on a timescale less than the age of the galaxy. For instance, the approximate scale of interstellar turbulence L_0 is $\sim$ 100 pc and this has an associated velocity $\sim$ 10 km s^{-1}. This implies a turbulent magnetic diffusivity β of

$$\beta \sim \frac{L_0 v}{3} \sim 10^{26} \text{ cm}^{-2}\text{s}^{-1} . \tag{5.4}$$

Therefore for the simple case of 1-dimensional diffusion it would be expected that the magnetic field would take $h^2/\beta \sim 5 \times 10^8$ years to dissipate, considering that our galaxy has a half thickness $h \sim 300$ pc. Unfortunately this is only 1/20 of the expected age of the galaxy (Parker, 1991).

Galactic Dynamo Model

The galactic dynamo theory relies on the presence of an initial turbulent magnetic field to generate the large scale non-random galactic magnetic field. This interstellar turbulence is thought to arise from supernova remnants whose expanding shells sweep into the interstellar medium. The idea that helical turbulent motions can give rise to large scale ordered magnetic fields in astrophysical plasmas was first proposed by Parker (1970). This method was then used to explain the generation of the galactic magnetic field (Parker, 1971a; Parker, 1971b). These theories have now been developed to explain the existence and configuration of magnetic fields in other galaxies (see e.g. Ruzmaikin, Shukurov and Sokoloff (1988), Ruzmaikin, Sokoloff and Shukurov (1988)). The dynamo equation is obtained by modelling the interstellar medium using the magnetohydrodynamic approximation which assumes that if L is a typical length scale over which fields vary and T is an associated time scale then

$$\frac{L}{T} \ll c \, , \tag{5.5}$$

where c is the velocity of light. Using this approximation the induction equation can be derived from Maxwell's equations. This is defined as

$$\frac{\partial \vec{B}}{\partial t} = \vec{\nabla} \times (\vec{v} \times \vec{B}) - \vec{\nabla} \times (\eta \vec{\nabla} \times \vec{B}) \, , \tag{5.6}$$

where $\eta = 1/\mu\sigma$ is the magnetic diffusivity ($\sim 10^9$ cm^2 s^{-1} for the galactic disk), σ is the electrical conductivity and μ is the magnetic permeability. For constant η the ratio

$$\frac{\vec{\nabla} \times (\vec{v} \times \vec{B})}{\eta \nabla^2 \vec{B}} \sim \frac{VL}{\eta} \equiv Re_m \, , \tag{5.7}$$

is called the magnetic Reynolds number, which for the galactic disk is estimated to be $\sim 3 \times 10^{17}$.

The dynamo equation is a modified induction equation which takes into account the effect of turbulent magnetic fields and is given by

$$\frac{\partial \vec{B}}{\partial t} = \underbrace{\vec{\nabla} \times (\vec{v} \times \vec{B})}_{\text{(i)}} + \underbrace{\vec{\nabla} \times (\alpha \vec{B})}_{\text{(ii)}} + \underbrace{\beta \nabla^2 \vec{B}}_{\text{(iii)}} , \tag{5.8}$$

where β is defined in Equation 5.4 and is many orders of magnitude larger than the magnetic diffusivity η (10^{26} cm^2 s^{-1} compared to 10^9 cm^2 s^{-1}). α is the mean helicity and is defined by

$$\alpha = -\frac{\tau}{3} \langle \vec{v} \cdot \vec{\nabla} \times \vec{v} \rangle , \tag{5.9}$$

where τ is the correlation time. α has a value of ~ 1 km s^{-1}. The overall mean helicity of the galactic disk originates from the rotation of turbulent cells as they rise from the galactic disk. This is thought to arise because of the lower density of interstellar material above the galactic plane. The rotation of the turbulent cells is due to Coriolis force from the rotation of the galactic disk. In general the rotation curve $\vec{v}(r)$ is defined by

$$\vec{v}(r) = \vec{\Omega}(r) \times \vec{r} \sim 200 \text{ km s}^{-1} , \tag{5.10}$$

where $\vec{\Omega}(r)$ is the angular velocity of the disk as a function of galactocentric radius.

In summary, terms (i) and (ii) of Equation 5.8 are adding to the overall ordered magnetic field while term (iii) is a diffusive loss term. Thus the dynamo process is a competition between the regeneration of the large scale magnetic field due to the helicity of turbulent cells and the differential rotation of the galaxy against the dissipation of the magnetic field due to turbulent diffusion. An example of a solution to Equation 5.8 is to assume uniform α and β and to use separation of variables into cylindrical co-ordinates (Ruzmaikin, Sokoloff and Shukurov, 1988). Solutions to this particular case of the dynamo equation are of the form

$$\vec{B} = \vec{H}(r,z) \exp(\Gamma t + im\phi) , \tag{5.11}$$

where $\vec{H}(r,z)$ is the radial and z dependence of the magnetic field, Γ is the growth rate, ϕ is the azimuthal angle, t is the time and m is the azimuthal wave number. The solution for our galaxy is thought to be with $m = 0$ i.e. the galactic magnetic field is axisymmetric. Generally solutions to the dynamo equation are typically complex requiring numerical computation or various simplifying approximations to be made (Ruzmaikin, Shukurov and Sokoloff, 1988).

5.2.3 Empirical Models of the Galactic Magnetic Field

Bisymmetric Spiral Model

The quasi-longitudinal model of Thielheim and Langhoff (Thielheim and Langhoff, 1968) has been used in previous simulations of EHE cosmic ray propagation (Berezinsky and Mikhailov, 1983; Berezinsky and Mikhailov, 1987; Berezinsky, Mikhailov and Syrovatskii, 1979; Karakula *et al.*, 1971; Smith and Clay, 1990). The structure of the magnetic field is aligned with the spiral arms. The field strength is strongest in the spiral arms with the field reversing in its orientation above and below the galactic plane. The geometrical form of the spiral arms is defined by $\phi(R)$ where

$$\phi(R) = \frac{b}{K} R \arctan \frac{R}{K} + \phi_0 \ , \tag{5.12}$$

$K = 1$ kpc, $b = 1$ and R is the radius from the centre of the galaxy in kpc. This function defines two spiral arms starting from opposite sides of the galactic centre. The magnetic field parallel to these spiral arms is defined in terms of the unit vector

$$\hat{a} = \hat{R} \cos \epsilon + (\hat{z} \times \hat{R}) \sin \epsilon \ , \tag{5.13}$$

where $\hat{R}$ is the unit vector in the radial direction, $\hat{z}$ is the unit vector perpendicular to the galactic plane and

$$\epsilon = \arctan \left(\frac{b}{K} R \arctan \frac{R}{K} + \frac{br^2}{K^2 + R^2} \right) \ , \tag{5.14}$$

Thus the form of the magnetic field is

$$\vec{B} = B_a \hat{a} + B_z \hat{z} \ , \tag{5.15}$$

where

$$B_a = cz\exp\left(-\frac{z^2}{z_0^2}\right)\exp\left(-\frac{R^2}{R_1^2}\right)\left(1-\exp\left(-\frac{R^2}{R_2^2}\right)\right)\left[1+a^2\cos^2\left(\phi_\odot-\phi(R)\right)\right] . \quad (5.16)$$

From B_a it can be seen that the magnetic field in the galactic plane is zero and changes value about the galactic plane. The parameters R_1 and R_2 determine the rate with which the field drops with respect to R. z_0 determines the rate the field diminishes with increasing height both above and below the galactic plane. These parameters are $z_0 = 0.175$ kpc, $R_1 = 10$ kpc and $R_2 = 4$ kpc respectively. a determines the ratio of the field strength within the arms to that between the arms and is set at 2. The position of our solar system in this coordinate system is at (10 kpc, 6.5°, -.085 kpc) corresponding to $(R_\odot, \phi_\odot, z_\odot)$. c determines the mean magnetic field and in the original Thielheim and Langhoff model is equal to 50 μG kpc^{-1}. This values gives a magnetic field of ~ 6 μG in the earth's vicinity.

The Axisymmetric Concentric Ring Model

The quasi-longitudinal model of Thielheim and Langhoff (1968) discussed in the previous section is based on measurements of the GMF circa 1965 and as such has become outdated. Subsequent analyses of the GMF using RMs from observations of pulsar and extragalactic sources have been inconclusive with regard to the overall magnetic field configuration but agree well in terms of the approximate direction and magnitude locally. Manchester (1974) used observations of RMs from 28 pulsars to determine the GMF and found that a longitudinal model represented well the local field with $l_B = 94 \pm 11°$ and a field strength of $B_{\text{reg}} = 2.2 \pm 0.4$ μG. All of the pulsars used in this analysis had distances from the sun of less than 2 kpc. Manchester (1974) also concluded that there was a random component to the GMF whose field strength was comparable to the regular component with a length scale of a few hundred parsecs.

A subsequent analysis of an increased sample of some 48 pulsars with $D \leq 3$ kpc by Thomson and Nelson (1980) found a field strength of $B_{\text{reg}} = 3.5 \pm 0.3$ μG and direction $l_B = 74 \pm 10°$. They also found evidence for a field reversal towards the inner galaxy at a distance $D_r = 170 \pm 90$ pc. They estimated that the random component of the GMF has a field strength in the range $4 < B_{\text{ran}} < 14$ μG. Chi and Wolfendale

(1990) used the rotation measures of 51 pulsars, all within a distance of 1.5 kpc of the sun. They make a distinction between the spiral arm and interarm region. They find a field strength for B_{reg} of 1.0 ± 0.4 μG in the direction $l_B = 80 \pm 19°$ for the Orion-Perseus arm and a strength of $B_{\text{reg}} = 3.2 \pm 1.0$ μG in the direction $l_B = 57 \pm 14°$ between the Orion and Sagittarius arm. They also find evidence for a field reversal towards the inner galaxy at $D_r = 190 \pm 90$ pc. The random component was found to have a magnitude of 5 μG with a scale size of 55 pc.

Another set of RM data is that which has been obtained from the observations of extragalactic sources. The analysis by Simard-Normandin and Kronberg (1980) of 552 RMs from the observation of extragalactic radio sources by Simard-Normandin, Kronberg and Button (1981), found that a spiral model with four arms and a field reversal at each arm agreed with observations. In this spiral model the closest field reversal is at $D_r = 600$ pc. An axisymmetric concentric ring model with one field reversal towards the inner galaxy also agrees with the data. Another catalogue listing the linear polarisations of extragalactic radio sources (Tabara and Inoue, 1980) has been used by Sofue, Fujimoto and Wielebinski (1986) to determine the GMF configuration. They prefer a bisymmetric field model with the nearest field reversal towards the inner galaxy at $D_r = 350$ pc.

When trying to determine the strength and direction of the uniform GMF it is important to take into account any sources of anomalous RM (Vallée, 1984). The source of these anomalous RM are magnetic bubbles close to the sun (see Figure 5-1). The prominent ones are the North Polar Spur (Loop I $l,\ b \sim (329°,18°)$), Cetus Arc (Loop II, $l,\ b \sim (110°,-32°)$) and the Gum Nebula (Vela, $l,\ b \sim (260°,0°)$). These magnetic bubbles are thought to be caused by collections of stars with stellar winds strong enough to push out interstellar matter and hence the magnetic field. Another possible cause for these magnetic bubbles are supernovae whose expanding envelopes sweep out interstellar matter.

For the purposes of simulating EHE cosmic ray propagation in this report the concentric ring model of Rand and Kulkarni (1989) has been used. Using the RMs of 116 pulsars with $D < 3$ kpc from the measurements of Hamilton and Lyne (1987) plus previous existing measurements, Rand and Kulkarni (1989) found that a simple

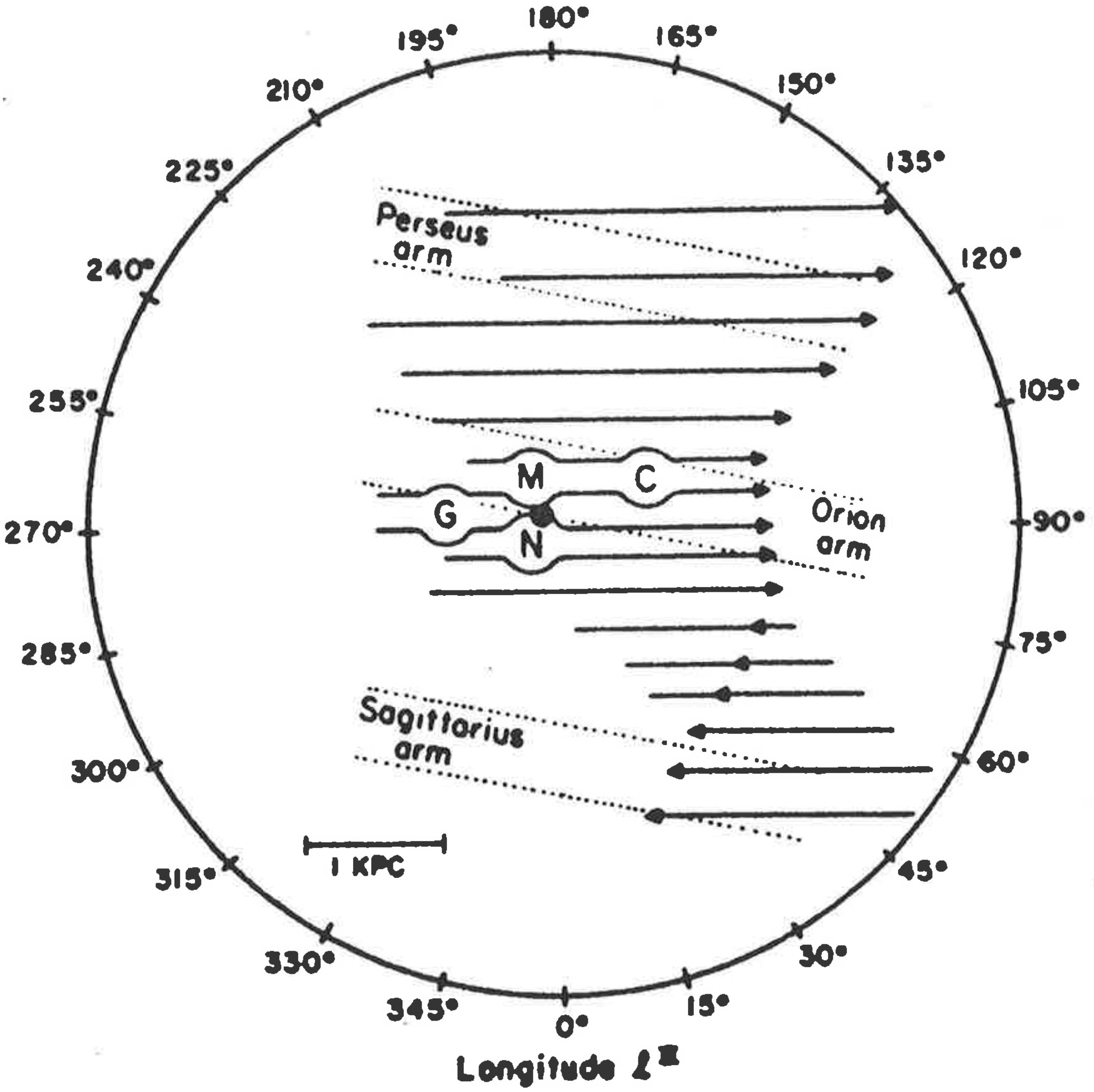

Figure 5-1: Three stellar arms and four interstellar magnetic bubbles near the sun in the Milky Way galaxy. The interstellar magnetic bubbles are lettered N-North Polar Spur(=Loop I), C-Cetus Arc(=Loop II), G-Gum Nebula, and M-Monogem Ring. The lines show the direction of the interstellar magnetic field. The arm to arm separation is approximately 2 kpc. The Sun, shown as a thick circular dot, is located on the inner side of the local Orion spiral arm (from Vallée (1984)).

axisymmetric concentric ring model agreed best with observations, in agreement with Manchester (1974) and Vallée (1983). Rand and Kulkarni (1989) found the local field strength to be $1.6 \pm 0.2\ \mu$G towards longitude $l_B = 96 \pm 4°$ and a reversal in the field 600 ± 80 pc towards the inner galaxy. The field model assumed for the galaxy characterises the GMF strength as varying sinusoidally with galactocentric radius. The field is assumed to vanish within a radius of 4 kpc and outside a radius of 15 kpc. There are assumed to be two field reversals within the solar circle ($R_\odot = 10$ kpc) and one outside. The spacing between reversals is 3.1 kpc with a reversal occurring at 650 pc interior to the solar circle. The amplitude of the sinusoidal variation is 2.15 μG. This concentric ring model was also found to be consistent with measurements of extragalactic objects.

For the purposes of simulation this field model is parameterised as follows

$$\vec{B}_{\text{reg}} = 2.15 \sin\left(1.0134 \left(R_{\text{kpc}} - 3.1876\right)\right) \hat{e}_\phi \ \mu\text{G} \ , \tag{5.17}$$

where R_{kpc} is the distance from the centre of the galaxy in kiloparsecs and $\hat{e}_\phi$ is the azimuthal unit vector. Figure 5-2 illustrates this parameterisation (Note: Figure 8 in Rand and Kulkarni (1989) is incorrect). This field model has also been used for cosmic ray simulations of a similar nature to those presented here (Berezinsky *et al.*, 1991; Giller *et al.*, 1993). Another analysis of the same RM data set (Lyne and Smith, 1989) found a value for the local magnetic field of $\sim$ 2–3 μG and directed towards $l_B = 90$, with evidence for a field reversal within 1 kpc of the sun in the direction of the centre of the galaxy. In the GMF model of Rand and Kulkarni (1989) the random component of the field has a strength of 5 μG and a scale length of 55 pc.

5.3 Modelling of the Propagation of Cosmic Rays in a Magnetic Field

5.3.1 Generation of the Turbulent Magnetic Field

From very general principles it is expected that there should be turbulence in the ISM. The Reynolds number for the ISM, Re_{ISM}, calculated using typical values for the ISM

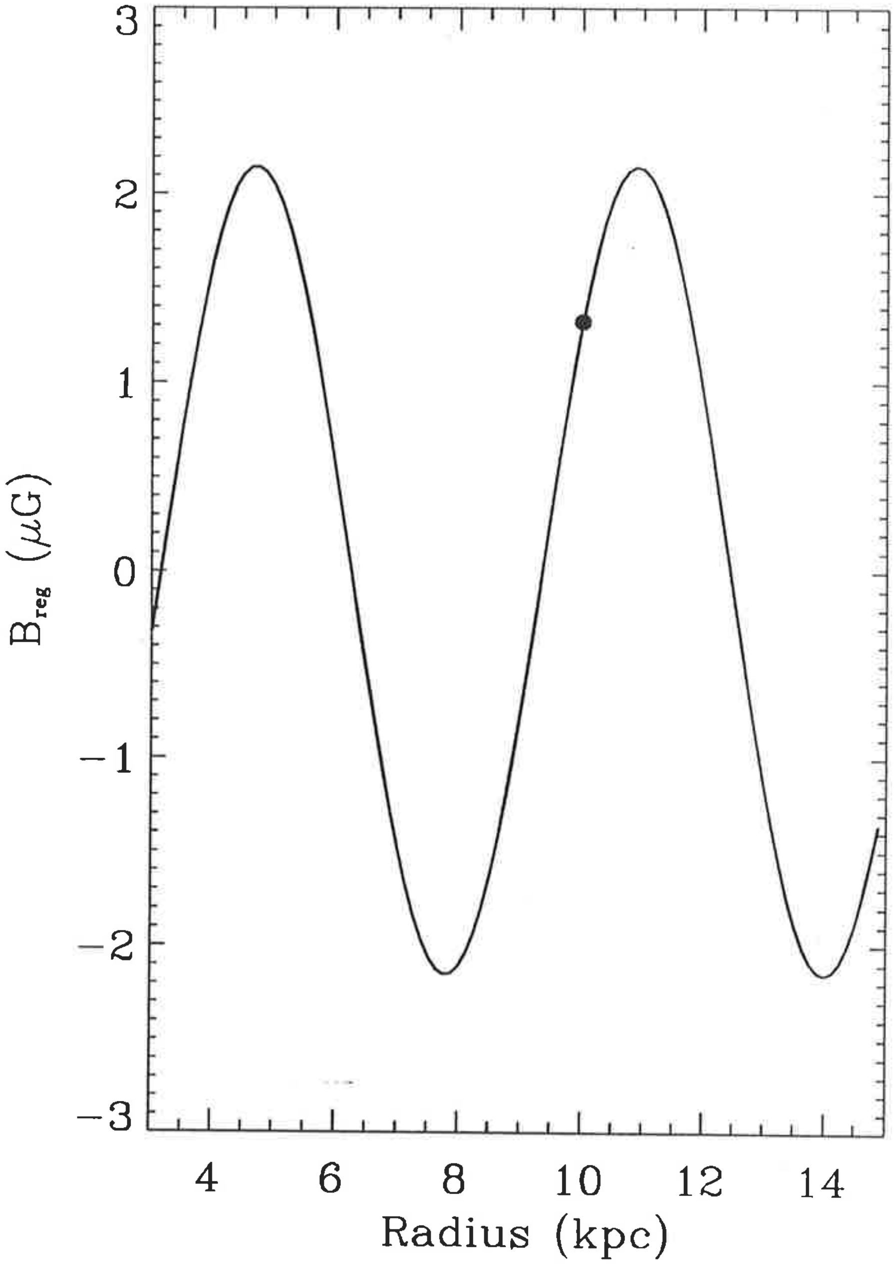

Figure 5-2: The strength of the regular galactic magnetic field as a function of galactocentric radius according to the model of Rand and Kulkarni (1989). The filled circle indicates the assumed position of our solar system. The field is assumed to be zero inside 4 kpc and outside 15 kpc. A positive value of the magnetic field indicates a clockwise rotation of the magnetic field when looking from above the galactic plane.

yields (Scalo, 1987)

$$Re_{\rm ISM} = 10^8 l_{\rm pc}^{-0.7} \ , \tag{5.18}$$

where $l_{\rm pc}$ is the length scale of the turbulence measured in parsecs.

This is far in excess of Reynolds number for turbulence obtained in laboratory conditions and led to the suggestion that the ISM can be modelled as a turbulent fluid (Von Weizäcker, 1951). The driving force for this turbulence is provided by supernovae which occur randomly in time and space throughout the galaxy. Since the magnetic diffusivity η of the ISM is low, the galactic magnetic field lines are frozen into the ISM, implying that there should be a turbulent component $\vec{B}_{\rm ran}$ associated with the large scale ordered component $\vec{B}_{\rm reg}$. It was thought initially that this random component $\vec{B}_{\rm ran}$ of the GMF was smaller or equal to the regular component $\vec{B}_{\rm reg}$. However more recent measurements imply that $\frac{|\vec{B}_{\rm ran}|}{|\vec{B}_{\rm reg}|} \sim 3$ (Chi and Wolfendale, 1990; Rand and Kulkarni, 1989). Thus the turbulent component of the magnetic field has a much larger effect on EHE cosmic ray propagation than at first thought. In order to simulate these effects it is necessary to formulate a method whereby turbulent effects can be taken into account.

Generally the approach taken to describe the propagation of cosmic rays in a turbulent magnetic field is to assume that the turbulent component is smaller than the uniform component i.e. $\langle B_{\rm ran}\rangle << \langle B_{\rm reg}\rangle$ (e.g. Jokipii (1966)). In this case the probability of finding a particle in a particular position and with a given pitch angle will satisfy the Fokker-Planck equation (for a discussion of the Fokker-Planck equation see Chandrasekhar (1943)). For the case of strong turbulence this approach is invalid as the turbulent component cannot be treated as a small perturbation.

In this report we use the method of Honda (1987) which calculates directly the effect of strong turbulence on cosmic ray propagation. Using this method a self consistent turbulent magnetic field can be generated with $\vec{\nabla} \cdot \vec{B}_{\rm ran} = 0$. This is done by finding a suitable form for the vector potential $\vec{A}_{\rm ran}$ and defining

$$\vec{B}_{\rm ran} = \vec{\nabla} \times \vec{A}_{\rm ran} \ . \tag{5.19}$$

In practice, to simulate a turbulent magnetic field a cubic lattice is considered to be embedded in the galaxy. This lattice has a length scale L_0 equal to the largest length scale of turbulence assumed. At each point k within the lattice, values for (A_x^k, A_y^k, A_z^k), the cartesian components of the vector potential, are sampled from a probability distribution of the form

$$p(A_i^k) = \frac{1}{|A|} \exp\left(-\frac{A_i^k}{|A|}\right) . \tag{5.20}$$

$|A|$ is chosen such that the magnitude of the random magnetic field $\vec{B}_{\text{ran}}$ is as required. To save on computing time, such a lattice is not generated throughout the simulation space. Instead a cubic lattice of dimension $10L_0$ is generated and reproduced throughout the galaxy. The rationale for this method is that a cosmic ray's direction after travelling through this volume will be independent of the direction it had when it entered this region. After a given number of increments in the galaxy the $10 \times 10 \times 10$ cubic lattice is regenerated.

The cosmic ray at any point in time will be located in a particular cube of length scale L_0. To find $\vec{B}_{\text{ran}}$ the curl of the vector potential must be found. In cartesian co-ordinates this is found using the well known formula

$$\vec{\nabla} \times \vec{A}_{\text{ran}} = \left(\frac{\partial A_z}{\partial y} - \frac{\partial A_y}{\partial z}\right)\hat{x} + \left(\frac{\partial A_x}{\partial z} - \frac{\partial A_z}{\partial x}\right)\hat{y} + \left(\frac{\partial A_y}{\partial x} - \frac{\partial A_x}{\partial y}\right)\hat{z} . \tag{5.21}$$

Given A_x, A_y and A_z for each of the eight points of the cube surrounding the position of the cosmic ray (x_c,y_c,z_c) then each of the terms $\frac{\partial A_z}{\partial y}$, $\frac{\partial A_x}{\partial z}$ ..., etc. can be calculated at the vertices of the cube by numerical differentiation on the length scale of the cube. To find the value of these differential terms at (x_c,y_c,z_c), a linear interpolation to the position of the cosmic ray is then done. $\vec{B}_{\text{ran}}$ is then found by applying Equation 5.21. Figure 5-3 shows the distribution of sampled $B_{\text{samp}} = \left|\vec{B}_{\text{ran}}\right|$ values. This procedure was tested by using known vector potentials (e.g. a magnetic dipole) and comparing the derived magnetic field using the numerical method described to the analytic solution.

To treat the transfer of energy from the largest length scale of turbulence L_0 in the magnetic field to the smaller scales of turbulence, an approximation first stated by Kolmogorov (Kolmogorov, 1961) is used. Kolmogorov stated that turbulence in an incompressible fluid should exhibit a dissipationless energy cascade from the largest

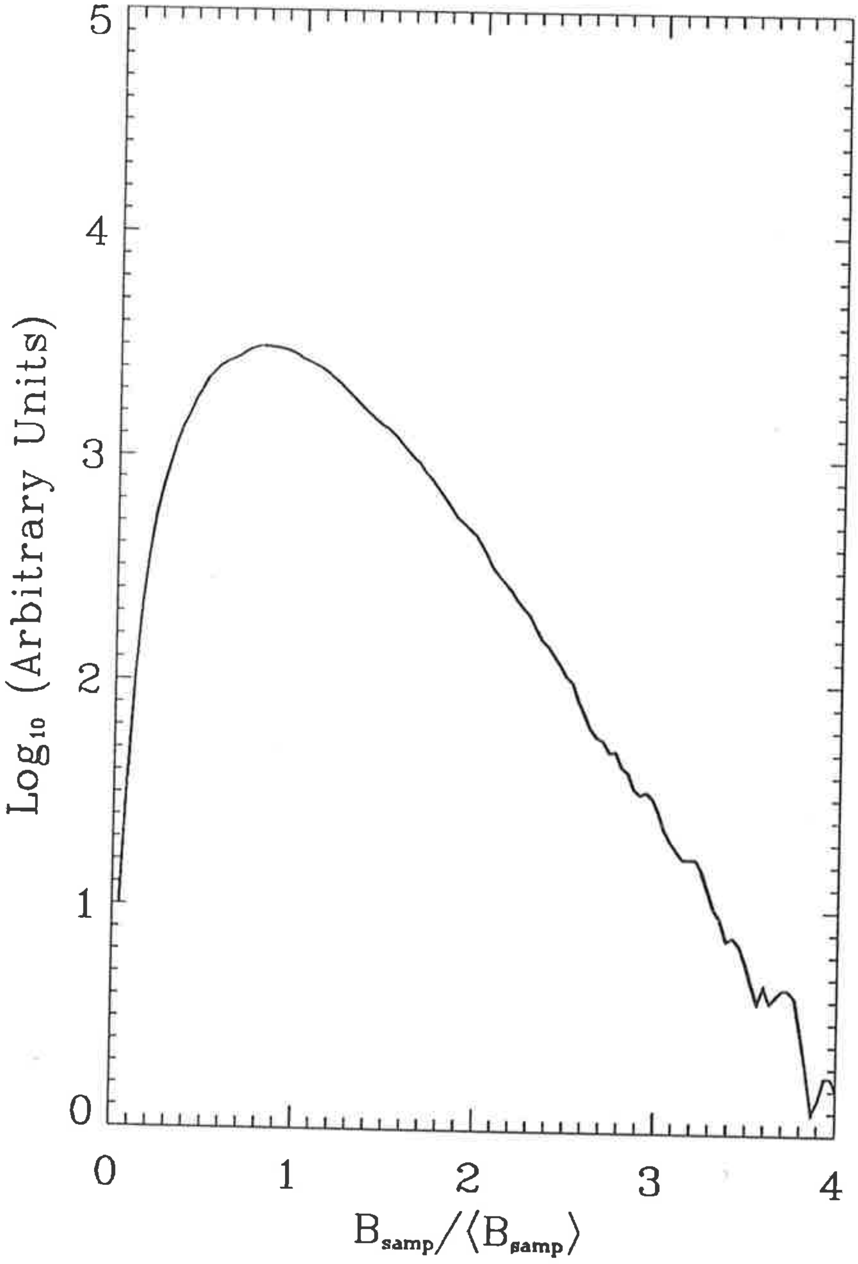

Figure 5-3: Distribution of sampled B_{samp} values.

scale of turbulence L_0 where the energy is injected, to a length scale l_k where energy is dissipated due to viscous losses. This length scale l_k is termed the Kolmogorov microscale and is given by (Tennekes and Lumley, 1972)

$$l_k = \left(\frac{\nu^3 L_0}{v^3}\right)^{1/4} , \tag{5.22}$$

where ν is the viscosity of the ISM and v is the velocity of the turbulence. l_k is approximately equal to $10^{10} l_{pc}^{-1}$ m for our galaxy. The range of length scales over which there is assumed to be no viscous losses is termed the "inertial sub-range". Between L_0 and l_k according to the Kolmogorov theory, the kinetic energy transfer rate $\epsilon \sim \frac{v^2}{t} = \frac{v^3}{l}$ should be constant. This implies that $v \propto l^{1/3}$. Defining $k = 1/l$ as the wavenumber associated with the length scale l then $v(k) \propto k^{-1/3}$. The energy spectrum $E(k)$ of the turbulence is thus defined as

$$E(k) \propto k^{-1} v^2(k) \propto k^{-5/3} . \tag{5.23}$$

Thus the energy spectrum is a power spectrum with an index of $-5/3$.

Evidence for the energy spectrum of interstellar turbulence can be obtained from the analysis of the scattering of radio waves in the ISM. Such scattering can cause intensity scintillations (Lee and Jokipii, 1975c), angular broadening of a radio source (Lee and Jokipii, 1975a) or pulse smearing (Lee and Jokipii, 1975b), or more generally a combination of these three effects. Lee and Jokipii (1976) deduced from measurements of radio wave intensity scintillations from three pulsars that the spectrum of interstellar turbulence was consistent with either a Kolmogorov-like power law spectrum or a Gaussian spectrum. Other measurements of interstellar scintillations from radio sources (Armstrong, Cordes and Rickett, 1981; Cordes, Weisberg and Boriakoff, 1985; Rickett, Coles and Bourgois, 1984) are consistent with a Kolmogorov power spectrum in the wavenumber range 10^{-8}–10^{-13} m^{-1}. When these measurements are combined with those at much lower wavenumbers which are also consistent with a Kolmogorov spectrum (Kaplan, 1966; Larson, 1979), the implication is that interstellar turbulence has a Kolmogorov spectrum over a scale size ranging from ~ 100 pc to $\sim 10^8$ m. It is also interesting to note that a Kolmogorov spectrum for interstellar turbulence is predicted by the galactic dynamo theory (Ruzmaikin and Shukurov, 1982).

For the purposes of this simulation the Kolmogorov spectrum has been assumed. Lattices are generated with length scales $L_i = 10^{-i/2}$, $i = 1, 2, 3, \cdots$. The smallest scale of turbulence L_s is determined by $L_s < \frac{R_g}{3}$ where R_g is the gyroradius of the cosmic ray in a magnetic field of the same strength as the turbulent component. Magnetic fields are generated for each of the length scales L_i and are summed to the magnetic field generated for the largest length scale L_0. Each magnetic field contribution for each length scale L_i is weighted according to the Kolmogorov spectrum i.e.

$$\left|\vec{B}_{\mathbf{ran}}(L_i)\right| \propto \left(\frac{L_i}{L_0}\right)^{5/3} . \tag{5.24}$$

The total average random field strength at the value being investigated is independent of the lowest level of turbulence assumed. This is accomplished by including a normalisation constant dependent on L_s. This process of generating the random magnetic field is computationally intensive and has to be done for each increment in the cosmic ray's position.

The total magnetic field $\vec{B}_{\mathbf{tot}}$ that the cosmic ray experiences is the vector sum of the random and non-random components

$$\vec{B}_{\mathbf{tot}} = \vec{B}_{\mathbf{reg}} + \vec{B}_{\mathbf{ran}} . \tag{5.25}$$

For the simulations presented here, $\vec{B}_{\mathbf{reg}}$ is given by Equation 5.17 which is obtained from the axisymmetric concentric ring model of Rand and Kulkarni (1989).

5.3.2 Propagation in the Galactic Magnetic Field

Following the method of Honda (1987), orthogonal axes $\hat{x}$, $\hat{y}$ and $\hat{z}$ are created. These orthogonal axes correspond to the co-ordinate system used to describe the galaxy (see Figure 5-4), with the centre of the galaxy at the centre of the cartesian co-ordinate system. The cosmic ray is defined to have momentum $\vec{p}$ whose magnitude is E/c where E is the energy of the cosmic ray and c is the velocity of light. In the rest frame of the

UNIVERSITY OF ADELAIDE LIBRARY

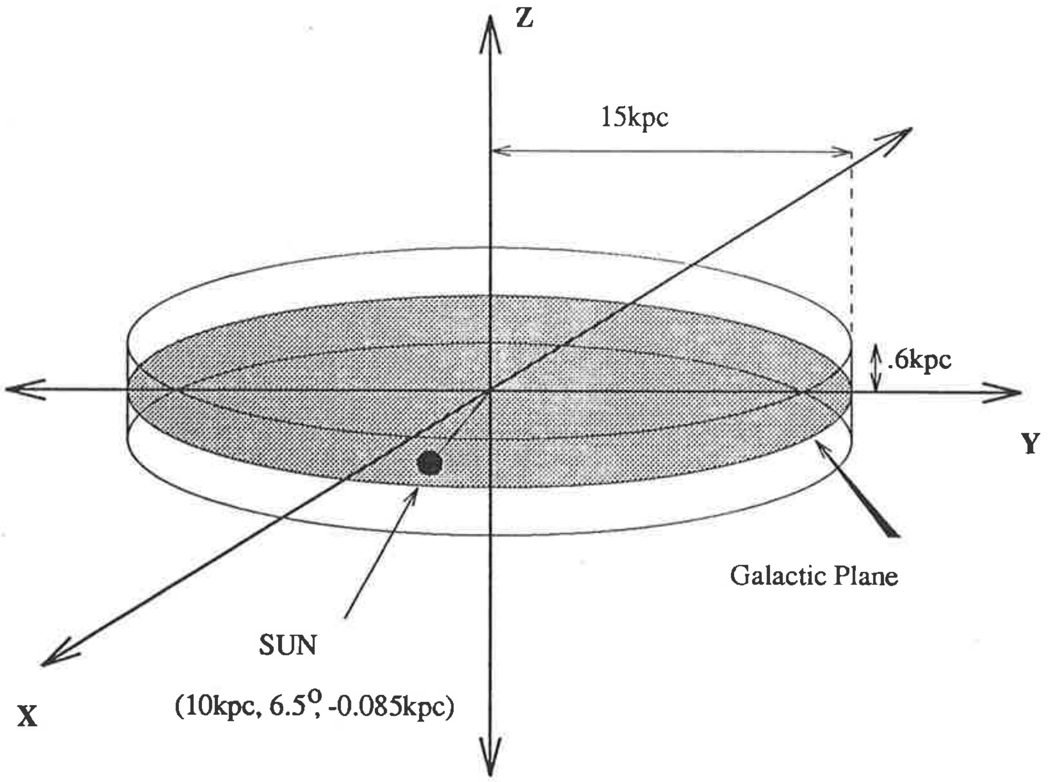

Figure 5-4: The co-ordinate system used for the galaxy. The galactic disk is assumed to have a half-thickness of 600 pc and a radius of 15 kpc. The sun has a position in this co-ordinate system of (10 kpc, 6.5°, 0.085 kpc) corresponding to cylindrical co-ordinates (R, ϕ, z). This unusual position of the earth is taken from Thielheim and Langhoff (1968) and is used to maintain consistency.

particle, orthogonal axes are defined, these being

$$\begin{aligned}\hat{u}_{\parallel} &= \hat{B} \, , \\ \hat{u}_{\perp} &= \hat{p} \times \hat{u}_{\parallel} \, , \\ \hat{u}_{\mathrm{T}} &= \hat{u}_{\perp} \times \hat{u}_{\parallel} \, . \end{aligned} \tag{5.26}$$

The components of momentum in this new co-ordinate system are found by forming the dot product of the momentum $\vec{p}$ with the cartesian unit vectors of the new co-ordinate system i.e.

$$\begin{aligned} p_{\parallel} &= \hat{B} \cdot \vec{p} \, , \\ p_{\perp} &= \hat{u}_{\perp} \cdot \vec{p} \, , \\ p_{\mathrm{T}} &= \hat{u}_{\mathrm{T}} \cdot \vec{p} \, . \end{aligned} \tag{5.27}$$

General propagation of a charged particle with charge q in a magnetic field $\vec{B}$ and electric field $\vec{E}$ has its motion determined by the Lorentz force $\vec{F}$ defined by

$$\vec{F} = \frac{d\vec{p}}{dt} = q(\vec{E} + \vec{v} \times \vec{B}) \, . \tag{5.28}$$

For the purpose of simulating the propagation of cosmic rays within the galaxy no electric field is assumed. In the rest frame of the particle the action of the Lorentz force is equivalent to the momentum transformation

$$\begin{aligned} p'_{\parallel} &= p_{\parallel} \, , \\ p'_{\perp} &= p_{\perp} \cos\omega\Delta t - p_{\mathrm{T}} \sin\omega\Delta t \, , \\ p'_{\mathrm{T}} &= p_{\perp} \sin\omega\Delta t + p_{\mathrm{T}} \cos\omega\Delta t \, . \end{aligned} \tag{5.29}$$

where

$$\omega = \frac{q\left|\vec{B}\right|}{Ec} \, , \tag{5.30}$$

and Δt is the time increment, E is energy and c is the velocity of light. This can be transformed back in terms of the original galactic cartesian co-ordinate system giving

$$\begin{aligned} p_x &= p'_{||}u_{||x} + p'_{\perp}u_{\perp x} + p'_{\mathrm{T}}u_{\mathrm{T}x} \;, \\ p_y &= p'_{||}u_{||y} + p'_{\perp}u_{\perp y} + p'_{\mathrm{T}}u_{\mathrm{T}y} \;, \\ p_z &= p'_{||}u_{||z} + p'_{\perp}u_{\perp z} + p'_{\mathrm{T}}u_{\mathrm{T}z} \;. \end{aligned} \tag{5.31}$$

For each of the components $\hat{x}$, $\hat{y}$ and $\hat{z}$ a distance increment is calculated and is added to the position of the cosmic ray. For example, the increment in the x component Δx of the position of the cosmic ray is given by

$$\Delta x = \frac{p_x}{|\vec{p}|} \times c \times \Delta t \;. \tag{5.32}$$

Δt is always defined to be the time necessary to complete 1/10 of a revolution, where the gyroradius is defined at the cosmic ray's position. In this way, if a cosmic ray encounters a large magnetic field, possibly due to turbulence, the step size will decrease because of the smaller gyroradius. A method used to check that computational numerical errors did not accumulate for large propagation times was to check that the absolute value of the cosmic ray's momentum did not change.

5.4 Propagation of EHE Cosmic Rays

5.4.1 Introduction

The purpose of this section is to establish whether cosmic rays of energies in the range of 10^{18}–10^{20}eV originate within the galaxy using the method of simulating cosmic ray propagation in a turbulent magnetic field described previously in this chapter. It is important to see whether the inclusion of turbulence, both in the galaxy or in a possible halo, is sufficient enough to randomise cosmic ray trajectories such that their detection on earth is isotropic. At the present time there is no statistical significance in the anisotropies detected in the energy range being considered (Bird *et al.*, 1993e; Bird *et al.*, 1993f; Chiba *et al.*, 1993a; Clay, 1987; Gillman and Watson, 1993; Krasilnikov, Ivanov and Nikolsky, 1993; Sokolsky, Sommers and Dawson, 1992).

5.4.2 Method of Simulation

To simulate the cosmic ray anisotropy observed at earth, the method first used by Karakula *et al.* (1971) is adopted. This method can be used test the theory that cosmic rays originate within our galaxy. One way to simulate the expected anisotropy measured on earth is to propagate cosmic rays from assumed sources through the galaxy and then analyse their arrival directions at earth. However this is impractical because of the miniscule volume the solar system occupies in comparison to the galactic disk. Instead of this, Karakula *et al.* (1971) analysed the trajectories of antiprotons emitted isotropically from earth. The amount of time spent (or equivalently distance travelled) by an antiproton in the galactic disk for a given emission direction is assumed to be directly proportional to the cosmic ray flux (assuming protons) detected from this same direction. This assumes that cosmic ray sources are distributed uniformly in the disk.

This approach has subsequently been used by Berezinsky and Mikhailov (1983), Berezinsky and Mikhailov (1987), Berezinsky, Mikhailov and Syrovatskii (1979) and more recently by Berezinsky *et al.* (1991) and Smith and Clay (1990). The galactic field model used by Berezinsky and Mikhailov (1983), Berezinsky, Mikhailov and Syrovatskii (1979), Karakula *et al.* (1971) and Smith and Clay (1990) is the bisymmetric spiral model of Thielheim and Langhoff (1968) (see Section 5.2.3). In this report the more recent axisymmetric model of Rand and Kulkarni (1989) is used. Equation 5.17 is modified to include an exponential decrease in field strength with distance above and below the galactic disk i.e.

$$\vec{B}_{\mathrm{reg}} = 2.15 \exp\left(-\frac{|z|}{175\ \mathrm{pc}}\right) \sin\left(1.0134\left(R_{\mathrm{kpc}} - 3.1876\right)\right) \hat{e}_{\phi}\ \mu\mathrm{G}\ . \qquad (5.33)$$

As discussed previously (see Section 5.2.3) this model is consistent with the more recent Faraday rotation data as well as agreeing with the predictions of the galactic dynamo theory (Vallée, 1991).

The galactic disk is assumed to have a radius of 15 kpc and also to extend to a distance of 300 pc above and below the galactic plane. Antiprotons are propagated throughout the galactic magnetic field using the methods described in Section 5.3 for assumed turbulent magnetic field configurations. The total path length of the antiproton in the galactic disk before it escapes the galaxy is then stored for each emission direction. Ten thousand antiprotons are emitted for each energy simulated. The amplitude and phase of the first harmonic in Right Ascension of incident cosmic rays are then calculated from these path lengths. In this report the anisotropies were calculated for an array located at the latitude of Haverah Park using an approximate form of that array's zenith angle distribution. This array's characteristics were chosen because it has had the longest exposure at EHE energies, with some 106 events detected with energies above 10^{19} eV. The gradient of the cosmic ray intensity with respect to galactic latitude is also calculated. The larger (more negative) the gradient, the steeper the fall off in cosmic ray intensity from the galactic plane. Clearly a large measured gradient would imply a galactic origin for the cosmic ray flux.

5.4.3 Effect of Turbulence in the Galactic Disk

The first galactic magnetic field configuration simulated assumed a random field $\vec{B}_{\mathrm{ran}} = 5\ \mu$G, as measured by Rand and Kulkarni (1989). The effect of varying the largest length scale of turbulence is investigated. Normally in simulations which model the irregular component of the galactic magnetic field, the galaxy is divided into cells of the assumed length scale of turbulence, L_0, and a random orientation of the irregular field is chosen for each cell e.g. Giller *et al.* (1993). The method of generating the irregular field presented here is far more realistic as it incorporates the effects of lower length scales of turbulence. Turbulent magnetic fields on these lower length scales may add to or subtract from the strength of the overall irregular field locally depending on their orientation. Also as discussed previously, the method used in this report ensures that $\vec{\nabla} \times (\vec{B}_{\mathrm{ran}} + \vec{B}_{\mathrm{reg}}) = 0$ at least locally, ensuring that there are no point sources of magnetic flux.

Figure 5-5 depicts the results of simulations which vary the assumed length scale of turbulence. The values chosen are $L_0 = 50$, 100 and 150 pc. The contour maps are used to plot the dependence of cosmic ray path length in the galaxy as a function of

Right Ascension and declination. These are equal area plots using a Hammer-Aitoff projection. Increasing the length scale L_0, reduces the amplitude of the first harmonic more rapidly with decreasing rigidity. This happens because the gyroradius of the cosmic ray becomes comparable to the length scale of turbulence at higher rigidities. This implies that scattering becomes more efficient at higher rigidities. If no turbulence is included in the simulation, the amplitude of the first harmonic is essentially constant at $\sim 90\%$ over the rigidity range considered. Some indicative points of the experimentally measured anisotropy and galactic latitude gradient can be seen in Figure 5-5 (d) and (f). These are plotted at rigidity values assuming a pure proton flux.

The measured cosmic ray anisotropy is inconsistent with a galactic origin if a proton flux is assumed. This is true for any of the length scales of turbulence assumed in the galactic disk. The same conclusion can also be drawn from the plot of galactic latitude gradient as a function of rigidity (Figure 5-5(f)). Simulated galactic gradients are 3–5 times higher than observed gradients assuming a galactic origin for the cosmic ray flux. A pure iron cosmic ray flux would be consistent with observations since the rigidity of a 10^{19} eV iron nuclei is 26 times smaller than the rigidity of a proton with the same energy.

Chi *et al.* (1992c) have stated that there exists a galactic plane excess which is dependent on composition. By analysing EHE air shower data they have concluded that showers initiated by protons are from directions closer to the galactic plane and that those initiated by heavy nuclei originate from directions offset from the galactic plane. They also conclude that the fraction of heavy nuclei in the cosmic ray flux continues to rise until an energy of 3×10^{19} eV, implying that the source of these cosmic rays is the galaxy. Above 3×10^{19} eV the flux is assumed to have an extragalactic origin and is dominated by protons. Sun, Wang and Watson (1993) however conclude, also from composition information derived from air shower data, that there isn't any evidence for any mass dependence of the cosmic ray flux as a function of galactic latitude or primary energy. The most recent Fly's Eye result (Bird *et al.*, 1993d; Gaisser *et al.*, 1993) using stereo analysis of some 5129 events between 0.3 to 30 EeV shows that the composition changes from heavy to predominantly light in the range 0.3 to 10 EeV. From 0.1 to 0.3 EeV the elongation rate is consistent with a constant but heavy flux. The Fly's Eye results are from the observation of the shower development of extensive air showers and as such carry much more weight than the inferred observations of Chi *et al.* (1992c).

Stereo Fly's Eye analysis of the arrival directions of cosmic rays in the energy range 0.3 EeV to greater than 10 EeV and with an angular uncertainty of $d\theta = 1.7°$ shows no evidence for a significant galactic plane excess (Bird *et al.*, 1993e). This is in disagreement with Figure 5-5 which shows a significant galactic gradient with latitude. Accepting that EHE cosmic rays are predominantly light in composition and that there exists no significant evidence for a galactic plane excess, then the results presented in Figure 5-5 which assume a galactic origin for the cosmic ray flux are inconsistent with experimental results.

5.4.4 Effect of a Galactic Halo Magnetic Field

A further factor affecting the anisotropy of EHE cosmic rays would be the existence of a galactic halo. This would enlarge the containment volume for EHE cosmic rays. If there exists a turbulent magnetic field in the halo of suitable strength and length scale then this may serve to further isotropise the cosmic ray flux. There have been detections of radio haloes for edge-on spiral galaxies (Hummel, Beck and Dahlem, 1991; Hummel *et al.*, 1988). These at least suggest the possibility that such a halo with its own magnetic field may exist in our Galaxy. It is worth pointing out however that radio haloes have only been reported from $\sim 5\%$ of all of the edge-on spiral galaxies observed by radio astronomers (Hummel, Beck and Dettmar, 1991).

There does exist some indirect evidence for our own galactic halo. These indications come from theoretical considerations resulting from the measured lifetime of cosmic rays (Jokipii, 1976), distribution of γ-ray emissivity with galactic radius (Bloemen, 1989) and primary to secondary ratios of cosmic ray abundances (e.g. Webber, Lee and Gupta (1992)). See Bloemen (1987) and Dogiel (1991) for a summary. Direct evidence for the existence of a galactic halo is complicated by our own observation position being in the galactic disk. The aim of this set of simulations is to establish whether the existence of a galactic halo magnetic field can sufficiently randomise cosmic ray trajectories to agree with the measured anisotropy.

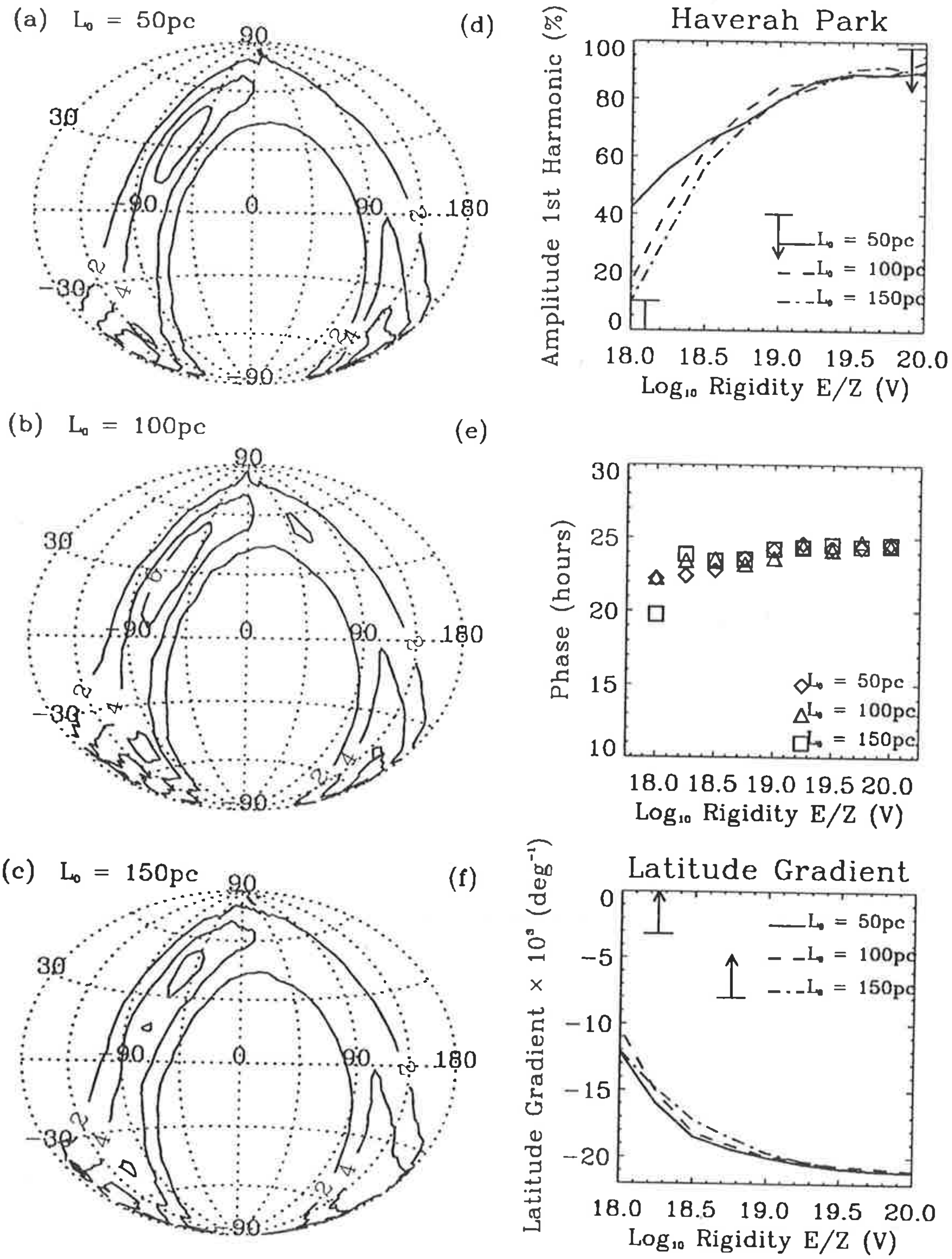

Figure 5-5: Results from simulation of EHE cosmic ray propagation. $\left|\vec{B}_{ran}\right|$ is assumed to be 5 μG. Path lengths in the galactic disk (in kpc) for different arrival directions at 10^{19} eV can be seen for an assumed length scale of turbulence L_0 of (a) 50 pc (b) 100 pc and (c) 150 pc. (d) and (e) plot the amplitude and phase of the first harmonic of the cosmic ray flux as would be seen by the Haverah Park array. Upper limits shown in figure (d) are indicative of anisotropy measurements at 10^{18}, 10^{19} and 10^{20} eV. In (f) the EHE cosmic ray galactic latitude gradient is plotted as a function of rigidity. Lower limits shown at 10^{18} and 10^{19} eV are indicative of experimental measurements.

5.4.5 Turbulent Halo Field

Initially the magnetic field in the halo is assumed to be purely non-ordered. The origin of the turbulence in the galactic halo is assumed to be from supernova remnants in the halo (McKee and Ostriker, 1977). The length scale for turbulence assumed in the halo is 800 pc. This value was chosen as an upper limit to the scale size of the turbulence. If it is found that this length scale is not sufficient to randomise cosmic ray trajectories then a more realistic lower value would not. The field configuration for the galactic disk assumed the field described in Section 5.4.3 with $L_0 = 100$ pc. Three different strengths of the random magnetic field in the halo are assumed, these being 2 μG, 5 μG and 10 μG. Three different halo geometries are assumed. Figure 5-6 presents the results from an assumed cylindrical halo of height 3 kpc above and below the galactic disk. Figure 5-7 presents the results from an assumed cylindrical halo of height 5 kpc above and below the galactic disk. The third halo configuration assumed is a 15 kpc spherical halo and this is shown in Figure 5-8. Again the experimental results are plotted assuming a protonic composition (Z=1).

Clearly the turbulent magnetic halo with the strongest field strength of 10 μG provides the best agreement with experimental results. The randomisation of cosmic ray trajectories can be seen quite clearly in the contour plots of the path length assuming a strength of 10 μG (Figures 5-6(c), 5-7(c) and 5-8(c)). This shows that cosmic rays whose initial directions do not intersect the galactic plane have had their trajectories sufficiently changed so that they actually intersect the galactic plane. However for a more realistic value of a 2 μG turbulent magnetic halo the results only vary $\sim$ 10% compared with the equivalent galactic disk results presented in Figure 5-5. This implies that a halo must have a strong ($> 2\mu$G) field in order to affect cosmic ray propagation in the rigidity range considered. At lower energies the plots of the amplitude of the first harmonic for each field strength converge. This is because at lower energies the effect of the galactic disk magnetic field configuration, which is assumed to be constant, determines the low rigidity turbulence.

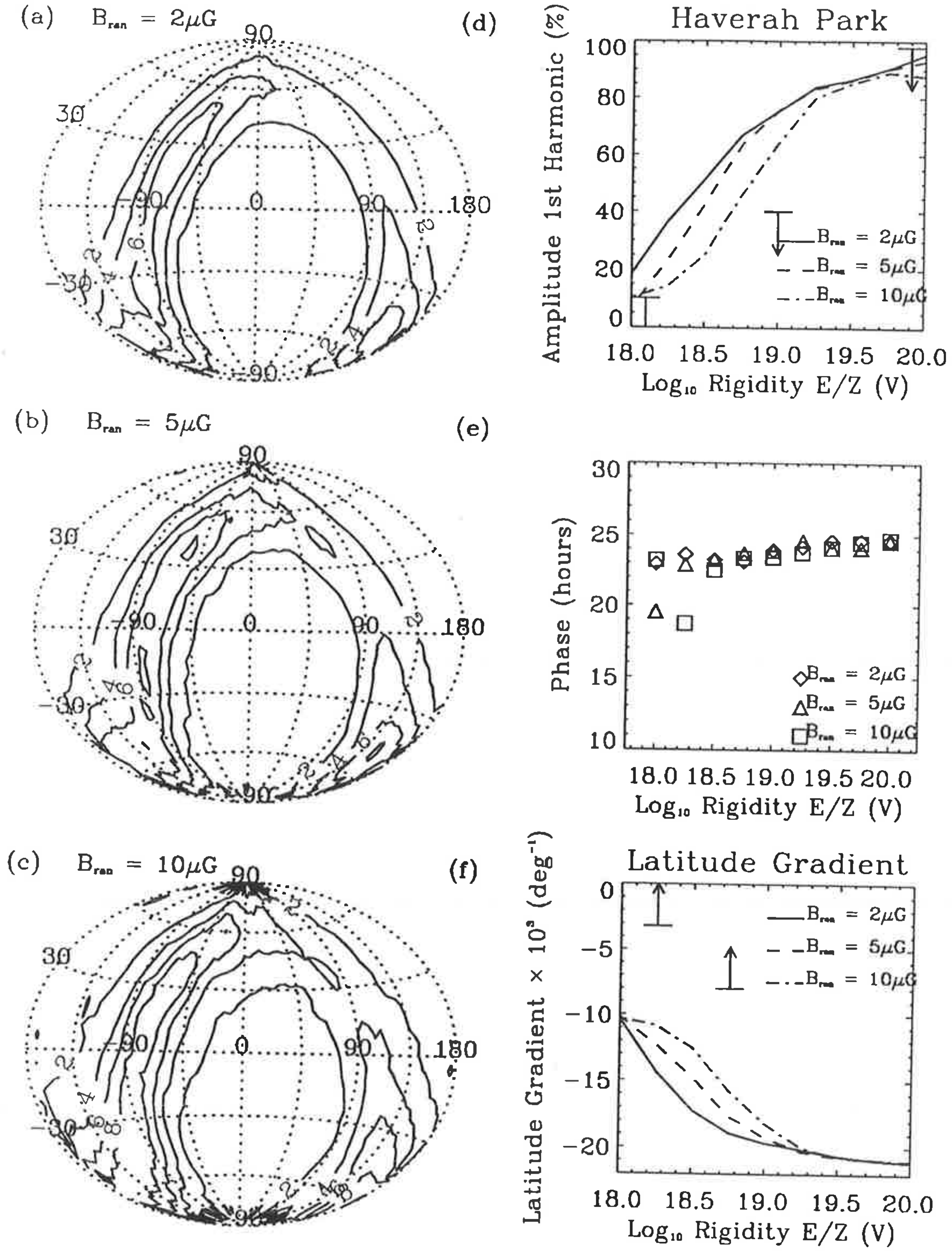

Figure 5-6: Results from simulations of EHE cosmic ray propagation. The assumed source distribution is uniform within the galactic disk. A 3 kpc cylindrical halo above and below the galactic disk is assumed. The magnetic field configuration in the disk is identical to Figure 5-5. Path lengths (in kpc) in the galactic disk for different arrival directions at 10^{19} eV can be seen for an assumed length scale of turbulence L_0 in the halo of 800 pc and turbulent magnetic field strengths of (a) 2 μG (b) 5 μG and (c) 10 μG.

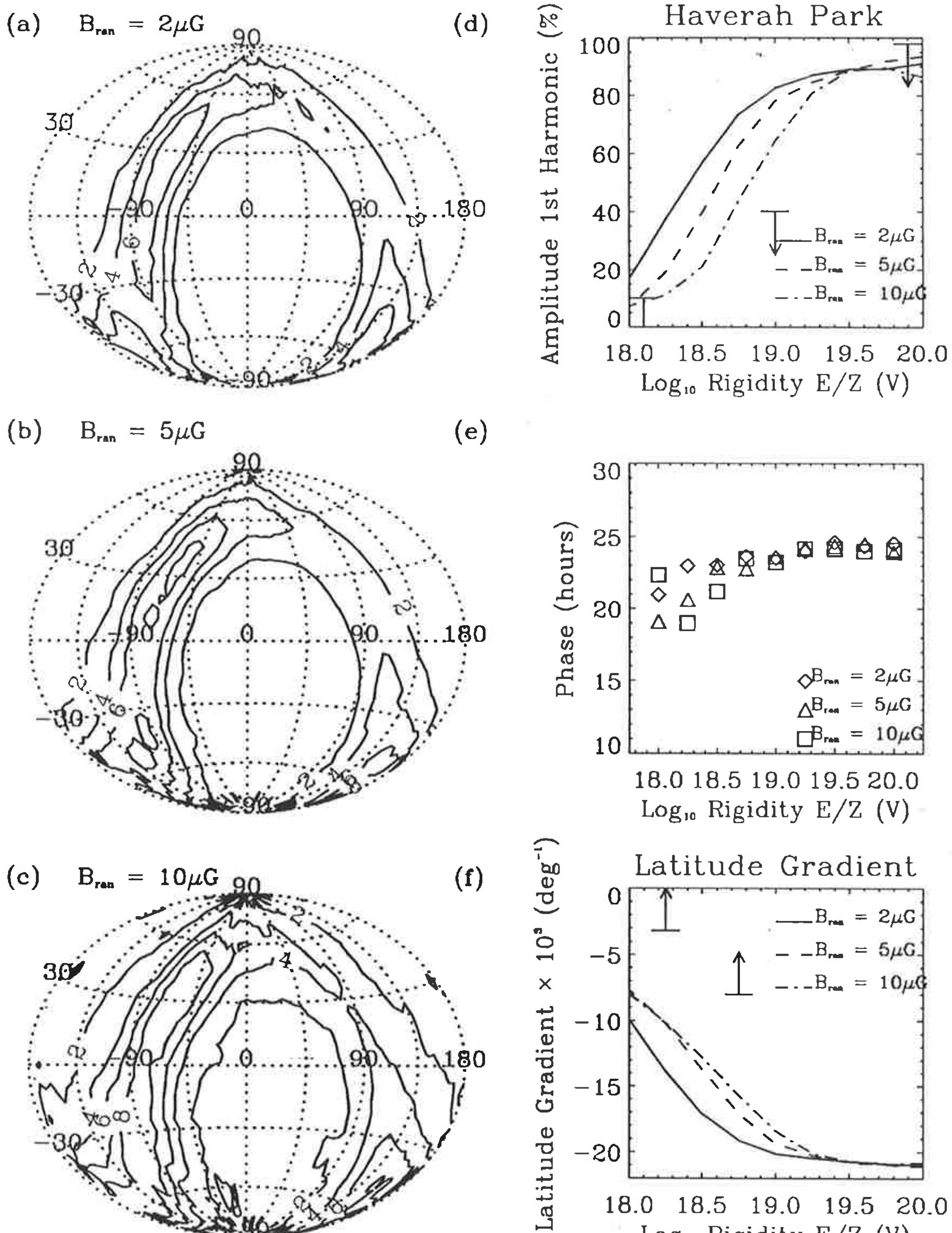

Figure 5-7: Results from simulations of EHE cosmic ray propagation. The assumed source distribution is uniform within the galactic disk. A 5 kpc cylindrical halo above and below the galactic disk is assumed. The magnetic field configuration in the disk is identical to Figure 5-5. Path lengths (in kpc) in the galactic disk for different arrival directions at 10^{19} eV can be seen for an assumed length scale of turbulence L_0 in the halo of 800 pc and turbulent magnetic field strengths of (a) 2 μG (b) 5 μG and (c) 10 μG.

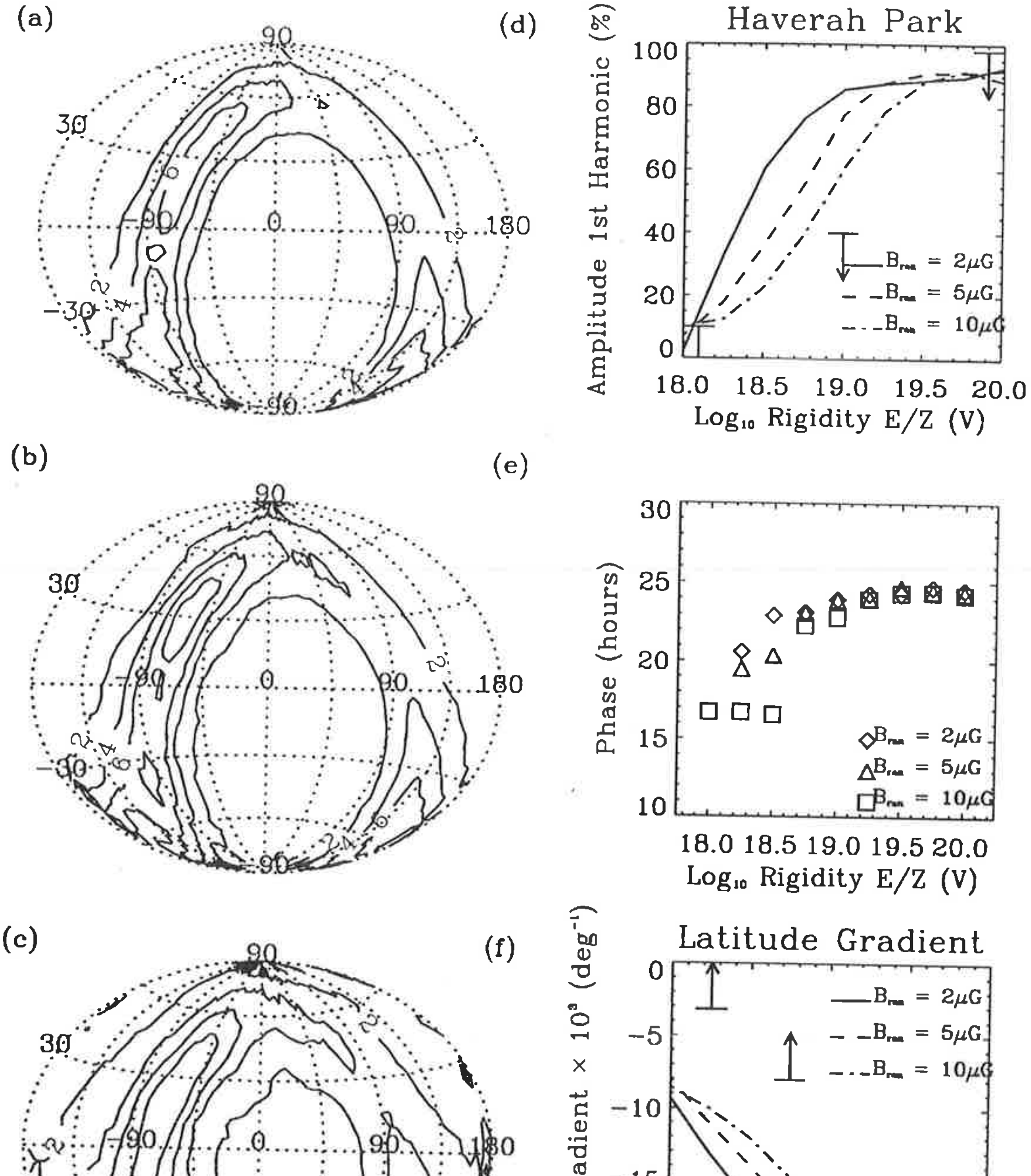

Figure 5-8: Results from simulations of EHE cosmic ray propagation. The assumed source distribution is uniform within the galactic disk. A 15 kpc spherical halo is assumed. The magnetic field configuration in the disk is identical to Figure 5-5. Path lengths (in kpc) in the galactic disk for different arrival directions at 10^{19} eV can be seen for an assumed length scale of turbulence L_0 in the halo of 800 pc and turbulent magnetic field strengths of (a) 2 μG (b) 5 μG and (c) 10 μG.

5.4.6 Non-Random Halo Field

At the present time there is no direct evidence for the presence of an ordered field in the halo. There is evidence for the existence of ordered magnetic field edge-on spiral galaxies, NGC 4631 (Hummel, Beck and Dahlem, 1991; Humm 1988) and NGC 891 (Hummel, Beck and Dahlem, 1991). Sokoloff and Shukur found by analysing conditions present in an assumed galactic halo and by ap dynamo theory (see Section 5.2.2) that conditions may exist for the generatio large scale ordered field. To this end Brandenburg *et al.* (1992) and Brandenb (1993) have extended the galactic dynamo theory to include the galactic halo Gorchakov *et al.* (1991), using analytical arguments, concluded that the fields described in Sokoloff and Shukurov (1990) are capable of confining protons of up to $\sim 3 \times 10^{19}$ eV in the halo. It was decided to test this result computatio using the method outlined in this report.

The non-random field in the halo is taken from Berezinsky *et al.* (1991) an adaption from Sokoloff and Shukurov (1990). This field is defined in terms $\hat{r}$, azimuthal $\hat{\phi}$ and zenith $\hat{\theta}$ components. The radial component H_r is defined

$$H_r = 0.26 H_{r1}(r) + 0.13 H_{r2}(r)\ \mu\text{G} ,$$

where

$$H_{r1}(r) = \frac{1.168}{r} Q(r) \cos\theta \,(5\cos(2\theta) - 1) ,$$

with $Q(r) = r^{1/2} \mathrm{J}_{7/2}(5.763r)$,

$$H_{r2} = 0.692 r^{-3/2} \mathrm{J}_{3/2}(\pi r) \cos\theta .$$

The zenith angle component is defined as

$$H_\theta = 0.26 H_{\theta 1} + 0.13 H_{\theta 2}\ \mu\text{G} ,$$

where

$$H_{\theta 1} = -0.584 \frac{\sin\theta}{r} \left(5\cos^2\theta - 1\right) \frac{d}{dr}\left(rQ(r)\right) ,$$

$$H_{\theta 2} = -0.346 \frac{\sin\theta}{r} \frac{d}{dr} \left(r^{-0.5} \mathrm{J}_{3/2}(\pi r) \right) . \tag{5.39}$$

The azimuthal component is defined as follows

$$H_{\phi} = 3.273 r^{-1/2} \mathrm{J}_{5/2}(5.763 r) \sin\theta \cos\theta \ \mu\mathrm{G} . \tag{5.40}$$

The radius of the spherical halo is taken to be 15 kpc.

Results shown in Figure 5-9 find for these simulations that the inclusion of an ordered field in the halo does not make any substantial difference from those results where the halo is assumed to be purely random. This is not surprising considering the weakness of the field, which has a maximum strength of ~ 1.5 μG. In conclusion, it is found that the addition of an ordered magnetic field of the type predicted by the dynamo model does not affect EHE cosmic ray propagation significantly.

5.5 Conclusions

The effects of magnetic field turbulence on the anisotropy of EHE cosmic rays has been investigated in this chapter. It is found that if the cosmic ray flux is made up predominantly of protons in the energy range 10^{18}–10^{20} eV, then the observed galactic magnetic field turbulence is not sufficient to scatter cosmic rays enough so that the computed anisotropy and galactic gradient agree with observations. The inclusion of a turbulent halo was also investigated. Some agreement with experimental results were found for the halo configurations tested. However, the magnetic field strength needed was ~ 10 μG and this is approximately five times the estimates of the halo field strength (Sofue, 1991). Analyses of the effect of an ordered field component in the halo have found that such a field can trap EHE cosmic ray protons up to an energy of 3×10^{19} eV. In the simulations presented here no such effect has been found. This is essentially in agreement with Berezinsky *et al.* (1991)

In conclusion, it seems unlikely in the context of this model that EHE cosmic rays originate within the galactic disk. The effects of magnetic field turbulence and a larger propagation region have both been analysed. Results such as Bird *et al.* (1993e) and Sun, Wang and Watson (1993) imply that there is no significant galactic plane

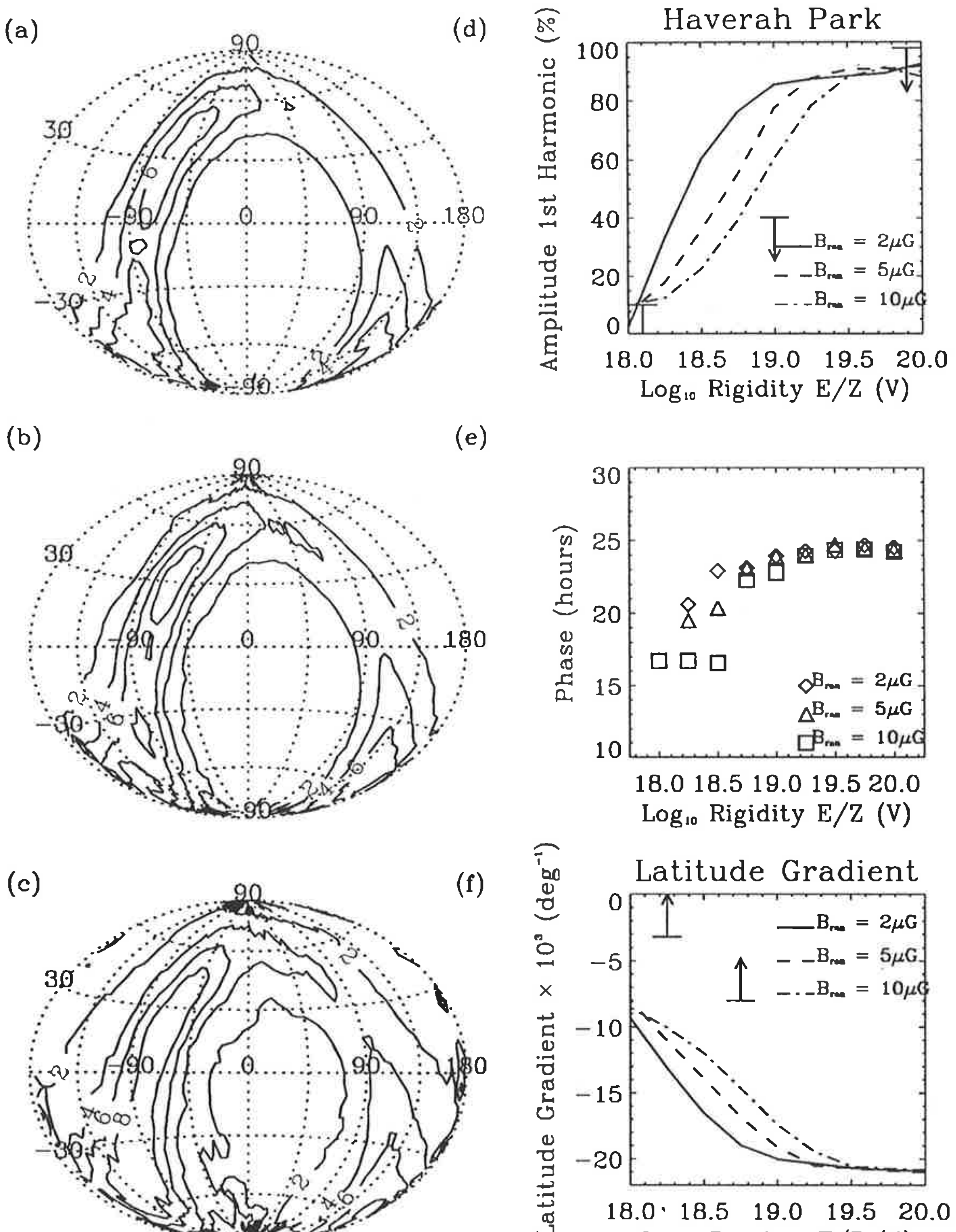

Figure 5-9: Results from simulations of EHE cosmic ray propagation. The assumed source distribution is uniform within the galactic disk. A 15 kpc spherical halo is assumed. The magnetic field configuration in the disk is identical to Figure 5-5. As well as a random field component in the halo, an ordered field component is included due to Sokoloff and Shukurov (1990). Path lengths (in kpc) in the galactic disk for different arrival directions at 10^{19} eV can be seen for an assumed length scale of turbulence L_0 in the halo of 800 pc and turbulent magnetic field strengths of (a) 2 μG (b) 5 μG and (c) 10 μG.

enhancement, which is in direct contrast to the results presented here which all show a marked dependence of the cosmic ray flux on galactic latitude.

The change in spectral index in the cosmic ray energy spectrum between 2×10^{18} eV and 5×10^{18} eV observed by the Fly's Eye, where the slope flattens from -3.27 to -2.71, may indicate the dominance of an extragalactic proton flux (Bird *et al.*, 1993c). This is in agreement with the results presented here which imply that the origin of EHE cosmic rays is not within our own galaxy since if galactic sources are assumed for the simulation then the computed results are in contradiction with the measured anisotropy.

Chapter 6

Extensive Air Showers

6.1 Introduction

The cascade of secondary particles which results from the interaction of a cosmic ray (nucleus or γ-ray) with an atmospheric nucleus is termed an Extensive Air Shower (EAS). The secondary particles produced by this interaction can be divided into three groups:

1. Hadronic Component: This consists of the nuclear component of an EAS.
2. Hard Component: This consists of the muon component of an EAS.
3. Electromagnetic Component: This is also called the soft component of an EAS and consists of the electrons, positrons and photons produced in the cascade.

There is also a neutrino component, but because of its extremely small chance of interaction, it is not usually taken into account when describing EAS.

The basic evolution of an EAS is as follows. The hadronic component of the shower feeds energy into the electromagnetic component via the decay of high energy unstable hadrons which produce photons. These photons then pair produce giving rise to electromagnetic cascades. Decay of the hadronic component of the shower also gives rise to the muon component. As the shower evolves, the number of particles (γ+ $e^{\pm}$ + nucleons + muons) reaches a maximum S_{max} and then becomes attenuated as energy for the creation of new particles dissipates.

Primary cosmic rays with energies $\leq 10^{13}$ eV do not give rise to EAS which are detectable at ground level. For primary cosmic rays with energies between 10^{12}–10^{13} eV, Čerenkov radiation is produced by EAS which can be detected by ground based light detectors. Above 10^{13} eV direct measurements of EAS are possible by detectors at mountain altitudes and above 10^{14} eV detection is possible using particle detectors at sea level. This progression continues on to the highest energies, where at energies $> 10^{19}$ eV, S_{max} can occur at sea level.

In this chapter the physics of the development of EAS is reviewed. Since the detection of EAS is the only method by which cosmic rays with energies greater than $\sim 10^{15}$ eV can be analysed, an understanding of EAS is necessary to be able to correctly determine the primary cosmic ray's energy and direction. Furthermore, conventional cosmic ray detectors only sample an EAS at one point in its development, so an understanding of the statistical fluctuations inherent in shower development needs to be gained.

6.2 Hadronic Component

A cosmic ray will produce an EAS when it interacts with an atmospheric molecule such as N_2 or O_2. For protons, the interaction length λ_P is given by

$$\lambda_P \sim 67.2 \left(\frac{E_{\mathrm{TeV}}}{100}\right)^{-0.065} \mathrm{g\,cm^{-2}} \, .$$

(Dawson, 1985; Ellsworth *et al.*, 1982)

In contrast, the interaction length for an iron primary λ_{Fe} is essentially energy independent with

$$\lambda_{Fe} \sim 13 \ \mathrm{g\,cm^{-2}} \, .$$

(Westfall *et al.*, 1979)

Because of the extreme relativistic energies involved in the interaction of a cosmic ray with an atmospheric molecule, the collision can be viewed as the interaction of a nucleon (from the cosmic ray primary) with one or two of the nucleons from the air molecule. These nucleons are ejected from the atmospheric nucleus, which consequently only gains a small percentage of the primary's energy. The fraction of energy lost by the primary in this type of interaction is termed the inelasticity. This energy goes into the production of new particles which form the hadronic component of the cascade.

The longitudinal momentum of the particles produced in the centre of momentum (CM) frame is divided up into three regions corresponding to the projectile fragmentation region, the target particle fragmentation region and the central region. The central region corresponds to particles of small momenta in the CM frame; it is where the bulk of new particle production occurs. This region is sometimes called the pionisation region. The transverse momentum p_T of the produced particles is small, ~ 0.4 GeV. This ensures that the hadronic core of an EAS is tightly bunched around the direction of the incoming primary. Coulomb scattering of these heavy energetic particles is small which ensures that the lateral extent of the hadronic core at sea level is only a few metres.

6.2.1 Pions

The majority of particles produced by a cosmic ray-air nucleus interaction are pions. Pions are generated in equal numbers of positive, negative and neutral varieties ($\pi^{\pm}\pi^{0}$). The mass of the neutral pion is $m_{\pi^0} \sim 135$ MeV and it has a half life $t_{1/2} \sim 8 \times 10^{-17}$ s, before decaying by photoproduction $\pi^0 \longrightarrow \gamma\gamma$ (98.8%). Charged pions $\pi^{\pm}$ have a mass of ~ 140 MeV and a half life $t_{1/2} \sim 2.60 \times 10^{-8}$ s. The decay channels for $\pi^{\pm}$ are

$$\pi^{\pm} \longrightarrow \mu^{\pm} + \nu_{\mu}(\overline{\nu}_{\mu}) \ (100\%) \ .$$

Charged pions may interact with atmospheric nuclei before decaying because of their relatively large lifetimes. The muons resulting from the decay of $\pi^{\pm}$ make up most of the muon component of an EAS.

6.2.2 Kaons

The next most commonly produced particle, accounting for up to $\sim 10\%$ of the particles produced, are kaons. These particles also occur in charged varieties ($m_{K^{\pm}}$ $=494$ MeV, $t_{1/2} = 1.2 \times 10^{-8}$ s) and neutral particles $\overline{K}^0$ and K^0. These neutral kaons are produced in quantum mechanical mixed states

$$K^0_S = \frac{1}{\sqrt{2}}(\mid K^0 > + \mid \overline{K}^0 >) \qquad (m_{K^0_S} = 497.7 \text{ MeV } t_{1/2} = 8.9 \times 10^{-11}\text{s}) \ ,$$

$$K^0_L = \frac{1}{\sqrt{2}}(\mid K^0 > - \mid \overline{K}^0 >) \qquad (m_{K^0_L} = 497.7 \text{ MeV } t_{1/2} = 5.1 \times 10^{-8}\text{s}) \ .$$

The neutral kaons have the following decay modes

$$\begin{array}{lll} K^0_S & \longrightarrow \pi^+\pi^- & , \\ K^0_L & \longrightarrow \pi^0\pi^0\pi^0 & (21.6\%) \\ & \longrightarrow \pi^+\pi^0\pi^- & (12.4\%) \\ & \longrightarrow \pi^\pm\mu^\mp\nu_\mu & (27.0\%) \\ & \longrightarrow \pi^\pm e^\pm\mu_e & (38.7\%) \ . \end{array}$$

Charged kaons are similar to charged pions, in that they have similar lifetimes and share a decay channel

$$K^\pm \longrightarrow \mu^\pm + \nu_\mu(\overline{\nu}_\mu) \ (63.5\%) \ ,$$

plus also

$$K^\pm \longrightarrow \pi^\pm + \pi^0 \ (21.2\%) \ .$$

6.2.3 Modelling of Nucleon-Nucleon Interactions

It can be seen from the previous section that the muonic and electromagnetic components of an EAS result from the decay of pions and kaons formed in the inelastic p-p and p-n collisions. Thus to model EAS it is necessary to know the cross sections for producing these particles. Unfortunately, man-made accelerators are not capable of reaching cosmic ray energies (i.e Fermilab TeVatron with centre of mass energy < 1.8 TeV $\equiv E_{lab} \equiv E_{cos-ray} < 2 \times 10^{15}$ eV) so that extrapolation of results obtained at lower energies must be used to model the development of EAS. Early models of pion production (i.e. Fermi (1951)) were statistical-hydrodynamical in nature and predicted multiplicities for the produced pions $< n >$ to vary as

$$< n > \propto E^{0.25} .$$

A more successful thermodynamic model, the CKP + isobar model (see Feinberg (1981)) explained pion production in terms of "fireballs". The advent of scaling theories meant that results from lower energy accelerator data could be extrapolated to higher cosmic ray energies.

6.2.4 Scaling of the Inclusive Cross Section

Scaling, in terms of nucleon-nucleon inclusive processes was first proposed by Feynman (1969). For two nucleons A and B, an inclusive process is defined by

$$\mathrm{A} + \mathrm{B} \longrightarrow \mathrm{C} + \mathrm{X} ,$$

where X is unmeasured and C is a given measured product of the interaction, e.g. a pion. The invariant cross section for finding particle C in the invariant phase space $\frac{d^3 p_C}{E_C}$ is defined as

$$\begin{aligned} \sigma_C &= E_C \frac{d^3 \sigma_{AB}}{d^3 p_C}(\sqrt{s}, p_{\|}^*, p_T) \\ &\equiv f_{ac}^{(b)}(\sqrt{s}, p_{\|}^*, p_T) , \end{aligned}$$

where $\sqrt{s}$ is defined as the total centre of mass energy of A+B and $*$ denotes the CM frame. $p_{\|}$ and p_T are the longitudinal and transverse momentum respectively.

Feynman and Radial Scaling

Feynman scaling is defined as the case where, as $\sqrt{s} \longrightarrow \infty$ then

$$f_{ac}^{(b)}(\sqrt{s}, p_{\|}^*, p_T) \overset{\sqrt{s}\rightarrow\infty}{\longrightarrow} f_{ac}^{(b)}(x^*, p_T) ,$$

where x^* is defined as $\frac{p_{\|}^*}{p_{\|(max)}^*}$. This implies that $f_{ac}^{(b)}$ is virtually independent of energy, as p_T is only weakly energy dependent. For Feynman scaling the invariance of the cross section with energy holds for $x^* \in [-1,1]$. Another form of scaling proposed by Yen (1974) is termed radial scaling. In this case the scaling variable x^* is defined as

$$x^* = \frac{E^*}{E^*_{(max)}} \ .$$

Scaling with this parameter describes more accurately the central region ($x^* \sim 0$) of the inclusive process. Both Feynman scaling and radial scaling predict for fixed p_T, that the multiplicity of produced secondaries $\langle n_c \rangle$ will vary logarithmically with energy i.e.

$$\langle n_c \rangle \propto \ln E \ ,$$

as compared to the limiting case, where the secondary particles share the energy equally in the CM system

$$\langle n_c \rangle \propto E^{\frac{1}{2}} \ ,$$

(Chantler *et al.*, 1982). Another consequence of Feynman scaling is that the inelastic cross section $\sigma^{\mathrm{AB}\rightarrow\mathrm{CX}}$ is predicted to be invariant with energy as $\sqrt{s} \longrightarrow \infty$

Hypothesis of Limiting Fragmentation

Another weaker form of scaling due to Benecke *et al.* (1969) is termed the Hypothesis of Limiting Fragmentation (HLF). In this form of scaling, the invariant cross section becomes independent of the primary's energy only in the non central regions ($x^* < 0$ and $x^* > 0$). This implies that the only particles in the beam and target fragmentation regions approach limiting distributions as $\sqrt{s} \longrightarrow \infty$.

6.2.5 Application of Scaling at Cosmic Ray Energies

It it believed that scaling should set in at energies as low as $10^{11}eV$ (Bøggild, Hansen and Suk, 1971). Whether some form of scaling is valid at cosmic ray energies is a contentious question. Observations of cosmic rays (Yodh, Pal and Trefil, 1972) and accelerator data (Amaldi *et al.*, 1977; Amos *et al.*, 1989) find that σ_{p-p} and σ_{p-air} increase with energy ($\propto \ln^2 s$) thus ruling out Feynman scaling.

Olejniczak, Wdowczyk and Wolfendale (1977) concluded that if the primary cosmic ray flux is composed of protons at 10^{15} eV then scaling is not likely to be valid at these energies. If scaling is valid at these energies then the most likely dominant component of the primary flux would be iron. This is the interpretation of EAS data by Yodh *et al.* (1984) who find evidence for heavy nuclei and minimal scaling violations. On the other hand Wdowczyk and Wolfendale (1987), Wdowczyk and Wolfendale (1983) suggest that EAS data are consistent with a proton dominant composition, similar to that at lower energies, and a break-down of scaling. The main problem with analysing EAS in this manner is that one is more sensitive to primary particle composition than to the the model of nuclear interaction being investigated (Chantler *et al.*, 1982).

6.3 Electromagnetic Component

The primary source of the electromagnetic component of an EAS initiated by a cosmic ray is the γ-rays resulting from π^0 decay ($\pi^0 \rightarrow \gamma\gamma$, see Section 6.2.1). γ-rays with energies above ~ 1 MeV will pair produce in the neighbourhood of an atomic nucleus, producing electron positron pairs ($\gamma \rightarrow e^+e^-$). Electrons and positrons produced by pair production will either interact with the atmosphere through ionisation or by production of photons by bremsstrahlung ("braking radiation"). The radiative mean free path X_o ($e^{\pm} + N \rightarrow \gamma + e^{\pm} + N$) in air for production of photons is given by

$$X_o = 2.92 \, \frac{1}{P} \, \frac{T}{273} 10^2 \text{ m} \,, \tag{6.1}$$

(Cocconi, 1961) where T is temperature in Kelvin and P is in atmospheres. A typical value for X_o in air is ~ 37.7 g cm^{-2}. The photons produced by bremsstrahlung can pair produce again creating another electron-positron pair. At lower energies (< 20 MeV) photons will Compton scatter with electrons and at lower energies still, photons are lost by the photoelectric effect (Rossi and Greisen, 1941). The combination of these processes produces an electromagnetic cascade.

The number of photons + electrons + positrons increases until the energy loss experienced by electrons and positrons by bremsstrahlung is equalled by the energy

	Approximation A	Approximation B
Pair Production	Yes	Yes
Bremsstrahlung	Yes	Yes
Ionisation	No	Yes

Table 6.1: Processes included for "Approximation A and B" (Rossi, 1952).

loss through ionisation. This occurs for electrons and positrons with energies of $E_c \sim$ 80 MeV (Rossi and Greisen, 1941). Since no more γ's are produced and the electrons lose their energy rapidly through ionisation, the cascade becomes rapidly attenuated. The average energy of each photon will also fall as the cascade develops and the number of particles increases, ensuring that Compton scattering and the photoelectric effect will dominate.

Two approximations used to treat the theory of electromagnetic cascades are "Approximations A and B" (see Table 6.1). A simple model of the electromagnetic cascade is the "Toy model" due to Heitler (1944). Consider the case of Approximation A where just the processes of pair production and bremsstrahlung are employed. Assume that both these processes have the same mean free path X_o (in fact $X_{\gamma \to e^+ e^-} = \frac{9}{7} X_o$). Consider an initial γ-ray with energy E_o which initiates a cascade where the energy is divided equally amongst all secondary particles. Define the shower unit X_r ($\sim$ 30 g cm^{-2}) as the distance travelled through the atmosphere at which there is a 50% chance of bremsstrahlung occurring for an electron or positron, or pair production for a γ-ray.

It then follows that

$$\exp\left(\frac{-X_r}{X_o}\right) = 0.5 \; ,$$

which implies

$$X_r = X_o \ln 2 \; . \tag{6.2}$$

Thus the number of particles (electrons + positrons + γ's) is doubled every shower unit and the average energy per particle halved. Thus after n interactions the number of particles N expected is

$$N = 2^n \; , \tag{6.3}$$

each with an average energy E equal to

$$E = \frac{E_o}{2^n} . \tag{6.4}$$

The increase in shower size will continue until the average energy per electron falls below the critical energy E_c, at which point electrons lose energy by ionisation. Therefore after some k shower units

$$E_c = \frac{E_o}{2^k} ,$$

which implies that

$$2^k = N_{max} = \frac{E_o}{E_c} . \tag{6.5}$$

At these lower energies, secondary photons will undergo Compton scattering and photoabsorption. Combining Equations 6.2 and 6.5 results in an estimate for X_{max}, the position at which shower maximum occurs, of

$$X_{max} = kX_r = X_o \ln\left(\frac{E_o}{E_c}\right) . \tag{6.6}$$

After X_{max} has been reached the shower becomes rapidly attenuated. Even so, for typical showers with primary energy $\geq 10^{15}$ eV, the electromagnetic component of the shower makes up some 95% of the number of particles at ground level. Although this model is quite crude, relations such as

$$\begin{aligned} N_{max} &\propto E_o , \\ X_{max} &\propto \ln E_o , \end{aligned}$$

and the exponential growth of the cascade before shower maximum are all observed (Allan, 1971). The rapid attenuation after shower maximum is characterised by an attenuation length of ~ 130 g cm^{-2} (Cocconi, 1961). One limitation of this model is the assumption that the energy is divided equally between all the particles, when in reality the lower energy particles are more abundant (Rossi, 1952). Also, fluctuations intrinsic to the development of the cascade are not included.

Ionisation in the electromagnetic cascade prior to shower maximum is important and is included in treatments using Approximation B, where a constant ionisation energy loss of $\sim$ 80 MeV is assumed per radiation length. A treatment of the longitudinal development of an electromagnetic cascade using Approximation B derived by Greisen (1956) yields the particle number N_e as a function of the primary photon energy E_o and atmospheric depth t by

$$N_e(E_o, t) = \frac{0.31}{\sqrt{t_{max}}} \exp\left[t(1 - \ln s)\right] \ , \qquad (6.7)$$

where

$$\begin{aligned} t_{max} &= \ln\left(\frac{E_o}{E_c}\right) && \text{depth of maximum ,} \\ s &= \frac{3t}{t + 2t_{max}} && \text{shower age ,} \end{aligned}$$

with all depths expressed in radiation lengths.

The parameter s is known as the shower age and is closely related to the development of the shower. It follows from the definition of s, that s equals 1 at shower maximum. s equal to 0 signifies the beginning of the cascade, reaching 1 at shower maximum and further increasing to a value of 2 when only 1 particle remains. Figure 6-1 plots the development of an electromagnetic cascade and the associated behaviour of the shower age (from Cocconi (1961)).

An extensive air shower initiated by a cosmic ray nucleus will have energy continuously fed to the electromagnetic cascade early in shower development by π^0 decay. Thus a cosmic ray initiated shower will develop more gradually in the atmosphere than a γ-ray initiated shower, reach shower maximum deeper in the atmosphere and also decay more slowly with an attenuation length of 185 g cm^{-2} (Clay and Gerhardy, 1982). For a more comprehensive discussion of the difference between cosmic and γ-ray initiated showers see Section 6.5.

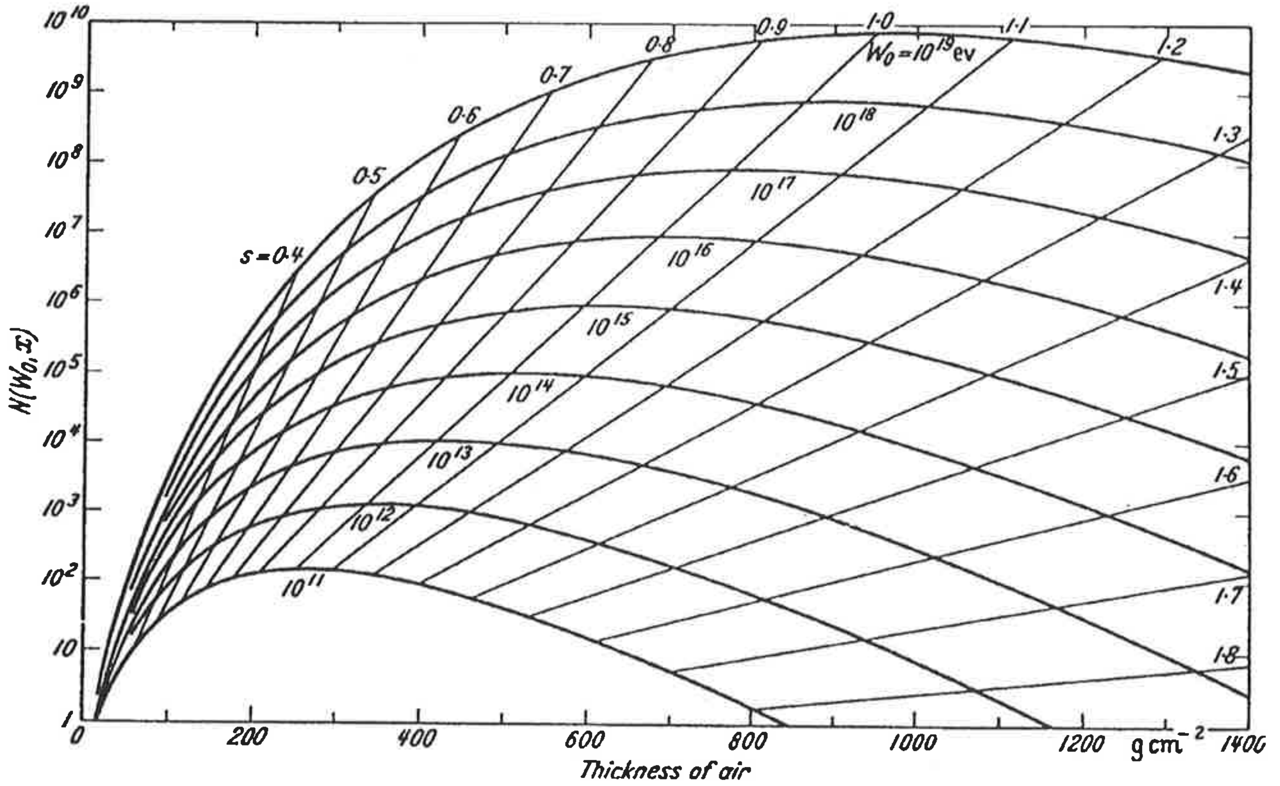

Figure 6-1: Development of an electromagnetic cascade through the atmosphere as described by Equation 6.7, for various values of W_0 ($W_0 \equiv E_0$). The curves indicate the electron number at a particular depth in the atmosphere measured in g cm^{-2}. The radial lines correspond to a fixed shower age s for the cascade (from Cocconi (1961)).

6.3.1 Lateral Distribution

Typically experiments which measure the properties of extensive air showers do so by sampling discretely the lateral spread of particles at a given atmospheric depth. Clearly, in order to interpret these measurements, knowledge of how the lateral distribution is related to primary energy and composition is important. This is accomplished by comparing the measured lateral distribution of detected particles with some theoretical lateral distribution which is a function of distance from the core r, some parameter related to the shower age s and the shower size N_e.

For the electromagnetic component of an extensive air shower, which makes up $\sim$ 95% of total particles detected at sea level, the lateral spread is caused by Coulomb scattering. The expression that gives the average angle $\langle \delta\theta \rangle$ after multiple Coulombic scatterings, for a single charged particle of energy E ($E >> mc^2$) in crossing a thickness δt, in units of radiation length, is

$$\langle \delta\theta^2 \rangle = \left(\frac{E_s}{E}\right)^2 \delta t \; , \tag{6.8}$$

(Rossi and Greisen, 1941)

where $E_s = 21.2$ MeV (Cocconi, 1961). The natural unit of lateral displacement, termed the Molière unit r_o is given by

$$r_o = \frac{E_s}{E_c} X_o = 9.50 \text{ g cm}^{-2} \; , \tag{6.9}$$

which is dependent on altitude in a similar way to Equation 6.1. Thus more energetic electrons will be scattered less than those of lower energy. This implies that electrons further out from the shower core will be generally of lower energy and suffer a time lag behind the arrival of the core. Thus the shower front will be curved, typically with a radius of curvature of $\sim$ 1 km. The shower front will move essentially at the speed of light and have a thickness of $\sim$ 2 metres near the core increasing in thickness as distance from the core increases. Extremely energetic primaries will give rise to, in some instances, extremely large showers with radii $>$ 2 km. The large thickness of the shower front at these great distances from the core would be a signature for these showers allowing them to be discerned by small arrays, whose elements can measure the width of the shower front (Linsley, 1983).

Lateral distribution functions are usually of the form

$$\rho(N_e, r) = \frac{N_e}{r_o^2} f\left(\frac{r}{r_o}\right) \text{ particles m}^{-2} , \tag{6.10}$$

where N_e is the shower size, r_o is the Molière radius ($\sim$ 80 metres at sea level, Greisen (1960)) and r is the distance from the core. $f\left(\frac{r}{r_o}\right)$ is termed the lateral structure function. One of the most common lateral structure functions used is the NKG (Nishimura-Kamata-Greisen) function. This is an empirical description by Greisen (1956) of the complicated theoretical description derived by Nishimura and Kamata (1951) to describe a purely electromagnetic cascade. f_{NKG} is defined as

$$f_{\mathrm{NKG}} = C(s) \left(\frac{r}{r_o}\right)^{s-2} \left(\frac{r}{r_o} + 1\right)^{s-4.5} , \tag{6.11}$$

(Greisen, 1956)

where $C(s)$ is defined as

$$C(s) = \frac{\Gamma(4.5 - s)}{2\pi\Gamma(s)\Gamma(4.5 - 2s)} .$$

The NKG function may however be too simplistic a description of the actual lateral distribution. Hillas and Lapikens (1977) have found that lateral distributions obtained from Monte Carlo simulations of electromagnetic cascades are narrower than the NKG function, with a median shower radius of $0.5r_o$ as opposed to r_o. This was supported by Lagutin, Pljasheshnikpv and Uchaikin (1979) who suggested an age dependence to the mean radius r_m given by

$$r_m = (0.78 - 0.4s)r_o .$$

This also agrees with the more recent result of Van Der Walt (1988) who found

$$r_m = (1.254 - 0.499s)r_o .$$

Capdevielle and Gawin (1982) found from theoretical considerations that the shower age, s, estimated by fitting to the NKG function, is a factor of 1.3 less than the true shower age. The true longitudinal shower age could be obtained from lateral electron densities by using a local age parameter dependent on distance from the core, although in practice this may be difficult.

Measurements of the electron lateral distribution have been carried out using the CASA array (Van Der Velde *et al.*, 1991) located at the Dugway proving grounds in Utah. This array consists of some 529 surface detectors arranged on a grid with 15 metre spacing (Gibbs, 1988) providing excellent spatial resolution of the lateral distribution. CASA is located at an atmospheric depth of ~ 860 g cm^{-2} which would imply a value for the Molière radius r_o of 105 metres. However, they find excellent agreement when fitting the lateral distribution by using the NKG function with a value for r_o of 80 metres which is $\sim 4/5 r_o$.

6.4 Muon Component

The muon is a weakly interacting particle and a member of the lepton family. The muon is a charged particle ($\mu^{\pm}$), with a mass $m_{\mu^{\pm}} \sim 106$ MeV. The mean lifetime of a muon is $\sim 2.2 \times 10^{-6}$ s (Brown, Nordstrom and Brown, 1992). The main decay modes for the muon are

$$\begin{aligned} \mu^{+} &\longrightarrow e^{+} + \nu_e + \overline{\nu}_{\mu} \ , \\ \mu^{-} &\longrightarrow e^{-} + \overline{\nu}_e + \nu_{\mu} \ . \end{aligned}$$

Thus muons which decay in the evolution of an EAS will contribute to the electromagnetic component. Muons with a Lorentz factor > 20 will survive to sea level because of the time dilation effect.

As noted in Section 6.2, muons are produced via the decay of π and K mesons. This implies that they are produced early in the development of an EAS, where effects due to the primary's composition are important (e.g. Elbert and Sommers (1987)). Other muon producing processes within an EAS are pair production ($\gamma \rightarrow \mu^{+}\mu^{-}$) and photoproduction of pions ($\gamma \rightarrow \pi^{+}\pi^{-}$) which then decay to muons. These production processes are only expected to become important for primaries with energies $> 10^{18}$ eV

(McComb, Protheroe and Turver, 1979). Muons are produced early in an EAS development and their attenuation length $\lambda_\mu \sim 1000$ g cm^{-2}, due almost entirely to ionisation (~ 2 MeV g cm^{-2}), is approximately 5 times that of the electromagnetic component (Hara *et al.*, 1983). This implies that the muon component of an EAS is relatively unaffected by fluctuations in shower development.

At sea level the average energy of the muon component is much greater than that of the electromagnetic component. Typically for a muon, the average energy is ~ 2 GeV compared to that of an electron with ~ 200 MeV . This ensures that at sea level the muon component carries $\sim$ 5–6 times more energy than the electromagnetic component (Greisen, 1956). However at shower maximum, where the number and average energy of electrons is much greater, this situation is reversed.

For small EAS, that is with energies $10^{11} < E < 10^{14}$ eV, only the muon component is detectable at sea level. Because of the sharply falling energy spectrum of cosmic rays, these muons make up the dominant component of the cosmic ray flux at sea level, and are termed "unaccompanied muons". The total flux of muons at sea level for momentum $p > 0.35$ GeV/c is

$$\begin{aligned} J &= (1.44 \pm 0.09) \times 10^{-2}\,\mathrm{cm}^{-2}\,\mathrm{s}^{-1} \\ &\sim 1\,\mathrm{cm}^{-2}\,\mathrm{min}^{-1} \ . \end{aligned}$$

(Allkofer *et al.*, 1975)

The zenith angle dependence for this flux is given by

$$J(\theta) \propto \cos^n(\theta) \ ,$$

where $n = 2.1 \pm 0.1$ (Crookes and Rastin, 1971)

6.4.1 Lateral Distribution

The lateral distribution for muons ρ_μ, is of the form (Greisen, 1956)

$$\rho_\mu(N, r) \propto r^{-3/4}\left(1 + \frac{r}{k(s,\theta)}\right)^{-2.5} ,$$

where k is a function of shower age s and zenith angle θ (Hara *et al.*, 1983). Although the transverse momentum of the parent K and π mesons are small, the muons are spread out at sea level by virtue of being produced at great heights in the atmosphere and essentially travelling in straight lines from their point of production.

The lateral distribution for muons is flatter than that of the electromagnetic component (see Equations 6.10 and 6.11) so that near the axis of an EAS the muon density is $\sim$ 50–100 less than that of the electrons. However, at distances from the core in excess of 1 km the muon component dominates. Because muons are so penetrating, measurements of muon fluxes are made by shielding detectors from the electromagnetic component using a large thickness of dense material. Usually this is achieved by locating muon detectors underground (e.g. Barrett *et al.* (1952)).

6.5 γ-ray Initiated Air Showers

Thus far the discussion of EAS has concentrated on those showers resulting from nucleon primaries. A subset of all cosmic ray EAS, however, are initiated by γ-ray primaries. Experiments which set out to measure a γ-ray flux from an astrophysical object will have the dominant cosmic ray flux as the background. Any method which can differentiate between γ-ray and cosmic ray initiated showers will greatly increase the ratio of signal to noise. In this section the expected characteristics of a γ-ray initiated shower are reviewed. The current state of experimental evidence pertaining to the detection of γ-rays from astrophysical sources is also discussed.

6.5.1 Muon Content

γ-ray initiated showers are expected to be deficient in muons as they are almost purely an electromagnetic cascade. The dominant source of muons in a cosmic ray initiated shower results from charged pion decay. As there are no pions being produced by the continual interaction of the hadronic core of a cosmic ray initiated shower with the atmosphere, γ-ray initiated showers are expected to be muon poor. Muons can be produced in a purely electromagnetic cascade by the decay of pions produced by photopion production ($\gamma + N \rightarrow \pi + X$). This process has a probability of occurring of

$\sim 2.8 \times 10^{-3}$ compared to that of electron-positron production. An even rarer process producing muons in an electromagnetic cascade is pair production ($\gamma \rightarrow \mu^+\mu^-$), with a relative probability of $\sim 2 \times 10^{-5}$ compared to electron-positron production. This has led to the belief that γ-ray EAS should have the muon content $\sim 10\%$ of an equivalent cosmic ray air shower (Braun and Sitte, 1965; Karakula and Wdowczyk, 1963; Maze and Zawadzki, 1960; Wdowczyk, 1965).

Claimed observations of γ-rays from Cygnus X-3 (Samorski and Stamm, 1983b) by detection of EAS, reported a comparatively high muon content, $\sim 77\%$ of cosmic ray EAS (Samorski and Stamm, 1983a). A detection of a signal from the Crab Nebula at an energy of $\sim 10^{16}$ eV, showed a muon content $\sim 60\%$ relative to proton initiated showers (Dzibowski *et al.*, 1983). These results prompted more detailed calculations (Edwards, Protheroe and Rawinski, 1985; Gaisser, Protheroe and Stanev, 1983; Stanev, Gaisser and Halzen, 1985) which in turn could find no justification for increasing a muon content above the 10% expected for γ-ray initiated showers in the energy range 10^{15}–10^{17} eV. The growth in detections of γ-ray sources has done nothing to make the situation clearer. Shower cuts preferring muon poor showers increased the significance of the Akeno detection of Cygnus X-3 (Kifune *et al.*, 1986). In contrast to this, detections of Cygnus X-3 (Dingus *et al.*, 1988b) and Hercules X-1 (Dingus *et al.*, 1988a) by the CYGNUS air shower array, reported that the muon content of these showers was higher than the background cosmic ray showers. Detection of excess events from the two X-ray binary systems LMC X-4 and 2A 1822-37.1 by the SUGAR air shower array is also puzzling since this array triggers on the muon content of incident air showers. However more muons are expected in the energy range of the SUGAR detector ($> 10^{18}$ eV) than at lower energies. These muons result from the pair production of muons and photoproduction of pions which then decay to muons.

As a possible explanation, the rapid increase of the photopion production cross section with energy above 1×10^{13} eV would enhance the muon content of γ-ray showers. Models of how the photopion production cross section varies with energy, taking into account the gluon content of high energy photons, predict a rapidly rising cross section (Drees and Halzen, 1988; Halzen, 1990; Krys, Krys and Wasilewski, 1991). However, while the number of TeV muons produced is increased ten-fold and the number of GeV muons doubled, the total number of muons is not the same as hadron initiated showers for a primary energy of 100 TeV (Gaisser *et al.*, 1990). The γ-ray showers which have the same characteristics as hadronic showers are those rare events where photoproduction occurs in the first interaction. Experimentally measured muon/electron ratios in cosmic ray showers have been used by Dumora, Procureur and Stamenov (1992) to rule out a rapid increase in the photopion cross section for constant composition up to energies of $\sim 10^{16}$ eV. In conclusion, the subject of the muon content of γ-ray initiated showers is still far from resolved.

6.5.2 Shower Age

γ-ray initiated EAS were conventionally expected to develop earlier than equivalent proton initiated showers. A proton initiated shower has energy fed continuously by π^0 decay from the hadronic core into the electromagnetic cascade as it propagates through the atmosphere. This is in direct contrast to a γ-ray initiated shower, where the electromagnetic cascade is initiated at a point. Also the mean free path for electron-positron pair production is shorter than the expected mean free path for hadronic interactions until 10^{17}–10^{18} eV. This leads to the conclusion that γ-ray showers should on average be more developed when detected, corresponding to a greater shower age.

Shower age cuts have been applied to enhance the γ-ray signal from Cygnus X-3 (Samorski and Stamm, 1983b; Tonwar *et al.*, 1988) and Vela X-1 (Protheroe, Clay and Gerhardy, 1984; Van Der Walt *et al.*, 1987). Observations of Vela X-1 and Centaurus X-3 by the BASJE collaboration also have used shower age cuts along with muon cuts (Suga, 1985). The value of age cut used depends on the altitude of the detector, as at higher altitudes the average shower age is less than that measured for sea-level detectors.

Monte Carlo simulations (Cheung and MacKeown, 1988; Fenyves, 1985; Hillas, 1987) suggest that the age parameter does not provide a statistically significant indicator for a γ-ray shower. Indeed simulations show that the average shower age of a γ-ray initiated air shower may be slightly less than that of a proton initiated shower of the same size. This is in direct contradiction to those results finding significant enhancements of a signal with shower age cuts. Importantly however, simulated distributions of shower age in showers do not agree with experimental results (Tonwar *et al.*, 1988).

Chapter 7

Simulations for an Experiment to Detect EHE Cosmic Rays

7.1 Introduction

The subject of this chapter is the design of an experiment to detect large numbers of EHE cosmic rays. The primary difficulty in detecting cosmic rays of these energies is their extremely low flux i.e. $J(E > 10^{18}\ \mathrm{eV}) \sim 100\ \mathrm{km}^{-2}\mathrm{sr}^{-1}\mathrm{yr}^{-1}$. Important requirements of an EHE cosmic ray detector are the abilities to be able to measure accurately the energy and direction of incident cosmic rays and to be able to distinguish the nature of the primary cosmic ray. By determining these properties of EHE cosmic rays, theories regarding EHE cosmic ray origin can be further refined.

As an introduction to the problem of detecting EHE cosmic rays, past and present detectors which have operated or are still operating in the EHE energy region are reviewed. Following this, the computational methods used to simulate an EHE ground array are presented. Configurations for the geometry and detector characteristics of a ground array are then analysed and the optimum detector design discussed. A new generation of detector is then proposed consisting of a ground array, as described in the first section of this chapter, working in tandem with an optical fluorescence detector. The chapter then concludes with a summary of the detector designs discussed.

7.2 Existing and Previous EHE Cosmic Ray Detectors

In order to detect EHE cosmic rays it is necessary to have an extremely large collecting area. There are at present two types of large collecting area detectors used. The first and most common type is a ground array consisting of individual detector components. The principle behind the ground array is the detection of secondary particles created by a cosmic ray incident on the earth's atmosphere (see Chapter 6). By measuring the spaced particle densities at a set atmospheric depth the incident energy of the cosmic ray can be inferred. By measuring the relative timing of the shower front at different detector positions the direction of the incident cosmic ray can also be determined.

The second type of detector measures directly the extensive air shower's passage through the atmosphere. By measuring the longitudinal development of the air shower, information on the composition of the incident cosmic ray is obtained. This method also provides a better estimator of the primary particle's energy as the total development of the shower is analysed rather than the development of the EAS at one elevation, as in the case of a ground array. A successful detector using this principle is the Fly's Eye detector which measures the nitrogen fluorescence of the atmosphere as it is being energised by an extensive air shower. One major drawback of this technique is that the experiment can only operate on moonless nights giving an effective duty cycle of 12%.

7.2.1 Ground Arrays

Haverah Park

The Haverah Park detector was operated by the University of Leeds during the period July 1968–July 1987. It was situated at 53°58.2′ North, 1°38.2′ West at an altitude of 220 metres above sea level. The detector consisted of a ground array whose individual detecting units were water Čerenkov detectors. These were in the main composed of galvanised iron tanks filled with water to a depth of 1.2 metres and varying in area from 1–54 m^2. The triggering condition for the array was a signal equivalent to 10 vertical muons travelling through a water depth of 1.2 metres, recorded at the central

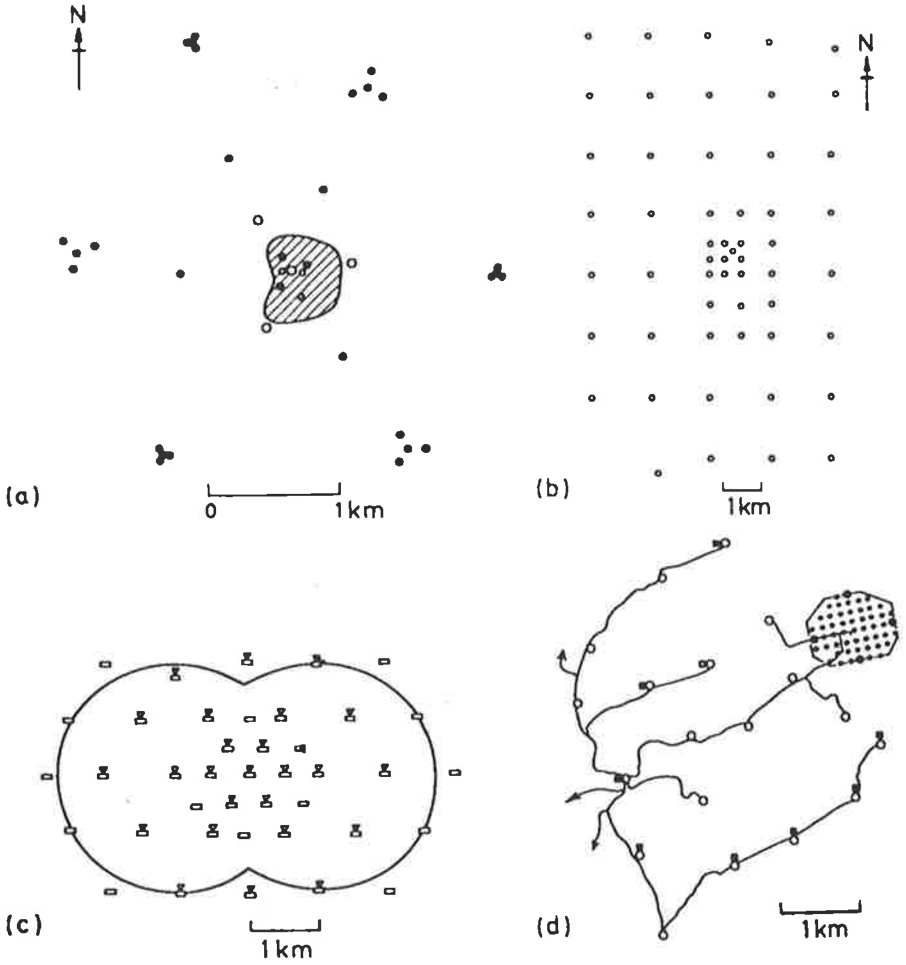

Figure 7-1: Diagram of four high energy cosmic ray detectors, (a) Haverah Park: water Čerenkov detectors of 34 m^2 (large open circles); 13.5 m^2 (filled circles); 9 m^2 (small open circles). (b) Sydney: positions occupied by stations (i.e. two 6 m^2 liquid scintillator detectors) at some time during the array's operation. (c) Yakutsk: scintillators of area 4 m^2 (rectangles); atmospheric Čerenkov light detectors of 15 cm diameter (triangles). (d) Akeno: the 20 km^2 array with the 1 km^2 array in the top right corner. Scintillation detectors are designated by open and closed circles (areas 2.25 m^2 and 1.0 m^2 respectively); muon detectors are designated by squares (from Sokolsky, Sommers and Dawson (1992)).

detector (see Figure 7-1(a)) and a similar signal in any two of the three other central detectors also recorded within 4 μs. These other detectors located at the centre of the array were separated by a distance of 500 metres from the central detector. The array arrangement with this triggering condition corresponded to an energy threshold of $\sim 6 \times 10^{16}$ eV (Lawrence, Reid and Watson, 1991).

The array encompassed an area of $\sim$ 12 km^2. To determine the shower direction a plane shower front was fitted to the times recorded at the 54 m^2 detectors. Energy was estimated by the ground parameter $\rho(600)$ which corresponds to the water Čerenkov signal density 600 metres from the shower axis. Monte Carlo simulations (Hillas *et al.*, 1971) imply that this quantity is a good estimator of primary energy, being relatively independent of primary interaction model and composition. Errors in the estimation of $\rho(600)$ are thought to be $\sim$ 30% (Cunningham *et al.*, 1980). The number of events observed by this detector with estimated energies above 10^{19} eV is 106.

Volcano Ranch

The earliest experiment designed specifically to detect EHE cosmic rays was the Volcano Ranch air shower detector. This detector was located at 35.16° North, 106.79° West at an elevation of 1.77 km, which corresponds to an atmospheric depth of 834 g cm^{-2}. In the period 1959–63 the array consisted of twenty detectors, 19 of which were positioned on a triangular grid. For the period 1959–60 the distance between adjacent detectors was 442 metres. This was then extended to 884 metres from 1961 onwards. Each of the individual detectors was composed of a 9 cm thick plastic scintillator with a surface area of 3.26 m^2. In order to trigger the array, a signal from three detectors was required. The shower direction was calculated by fitting a plane front to the particle arrival times on a subset of the total detectors.

The energy of the primary cosmic ray was estimated by fitting a lateral distribution to the measured particle densities and integrating to find total shower size and hence the primary energy. Because of its elevation it was expected that the shower size maximum S_{max} would occur at about the detector's atmospheric depth and, since this is expected to be directly proportional to the primary energy, the energy of the primary cosmic ray can be inferred from the shower size measured by the array. In this time period, 44 cosmic ray showers with estimated primary energies of 10^{19} eV or greater were detected.

SUGAR

The Sydney University giant air shower recorder (SUGAR) was a ground array which operated in the period between 1968–1979. It has been the only southern hemisphere detector designed for detecting EHE cosmic rays, being positioned at 30°32′ South, 149°43′ East. The area covered by the array was ~ 70 km^2 with 47 individual detecting stations (see Figure 7-1(b)), each of which consisted of two 6 m^2 conical liquid scintillator tanks separated by 50 metres. These tanks were buried underground to provide a muon threshold of ~ 1 GeV (Winn *et al.*, 1986b). Each individual detector station was autonomous in the sense that a detector was triggered whenever three particles were detected in each of the tanks. No multiple station triggering criteria was required and coincidences were found from analysis of the taped data at each site. Three stations triggered within a given time period signified an event in the analysis. A timing reference was sent by radio signal to each of the stations so that directional analysis could be undertaken by fitting a plane shower front. This gave an angular resolution for the detector of between 3°–6°.

In order to estimate the primary cosmic ray energy the total muon number was used. This was estimated by fitting a lateral distribution to the measured particle densities (Winn *et al.*, 1986b). Substantial experimental and analysis difficulties had to be overcome because of photomultiplier afterpulsing affecting the deduced particle numbers at each site. The number of showers detected by the SUGAR array with estimated energies above 10^{19} eV was 80.

Yakutsk

The Yakutsk cosmic ray detector array is located at 62° North, 129° East and covers an area of approximately 20 km^2. This detector is a particle detecting ground array consisting primarily of plastic scintillators, thirty five of which have a surface area of 4 m^2 and five with an area of 2 m^2. These detectors are arranged on a triangular grid (see Figure 7-1(c)). The detector spacing is ~ 1 km with seven of the detectors on a

500 metre grid at the centre of array. This allows a varying threshold to be set with (a) a threshold of $\sim 1 \times 10^{17}$ eV requiring 2 particles m^{-2} in three detectors on the 500 metre grid and (b) a threshold of $\sim 1 \times 10^{18}$ eV requiring 2 particles m^{-2} in three detectors on the 1 km grid (Glushkov *et al.*, 1987). The primary energy is estimated in a similar manner to the Haverah Park array, using the particle density at 600 metres, $\rho(600)$. Another means of energy calibration is provided by 50 Čerenkov light detectors. In order to study cosmic ray primary composition, a total of 116 m^2 of muon detectors with a threshold energy of ~ 1 GeV are located in the center of the array.

Akeno

The Akeno cosmic ray detector array is located in Japan at 138°30′ East, 35°30′ North at an altitude of ~ 900 metres above sea level. The array is composed of two sub-arrays each of different spacing. The 1 km^2 array consists of 156 scintillation detectors, each with an area of 1 m^2, in addition to six detectors with surface areas of 2.25 m^2. The detectors are spaced on a cartesian grid with a detector spacing of 120 metres. Within this array there are three clusters of detectors on a 30 metre grid used to observe small showers (Nagano *et al.*, 1992). The triggering condition for this array requires 7 individual detectors from the 120 metre grid to be alerted.

The 20 km^2 array was completed in 1984 and consists of a further 19 detectors, each with an area of 2.25 m^2, and an inter-detector spacing of ~ 1 km (see Figure 7-1(d)). The array trigger is generated by the detection of a signal in at least six of the individual detectors within a 40 μs gate (Teshima *et al.*, 1986b). For the 1 km^2 array, the primary cosmic ray energy is estimated from the total integrated shower size, whereas for the 20 km^2 array, the scintillator density at 600 metres from the shower axis is used (Nagano *et al.*, 1992). The approximate angular resolution of the large array is 3° for vertical showers (Teshima *et al.*, 1986a). Recently the Akeno Giant Air Shower Array (AGASA) covering 100 km^2 has been completed, which further extends the 20 km^2 array (Chiba *et al.*, 1992).

7.2.2 Optical Fluorescence Technique

Fly's Eye

The Fly's Eye detector is located at Dugway, Utah at 40° North, 112° West at an atmospheric depth, of 860 g cm^{-2}. The Fly's Eye detector relies on a radically different principle to the ground arrays discussed previously. Rather than sampling an EAS at a unique atmospheric depth, the Fly's Eye technique detects the light emitted isotropically by nitrogen fluorescence as an EAS travels through the atmosphere. This allows direct measurement of the longitudinal development of the shower and a direct estimate of the atmospheric depth at which an extensive air shower will reach its maximum shower size (Baltrusaitis *et al.*, 1985b).

The detector began operation in 1981 with the Fly's Eye I station. This detector consists of 67 1.5 metre diameter spherical section mirrors, each with 12 or 14 photomultipliers in the focal plane of the mirror. Each of the photomultipliers images a portion of the sky 5° in diameter and the entire night sky is imaged by 880 "eyes" (Baltrusaitis *et al.*, 1985b). Fly's Eye II, which commenced operation in 1986, is located 3.3 km from Fly's Eye I. It consists of 36 mirrors and 464 associated photomultipliers. The Fly's Eye II images the half of the night sky in the direction of Fly's Eye I so that a stereo view can be gained of a subset of EAS. It also has the capability to work as a stand alone detector (Baltrusaitis *et al.*, 1988). For EAS observed by both detectors, the shower axis can be found from the intersection of the two planes defined by the triggered phototubes, providing enhanced angular resolution. Although the experiment has a large collecting area, which increases with energy (~ 1000 km^2 at 100 EeV), the duty cycle is low at $\sim 12\%$. A new detector, the HiRes Fly's Eye, using the same principle is currently in the prototype stage. This is discussed in Section 7.5.3.

7.3 Simulations for a Ground Based Particle Array

An important consideration in the design of an array which will detect EHE cosmic rays is the ability to be able to determine their direction, energy and composition. In this section various array designs are investigated, particular emphasis being placed on determining the most efficient configuration in terms of covering the same collecting area with the smallest number of detectors, without compromising detection ability. The approach used is similar to Cronin (1992) in that a fairly simple lateral distribution is used. This allows the testing, in a straightforward manner, of the ability of different array configurations to resolve a cosmic ray's primary energy. The parameters varied in these simulations were inter-detector spacing, triggering requirements and array configuration.

7.3.1 Lateral Distribution

The lateral distribution used in these simulations has been derived from the Volcano Ranch Data (Linsley, 1980) by Cronin (1992). Showers with energies greater than 10^{19} eV and zenith angles less than 10° were used to derive the lateral distribution. The particle density is assumed to be proportional to the incident energy because the Volcano Ranch array is assumed to be situated at the atmospheric depth where S_{max} will occur. This is a reasonable assumption since the Volcano Ranch array was located at an atmospheric depth of 840 g cm^{-2}. For these simulations the lateral distribution is scaled according to the energy of the primary cosmic ray and attenuated according to the incident zenith angle θ of the primary cosmic ray shower. The attenuation length λ is defined to be 680 g cm^{-2}. This has been estimated by determining the decrease in shower size as a function of zenith angle for a fixed shower rate (Cronin, 1992). This results in an expression for the lateral distribution of a shower at an assumed atmospheric depth of 1000 g cm^{-2}

$$\rho(r) = 37.0 \left(\frac{E}{10^{19}\ \mathrm{eV}}\right) \exp\left(-\frac{1000 \sec\theta - 840}{\lambda}\right) \left(\frac{r_{\mathrm{km}}}{0.6}\right)^{-3.8} \text{ particles m}^{-2}\ , \qquad (7.1)$$

where E is the energy in electron volts, λ is the attenuation length and r is the distance from the core measured in kilometres. Even though this lateral distribution is relatively simple, the use of a more detailed lateral distribution is not warranted as the detailed form of the EHE extensive air shower's lateral distribution is not known. It is also dependent only on two parameters r and θ. This makes simpler the use of core fitting routines and the subsequent estimate of $\rho(600)$. It has also been used in other simulations of EHE detector performance (e.g. de Souza *et al.* (1992)).

To calculate particle densities for detectors in the simulated array, a core position for the shower was sampled uniformly within the detector boundaries. A zenith angle θ was sampled from a solid angle distribution in the range 0° to 70°. The azimuthal angle ϕ was sampled uniformly in the range 0° to 360°. Particle densities were calculated for detectors of a given area at a given distance r from the core. To take into account the shrinking of projected detector area with zenith angle, the number of particles at a detector position is multiplied by $\cos\theta$. The particle density is then fluctuated using a Poisson distribution and following this divided by $\cos\theta$. This is to take into account the extra pathlength of an inclined particle passing through the thin scintillator. This yields $\rho(r_i)_m$, the simulated detector density for detector i located r_i kilometres from the core of the EAS.

7.3.2 Shower Front Curvature

As the distance from the shower axis increases, the mean delay in arrival time of the shower front increases (see Section 6.3.1) due to the increased scattering of the electromagnetic component as distance from the shower axis increases. Assuming a plane front for the shower, particle arrival times are assigned to each triggered detector for a given shower axis defined by θ and ϕ. A delay σ behind the theoretical plane shower front is then introduced. This is defined by

$$\sigma = 1.5\left(1 + \frac{r_{\mathrm{km}}}{0.03}\right)^{1.6} 10^{-9}\ \mathrm{s}\ , \tag{7.2}$$

where r is measured in the plane of the shower front in units of kilometres. This is an approximation to the average dispersion in arrival time $\langle\sigma_t\rangle$ of air shower particles derived from experimental data by Linsley (1986) and defined as

$$\langle \sigma_t \rangle = 1.6 \left(1 + \frac{r_{\mathrm{km}}}{0.03}\right)^{\gamma} \ 10^{-9} \ \mathrm{s} \ , \tag{7.3}$$

where $\gamma = (2.08 \pm 0.08) - (0.04 \pm 0.06)\sec\theta + (0 \pm 0.06)\log(E/10^{17} \ \mathrm{eV})$.

To simulate the spread in arrival times, the delay of a particle at a given radius r is sampled from a gaussian whose mean is equal to its variance, defined to be σ. Although there is little knowledge about the distribution of arrival times of particles in the shower front, using this method will at least yield the expected behaviour of air shower particles, i.e. increasingly spread out in time as distance from the core increases. The average of these sampled times is then taken to be the delay time, which is added to the value obtained by assuming a plane shower front. For particle numbers greater than ten, the mean delay was assumed to be σ.

7.3.3 Event Reconstruction

Array Triggering

To reconstruct the energy and direction of an incident cosmic ray air shower, the density and arrival times of shower particles measured by the ground array are used. A minimum of three detectors must be triggered to provide enough information to reconstruct the event.

Determination of Core Position

The most important shower parameter to be determined initially is the position of the core within the array. From this parameter the estimation of energy and direction follow directly. The core position of a shower in the array can be estimated by using the centre of mass of the shower. The x and y co-ordinates x_c and y_c of the shower core position are defined by

$$\begin{aligned} x_c &= \frac{\sum_{i=1}^{N} \rho(r_i)_m x_i}{\sum_{i=1}^{N} \rho(r_i)_m} , \\ y_c &= \frac{\sum_{i=1}^{N} \rho(r_i)_m y_i}{\sum_{i=1}^{N} \rho(r_i)_m} , \end{aligned} \tag{7.4}$$

where x_i and y_i are the individual x and y co-ordinates of each detector i and $\rho(r_i)_m$ is the particle density at each detector i. This represents a poor estimate of the core position within the array for a small number of triggered detectors.

A more sophisticated method is to fit a known lateral distribution to the measured detector densities. The position of the core is determined by using an iterative minimisation method. The lateral distribution used is that defined by Equation 7.1. Since this is the same lateral distribution used in simulating detector particle densities, this will represent the best estimate of the core position. One other benefit of using this lateral distribution is that it allows a number related directly to $\rho(600)$ to be calculated.

The goodness of fit statistic, χ^2, is defined as

$$\chi^2 = \frac{\sum_{i=1}^{N} \frac{(\rho(r_i)-\rho(r_i)_m)^2}{\rho(r_i)_m}}{N-1} , \tag{7.5}$$

where

$$\rho(r_i) = K(E,\theta) f(r_i) , \tag{7.6}$$

is the theoretical detector density for detector i, given r_i is the distance from the core measured in kilometres, and N is the total number of triggered detectors used to determine the core position. Now $f(r_i) = (r_i/0.6)^{-3.8}$, which implies from Equation 7.1 that

$$K(E,\theta) = 37.0 \left(\frac{E}{10^{19}\ \mathrm{eV}}\right) \exp\left(\frac{1000 \sec\theta - 840}{\lambda}\right) , \tag{7.7}$$

$\rho(r_i)_m$ is again the actual measured density for detector i. Since $K(E,\theta)$ is unknown, it is estimated by minimising the χ^2 statistic with respect to $K(E,\theta)$ to give

$$K(E,\theta) = \frac{\sum_{i=1}^{N} \rho(r_i)_m f(r_i)}{\sum_{i=1}^{N} f(r_i)^2} . \tag{7.8}$$

The first core position used to calculate $K(E,\theta)$ is the centre of mass of the shower.

Clearly, the closer the suggested core position is to the actual core position the lower the value of χ^2 becomes. An IMSL Fortran library routine DBCONF was used to minimise χ^2. This routine searches through parameter space until it finds a position for the core that minimises χ^2. This is then compared with some value ϵ to determine if a core position is accepted. This routine was tested by analysing simulated showers which did not include any fluctuations in the particle densities. The core position was then found exactly using the procedure described above.

Determination of Cosmic Ray Arrival Direction

To find the direction of the cosmic ray, a plane shower front is fitted to the detector arrival times. This gives a first estimate of both the zenith and azimuth angles of the shower axis and hence the direction of the incident cosmic ray shower. Having an estimate of the direction of the plane of the shower front and also the core position as determined from the fitting algorithm or the centre of mass of the air shower, a compensating factor can be introduced to each of the detector times using Equation 7.2. This flattens out the measured curved shower front, ensuring a better fit for the plane fitting algorithm. An angular cut is then introduced for any events falling outside of a zenith angle of 70°. The resultant zenith and azimuth angles from the second curvature compensated fit are then compared with the true arrival direction to estimate the angular resolution of the array configuration.

Angular Resolution

To estimate the angular resolution of an array, the distribution of space angles between the true and fitted directions of the incident cosmic ray are analysed. The space angle $d\Omega$ is calculated from $d\phi$, the angle between the true and fitted directions by

$$d\Omega = \frac{d\phi}{2\pi \sin\phi} \,. \tag{7.9}$$

The normalised distribution $dN/d\Omega$, where N is the number of events for a given Ω, is fitted to a normal distribution. The measure of the angular resolution is taken to be the standard deviation σ_ϕ of this fitted distribution i.e.

$$\frac{1}{N}\frac{dN}{d\Omega} = \frac{1}{\sqrt{2\pi}\sigma_\phi} \exp\left(-\frac{\phi^2}{2\sigma_\phi^2}\right) \,. \tag{7.10}$$

7.3.4 Estimation of Cosmic Ray Primary Energy

Referring to Equations 7.6 and 7.7 it can be seen that $K(E,\theta)$ is equal to $\rho(600)$, the attenuated particle density at 600 metres, and that it can be directly calculated from the inferred core position. To obtain the equivalent $\rho(600)$ for a vertical shower and hence have an estimate of cosmic ray primary energy, it is necessary to divide by the atmospheric attenuation term i.e. $\exp\left(-\frac{(1000\sec\theta-840)}{680}\right)$. This can be accomplished since the shower axis has been determined. The energy of the primary E in eV is then found from the value for unattenuated $\rho(600)$ by

$$E = \frac{\rho(600)\times 10^{19}}{37}\ \mathrm{eV}\ . \tag{7.11}$$

This does not take into account any systematic error in the determination of primary energy from $\rho(600)$, but even so it allows comparisons to be made between different array configurations. In the χ^2 minimisation process, a value for $K(E,\theta)$ is calculated for each trial core position and as this trial core position gets closer to the actual core position, the value for $K(E,\theta)$ gets closer to the correct value.

Energy Resolution

The energy resolution for a given array configuration is estimated in much the same way as the angular resolution. A normal distribution is fitted to the distribution of reconstructed energies versus $\log E$. This distribution is centred on the incident cosmic ray energy at which the energy resolution is being analysed. For the purposes of this report, the cosmic ray primary energy analysed is 10^{19} eV (e.g.Table 7.1). The energy resolution is then defined by the standard deviation of the fitted normal distribution.

7.3.5 A More Realistic Lateral Distribution

Using the same lateral distribution to fit for shower parameters as was used to initially characterise the cosmic ray shower will simulate the expected best performance of any array configuration. In addition to the lateral distribution defined in Equation 7.6 being used to fit for shower parameters, a more realistic lateral distribution was also used. This is defined as

$$\rho(r_i) = K(E,\theta)\left(\frac{r_i}{0.06}\right)^{-\alpha} , \tag{7.12}$$

where α is also a free parameter in the χ^2 fit. The fitting of an EAS with this lateral distribution will degrade the quality of the fit since another free parameter has been introduced. However, this will be a more realistic representation of the performance of a real array.

7.4 Comparison of Different Array Configurations

7.4.1 Introduction

In this section the results from the simulations as described previously are presented. The generic detector covers an area of 5,000 km^2. It is assumed that technical difficulties such as interdetector communications, individual detector timing resolution and the ability of each detector to discriminate accidental coincidences have been solved in the generic detector, so that shower parameters such as particle density and timing can be determined accurately. Each detector is assumed to have a surface area of 10 m^2. The energy region 1–100 EeV is divided into eight equal bins in log energy. In each energy bin 500 showers are thrown onto the array.

7.4.2 Dependence on Interdetector Spacing

Figures 7-2 and 7-3 examine the dependence of array performance on detector spacing for two different triggering thresholds. The array spacings examined are 1, 1.15 and 1.5 kilometres. For a triggering threshold of 0.1 m^2, there are no significant differences for different array spacings for both lateral distributions assumed. There is a great degree of variability in the plots of angular resolution as a function of energy. This implies that the distribution of fitted space angle is not necessarily normal, as the angular resolution is assumed to be the standard deviation of the fitted normal distribution. Clearly for low triggering thresholds this is not a good assumption. From the plots of the angular resolution the only conclusion that can be made is that the angular resolution lies somewhere between 3° and 6°.

Variable Exponent Lateral Distribution			
Array Spacing (km)	Threshold		
	0.1 m^{-2}	0.2 m^{-2}	0.3 m^{-2}
1	20	8	8
1.15	18	9	8
1.5	23	14	12
Simple Lateral Distribution			
1	14	8	7
1.15	14	8	7
1.5	15	9	9

Table 7.1: Energy resolution $\frac{\Delta E}{E}$% for various array configurations at 10^{19} eV. Individual detector area is assumed to 10 m^2. The energy resolution quoted does not include the error in estimating cosmic ray primary energy from ρ_{600}. The use of the variable exponent lateral distribution results in a significant deterioration in energy resolution for low thresholds and large array spacing. As expected, energy resolution improves with the reducing of array spacing and the increasing of individual detector threshold level.

Figure 7-3 is identical to Figure 7-2 except the dependence on array spacing for a triggering threshold of 0.3 m^{-2} is plotted. Again there is little dependence on array spacing except for the efficiency of the array. A ground array with 1.5 km spacing would have a triggering efficiency only ~ 20% at 10^{18} eV. If the aim of the experiment is to determine the properties of cosmic rays with primary energies above 10^{19} eV then this array spacing would be suitable. As in Figure 7-2, there is a degree of variability in the plots of angular resolution as a function of energy and the angular resolution would be estimated to be between 1° and 3° over the energy range considered. Referring to Table 7.1, there is in general only a small dependence of energy resolution on array spacing.

7.4.3 Dependence on Triggering Threshold

Figures 7-4 and 7-5 demonstrate the effect on array performance when the triggering threshold is varied. The array spacings assumed are 1 km and 1.5 km respectively. The levels of threshold chosen are 0.1 m^{-2}, 0.2 m^{-2} and 0.3 m^{-2}, which correspond to the 1, 2 and 3 particle level for a 10 m^2 detector. It is quite clear that there is a marked dependence of array performance on triggering threshold. For example, for an array with 1 km spacing and a triggering threshold of 0.1 m^{-2}, the angular resolution is

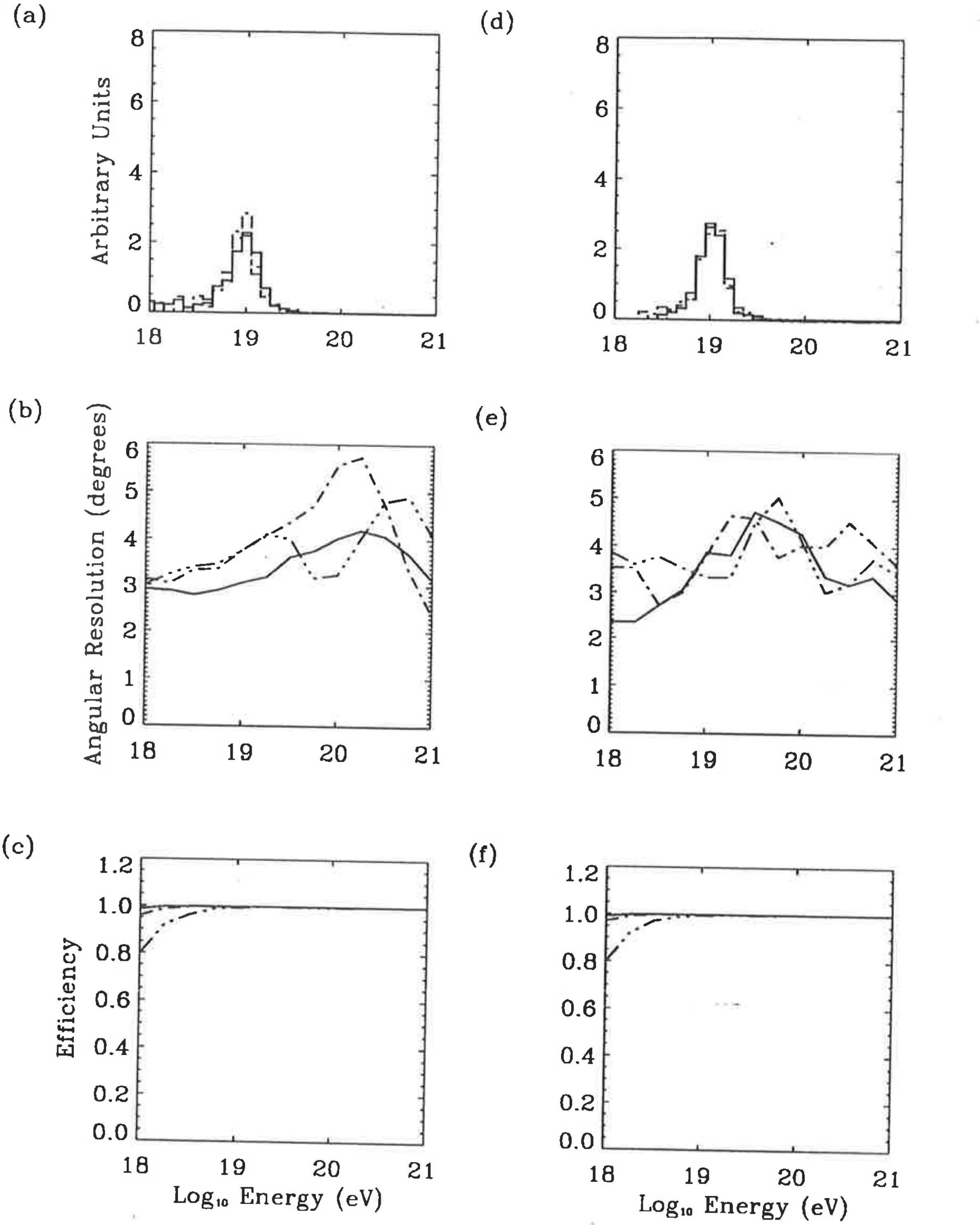

Figure 7-2: Effect of varying array spacing. Column 1 ((a),(b),(c)) indicates the energy resolution at 10^{19} eV, angular resolution and array efficiency for a lateral distribution with a variable exponent (column 2 ((d),(e),(f)) is for the simple two parameter lateral distribution). Plots assume a 0.1 m^{-2} triggering threshold with spacing of 1 km —, 1.15 km – - – and 1.5 km – · · · · –.

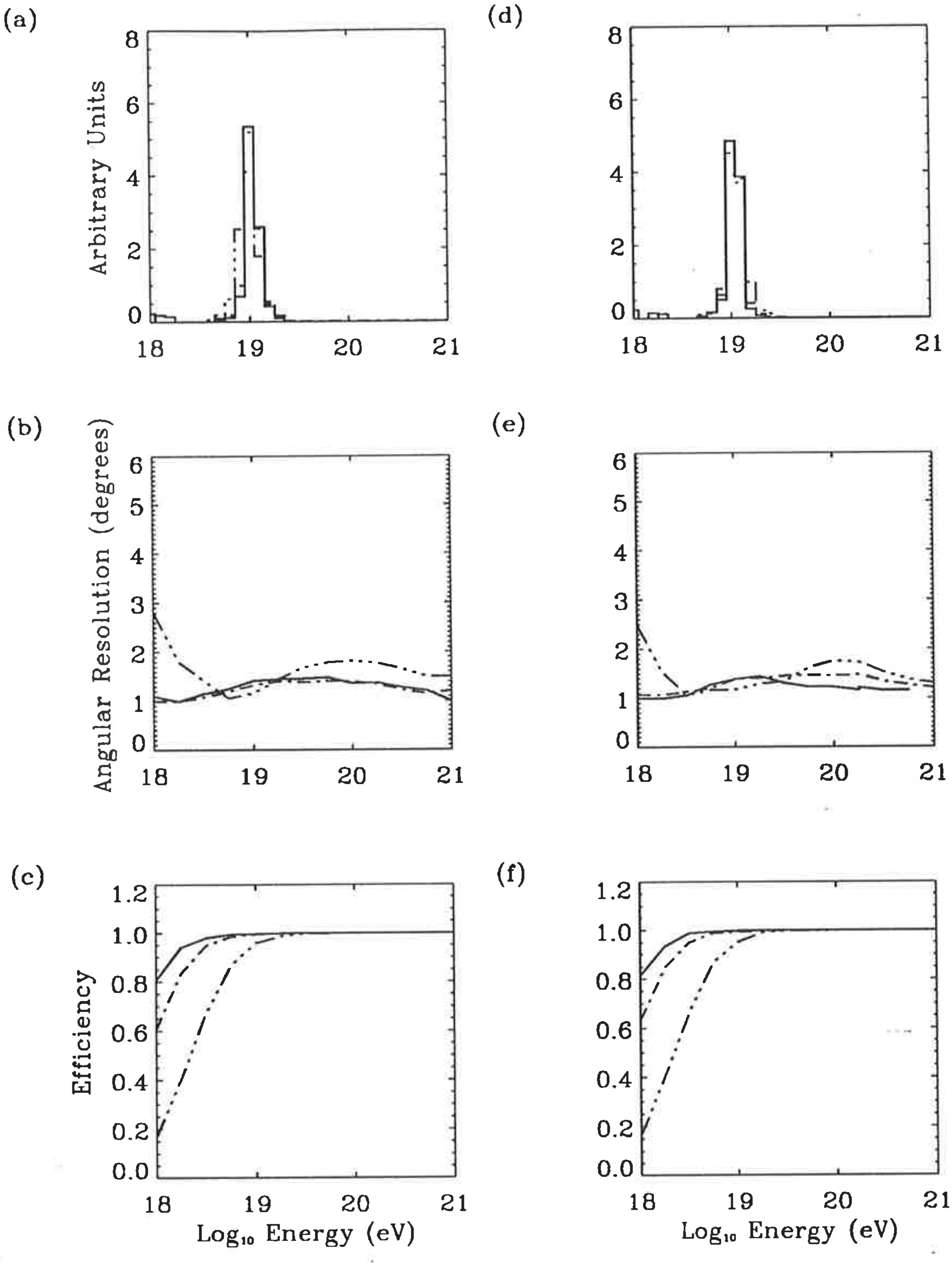

Figure 7-3: Effect of varying array spacing. Column 1 ((a),(b),(c)) indicates the energy resolution at 10^{19} eV, angular resolution and array efficiency for a lateral distribution with a variable exponent (column 2 ((d),(e),(f)) is for the simple two parameter lateral distribution. Plots assume a 0.3 m^{-2} triggering threshold with spacing of 1 km —, 1.15 km – · – and 1.5 km – · · · · –.

between 3° and 4°. This can compared to a threshold of 0.3 m^{-2} which has an associated angular resolution of $\sim 1°$. The same level of variation is also observed in Figure 7-5 for an assumed array spacing of 1.5 km. This implies that for determining the direction of EAS, that information should be used from individual detectors which have been triggered at the 0.3 m^{-2} level. However, information from detectors triggered at the 0.1 m^{-2} level may prove useful in fitting a lateral distribution and hence determining core location (e.g. Chiba *et al.* (1992)).

This large dependence on triggering threshold is interpreted as arising from the large fluctuations in arrival times at large core distances. For a triggering threshold of 0.1 m^{-2}, an estimate of shower front arrival time is made from the timing of one particle. The particle's arrival time will be a poor representation of the true shower front arrival time as it may be fluctuated significantly. By increasing the threshold, the shower front arrival time can be estimated more precisely by averaging over the particles' arrival times. The angular resolution of a ground array is directly related to its ability to estimate the cosmic ray primary energy and Table 7.1 demonstrates the expected dependence of energy resolution on triggering threshold.

7.4.4 Comparison of Cartesian and Triangular Array Geometries

Thus far the array geometry has been assumed to have a base unit of a square. The Yakutsk array (Glushkov *et al.*, 1987) and the Volcano Ranch array (Linsley, 1980) each have (or had) as their base unit a triangle. The perceived advantage of a triangular array configuration is that fewer detectors are needed to cover a given surface area than for a square array without compromising the performance of the detector. A triangular array configuration also has advantages over the square geometry if it is necessary for individual detectors to communicate with their neighbours by radio signal (Clay *et al.*, 1992).

That the number of detectors needed to cover a given area can be reduced for a triangular configuration as opposed to a square configuration can be seen by considering the distance d_m from a detector to the centre of the base unit shape of the array (see Figure 7-6). If it is assumed as a first approximation that the distance d_m

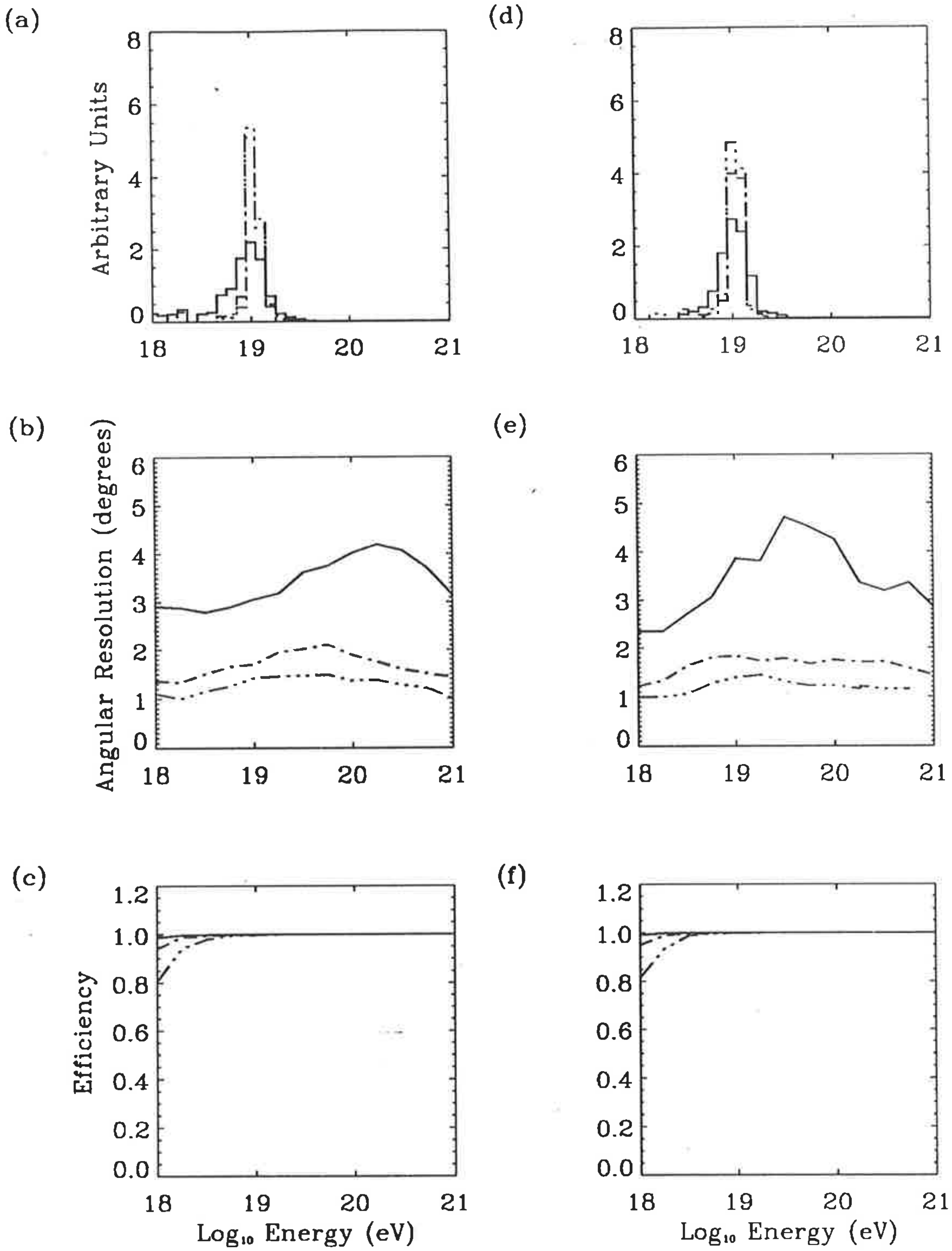

Figure 7-4: Effect of varying triggering threshold. Column 1 ((a),(b),(c)) indicates the energy resolution at 10^{19} eV, angular resolution and array efficiency for a lateral distribution with a variable exponent (column 2 ((d),(e),(f)) is for the simple two parameter lateral distribution). Plots assume a 1 km array spacing with thresholds of 0.1 m^{-2} —, 0.2 m^{-2} – · – and 0.3 m^{-2} – · · · –.

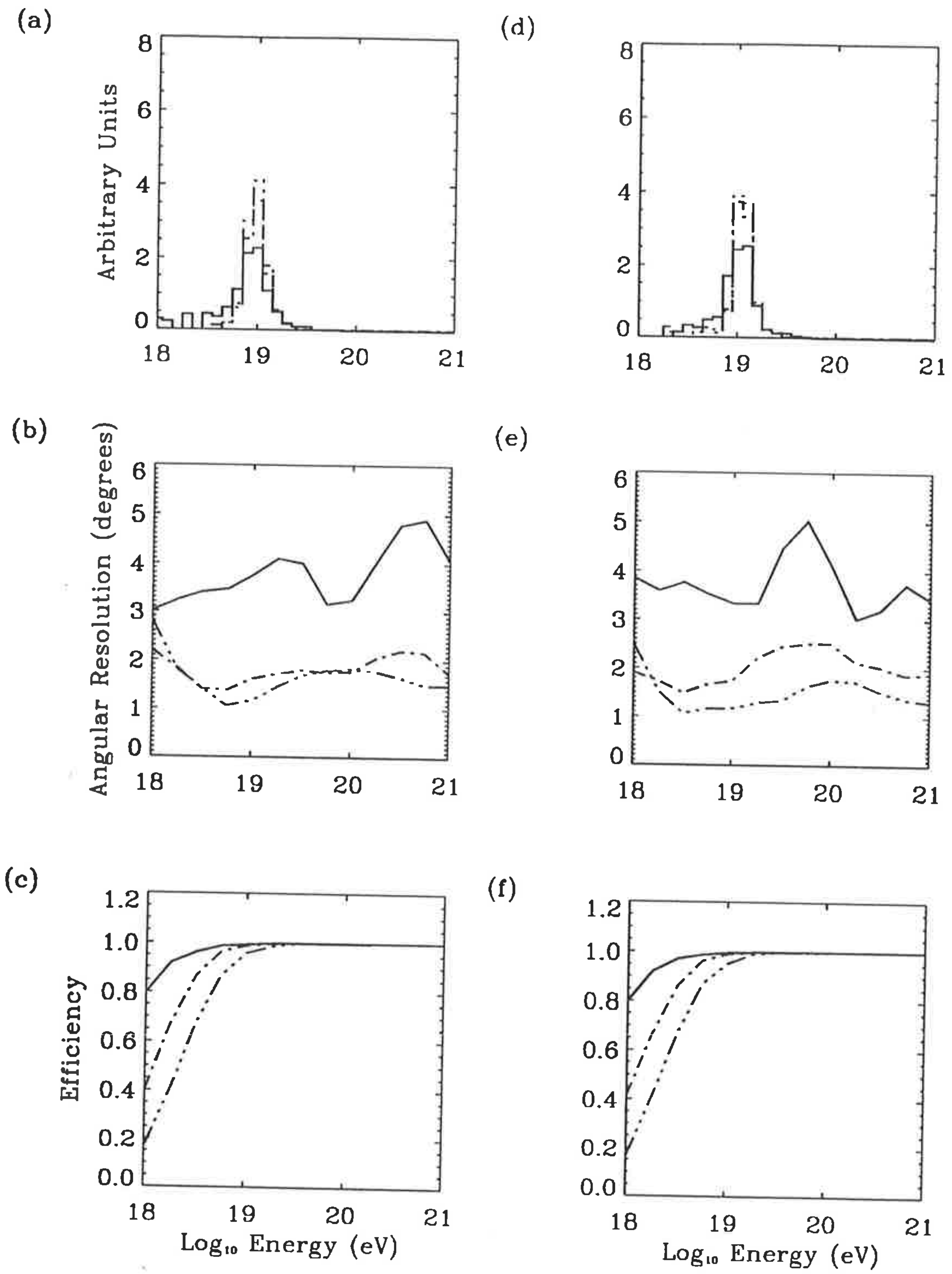

Figure 7-5: .Effect of varying triggering threshold. Column 1 ((a),(b),(c)) indicates the energy resolution at 10^{19} eV, angular resolution and array efficiency for a lateral distribution with a variable exponent (column 2 ((d),(e),(f)) is for the simple two parameter lateral distribution). Plots assume a 1.5 km array spacing with thresholds of 0.1 m^{-2} —, 0.2 m^{-2} – · – and 0.3 m^{-2} – · · · · –.

will control the triggering threshold, than a triangular grid will cover a given area more efficiently. For example, a square one kilometre grid will have d_m equal to $\frac{1}{\sqrt{2}}$km. For a triangular grid, d_m is equal to $\frac{1}{\sqrt{3}}$km which implies a lower triggering threshold or more triggered detectors for a given cosmic ray primary energy.

The number of detectors used is a critical factor in the construction of a proposed array for the detection of EHE cosmic rays. For a 1 km square array covering 5,000 km^2, 5,000 detectors would be used. For a cost per detector of $10,000 this would imply a cost of $50,000,000 for the total array. Clearly any reduction in the number of detectors used will result in large cost savings. If a 5,000 km^2 array is filled with detectors as depicted in Figure 7-6(b), then this results in a saving of $\sim$ 25% compared with the square configuration shown in Figure 7-6(a).

Results

The proposition that a square and a triangular array configuration with equal d_m will have similar detector characteristics was tested by performing the array simulation using the different array configurations. Three array sizes were compared for each configuration. These were equivalent to the three spacings tested in the previous section i.e. square arrays with spacings of 1, 1.15 and 1.5 kilometres, implying values for d_m of 0.71, 0.81 and 1.06 kilometres respectively. The detector particle threshold assumed was 0.3 m^{-2} for a detector surface area of 10 m^2.

As can be seen from Figure 7-7 the average number of detectors triggered, as a function of energy, for the triangular array is less than that for the square array. This is expected because there are 25% fewer detectors in the triangular configuration for the same area. Figures 7-8 and 7-9 compare the energy resolution at 10^{19} eV and the angular resolution as a function of primary energy for both array configurations. In both cases the performance of each configuration is extremely similar implying that by adopting the triangular configuration there is very little, if any loss of array performance.

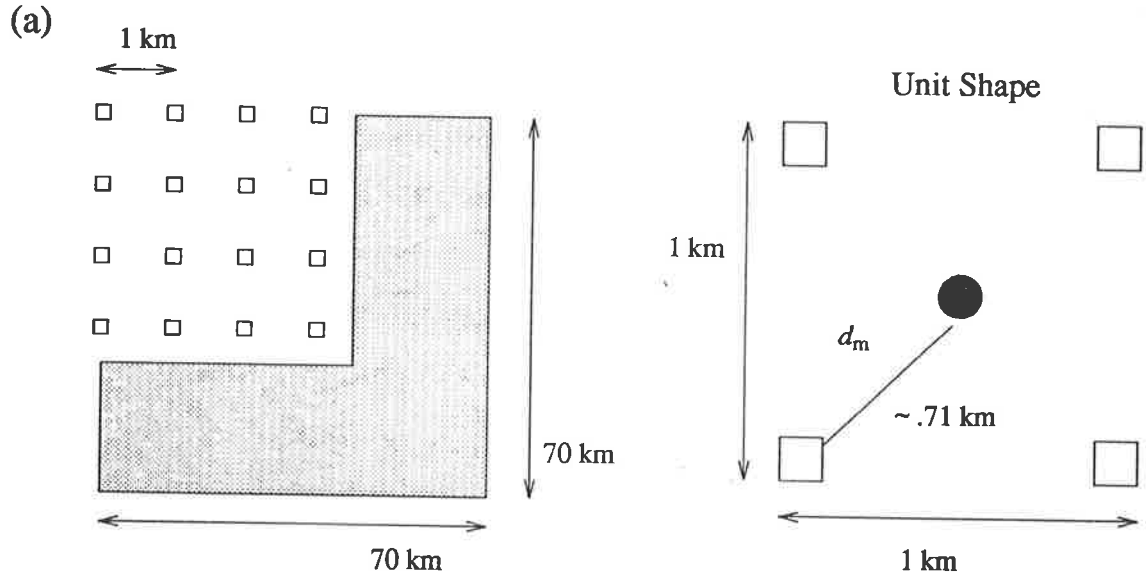

Square Array

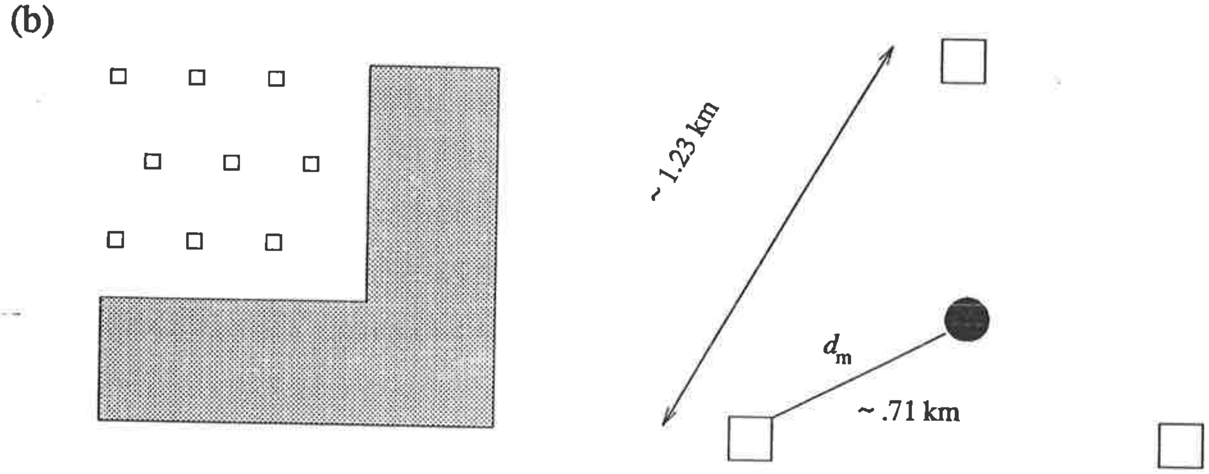

Triangular Array

Figure 7-6: Comparison of the (a) cartesian and (b) triangular array geometries and their base units. For the same distance to centroid (d_m) the array spacing is increased by 25% in the case of the triangular array geometry compared to to the cartesian array geometry.

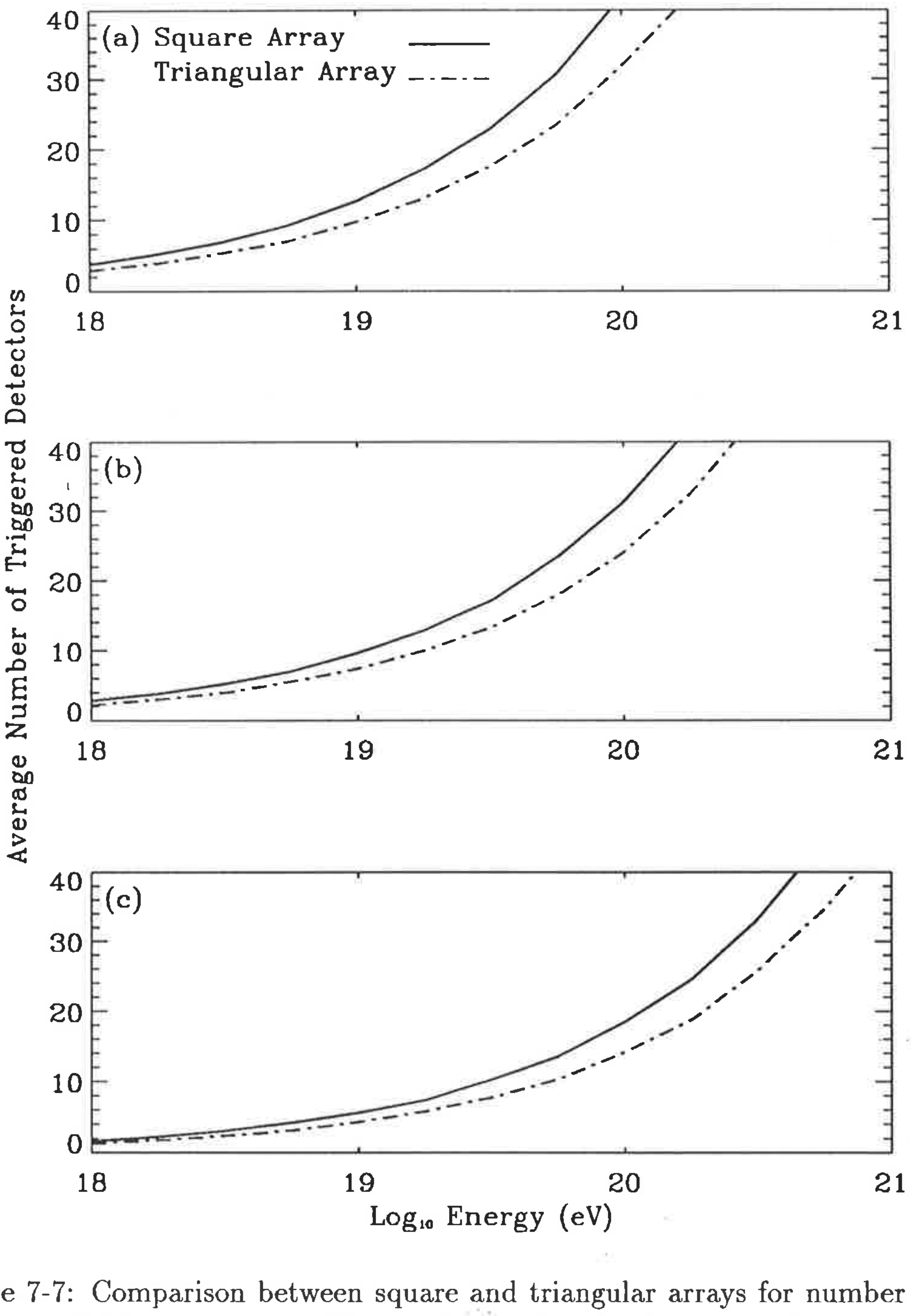

Figure 7-7: Comparison between square and triangular arrays for number of triggered detectors. (a) Square array with l = 1 km and equivalent triangular array. (b) Square array with l = 1.15 km and equivalent triangular array. (c) Square array with l = 1.5 km and equivalent triangular array.

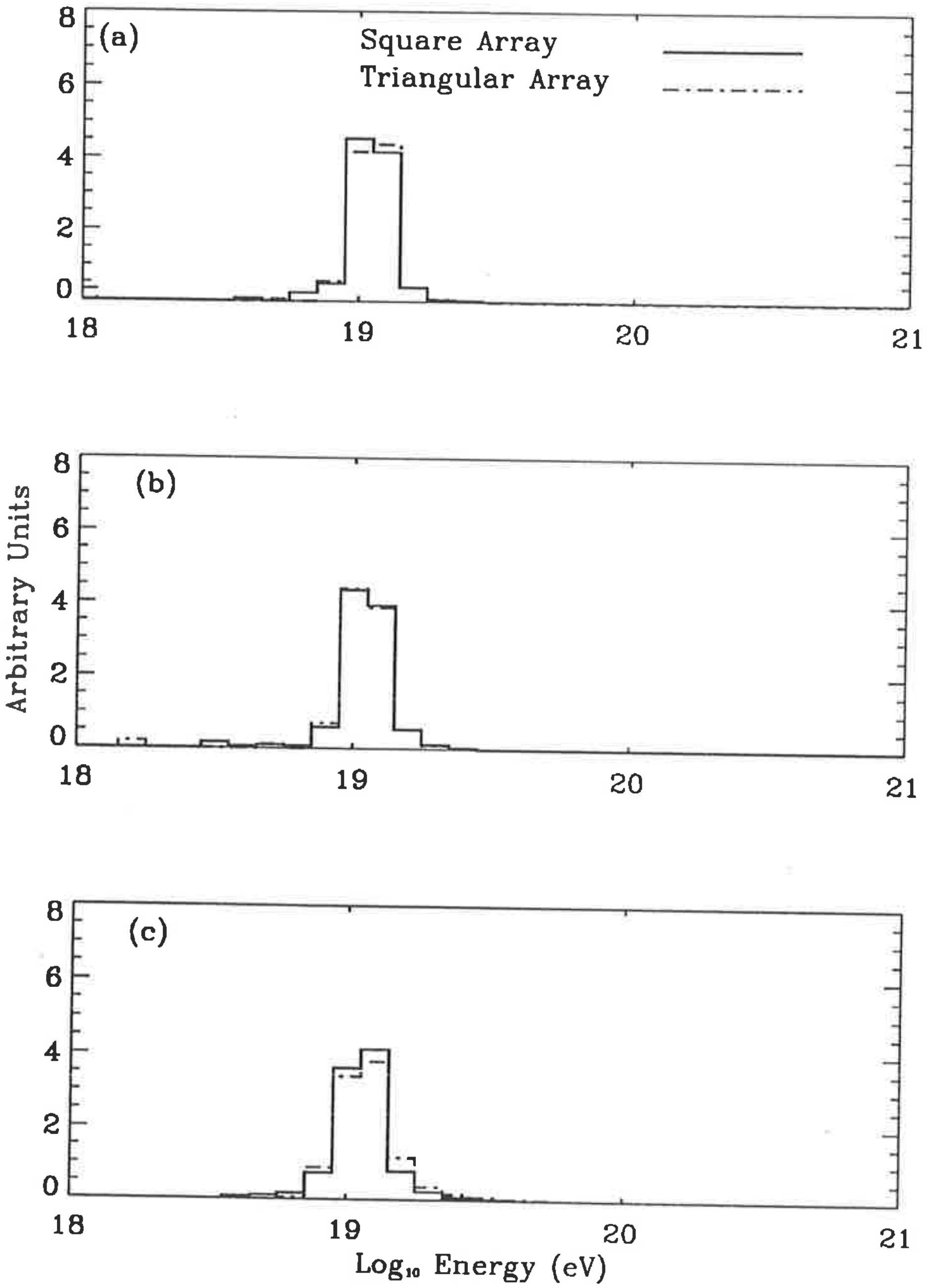

Figure 7-8: Comparison between square and triangular arrays for energy resolution. (a) Square array with $l = 1$ km and equivalent triangular array. (b) Square array with $l = 1.15$ km and equivalent triangular array. (c) Square array with $l = 1.5$ km and equivalent triangular array.

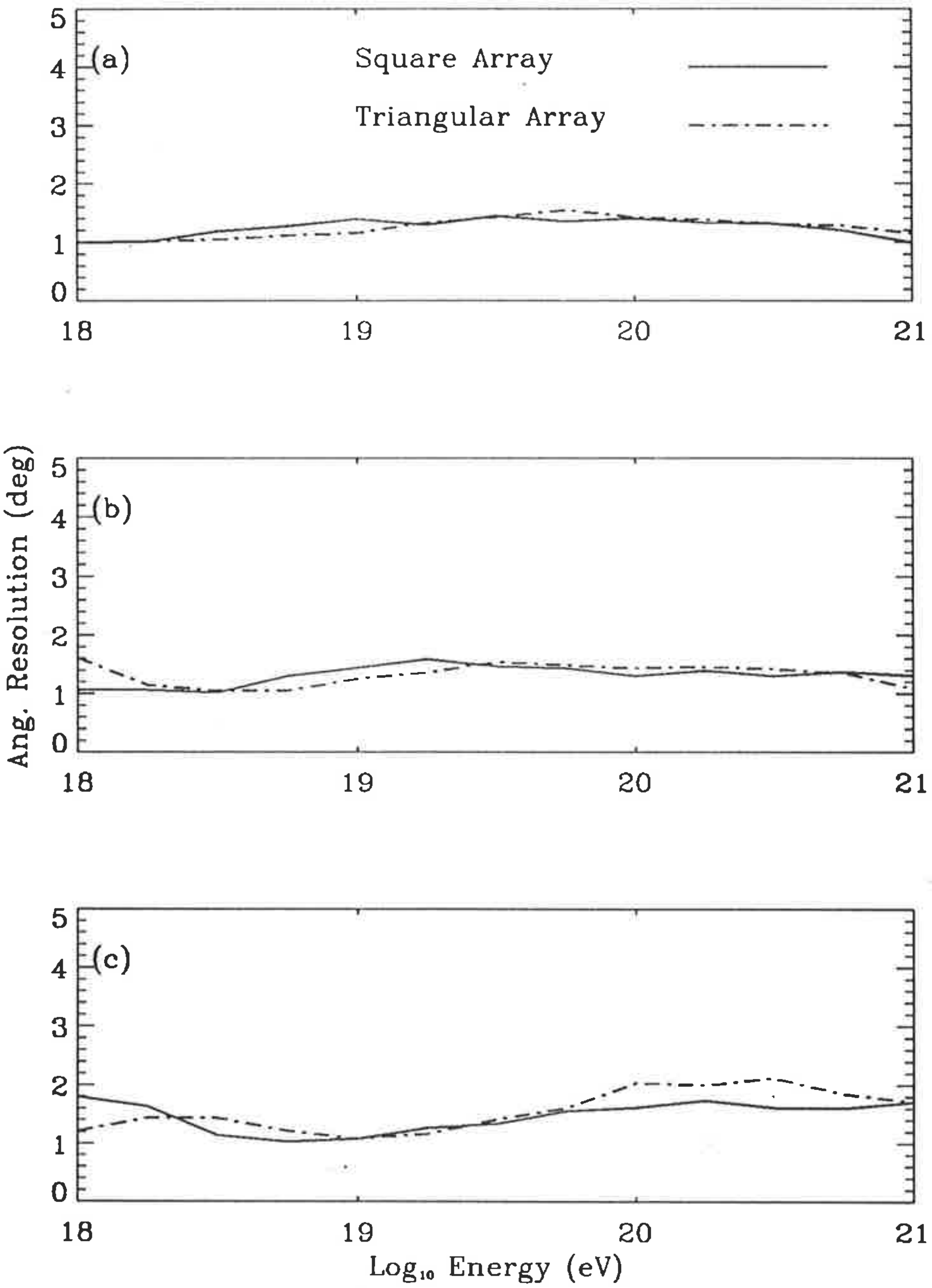

Figure 7-9: Comparison between square and triangular arrays for angular resolution. (a) Square array with $l = 1$ km and equivalent triangular array. (b) Square array with $l = 1.15$ km and equivalent triangular array. (c) Square array with $l = 1.5$ km and equivalent triangular array.

7.5 Hybrid Detector

7.5.1 Introduction

The ground array configuration considered in the first part of this chapter measures parameters of an EAS at a single point in its development. From these parameters, the particle density and arrival times and the direction of the shower axis are estimated. The energy of the cosmic ray primary is inferred by estimating the integrated particle density at the atmospheric depth of detection, or by calculating the particle density at a given distance from the core i.e. $\rho(600)$. Both of these quantities can then be related to primary cosmic ray energy. The advantages of such a detector are 100% duty cycle and consequently uniform exposure in Right Ascension. Some of the disadvantages of the array are relatively poor angular resolution ($\sim 3°$) and it not providing a direct method for measuring both the cosmic ray's primary energy and composition.

An instrument such as the Fly's Eye detector measures directly the nitrogen fluorescence caused by the passage of an EAS through the atmosphere (Baltrusaitis *et al.*, 1985b). From this the shower size can be derived as a function of atmospheric depth. Because a more direct measurement is made of the evolution of the shower, the energy can be estimated by integrating the shower profile over the total path in the atmosphere. The distribution of shower size with atmospheric depth and the depth of maximum are both directly related to the composition of the cosmic ray primary. There are two main disadvantages to the Fly's Eye technique. One is the low duty cycle of $\sim$ 12%. Moonless nights are required for the Fly's Eye technique to work since any background illumination will saturate the sensitive detection system. Because of the low duty cycle, the detector has a non-uniform sky coverage which complicates the analysis of cosmic ray anisotropy. The second disadvantage is that the atmosphere must be well characterised, as the measured light intensities are affected by atmosphere clarity and scattering.

Because of the apparent complementarity of the two EHE cosmic ray detection systems, a combination of the two techniques has been considered. There are several distinct advantages to such a hybrid detector, these being

1. By using two separate detectors to measure cosmic ray showers, each using a

different principle, redundancy of measurements is introduced. For a cosmic ray shower measured using both detectors, energy estimation from the array using $\rho(600)$ can be directly compared with the energy estimated by the fluorescence technique on a shower by shower basis. This allows for the direct calibration of the ground array's estimation of the energy with the fluorescence technique's calorimetric estimation of energy, the latter being expected to be more accurate.

2. The position of the shower core within the array can be used in the analysis of cosmic ray showers by the fluorescence technique. By locating the core position to within 100 metres, the shower axis estimate calculated by the Fly's Eye can be greatly improved, resulting in an improvement of angular resolution for showers which have triggered both detectors.

3. With regard to the composition of the cosmic ray primary, the measurements of the depth of first interaction and X_{max} made by the Fly's Eye technique will imply a certain composition This can be compared with measured properties of the EAS from the array such as μ to e^- ratios, which are thought also to be related to composition. The comparisons could be used to find systematic relationships between the array determined quantities and the composition as determined by the Fly's Eye technique. Thus it is envisaged that the array could be "taught" by the air fluorescence detector how to discriminate between showers initiated by different nuclei.

7.5.2 Ground Array

For the simulation of the hybrid detector two different array configurations were assumed.

Uniform Cartesian Array

The first is a cartesian array laid out on a 70 km × 70 km grid with a spacing of 1 km. Each detector is assumed to have a 10 m^2 surface area and a triggering threshold of 0.3 m^{-2}.

Graded Triangular Array

The second type of array used in conjunction with the air fluorescence detector is a graded triangular array. This is expected to closely represent a detector that would be likely to be constructed in an experiment to detect EHE cosmic rays. A triangular format having as its base unit a triangular arrangement of detectors (see Section 7.4) is preferable as it covers a given area more efficiently than a cartesian configuration. A graded array ensures that a large energy range can be covered using the detector. The design used in this simulation is adapted from de Souza *et al.* (1992). This array consists of 169 detectors on a triangular grid with 500 metre spacing, a further 417 detectors on a triangular grid with a spacing of 866 metres and a larger triangular grid surrounding these detectors consisting of 1554 detectors on a grid with a spacing of 1500 metres (see Figure 7-10). Each detector is assumed to have a 10 m^2 surface area and a triggering threshold of 0.3 m^{-2}.

7.5.3 Atmospheric Fluorescence Detector

The atmospheric fluorescence detector operating in conjunction with the ground based particle array is assumed to be of the type used in the proposed HiRes Fly's Eye (Au *et al.*, 1991; Bird *et al.*, 1993a; Cooper *et al.*, 1991b) which is an improved version of the current Fly's Eye (see Section 7.2.2).

The proposed HiRes Fly's Eye will also be located at the Dugway Proving Ground in Utah. This detector is still in the prototype stage (Bird *et al.*, 1993a). For the final proposed HiRes detector there will be three individual sites on a triangular grid approximately 15 kilometres apart. Each site is to have a 240° azimuthal coverage and will contain 54 units, each consisting of a 2 metre diameter mirror viewed by 256 hexagonal photomultiplier tubes each having $1^\circ \times 1^\circ$ aperture (Cooper *et al.*, 1991b). This can be compared to the 1.5 metre diameter mirrors and $5.5^\circ \times 5.5^\circ$ photomultiplier apertures for the current Fly's Eye and should improve signal to noise by a factor of seven. The proposed HiRes detector is expected to have a point source resolution at 1 EeV of 0.3°, an energy resolution of better than 20% and a X_{max} resolution at 1 EeV of 20–30 g cm^{-3}.

The detector configuration assumed for the purpose of these simulations is a

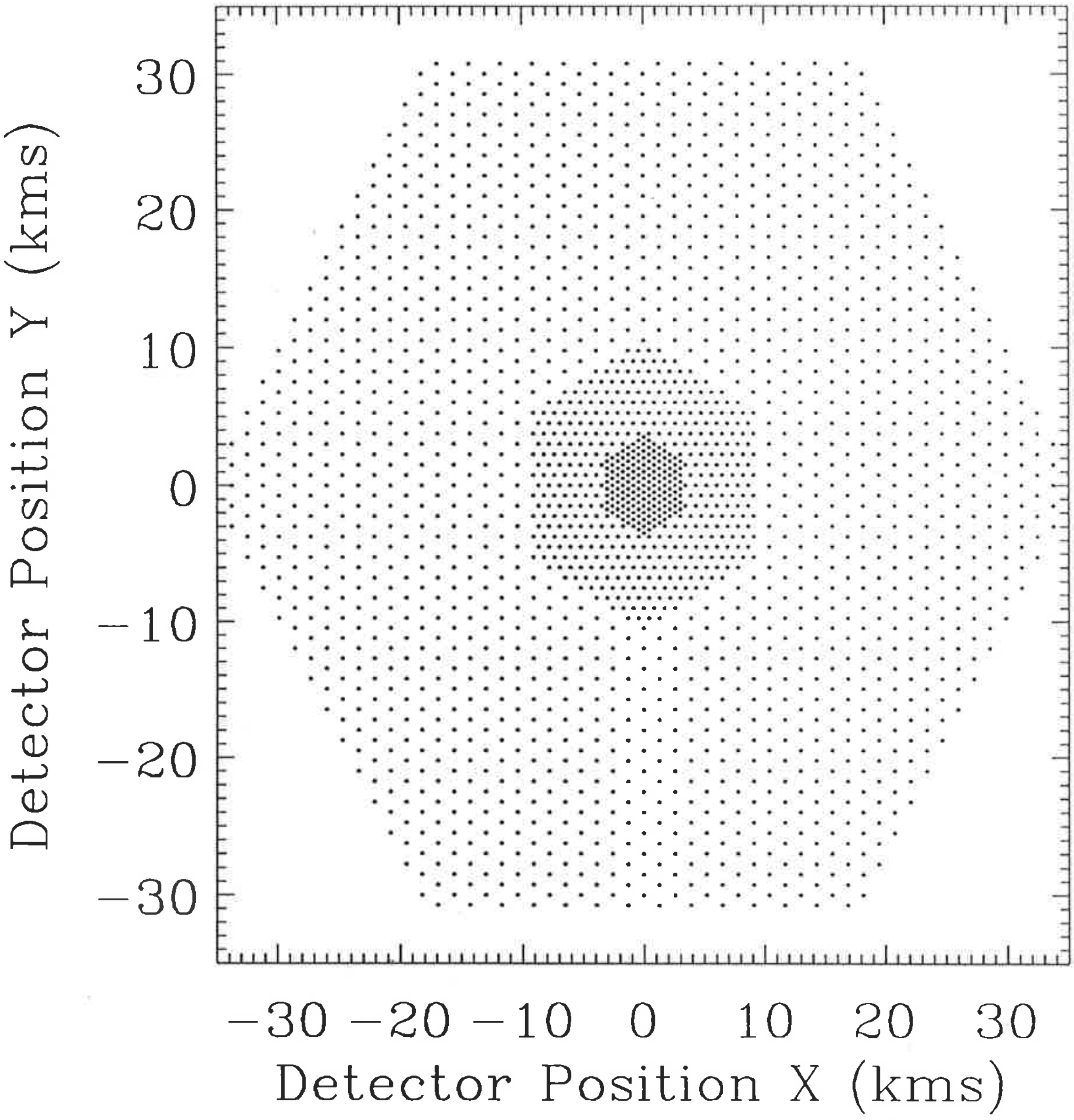

Figure 7-10: Graded Triangular Array configuration from de Souza *et al.* (1992). This array arrangement consists of 169 detectors on a triangular grid with 500 metre spacing, a further 417 detectors on a triangular grid with a spacing of 866 metres and a larger triangular grid consisting of 1554 detectors with a spacing of 1500 metres. The MonoEye is positioned at the centre of the array.

single HiRes station with a 360° azimuthal coverage (MonoEye). As opposed to the proposed HiRes Fly's Eye which combines the information from each of the separate stations to reconstruct the shower axis, the MonoEye will be assisted by core location information from the particle array.

7.5.4 Method of Simulation

The simulation employed for the air fluorescence section of the Hybrid detector is the HiRes Monte Carlo code developed in Utah. This code was modified by H. Y. Dai to simulate one HiRes site with 360° coverage.

The Fly's Eye Monte Carlo generates triggered showers in the following manner. The impact parameter R_p, shower direction and primary energy are all chosen from appropriate distributions. The depth of maximum X_{max} is chosen from a parameterisation of the experimentally determined distribution of X_{max}, representing a mixed primary cosmic ray composition. X_0, the depth of first interaction is chosen from an exponential distribution. From X_0 and X_{max} the shower profile can be defined by

$$N_e(X) = f(X_0, X_{max}) \ , \tag{7.13}$$

where $N_e(X)$ is the shower size as a function of atmospheric depth X and $f(X_0, X_{max})$ is a parameterisation of the development of an EAS calculated by Gaisser and Hillas (1977).

From the shower size, the total light from the EAS reaching the detector can be calculated from the following three mechanisms. These are the direct fluorescence resulting from excitation of atmospheric nitrogen molecules, the direct Čerenkov light which is directed forward in the direction of the shower and is only important for showers whose axis approximately intersects with the position of the detector, and thirdly, the scattered Čerenkov light due to Rayleigh and Mie scattering of the originally emitted Čerenkov radiation. The latter can be in some cases more intense than the nitrogen fluorescence.

The detector's response to the emitted light is then modelled. This includes the effects of mirror reflectivity and aberrations which may affect the triggering and the

PMT signal strength. By folding in the quantum efficiency of the PMT, the number of photoelectrons is found and hence the measured signal. Care is taken to include the response of the triggering circuitry in determining a pulse shape. From the pulse shape and an assumed triggering condition it can be determined if any one PMT is triggered. If a trigger occurs, the PMT signal strength and time are recorded.

The simulation was run for a Hybrid site at sea level. Showers were thrown down with zenith angles less than 60°. Showers which trigger the MonoEye were then thrown onto the particle array. From the HiRes Monte Carlo, the shower size at ground level, the original cosmic ray direction and the core location are then used as input into the array simulation. This simulation is similar to that described in Section 7.3 except that the lateral distribution $\rho_A(r)$, derived from the Akeno array, is used. This is parameterised as follows

$$\rho_A(r) \propto N_e R^{\alpha}(1+R)^{-(\eta-\alpha)}(1+r_m/2000)^{-0.05} \;, \qquad (7.14)$$

where $R = r/R_0$ (R_0 is the Molière radius = 80 m at sea level), $\alpha = 1.2$, $\eta = (3.80 \pm 0.05) + (0.10 \pm 0.05)\log_{10}(N_e/10^9)$ and N_e is the shower size (Teshima *et al.*, 1986a). As described previously, particle densities are fluctuated according to Poisson statistics and the shower front curvature is allowed for in assigning arrival times to air shower particles. The Akeno lateral distribution is used, since it represents a recent measurement of the lateral distribution for EAS of EHE energies.

The position of the core is estimated by finding the centre of mass of particle densities in the plane of the shower. This method is used rather than a more sophisticated core location procedure because it provides an upper limit to the core location error. Other than using the Akeno lateral distribution and estimating the core location by the centre of mass of the shower, the array simulation is identical to that discussed previously (see Section 7.3). The core location as determined by the array simulation is then used by the HiRes Monte Carlo in the reconstruction of the EAS shower parameters.

To reconstruct the shower axis of the EAS as it travels through the atmosphere, the HiRes reconstruction algorithm uses the information from triggered phototubes from up to three sites. For the case of the MonoEye, the plane which contains the

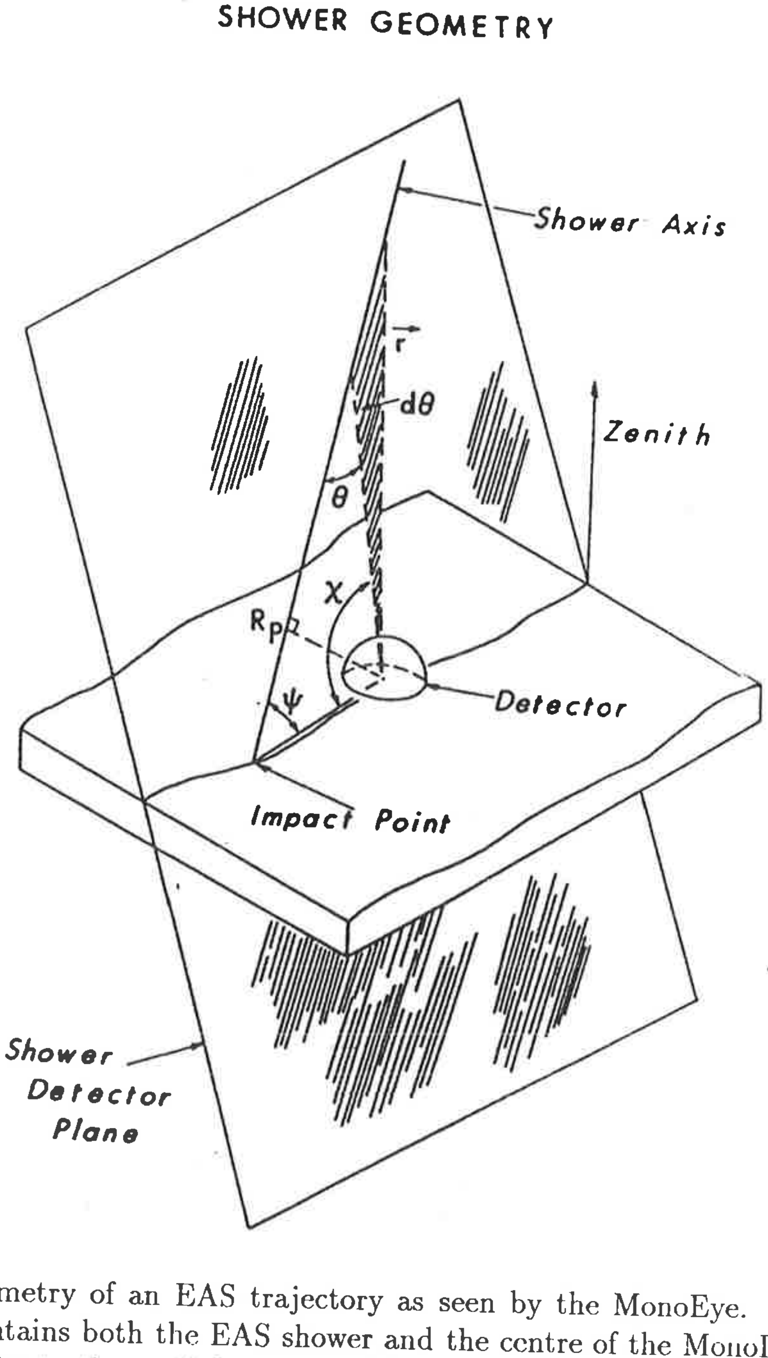

Figure 7-11: Geometry of an EAS trajectory as seen by the MonoEye. The shower-detector plane contains both the EAS shower and the centre of the MonoEye detector. It is specified by fits to the spatial pattern of "hit" PMTs which must lie along a great circle on the celestial sphere. The angle ψ and impact parameter R_p are obtained by fits to observation angle χ vs time of observation (from Baltrusaitis *et al.* (1985b)).

centre of the detector and the EAS shower path is defined by the geometry of the triggered phototubes (see Figure 7-11). The orientation of the EAS axis in this plane is then determined by timing fits to triggered phototubes (Baltrusaitis *et al.*, 1985b) using a χ^2 minimisation fit. Considering Figure 7-12, it can be seen that the time delay $\delta t(\theta)$ for light arriving from a point P is delayed from the time of the passing EAS by

$$\delta t(\theta) = \frac{R_p \tan \theta/2}{c} , \tag{7.15}$$

where θ is the light emission angle from the shower axis. By inspection of Figure 7-12 it can be seen that $\chi_0 = \chi + \theta$. If χ_i is defined as the observation angle in the shower-detector plane of the i^{th} PMT triggered at time t_i and χ_0 represents the direction of the EAS in the shower-detector plane then

$$\chi_i(t_i) = \chi_0 - 2\tan^{-1}\left(c(t_i - t_0)/R_p\right) . \tag{7.16}$$

A χ^2 minimisation fit is then performed using the measured $\chi_i(t_i)$, yielding R_p and χ_0. Along with the orientation of the shower-detector plane, this then fully specifies the trajectory of the EAS. For showers whose tracks lengths are between less than 30° and 50° the shower fitting routine poorly determines χ_0. This leads to an overall angular resolution performance of $\sim 5°$ in the case of Fly's Eye I. The core location from the array will determine the position of the "Impact Point" and hence r_0. From Figure 7-12 it can be seen that $r_0 = \frac{R_p}{\sin \chi_0}$. This then provides a powerful constraint on the direction reconstruction for the MonoEye detector.

Recent results from the HiRes prototype show that this design is capable of defining the shower-detector plane to better than 0.1° in some cases (Bird *et al.*, 1993b). Thus the chief source of error in determining the shower axis will be the projection of the core location error in the shower-detector plane, which will be $\sim \frac{1}{\sqrt{2}} \times$ the core location error.

Once the shower axis and R_p have been determined by the reconstruction algorithm, the dependence of shower size on atmospheric depth, $N_e(X)$, can be determined by working in reverse from the PMT signals to the nitrogen fluorescence. Again the quantum efficiency of the PMTs, mirror aberrations and scattered Čerenkov

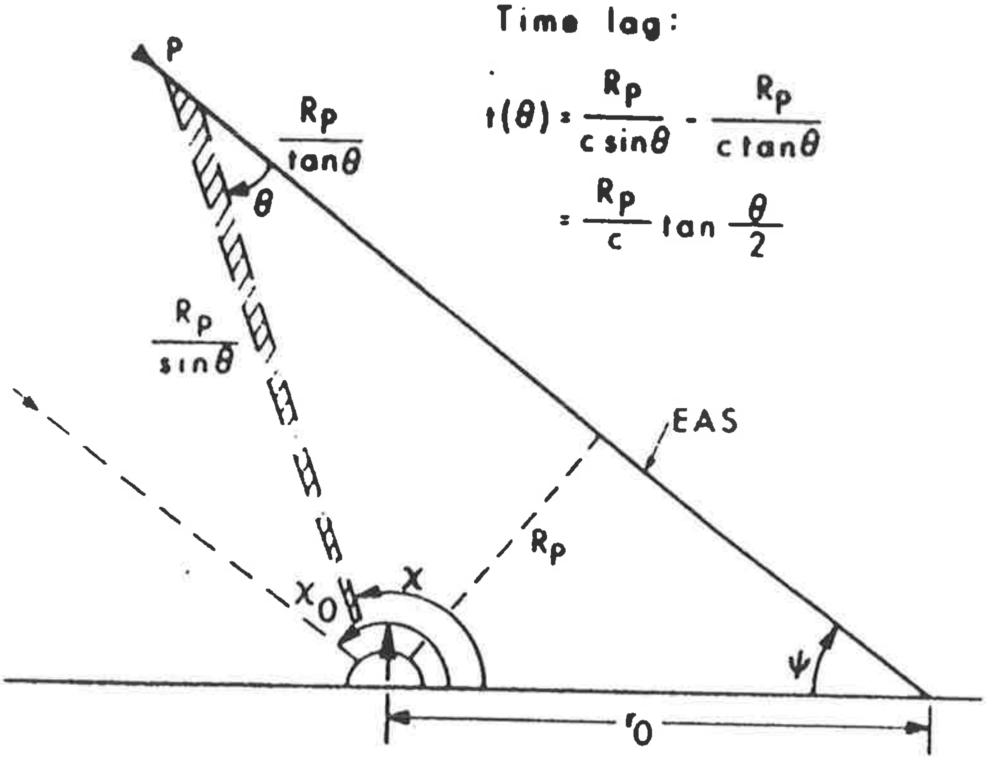

Figure 7-12: Geometry for determining shower axis in shower-detector plane. $\delta t(\theta)$ is the time lag for light arriving from the EAS relative to time of passage of the shower (from Baltrusaitis *et al.* (1985b)).

light are taken into account when deriving the fluorescence light and hence $N_e(X)$. A χ^2 fit of the Gaisser-Hillas function $f(X_0, X_{max})$ (Gaisser and Hillas, 1977) to $N_e(X)$ is then performed, yielding X_{max} and X_0. The cosmic ray primary energy is obtained by integrating $f(X_0, X_{max})$ over the total development of the shower, providing a calorimetric estimation of the energy.

7.6 Results from the Hybrid Simulation

The important characteristics which quantify the performance of the Hybrid are the angular resolution, energy resolution and the error in determining X_{max}. Two different techniques are used to simulate the performance of the Hybrid. Firstly the performance is simulated at discrete cosmic ray primary energies of 1, 10 and 100 EeV. 500 triggered showers for each energy were analysed. This allows the energy resolution to be calculated discretely at these energies. Secondly the energy region 1–100 EeV was divided into 8 equal bins in log E and 1000 triggered showers in each bin analysed. In each of these bins cosmic ray primary energies were sampled from the cosmic ray energy spectrum. This allows the testing of the Hybrid performance over an energy range.

7.6.1 Core Location Error

Cartesian Array

The mean error in core location for the cartesian array is $\sim$ 180 metres and is independent of energy. The magnitude and relative lack of variation with energy is due to the unsophisticated method of locating cores and also because the array has an almost uniform efficiency over the energy range considered. Conventional wisdom argues that ΔR_{core} is typically 10% of the array spacing when more sophisticated algorithms are used for core location. This implies that the core location error listed here will give some indication of the results expected for a Hybrid detector with a detector spacing close to 1.5 km.

$\log E$ eV	mean ΔR_{core}(m)	$\Delta\theta_{array}$ degrees	σX_{max} g cm^{-2}	$\frac{\Delta E}{E}$ %
18.00-18.25	185	1.95	34	
18.25-18.50	187	1.56	33	
18.50-18.75	184	1.75	30	
18.75-19.00	186	1.55	26	
19.00-19.25	186	1.76	24	
19.25-19.50	184	1.94	21	
19.50-19.75	182	1.58	20	
19.75-20.00	181	1.74	19	
18.00	189	1.57	35	5.7
19.00	191	1.54	24	3.1
20.00	176	1.22	18	2.3
19.00	125		22	3.0
19.00	190		26	4.0
19.00	250		30	4.4

Table 7.2: Some results from a simulation of the Hybrid detector for zenith angles less than 60°. A cartesian array is used with a spacing of 1 km and a triggering threshold of 0.3 m^{-2} and an individual detector area of 10 m^2. The array core location error is derived from a simple centre of mass fitting procedure, and is expressed as a mean error. The errors in array arrival direction, X_{max} and energy are standard deviations and were calculated from gaussian fits to the appropriate error distributions. The final three rows show the sensitivity of parameters to core location errors. For those three simulations, no array fitting was done and core errors were sampled from a gaussian error distribution with mean errors as shown.

$\log E$ eV	mean ΔR_{core}(m)	$\Delta\theta_{array}$ degrees	σX_{max} g cm^{-2}	$\frac{\Delta E}{E}$ %
18.00-18.25	197	1.78*	31	
18.25-18.50	209	0.10	31	
18.50-18.75	229	1.43	28	
18.75-19.00	230	1.16	27	
19.00-19.25	236	1.61	24	
19.25-19.50	240	1.54	22	
19.50-19.75	247	1.62	20	
19.75-20.00	271	1.86	19	
17.50	133	1.39	49	16.2
18.00	166	1.47	35	4.7
19.00	238	1.77	27	3.6
20.00	295	2.00	18	2.6

Table 7.3: As in the first part of Table 7.2 except that the graded triangular array was used. * Note: distribution of fitted directions for array is non-gaussian. This is not entirely unexpected since the distribution of space angles will encompass contributions from each graded component of the array.

Graded Triangular Array

The performance of the graded triangular array (see Table 7.3) with respect to core location is comparable to the cartesian array. The core location error is larger, reflecting the greater spacing between detectors on average. Once again the core location resolution can be improved by using a more sophisticated algorithm.
Figure 7-13 shows the distribution of cores of Hybrid triggered events as a function of energy. From this it is clear why there is a variation of core location error with energy, as regions of the array with different detector spacing are favoured for different energies.

7.6.2 Energy Resolution

The energy resolution $\frac{\Delta E}{E}$ at 1, 10 and a 100 EeV quoted in Tables 7.2 and 7.3 represents the statistical error in the Hybrid's determination of energy. The energy resolution is calculated using the same method as employed previously for determining an array's energy resolution. The uncertainties introduced by atmospheric variability have not been included here, but would be similar to those allowed for in the HiRes

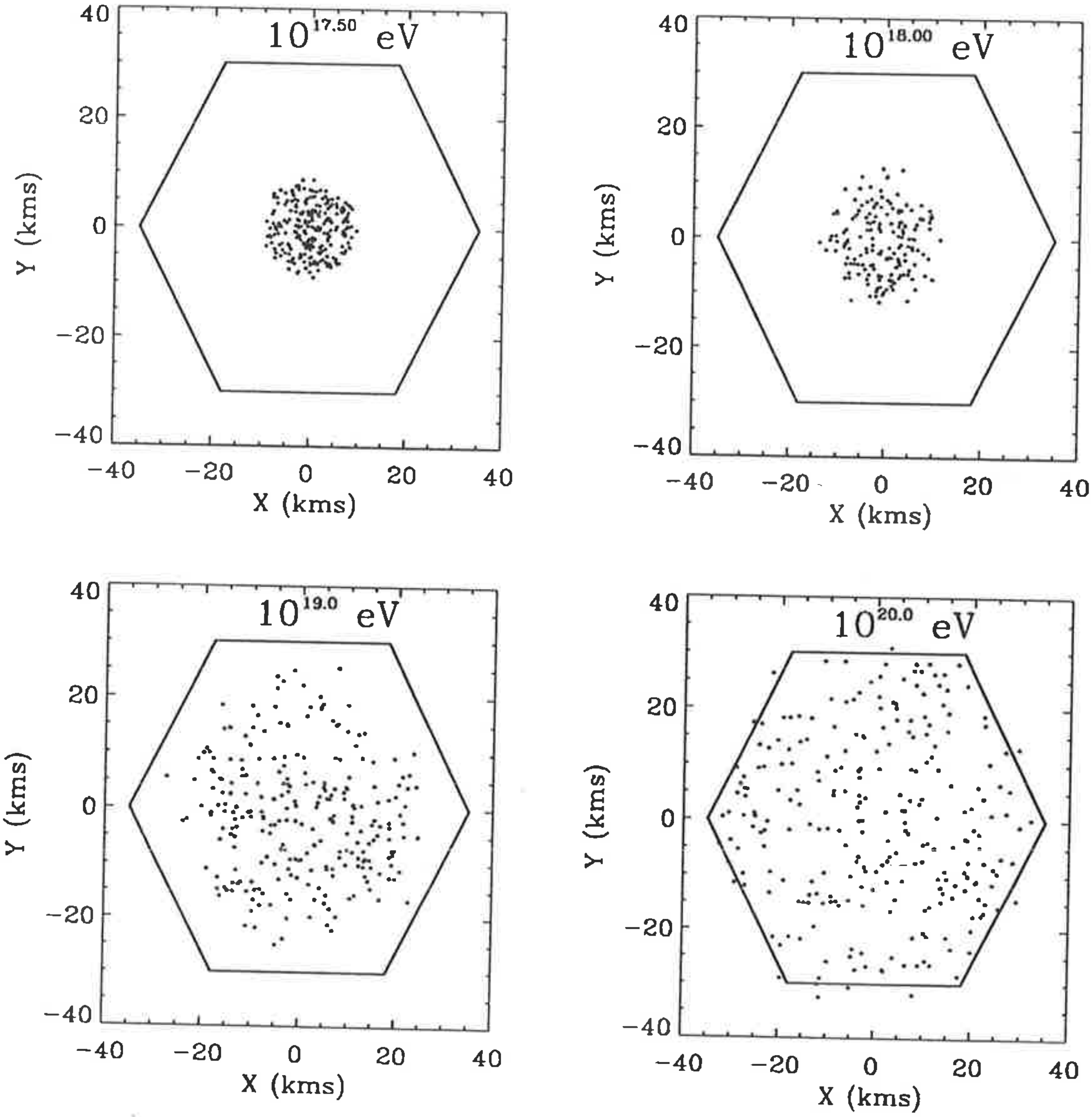

Figure 7-13: Distribution of triggered core locations for the graded triangular array plus air fluorescence detector in the energy range $10^{17.5}$–10^{20} eV.

Fly's Eye, bringing the typical energy uncertainty to 20%. This assumes that the atmosphere has been well characterised using laser based atmospheric monitoring. It is expected that atmospheric variability will dominate the error in determining cosmic ray primary energy.

The sensitivity of energy resolution to array core location errors appears small in the range of ΔR_{core} from 125 to 250 m (see Table 7.2). This was tested by using gaussian generated core location errors fluctuated from the true core location at an energy of 10^{19} eV using three different mean errors of 125, 190 and 250 metres. In these cases the statistical energy resolution (ignoring atmospheric effects) varied by less than 1%.

7.6.3 Angular Resolution

Cartesian Array

The angular resolution of the cartesian array alone is $\sim 2°$. The angular resolution of the Hybrid is markedly improved over the array alone and is comparable to that expected with the stereo HiRes detector. Figure 7-14 shows the integrated event count as a function of the cone angle between the true cosmic ray direction and the reconstructed direction. This method was used to quantify the angular resolution, as the corresponding $(dN/d\Omega)$ plots are peaked at small angular error and are not gaussian in form. At 10^{19} eV, the expected proportion of Hybrid events which are resolved to less than 1° is ~ 0.65. The dependence of angular resolution on core location error can also be seen in Figure 7-14. Angular resolution shows some sensitivity to core location error, with the proportion of Hybrid events which are resolved to less than 1° varying from approximately 0.5 to 0.75 for the core location errors considered.

Graded Triangular Array

In Figure 7-15 the Hybrid angular resolution results for the graded triangular detector are presented. The angular resolution for the hybrid with a graded triangular array is somewhat poorer than the hybrid with the cartesian array (see Figure 7-15). The dependence of angular resolution on array detector spacing is also plotted in

Figure 7-15. It is interesting to note that the angular resolution of the hybrid improves as the core position moves away from the centre of the array, even though overall core resolution worsens. The reason for this has not been fully investigated but one possibility is that the timing resolution for a HiRes detector (~ 20 ns) may not be sufficient to allow a good reconstruction of the shower axis for small R_p.

7.6.4 X_{max} Resolution

The resolution in X_{max} varies from 35 g cm^{-2} to less than 20 g cm^{-2} for both array configurations over the energy range 10–100 EeV. This is directly comparable to the Stereo HiRes figure of ~ 30 g cm^{-2}. The X_{max} resolution is limited by errors in shower axis determination and the finite sampling of the shower profile by the HiRes detector. Atmospheric uncertainties play a secondary role here because it is usually straightforward to locate shower maximum, even on a profile distorted by atmospheric transmission effects. The sensitivity of X_{max} resolution to array core location errors is small for the range of ΔR_{core} from 125 to 250 metres (see Table 7.2).

7.6.5 General Performance

The aperture as a function of energy for Hybrid events is plotted in Figure 7-16 for both array configurations. A 60° zenith angle cut has been applied and reconstruction efficiencies have been included. The integrated number of good quality Hybrid events expected in 5 years is plotted in Figure 7-17, also for both configurations. From Figures 7-16 and 7-17 it can be see that the aperture and expected number of Hybrid events is ~ 10% less for the graded triangular array than that for the cartesian array. This is due almost entirely to the smaller size of the graded triangular array.

7.7 Conclusions

The construction of an experiment to detect EHE cosmic rays in significant numbers will require a large amount of material and financial resources. Clearly before any construction is undertaken it is necessary to determine the expected behaviour of any proposed detector. The analysis of detector configurations presented in this chapter

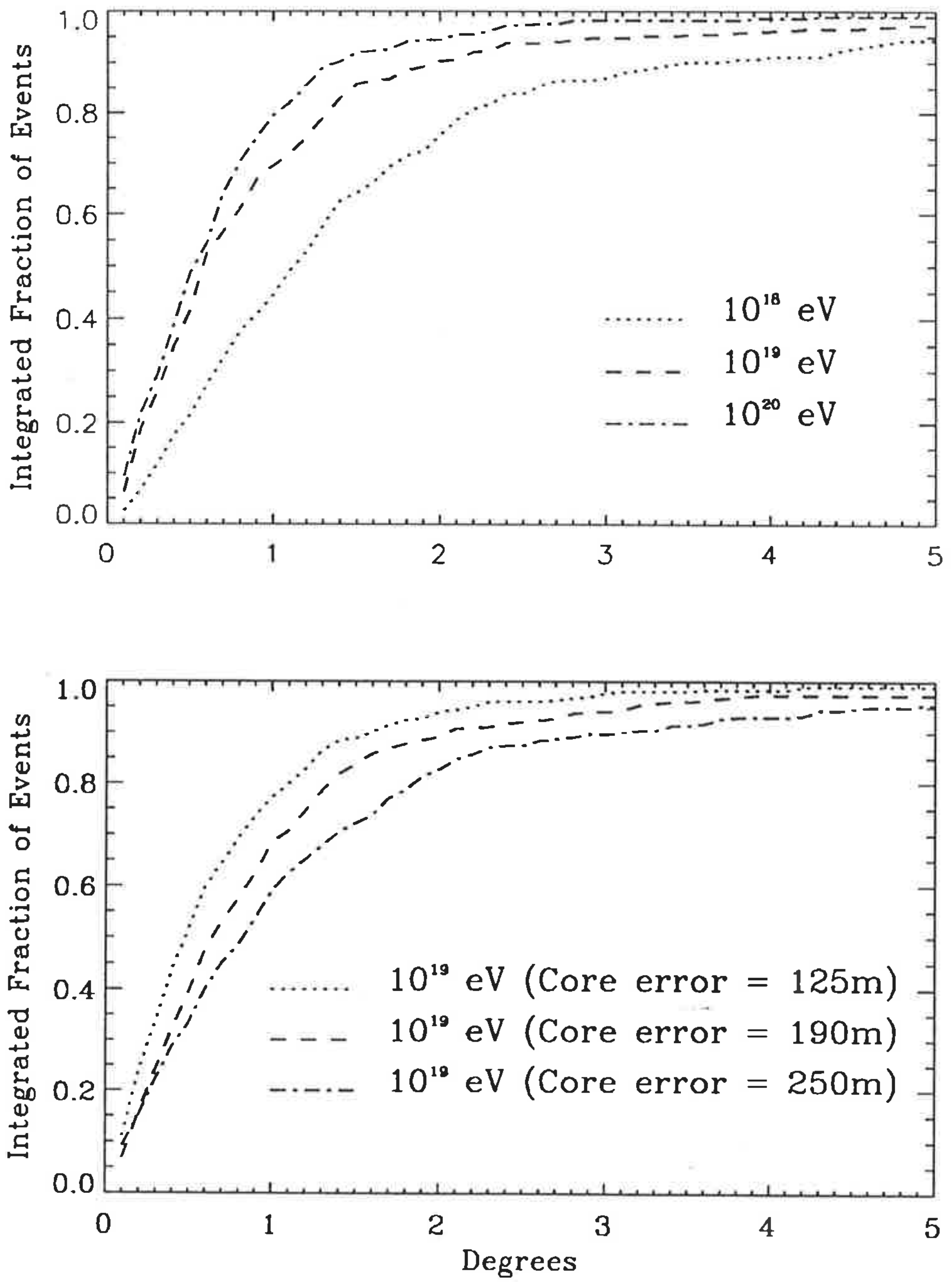

Figure 7-14: Hybrid angular resolution results for the cartesian array. Detector spacing is assumed to be 1 km. Shown are the distributions of integrated event number as a function of the space angle between the true shower direction and the reconstructed direction (Top) using centre of mass of the shower as core location estimator and (Bottom) sampling the core location error from a normal distribution.

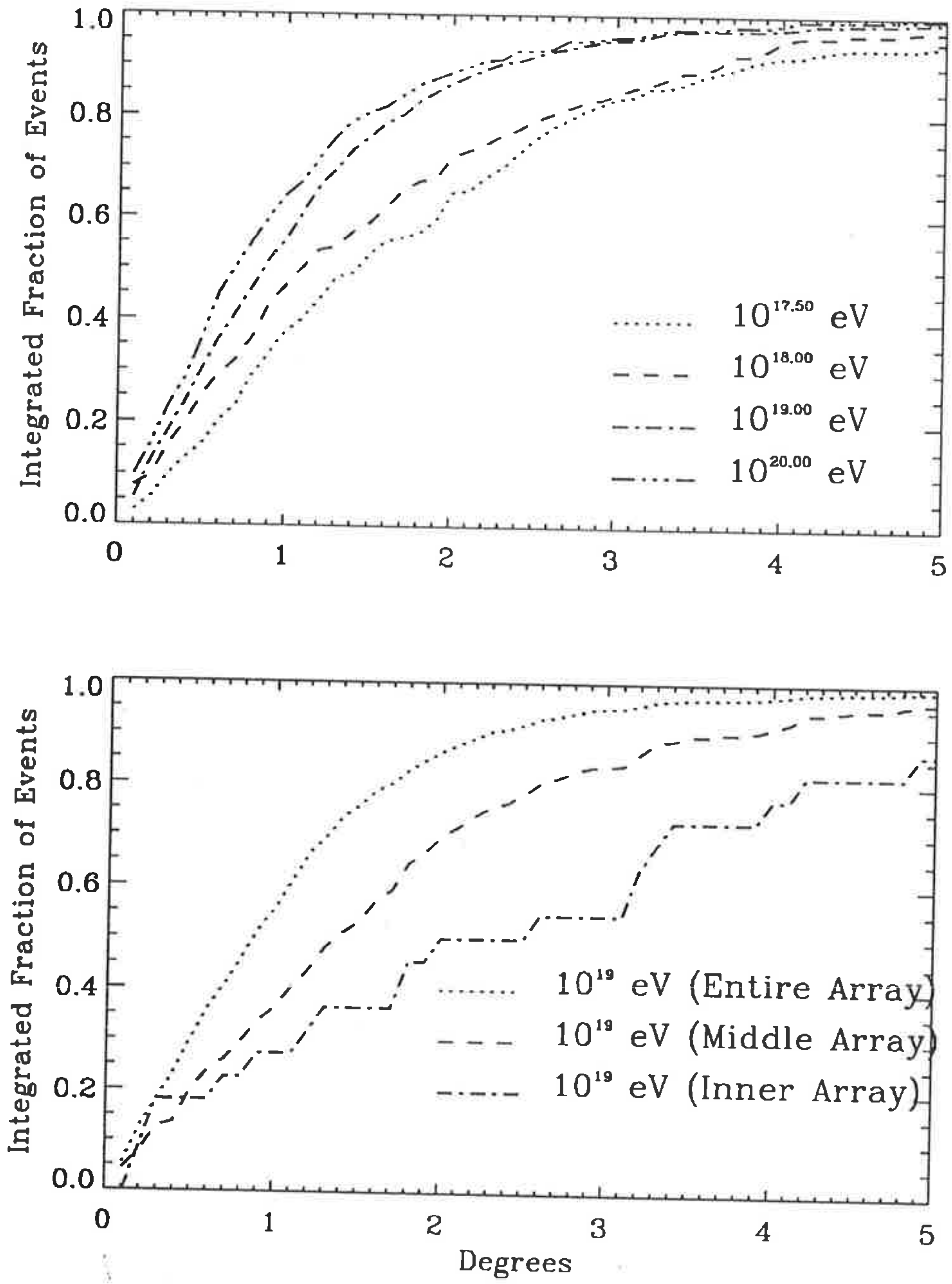

Figure 7-15: Hybrid angular resolution results for the graded triangular array. Shown are the distributions of integrated event number as a function of the space angle between the true shower direction and the reconstructed direction. The bottom figure shows the angular resolution change, moving out from the inner array for showers at 10^{19} eV.

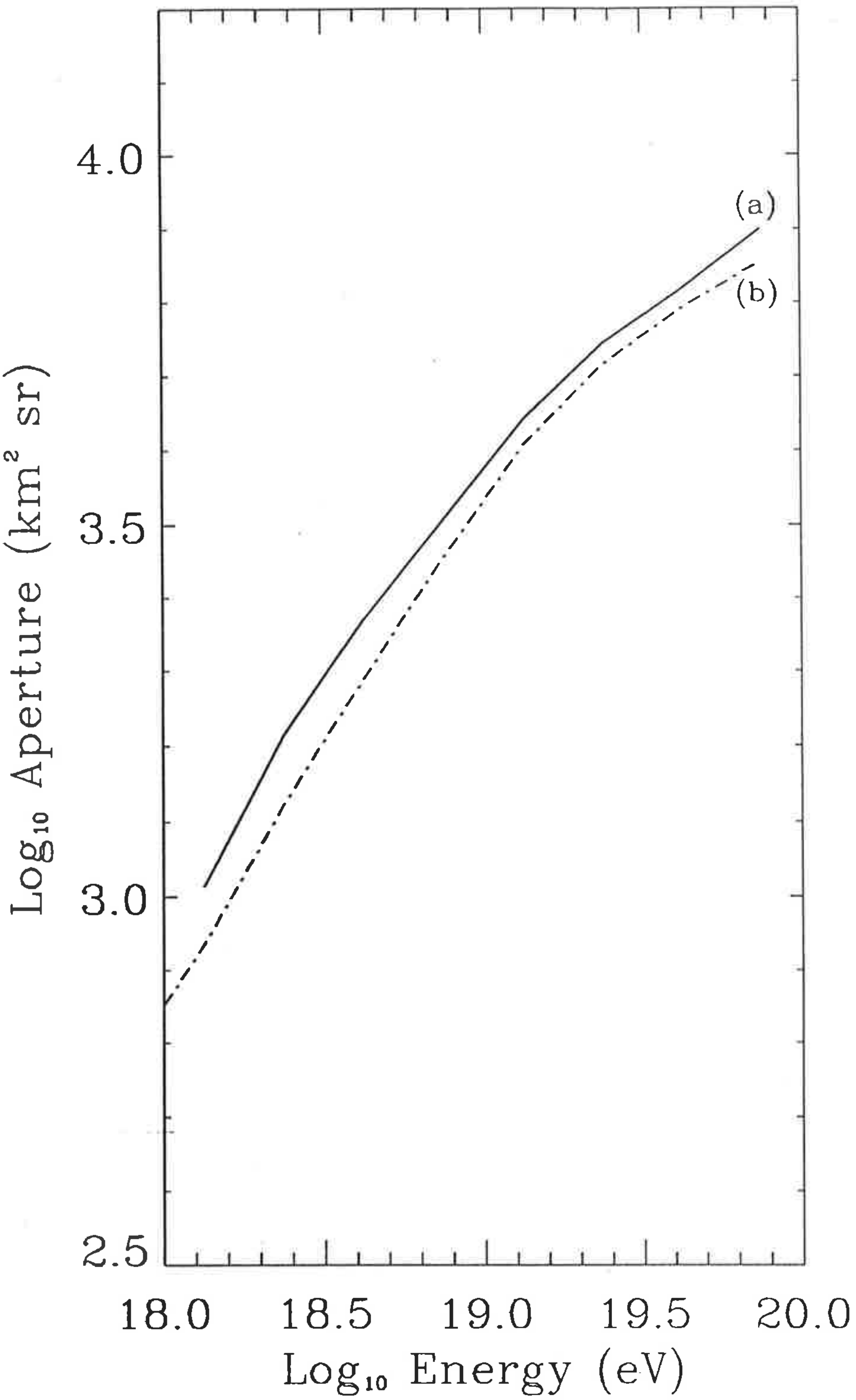

Figure 7-16: Predicted aperture as a function of log(E) for Hybrid Detector with zenith angles less than 60°. Reconstruction efficiencies have been included.(a) Cartesian array: (b) Graded triangular array.

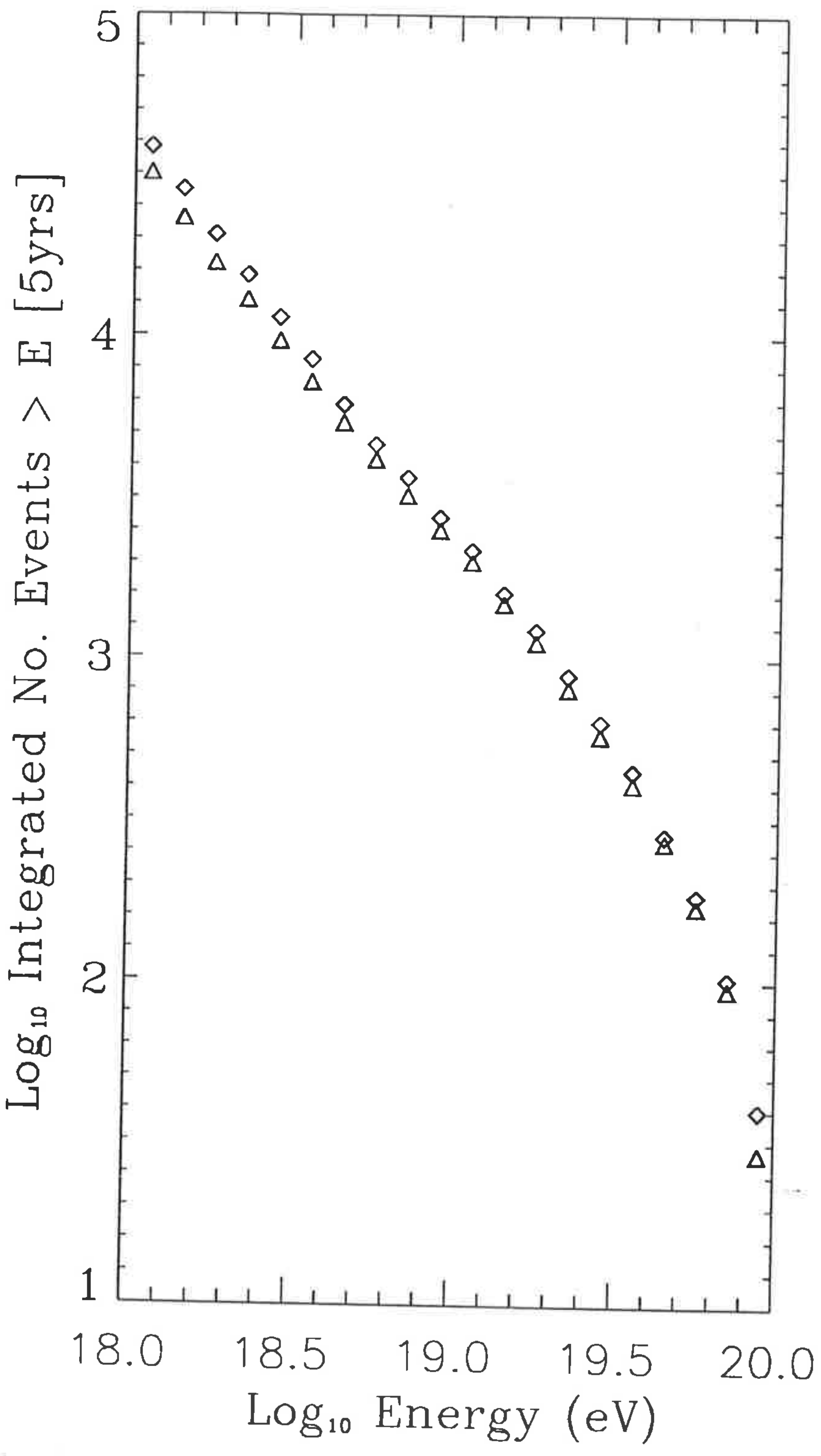

Figure 7-17: Predicted integral event number for Hybrid Detector after a five year period, based on a 12% duty cycle and a spectrum of the form $J(E)dE = 10^{-11.5}(E/\text{EeV})^{-3.1}$ $\text{m}^{-2}\ \text{s}^{-1}\ \text{sr}^{-1}\ \text{EeV}^{-1}$ up to 5.5 EeV. At that point the spectral slope flattens to -2.5. (a) Cartesian Array (diamonds): (b) Graded triangular Array (triangles).

represents the first step in analysing detector designs.

The first section of this chapter analyses ground array designs. It is found that a ground array is capable of an angular resolution of 2°–3° and an energy resolution of between 10% and 20%. The energy resolution is quite likely to be shown to be poorer with a more comprehensive analysis, as this simulation does not include the expected fluctuations in $\rho(600)$ for constant cosmic ray primary energy. Also, there may be some systematic error in assigning an energy for a given $\rho(600)$. An angular resolution of between 2° and 3° implies that to detect point sources a large number of events will need to be detected. Because of the large spacing of detectors, particle density and arrival time fluctuations become important. It is necessary to have a reasonable triggering threshold for direction fits (i.e. ~ 0.3 m^{-2} for a detector with a 10 m^2 surface area), because below this level the spread in the arrival time of shower front particles will rapidly degrade the angular resolution of the array. Another factor which necessitates not having too large an array spacing is that the array needs to operate at 100% efficiency in the energy region of interest so that array threshold effects can be ignored. The most recent measurement of the EHE lateral distribution (Chiba *et al.*, 1993b) is steeper than that assumed here, for distances from the core of greater than 1 km. This effect has not been considered here, but it will have a substantial impact in determining array spacing. It has been shown quantitatively that a triangular array out performs a cartesian array on a cost per event basis.

The second type of detector investigated in this chapter is a Hybrid, consisting of a ground array operating in conjunction with a nitrogen fluorescence detector modelled on the HiRes Fly's Eye. The core locations obtained from the array are used to constrain the shower axis fit. The result is that a single 360° HiRes detector located at the centre of an array performs at the same level as the proposed full HiRes detector. The depth of maximum resolution, $\sigma_{X_{max}}$, is found to be ~ 30 g cm^{-2}. This is low enough to separate the iron and proton component of the primary cosmic ray flux, which have a typical mean separation of X_{max} of 100 g cm^{-2}. The increased angular resolution ($< 1°$) from the Hybrid subset of events will aid in the search for EHE point sources. The increased energy resolution of the Hybrid detector implies that finer changes in the cosmic ray energy spectrum can be discerned.

Another significant potential benefit is that the fluorescence detector will be able to "teach" the ground array. By analysing Hybrid events and comparing the measured array parameters on an event by event basis with the energy and composition information determined by the fluorescence detector, improved techniques for determining energy and composition from the array alone may be developed. Clearly it is important that the individual detector elements of the array should be designed so as to measure the parameters expected to be linked with composition (i.e. μ to e^- ratios). The Hybrid concept could also be applied by building an array around the proposed HiRes site at Dugway, Utah.

Chapter 8

Summary and Further Work

In this thesis three areas of interest in High Energy Astrophysics were investigated by the use of Monte Carlo modelling of the physical processes involved.

8.1 Heavy Element Clumping in SN 1987A

A Monte Carlo code describing the propagation of X-rays in the ejecta of SN 1987A was developed. The elemental abundance structure was adopted from Model 10HMM (Pinto and Woosley, 1988a) and was simplified for the purposes of this calculation. Results from the simulation were compared with experimental measurements of the X-ray lightcurve and spectra from SN 1987A (Syunyaev *et al.*, 1990). It was found that there was disagreement between the results of the simulation and measurements of the X-ray lightcurve in the 15–45 keV energy region.

Clumping of heavy elements within the ejecta was invoked to explain this discrepancy. The Monte Carlo model was modified to include the effects of clumping within the ejecta. It was found that clumping in the region of 0.1 to 0.2 times the total ejecta radius provided far better agreement with experimental measurements in the 15–45 keV energy region, without affecting the compatibility with experimental results in the higher energy regions (Lee, Mastichiadis and Protheroe, 1991). Furthermore, the position and extent of clumping was in accord with predictions of the regions of instability in the ejecta of SN 1987A found from modelling the dynamics of the expansion of SN 1987A (Arnett, Fryxell and Muller, 1989).

8.2 Propagation of EHE Cosmic Rays

The passage of EHE cosmic rays through the galaxy (and halo) was modelled by Monte Carlo methods in order to determine the origin of these extremely energetic cosmic rays. The model simulated the propagation of EHE cosmic rays in the galactic magnetic field and took into account the strong magnetic field turbulence measured in the galaxy. This turbulence was assumed to have a Kolmogorov spectrum and the lower length scales of turbulence were included in the simulation. It was found that the measurements of the cosmic ray anisotropy and galactic gradient were inconsistent with a galactic origin to the EHE cosmic ray flux, assuming a prominent proton component to the cosmic ray flux at these energies.

The effect of including a galactic halo containing a turbulent magnetic field on EHE cosmic ray anisotropy was also investigated. It was found, for all reasonable halo size and field strength configurations, that the simulated anisotropy was still inconsistent with the measured anisotropy. Once again a prominent proton flux has been assumed (Lee and Clay, 1993).

This work could be further extended by taking the measured composition as a function of energy (e.g. from Bird *et al.* (1993d)) and investigating the energy at which the galactic magnetic field turbulence can no longer account for the measured anisotropy. It would then be interesting to investigate whether this energy, above which cosmic rays are not contained within the galaxy, corresponds to any features in the cosmic ray energy spectrum.

8.3 Design of an Experiment to Detect EHE Cosmic Rays

At present, measurements of the EHE energy spectrum, anisotropy and primary composition are limited by the low cosmic ray flux at these energies. This section of the thesis deals with the simulation of various detectors, designed to increase substantially the frequency of observations of EHE cosmic rays. A Monte Carlo code modelling the performance of different array configurations has been developed. It was found that the shower front curvature at large core distances affects the array performance significantly. This implies that relatively high triggering thresholds must be set (e.g. 2–3 particles for a detector surface area of 10 m^2 Clay *et al.* (1992)). The performance of two different array geometries was also modelled and it was found that a triangular array geometry out performs a cartesian array on a cost per quality event basis.

A new type of Hybrid detector was modelled, this being a combination of a ground array and a single atmospheric fluorescence detector located in the centre of the array. The fluorescence detector was assumed to be of the type proposed for the HiRes Fly's Eye. This was simulated by combining the HiRes Monte Carlo code developed in Utah and the ground array simulation. The array simulation provides a core location to showers which trigger the fluorescence detector. It is found that the Hybrid performs comparably to the HiRes Fly's Eye. This implies that $\sim 10\%$ of the total number of detected events will have superior energy resolution, angular resolution and composition information.

The simulations for this experiment represent only the first step towards a detector design. As decisions are made as to the precise aims of such an experiment and the type of detector, Monte Carlo simulations will need to be further refined.

REFERENCES

Akhiezer, A. I. and V. B. Berestetskii, *Quantum Electrodynamics.*, 1965, Interscience Monographs and Texts in Physics and Astronomy., **11**, Interscience Publishers., New York, *Kvantovaia elektrodinamika.*

Allan, H. R., 1971, *Prog. Elem. Part. and Cos. Ray Phys.*, **10**, 170.

Allkofer, O. C., K. Carstensen, W. D. Dau and H. Jokisch, 1975, *J. Phys. G*, **1**(6), L51.

Alvarez, L. .W. and A. H. Compton, 1933, *Phys. Rev.*, **43**, 835.

Amaldi, U., G. Cocconi, A. N. Diddens, R. W. Robinson, J. Dorenbosch, W. Duinker, D. Gustavson, J. Meyer, K. Potter, A. M. Wetherell, A. Baroncelli and C. Bosio, 1977, *Phys. Lett. B*, **66**(4), 390.

Ambwani, K. and P. Sutherland, 1988, *Ap. J.*, **325**, 821.

Amos, N. A., C. Avila, W. F. Baker, M. Bertani, M. M. Block, D. A. Dimitroyannis, D. P. Eartly, R. W. Ellsworth, G. Giacomelli, B. Gomez, J. A. Goodman, C. M. Guss, A. J. Lennox, M. R. Mondarni, J. P. Negret, J. Orear, S. M. Pruss, R. Rubinstein, S. Sadr, S. Shukla, I. Veronesi and S. Zuchelli, 1989, *Phys. Rev. Lett.*, **63**(26), 2784.

Anderson, C. D., 1933, *Phys. Rev.*, **43**, 368.

Armstrong, J. W., J. M. Cordes and B. J. Rickett, 1981, *Nature* , **291**, 561.

Arnett, D., B. Fryxell and E. Muller, 1989, *Ap. J. Lett.*, **341**, L63.

Arnett, W. D., 1987, *Ap. J.*, **319**, 136.

Arnett, W. D., J. N. Bachall, R. P. Kirshner and S. E. Woosley, 1989, *Ann. Rev. Astron. Ap.*, **27**, 629.

Arnett, W. D. and A. Fu, 1989, *Ap. J.*, **340**, 396.

Asakimori, K., T. H. Burnett, M. L. Cherry, M. J. Christl, S. Dake, J. H. Derrickson, W. F. Fountain, M. Fuki, J. C. Gregory, T. Hayashi, R. Holynski, J. Iwai, A. Iyono, W. V. Jones, A. Jurak, J. J. Lord, O. Miyamura, H. Oda, T. Ogata, T. A. Parnell, F. E. Roberts, S. Strausz, Y. Takahashi, T. Tominaga, J. W. Watts, J. P. Wefel, B. Wilczynska, H. Wilczynski, R. J. Wilkes, W. Wolter and B. Wosiek, 1991, *Proc. 22nd Int. Cosmic Ray Conf. (Dublin)*, **2**, 57.

———, 1991, *Proc. 22nd Int. Cosmic Ray Conf. (Dublin)*, **2**, 97.

Astley, S. M., G. Cunningham, J. Lloyd-Evans, R. J. O. Reid and A. A. Watson, 1981, *Proc. 17th Int. Cosmic Ray Conf. (Paris)*, **2**, 156.

Au, W., J. Boyer, C. Y. Chi, Y. Ho, W. Lee, J. Mechalakos, D. Bird, R. Downing, M. Kidd, T. O'Halloran, V. Simitas, R. G. Cooper, S. C. Corbató, H. Y. Dai, B. R. Dawson, J. W. Elbert, B. L. Emerson, D. B. Kieda, S. Ko, E. C. Loh, M. Z. Luo, M. H. Salamon, J. D. Smith, P. Sokolsky, P. Sommers, J. K. K. Tang and S. B. Thomas, 1991, *Proc. 22nd Int. Cosmic Ray Conf. (Dublin)*, **2**, 692.

Auger, P., R. Maze and T. Grivet-Mayer, 1938, *C. R. Acad. Sci (Paris)*, **206**, 151.

Axford, W. I., E. Leer and G. Skadron, 1977, *Proc. 15th Int. Cosmic Ray Conf. (Plovdiv)*, **11**, 132.

Baltrusaitis, R. M., R. Cady, G. L. Cassiday, R. Cooper, J. W. Elbert, P. R. Gerhardy, S. Ko, E. C. Loh, Y. Mizumoto, M. H. Salamon, P. Sokolsky and D. Steck, 1985, *Proc. 19th Int. Cosmic Ray Conf. (La Jolla)*, **2**, 146.

Baltrusaitis, R. M., R. Cady, G. L. Cassiday, R. Cooper, J. W. Elbert, P. R. Gerhardy, S. Ko, E. C. Loh, M. Salamon, D. Steck and P. Sokolsky, 1985, *Nucl. Instr. Meth.*, **A240**, 410.

Baltrusaitis, R. M., G. L. Cassiday, R. Cooper, B. R. Dawson, J. W. Elbert, B. E. Fick, D. F. Liebing, E. C. Loh, P. Sokolsky and D. Steck, 1988, *Nucl. Instr. Meth.*, **A264**, 87.

Barrett, P. H., L. M. Bollinger, G. Cocconi, Y. Eisenburg and K. Greisen, 1952, *Rev. Modern Phys.*, **24**(3), 133.

Begelman, M. C., R. D. Blandford and M. J. Rees, 1984, *Rev. Modern Phys.*, **56**(2), 255.

Bell, A. R., 1978, *Mon. Not. R. Astron. Soc.*, **182**, 443.

———, 1978, *Mon. Not. R. Astron. Soc.*, **182**, 147.

Benecke, J., T. T. Chou, C. N. Yang and E. Yen, 1969, *Phys. Rev.*, **188**(5), 2159.

Benz, W. and F-K. Thielemann, 1990, *Ap. J. Lett.*, **348**, 17.

Berezinsky, V. S., S. I. Grigoryeva, A. A. Mikhailov, H. Rubinstein, A. A. Ruzmaikin, D. D. Sokoloff and A. M. Shukurov, 1991, in *Astrophysical Aspects of the most Energetic Cosmic Rays, Proceedings of the ICCR International Symposium*, ed. M. Nagano and F. Takahara, p. 134, World Scientific, Kofu, Japan, Singapore.

Berezinsky, V. S. and A. A. Mikhailov, 1983, *Proc. 18th Int. Cosmic Ray Conf. (Bangalore)*, **2**, 174.

———, 1987, *Proc. 20th Int. Cosmic Ray Conf. (Moscow)*, **2**, 54.

Berezinsky, V. S., A. A. Mikhailov and S. I. Syrovatskii, 1979, *Proc. 16th Int. Cosmic Ray Conf. (Kyoto)*, **2**, 86.

Bionta, R. M., G. Blewitt, C. B. Bratton and D. Casper, 1987, *Phys. Rev. Lett.*, **58**(14), 1494.

Bird, D. J., J. Boyer, R. W. Clay, S. C. Corbató, H. Y. Dai, B. R. Dawson, R. W. Downing, J. W. Elbert, M. A. Huang, D. B. Kieda, M. J. Kidd, S. Ko, C. G. Larsen, W. Lee, E. C. Loh, E. Mannel, T. A. O'Halloran, M. H. Salamon, J. D. Smith, P. Sokolsky, P. Sommers, J. K. K. Tang and S. B. Thomas, 1993, *Proc. 23rd Int. Cosmic Ray Conf. (Calgary)*, **2**, 458.

———, 1993, *Proc. 23rd Int. Cosmic Ray Conf. (Calgary)*, **2**, 454.

Bird, D. J., S. C. Corbató, H. Y. Dai, B. R. Dawson, J. W. Elbert, B. L. Emerson, M. A. Huang, D. B. Kieda, M.Luo, S. Ko, C. G. Larsen, E. C. Loh, M. H. Salamon, J. D. Smith, P. Sokolsky, P. Sommers, J. K. K. Tang and S. B. Thomas, 1993, *Proc. 23rd Int. Cosmic Ray Conf. (Calgary)*, **2**, 34.

Bird, D. J., S. C. Corbató, H. Y. Dai, B. R. Dawson, J. W. Elbert, M. A. Huang, D. B. Kieda, S. Ko, C. G. Larsen, E. C. Loh, M. H. Salamon, J. D. Smith, P. Sokolsky, P. Sommers, T. Stanev, S. Tilav, J. K. K. Tang and S. B. Thomas, 1993, *Proc. 23rd Int. Cosmic Ray Conf. (Calgary)*, **2**, 38.

Bird, D. J., S. C. Corbató, H. Y. Dai, B. R. Dawson, J. W. Elbert, M. A. Huang, D. B. Kieda, S. Ko, C. G. Larsen, E. C. Loh, M. H. Salamon, J. D. Smith, P. Sokolsky, P. Sommers, J. K. K. Tang and S. B. Thomas, 1993, *Proc. 23rd Int. Cosmic Ray Conf. (Calgary)*, **2**, 55.

———, 1993, *Proc. 23rd Int. Cosmic Ray Conf. (Calgary)*, **2**, 51.

Blandford, R. D. and J. P. Ostriker, 1978, *Ap. J. Lett.*, **221**, L29.

Bloemen, H., 1987, in *Interstellar Processes*, ed. D. J. Hollenbach and H. A. Thronson, Astro. Space Sci. Lib., **134**, p. 143, D. Reidel Publishing Company.

———, 1989, *Ann. Rev. Astron. Ap.*, **27**, 469.

Bodansky, D., D. D. Clayton and W. A. Fowler, 1968, *Phys. Rev. Lett.*, **20**(4), 161.

Bøggild, H., K. H. Hansen and M. Suk, 1971, *Nuclear Phys. B*, **27**, 1.

Bowyer, S. and G. B. Field, 1969, *Nature*, **223**, 573.

Brandenburg, A., K. J. Donner, D. Moss, A. M. Shukurov, D. D. Sokoloff and I. Tuominen, 1992, *Astron. Ap.*, **259**, 453.

———, 1993, *Astron. Ap.*, **271**, 36.

Braun, O. and K. Sitte, 1965, *Proc. 9th Int. Cosmic Ray Conf. (London)*, **9**, 712.

Bridle, A. H. and R. A. Perley, 1984, *Ann. Rev. Astron. Ap.*, **22**, 319.

Brown, L. S., D. L. Nordstrom and S. G. Brown, 1992, *Phys. Rev. D* , **45**.

Bussard, R. W., A. Burrows and L. S. The, 1989, *Ap. J.*, **341**, 401.

Capdevielle, J. N. and J. Gawin, 1982, *J. Phys. G*, **8**, 1317.

Cassé, M. and J. A. Paul, 1980, *Ap. J.*, **237**, 236.

Cebula, D., S. C. Corbató, T. Daily, D. B. Kieda, K. Lande and C. K. Lee, 1990, *Ap. J.*, **358**, 637.

Chandrasekhar, S., 1943, *Rev. Modern Phys.*, **15**, 1.

Chantler, M. P., M. A. B. Craig, T. J. L. McComb, K. J. Orford, K. E. Turver and G. M.Walley, 1982, *J. Phys. G Lett.*, **8**, L51.

Châtelet, E., T. V. Danilova, A. D. Erlykin and J. Procureur, 1991, *Proc. 22nd Int. Cosmic Ray Conf. (Dublin)*, **2**, 45.

Cheung, T. and P. K. MacKeown, 1988, *Nuovo Cimento C (1)*, **11C**(2), 193.

Chevalier, R. A. and C. Fransson, 1987, *Ap. J. Lett.*, **322**, L15.

———, 1987, *Nature* , **328**, 44.

Chevalier, R. A., 1976, *Ap. J.*, **207**, 872.

Chi, X., J. Szabelski, M. N. Vahia, J. Wdowczyk and A. W. Wolfendale, 1992, *J. Phys. G*, **18**, 539.

———, 1992, *J. Phys. G*, **18**, 567.

Chi, X., M. N. Vahia, J. Wdowczyk and A. W. Wolfendale, 1992, *J. Phys. G*, **18**, 553.

Chi, X., J. Wdowczyk and A. W. Wolfendale, 1992, *J. Phys. G*, **18**, 1259.

Chi, X. and A. W. Wolfendale, 1990, *J. Phys. G*, **16**, 1409.

Chiba, N., K. Hashimoto, N. Hayashida, K. Honda, M. Honda, N. Inoue, F. Kakimoto, K. Kamata, S. Kawaguchi, N. Kawasumi, Y. Matsubara, K. Murakami, M. Nagano, S. Ogio, H. Ohaka, T. Saito, Y. Sakuma, I. Tsushima, M. Teshima, T. Umezawa, S. Yoshida and H. Yoshii, 1992, *Nucl. Instr. Meth.*, **311**, 338.

Chiba, N., N. Hayashida, K. Honda, M. Honda, S. Imaizumi, N. Inoue, K. Kadota, F. Kakimoto, K. Kamata, S. Kawaguchi, N. Kawasumi, Y. Matsubara, K. Murakami, M. Nagano, H. Ohaka, Y. Suzuki, M. Teshima, I. Tsushima, S. Yoshida and H. Yoshii, 1993, *Proc. 23rd Int. Cosmic Ray Conf. (Calgary)*, **2**, 59.

———, 1993, *Proc. 23rd Int. Cosmic Ray Conf. (Calgary)*, **4**, 315.

Clark, G. W., G. P. Garmire and W. L. Kraushaar, 1968, *Ap. J. Lett.*, **153**, 203.

Clay, J., 1927, *Proc. Roy. Acad. Amsterdam*, **36**, 1115.

Clay, R. W., 1985, *Proc. 19th Int. Cosmic Ray Conf. (La Jolla)*, **9**, 357.

———, 1987, *Aust. J. Phys.*, **40**, 423.

Clay, R. W., B. R. Dawson, A. G. Gregory, A. A. Lee, P. G. Edwards, G. J. Thornton, J. L. Reid, A. G. K. Smith, M. S. Talbot and N. R. Wild, 1992, *Nuclear Phys. B Proc. Suppl.*, **28B**, 101.

Clay, R. W. and P. R. Gerhardy, 1982, *Aust. J. Phys.*, **35**, 59.

Clayton, D. D., S. A. Colgate and G. J. Fishman, 1969, *Ap. J.*, **155**, 75.

Cocconi, G., 1961, in *Handbuch der Physik*, ed. S. Flugge, Springer-Verlag, p. 215, Berlin.

Cooper, R., S. C. Corbató, H. Y. Dai, J. W. Elbert, B. Emerson, B. E. Fick, D. B. Kieda, S. Ko, E. C. Loh, M. Z. Luo, M. H. Salomon, J. D. Smith, P. Sokolsky, P. Sommers, J. K. K. Tang and S. B. Thomas, 1991a, in *Astrophysical Aspects of the most Energetic Cosmic Rays, Proceedings of the ICCR International Symposium*, ed. M. Nagano and F. Takahara, p. 34, World Scientific, Kofu, Japan, Singapore.

Cooper, R., S. C. Corbató, H. Y. Dai, J. W. Elbert, B. Emerson, D. B. Kieda, S. Ko, E. C. Loh, M. Z. Luo, M. H. Salomon, J. D. Smith, P. Sokolsky, P. Sommers, J. K. K. Tang, S. B. Thomas, L. Borodovsky, J. Boyer, C. Y. Chi, Y. Ho, W. Lee, J. Mechalakos, R. Downing, T. A. O'Halloran and V. Simaitis, 1991b, in *Astrophysical Aspects of the most Energetic Cosmic Rays, Proceedings of the ICCR International Symposium*, ed. M. Nagano and F. Takahara, p. 345, World Scientific, Kofu, Japan, Singapore.

Cordes, J. M., J. M. Weisberg and V. Boriakoff, 1985, *Ap. J.*, **288**, 221.

Cronin, J. W., University of Chicago preprint, EFI 92-08, 1992.

Crookes, I. N. and B. C. Rastin, 1971, *Proc. 12th Int. Cosmic Ray Conf. (Hobart)*, **10**, 171.

Cunningham, G., J. Lloyd-Evans, A. M. T. Pollock, R. J. O. Reid and A. A. Watson, 1980, *Ap. J. Lett.*, **236**, L71.

Dawson, B. R., University of Adelaide, Ph.D. Thesis, 1985.

Den, M., T. Yoshida and Y. Yamada, 1990, *Progr. Theoret. Phys.*, **83**(4), 723.

Dingus, B. L., D. E. Alexandreas, R. C. Allen, R. L. Burman, K. B. Butterfield, R. Cady, C. Y. Chang, R. W. Ellsworth, J. A. Goodman, S. K. Gupta, T. J. Haines, D. A. Krakauer, J. Lloyd-Evans, D. E. Nagle, M. Potter, V. D. Sandberg, R. L. Talaga, C. A. Wilkinson and G. B. Yodh, 1988, *Phys. Rev. Lett.*, **61**(17), 1906.

Dingus, B. L., C. Y. Chang, J. A. Goodman, S. K. Gupta, D. A. Krakauer, R. L. Talaga, G. B. Yodh, R. W. Ellsworth, R. L. Burman, K. B. Butterfield, R. Cady, R. D. Carlini, J. Lloyd-Evans, D. E. Nagle, V. D. Sandberg, C. A. Wilkinson, J. Linsley and R. C. Allen, 1988, *Phys. Rev. Lett.*, **60**(18), 1785.

Dogiel, V. A., 1991, in *The Interstellar Disk-Halo Connection in Galaxies*, ed. H. Bloemen, IAU, **144**, p. 185.

Dotani, T., K. Hayashida, H. Inoue, M. Itoh, K. Koyama, F. Makino, K. Mitsuda, T. Murakami, M. Oda, Y. Ogawara, S. Takano, Y. Tanaka, A. Yoshida, K. Makishima, T. Ohashi, N. Kawai, M. Matsuaoka, R. Hoshi, S. Hayakawa, T. Kii, H. Kunieda, F. Nagase, Y. Tawara, I. Hatsukade, S. Kitamoto, S. Miyamoto, H. Tsunemi, K. Yamashita, M. Nakagawa, M. Yamauchi, M. J. L. Turner, K. A. Pounds, H. D. Thomas, G. C. Stewart, A. M. Cruise, B. E. Patchett and D. H. Reading, 1987, *Nature*, **330**, 230.

Drees, M. and F. Halzen, 1988, *Phys. Rev. Lett.*, **61**(3), 275.

Dumora, D., J. Procureur and J. N. Stamenov, 1992, *J. Phys. G*, **18**, 1839.

Dzibowski, T., J. Gawin, B. Grochalska and J. Wdowczyk, 1983, *J. Phys. G*, **9**, 459.

Ebisuzaki, T. and N. Shibazaki, 1988, *Ap. J. Lett.*, **327**, L5.

———, 1988, *Ap. J.*, **328**, 699.

Edwards, P. G., R. J. Protheroe and E. Rawinski, 1985, *J. Phys. G Lett.*, **11**, L101.

Efimov, N. N., T. A. Egorov, A. V. Glushkov, M. I. Pravdin and I. Y. Sleptsov, 1991, in *Astrophysical Aspects of the most Energetic Cosmic Rays, Proceedings of the ICCR International Symposium*, ed. M. Nagano and F. Takahara, p. 20, World Scientific, Kofu, Japan, Singapore.

Efimov, N. N., A. A. Mikhailov and M. I. Pravdin, 1983, *Proc. 18th Int. Cosmic Ray Conf. (Bangalore)*, **2**, 149.

Elbert, J. W. and P. Sommers, 1987, *Proc. 20th Int. Cosmic Ray Conf. (Moscow)*, **2**, 458.

Ellison, D. C. and E. Möbius, 1987, *Ap. J.*, **318**, 474.

Ellsworth, R. W., T. K. Gaisser, T. Stanev and G. B. Yodh, 1982, *Phys. Rev. D* , **26**(1), 336.

Engelmann, J. J., P. Ferrando, A. Soutoul, P. Goret, E. Juliusson, L. Koch-Miramond, N. Lund, P. Masse, B. Peters, N. Petrou and I. L. Rasmussen, 1990, *Astron. Ap.*, **233**, 96.

Feinberg, E. L., 1981, *Proc. 17th Int. Cosmic Ray Conf. (Paris)*, **12**, 273.

Fenyves, E. J., 1985, in *Proc. Workshop on Techniques in Ultra-High-Energy Gamma-Ray Astronomy (La Jolla)*, ed. R. J. Protheroe and S. A. Stephens, p. 124, University of Adelaide.

Fermi, E., 1951, *Phys. Rev.*, **81**(5), 683.

Fermi, E., 1949, *Phys. Rev.*, **73**(8), 1169.

Feynman, R. P., 1969, *Phys. Rev. Lett.*, **23**(24), 1415.

Fichtel, C. E. and J. Linsley, 1986, *Ap. J.*, **300**, 474.

Fowler, P. H., R. A. Adams, V. G. Cowen and J. M. Kidd, 1967, *Proc. Roy. Soc.*, **301**, 39.

Fowler, P. H., R. N. F. Walker, M. R. W. Masheder, R. T. M. v, A. M. Gay, 1987, *Ap. J.*, **314**, 739.

Fransson, C., A. Cassatella, R. Gilmozzi, R. P. Kirshner, N. Panagia, G. Sonneborn and W. Wamsteker, 1989, *Ap. J.*, **336**, 429.

Freudenreich, H. T., A. I. Mincer, D. Berley, J. A. Goodman, S. Tonwar, A. Wrotniak and G. B. Yodh, 1990, *Phys. Rev. D* , **41**(9), 2732.

Fu, A. and W. D. Arnett, 1989, *Ap. J.*, **340**, 414.

Gaisser, T. K., F. Halzen, T. Stanev and E. Zas, 1990, *Phys. Lett. B*, **243**(4), 444.

Gaisser, T. K. and A. M. Hillas, 1977, *Proc. 15th Int. Cosmic Ray Conf. (Plovdiv)*, **8**, 353.

Gaisser, T. K., R. J. Protheroe and T. Stanev, 1983, *Proc. 18th Int. Cosmic Ray Conf. (Bangalore)*, **5**, 174.

Gaisser, T. K., T. Stanev, S. Tilav, S. C. Corbato, H. Y. Dai, B. R. Dawson, J. W. Elbert, B. Emerson, D. B. Kieda, M. Luo, S. Ko, C. Larsen, E. C. Loh, M. H. Salamon, J. D. Smith, P. Sokolsky, P. Sommers, J. Tang, S. B. Thomas and D. J. Bird, 1993, *Phys. Rev. D* , **47**, 1919.

Gehrels, N., C. J. MacCullum and M. Leventhal, 1987, *Ap. J. Lett.*, **320**, L19.

Giacconi, R., H. Gursky, F. R.Paoline, B. Rossi, 1912, *Physik. Zeitschr.*, **13**, 1804.

Gibbs, K. G., 1988, *Nucl. Instr. Meth.*, **A264**, 67.

Giller, M., J. L. Osborne, J. Wdowczyk and M. Zielinska, 1993, *Proc. 23rd Int. Cosmic Ray Conf. (Calgary)*, **2**, 81.

Gillman, M. S. and A. A. Watson, 1993, *Proc. 23rd Int. Cosmic Ray Conf. (Calgary)*, **2**, 47.

Glushkov, A. V., V. M. Grigoryev, M. N. Dyakonov, V. P. Egorova, A. N. Efimov, N. N. Efimov, N. N. Efremov, A. A. Ivanov, S. P. Knurenko, V. A. Kolosov, A. D. Krasilnikov, I. T. Makarov, V. N. Pavlov, P. D. Petrov, M. I. Pravdin, I. Y. Sleptsov and N. I. Sleptsov, 1987, *Proc. 20th Int. Cosmic Ray Conf. (Moscow)*, **5**, 494.

Gorchakov, E., I. Karchenko, A. Shukurov and D. Sokoloff, 1991, *Ap. Space Sci.*, **179**, 141.

Grebenev, S. A. and R. A. Syunyaev, 1987, *Sov. Astron. Lett.*, **13**(6), 438.

———, 1987, *Sov. Astron. Lett.*, **13**(6), 397.

Greisen, K., 1956, *Prog. Cos. Ray Phys.*, **3**, 3.

Greisen, K., 1960, *Ann. Revs. Nuc. Sci.*, **10**, 63.

———, 1966, *Phys. Rev. Lett.*, **16**(17), 748.

Haas, M. R., S. W. J. Colgan, E. F. Erickson, S. D. Lord, M. G. Burton and D. J. Hollenbach, 1990, *Ap. J.*, **360**, 257.

Halzen, F., 1990, *Proc. 21st Int. Cosmic Ray Conf. (Adelaide)*, **12**, 101.

Hamilton, P. A. and A. G. Lyne, 1987, *Mon. Not. R. Astron. Soc.*, **224**, 1073.

Hara, T., Y. Hatano, N. Hayashida, K. Kamata, T. Kifune, Y. Mizumoto, M. Nagano, G. Tanahashi and M. Teshima, 1983, *Proc. 18th Int. Cosmic Ray Conf. (Bangalore)*, **11**, 281.

Heiles, C., 1976, *Ann. Rev. Astron. Ap.*, **14**, 1.

———, 1987, in *Interstellar Processes*, ed. D. J. Hollenbach and H. A. Thronson, Astro. Space Sci. Lib., **134**, p. 171, D. Reidel Publishing Company.

Heitler, *The Quantum Theory of Radiation*, 1944 (second edition), The International Series of Monographs on Physics, Oxford University Press.

Hill, C. T. and D. N. Schramm, 1985, *Phys. Rev. D* , **31**(3), 564.

Hill, C. T., D. N. Schramm and T. P. Walker, 1986, *Phys. Rev. D* , **34**(5), 1622.

———, 1987, *Phys. Rev. D* , **36**(4), 1007.

Hillas, A. M., 1981, *Proc. 17th Int. Cosmic Ray Conf. (Paris)*, **13**, 69.

———, 1984, *Ann. Rev. Astron. Ap.*, **22**, 425.

———, 1987, *Proc. 20th Int. Cosmic Ray Conf. (Moscow)*, **6**, 432.

Hillas, A. M. and J. Lapikens, 1977, *Proc. 15th Int. Cosmic Ray Conf. (Plovdiv)*, **8**, 460.

Hillas, A. M., D. J. Marsden, J. D. Hollows and H. W. Hunter, 1971, *Proc. 12th Int. Cosmic Ray Conf. (Hobart)*, **3**, 1001.

Hillebrandt, W., P. Hoflich, J. W. Truran and A. Weiss, 1987, *Nature*, **327**, 597.

Hiltner, 1949, *Ap. J.*, **109**, 471.

Hirata, K., T. Kajita, M. Koshiba, M. Nakahata and Y. Oyama, 1987, *Phys. Rev. Lett.*, **58**, 1490.

Honda, M., 1987, *Ap. J.*, **319**, 836.

Hummel, E., R. Beck and M. Dahlem, 1991, *Astron. Ap.*, **248**, 23.

Hummel, E., R. Beck and R. J. Dettmar, 1991, *Astron. Ap. Suppl. Ser.*, **87**, 309.

Hummel, E., H. Lesch, R. Wielebinski and R. Schlickheiser, 1988, *Astron. Ap.*, **197**, L29.

Itoh, M., S. Kumagai, T. Shigeyama, K. Nomoto and J. Nishimura, 1987, *Nature*, **330**, 233.

Johnson, T. J., 1933, *Phys. Rev.*, **43**, 834.

Jokipii, J. R., 1966, *Ap. J.*, **146**, 480.

———, 1976, *Ap. J.*, **208**, 900.

———, 1987, *Ap. J.*, **313**, 842.

Jokipii, J. R. and G. E. Morfill, 1985, *Ap. J. Lett.*, **290**, L1.

———, 1987, *Ap. J.*, **312**, 170.

Jones, L. W., 1985, *Proc. 19th Int. Cosmic Ray Conf. (La Jolla)*, **9**, 323.

Kaplan, S. A., *Interstellar Gas Dynamics*, 1966, Pergamon, Oxford.

Karakula, S., J. L. Osborne, E. Roberts and W. Tkaczyk, 1971, *Proc. 12th Int. Cosmic Ray Conf. (Hobart)*, **1**, 310.

Karakula, S., J. L. Osborne and J. Wdowczyk, 1974, *J. Phys. A*, **7**(3), 437.

Karakula, S. and J. Wdowczyk, 1963, *Acta. Phys. Pol.*, **24**, 231.

Kifune, T., K. Nishijima, T. Hara, Y. Hatano, N. Hayashida, M. Honda, K. Kamata, Y. Matsubara, M. Mori, M. Nagano, G. Tanahashi and M. Teshima, 1986, *Ap. J.*, **301**, 230.

Kifune, T., J. Wdowczyk and A. W. Wolfendale, 1986, *J. Phys. G*, **12**, 143.

Kirshner, R. P., 1987, in *Proceedings of the Fourth George Mason Workshop: Supernova 1987A in the Large Magellanic Cloud*, ed. M. Kafatos and A. G. Michalitsianos, p. 86, Cambridge University Press.

Kolhörster, W., I. Matthes and E. Webber, 1938, *Naturwiss.*, **26**, 576.

Kolmogorov, A. N., 1961, in *Turbulence: Classic Papers on Statistical Theory*, ed. S. K. Friedlander and L. Topper, p. 151, Interscience Publishers Inc., New York.

Krasilnikov, A. D., A. A. Ivanov, V. A. Kolosov, A. D. Krasilnikov, K. N. Makarov, V. R. Pavlov, I. Y. Sleptsov, F. K. Shamsatdinova, G. G. Struchkov, T. A. Yegerov and V. P. Yegorova, 1983, *Proc. 18th Int. Cosmic Ray Conf. (Bangalore)*, **9**, 223.

Krasilnikov, A. D., A. A. Ivanov and S. I. Nikolsky, 1993, *Proc. 23rd Int. Cosmic Ray Conf. (Calgary)*, **2**, 60.

Krymskii, G. F., 1977, *Dokl. Akad. Nauk SSSR*, **234**, 1306.

Krys, A., E. Krys and A. Wasilewski, 1991, *J. Phys. G*, **17**, 1261.

Kumagai, S., T. Shigeyama, K'ichi Nomoto, M. Itoh, J. Nishimura and S. Tsuruta, 1989, *Ap. J.*, **345**, 412.

Lagage, P. O. and C. J. Cesarsky, 1983, *Astron. Ap.*, **125**, 249.

Lagutin, A. A., A. V. Pljasheshnikpv and V. V. Uchaikin, 1979, *Proc. 16th Int. Cosmic Ray Conf. (Kyoto)*, **7**, 18.

Larson, R. B., 1979, *Mon. Not. R. Astron. Soc.*, **186**, 479.

Lawrence, M. A., R. J. O. Reid and A. A. Watson, 1991, *J. Phys. G*, **17**, 733.

Lee, A. A. and R. W. Clay, 1993, *Proc. 23rd Int. Cosmic Ray Conf. (Calgary)*, **2**, 77.

Lee, A. A., A. Mastichiadis and R. J. Protheroe, 1991, *Proc. 22nd Int. Cosmic Ray Conf. (Dublin)*, **1**, 37.

Lee, L. C. and J. R. Jokipii, 1976, *Ap. J.*, **206**, 735.

———, 1975, *Ap. J.*, **196**, 695.

———, 1975, *Ap. J.*, **201**, 532.

———, 1975, *Ap. J.*, **202**, 439.

Leising, M. D., 1988, *Nature*, **332**, 516.

Leising, M. D. and G. H. Share, 1990, *Ap. J.*, **357**, 100.

Linsley, J., 1975, *Proc. 14th Int. Cosmic Ray Conf. (Munich)*, **2**, 592.

———, 1980, in *Catalogue of Highest Energy Cosmic Rays*, ed. M. Wada, **1**, p. 5, Institute of Physical and Chemical Research, Itabashi, Tokyo: World Data Center.

———, 1983, *Proc. 18th Int. Cosmic Ray Conf. (Bangalore)*, **12**, 135.

———, 1986, *J. Phys. G*, **12**, 51.

———, 1975, *Phys. Rev. Lett.*, **34**(24), 1530.

Lloyd-Evans, J., 1991, *Proc. 22nd Int. Cosmic Ray Conf. (Dublin)*, **5**, 215.

Lloyd-Evans, J., R. N. Coy, A. Lambert, J. Lapikens, M. Patel, R. J. O. Reid and A. A. Watson, 1983, *Nature*, **305**, 784.

Lyne, A. G. and F. G. Smith, 1989, *Mon. Not. R. Astron. Soc.*, **237**, 533.

Manchester, R. N., 1974, *Ap. J.*, **188**, 637.

Mastichiadis, A., N. Kylafis and J. Ventura, 1988, *Astron. Ap. Lett.*, **208**, L11.

Mastichiadis, A., H. Ogelman and J. G. Kirk, 1988, *Astron. Ap. Lett.*, **201**, L19.

Matz, S. M., G. H. Share, M. D. Leasing, E. L. Chupp, W. T. Vestrand, W. R. Purcell, M. S. Strickman and C. Reppin, 1988, *Nature*, **331**, 416.

Maze, R. and A. Zawadzki, 1960, *Nuovo Cimento C (1)*, **17**(5), 625.

McComb, T. J. L., R. J. Protheroe and K. E. Turver, 1979, *J. Phys. G*, **5**, 1613.

McCray, R., J. M. Shull and P. Sutherland, 1987, *Ap. J. Lett.*, **317**, L73.

McKee, C. F. and J. P. Ostriker, 1977, *Ap. J.*, **218**, 148.

Meyer, J-P., 1985, *Proc. 19th Int. Cosmic Ray Conf. (La Jolla)*, **9**, 141.

———, 1985, *Ap. J. Supp.*, **57**, 151.

Morfill, G. E., P. Meyer and R. Lust, 1985, *Ap. J.*, **296**, 670.

Moseley, S. H., E. Dwek, W. Glaccum, J. R. Graham, R. F. Loewenstein and R. F. Silverberg, 1989, *Ap. J.*, **347**, 1119.

Müller, E., W. Hillebrandt, M. Orio, P. Hoflich, R. Monchmeyer and B. A. Fryxell, 1989, *Astron. Ap.*, **220**, 167.

Nagano, M., M. Teshima, Y. Matsubara, H. Y. Dai, T. Hara, N. Hayashida, M. Honda, H. Ohaka and S. Yoshida, 1992, *J. Phys. G*, **18**, 423.

Nagasawa, M., T. Nakamura and S. M. Miyama, 1988, *Pub. Astron. Soc. Japan*, **40**, 691.

Nagle, D. E., T. K. Gaisser and R. J. Protheroe, 1988, *Ann. Rev. Part. Sci.*, **38**, 609.

Nishimura, J. and K. Kamata, 1951, *Prog. Theor. Phys.*, **6**, 628.

Olejniczak, J., J. Wdowczyk and A. W. Wolfendale, 1977, *J. Phys. G*, **3**(6), 847.

Ormes, J. F. and R. J. Protheroe, 1983, *Ap. J.*, **272**, 756.

Ostriker, J. P. and J. E. Gunn, 1969, *Ap. J.*, **157**, 1395.

Parker, E. N., 1991, 1991.

———, 1970, *Ap. J.*, **162**, 665.

———, 1971, *Ap. J.*, **163**, 279.

———, 1971, *Ap. J.*, **163**, 255.

Penzias, A. A. and R. W. Wilson, 1965, *Ap. J. Lett.*, **142**(1), 419.

Peters, B., 1961, *Nuovo Cimento C (1)*, **22**(4), 800.

Piddington, J. H., 1964, *Mon. Not. R. Astron. Soc.*, **128**, 345.

Pinto, P. A. and S. E. Woosley, 1988, *Nature*, **333**, 534.

———, 1988, *Ap. J.*, **329**, 820.

Powell, C. F., P. H. Fowler and D. H. Perkin, *The Study of Elementary Particles by the Photographic Method*, 1959, Pergammon Press.

Pozdnyakov, L. A., I'yaM. Sobol' and R. A. Syunyaev, 1983, *Sov. Sci. Rev., Ap. Space Phys.*, **2**, 189.

Protheroe, R. J., 1984, *Nature*, **310**, 296.

Protheroe, R. J., R. W. Clay and P. R. Gerhardy, 1984, *Ap. J. Lett.*, **280**, L47.

Protheroe, R. J., J. F. Ormes and G. M. Comstock, 1981, *Ap. J.*, **247**, 362.

Protheroe, R. J. and A. P. Szabo, 1992, *Phys. Rev. Lett.*, **69**, 2885.

Rand, R. J. and S. R. Kulkarni, 1989, *Ap. J.*, **343**, 760.

Ren, J. R., A. X. Huo, S. L. Lu, S. Su, C. R. Wang, N. J. Chang, P. Y. Cao, J. Y. Li, B. T. Zou, S. Z. Wang, G. Z. Bai, Z. H. Liu, G. J. Li, Q. X. Leng, R. D. He, W. D. Zhou, M. Amenomori, H. Nanjo, N. Hotta, I. Ohta, K. Mizutani, K. Kasahara, T. Yuda, T. Shirai, N. Tateyama, S. Torii, M. Shibata, H. Sugimoto and K. Taira, 1988, *Phys. Rev. D* , **38**(5), 1404.

Rickett, B. J., W. A. Coles and G. Bourgois, 1984, *Astron. Ap.*, **134**, 390.

Robinson, J. W., ed., *CRC Handbook of Spectroscopy*, 1974, **1**, CRC Press, Cleveland.

Rossi, B., 1933, *Z. Phys.*, **82**, 151.

Rossi, B., *High-Energy Particles*, 1952, Prentice-Hall Physics Series, Prentice-Hall, New York.

Rossi, B. and K. Greisen, 1941, *Rev. Modern Phys.*, **13**, 240.

Rousseau, J., N. Martin, L. Prevot, E. Rebeirot, A. Robin and J. P. Brunet, 1978, *Astron. Ap. Supp.*, **31**, 243.

Ruzmaikin, A. A. and A. M. Shukurov, 1982, *Ap. Space Sci.*, **82**, 397.

Ruzmaikin, A. A., A. M. Shukurov and D. D. Sokoloff, *Magnetic Fields of Galaxies*, 1988, Astrophysics and Space Science Library, **133**, Kluwer Academic Publishers.

Ruzmaikin, A., D. Sokoloff and A. Shukurov, 1988, *Nature*, **336**, 341.

Saio, H., M. Kato and K. Nomoto, 1988, *Ap. J.*, **331**, 388.

Saio, H., K. Nomoto and M. Kato, 1988, *Nature*, **334**, 508.

Samorski, M. and W. Stamm, 1983, *Proc. 18th Int. Cosmic Ray Conf. (Bangalore)*, **11**, 244.

———, 1983, *Ap. J. Lett.*, **268**, L17.

Scalo, J. M., *Interstellar Processes*, 1987, Ap. Space Sci., **134**, D. Reidel Publishing Company.

Shapiro, M. M. and R. Silberberg, 1983, *Ap. J.*, **265**, 570.

Share, G. H., R. L. Kinzer, J. D. Kurfess, D. C. Messina, W. R. Purcell, E. L. Chupp, D. J. Forrest and C. Reppin, 1988, *Ap. J.*, **326**, 717.

Shigeyama, T., K. Nomoto and M. Hashimoto, 1988, *Astron. Ap.*, **196**, 141.

Shigeyama, T., K. Nomoto, M. Hashimoto and D. Sugimoto, 1987, *Nature*, **328**, 320.

Shigeyama, T. and K'ichi Nomoto, 1990, *KEK Prog. Rep.*, **89**, 207.

Silberberg, R., C. H. Tsao, M. M. Shapiro and P. L. Biermann, 1990, *Ap. J.*, **363**, 265.

Simard-Normandin, M. and P. P. Kronberg, 1980, *Ap. J.*, **242**, 74.

Simard-Normandin, M., P. P. Kronberg and S. Button, 1981, *Ap. J. Supp.*, **45**, 97.

Simpson, J. A., 1983a, in *Composition and Origin of Cosmic Rays*, ed. M. M. Shapiro, NATO ASI, **107**, p. 1, D. Reidel Publishing Company.

———, 1983, *Ann. Rev. Part. Sci.*, **33**, 323.

Skobelzyn, D., 1929, *Z. Phys.*, **54**, 686.

Smith, A. G. K. and R. W. Clay, 1990, *Aust. J. Phys.*, **43**, 373.

Sofue, Y., M. Fujimoto and R. Wielebinski, 1986, *Ann. Rev. Astron. Ap.*, **24**, 459.

Sofue, Y., 1991, in *The Interstellar Disk-Halo Connection in Galaxies*, ed. H. Bloemen, IAU, **144**, p. 169.

Sokoloff, D. and A. Shukurov, 1990, *Nature*, **347**, 51.

Sokolsky, P., P. Sommers and B. R. Dawson, 1992, *Phys. Rep.*, **217**(5), 227.

de Souza, K., M. Gillman, S. Hart, J. Lloyd-Evans, J. E. McMillan and A. A. Watson, 1992, *Nuclear Phys. B Proc. Suppl.*, **28B**, 135.

Spitzer, L., *Physical Processes in the Interstellar Medium*, 1978, John Wiley and Sons, New York.

Spyromilio, J., W. P. S. Miekle and D. A. Allen, 1990, *Mon. Not. R. Astron. Soc.*, **242**, 669.

Stanev, T., T. K. Gaisser and F. Halzen, 1985, *Phys. Rev. D* , **32**(5), 1244.

Stecker, F. W., 1989, *Nature*, **342**, 401.

Strong, A. W., J. Wdowczyk and A. W. Wolfendale, 1974, *J. Phys. A*, **7**(1), 120.

Suga, K., 1985, in *Proc. Workshop on Techniques in Ultra-High-Energy Gamma-Ray Astronomy (La Jolla)*, ed. R. J. Protheroe and S. A. Stephens, p. 48, University of Adelaide.

Sun, L., S. Wang and A. A. Watson, 1993, *Proc. 23rd Int. Cosmic Ray Conf. (Calgary)*, **2**, 43.

Syunyaev, R. A., A. Kaniovskii, V. Efremov, M. Gil'fanov, E. Churazov, S. A. Grebenev, A. V. Kuznetsov, A. S. Melioranskii, N. S. Yamburenko, S. Yunin, D. Stepanov, I. Chulkov, N. Pappe, M. N. Boyarskii, E. A. Gavrilova, V. M. Loznikov, A. Prudkoglyad, V. G. Rodin, C. Reppin, W. Pietsch, J. Engelhauser, J. Trumper, W. Voges, E. Kendziorra, M. Bezler, R. Staubert, A. C. Brinkman, G. K. Skinner, O. Al-Emam, T. G. Patterson and A. P. Wilmore, 1987, *Nature*, **330**, 227.

Syunyaev, R. A., A. Kaniovskii, V. Efremov, M. Gil'fanov, E. Churazov, S. A. Grebenev, A. V. Kuznetsov, A. S. Melioranskii, N. S. Yamburenko, S. Yunin, D. Stepanov, I. Chulkov, N. Pappe, M. N. Boyarskii, E. A. Gavrilova, V. M. Loznikov, A. Prudkoglyad, V. G. Rodin, C. Reppin, W. Pietsch, J. Engelhauser, J. Trumper, W. Voges, E. Kendziorra, M. Bezler, R. Staubert, A. C. Brinkman, G. K. Skinner, O. Al-Emam, T. G. Patterson, A. P. Wilmore, J. Heise, W. A. Mels and R. Jager, 1987, *Sov. Astron. Lett.*, **13**(6), 431.

Syunyaev, R. A., A. Kaniovskii, V. Efremov, S. A. Grebenev, A. V. Kuznetsov, V. M. Loznikov, A. S. Melioranskii, S. N. Yunin, D. K. Stepanov, A. Prudkoglyad, V. G. Rodin, C. Reppin, W. Pietsch, J. Engelhauser, J. Trumper, W. Voges, E. Kendziorra, M. Bezler and R. Staubert, 1988, *Sov. Astron. Lett.*, **14**(4), 247.

Syunyaev, R. A., A. S. Kaniovskii, V. V. Efremov, S. A. Grebenev, A. V. Kuznetsov, J. Engelhauser, S. Dobereiner, W. Pietsch, C. Reppin, J. Trumper, E. Kendziorra, M. Maisack, B. Mony and R. Staubert, 1990, *Sov. Astron. Lett.*, **16**(3).

Szabelski, J., J. Wdowczyk and A. W. Wolfendale, 1986, *J. Phys. G*, **12**, 1433.

Szabo, A. P., University of Adelaide, Ph. D. Thesis, 1992.

Tabara, H. and M. Inoue, 1980, *Astron. Ap. Supp.*, **39**, 379.

Tennekes, H. and J. L. Lumley, *A First Course on Turbulence*, 1972, The MIT Press, Cambridge, Massachusetts.

Teshima, M., Y. Matsubara, T. Hara, N. Hayashida, M. Honda, F. Ishikawa, K. Kamata, T. Kifune, M. Mori, M. Nagano, K. Nishijima, H. Ohaka, Y. Ohno and G. Tanahashi, 1986, *J. Phys. G*, **12**, 1097.

Teshima, M., H. Ohoka, Y. Matsubara, T. Hara, Y. Hatano, N. Hayashida, C. X. He, M. Honda, F. Ishikawa, K. Kamata, T. Kifune, M. Mori, M. Nagano, K. Nishijima, Y. Ohno and G. Tanahashi, 1986, *Nucl. Instr. Meth.*, **A247**, 399.

Thielheim, K. O. and W. Langhoff, 1968, *J. Phys. A*, **1**, 694.

Thomson, R. C. and A. H. Nelson, 1980, *Mon. Not. R. Astron. Soc.*, **191**, 863.

Tonwar, S. C., N. V. Gopalakrishnan, M. R. Rajeev and B. V. Sreekantan, 1988, *Ap. J. Lett.*, **330**, L107.

Truran, J. W., W. D. Arnett and A. G. W. Cameron, 1967, *Canad. J. Phys.*, **45**, 2315.

Vallée, J. P., 1983, *Astron. Ap.*, **124**, 147.

———, 1984, *Astron. Ap.*, **136**, 373.

———, 1991, *Ap. J.*, **366**, 450.

Van Der Velde, J. C., M. Catanese, K. D. Green, J. Matthews, D. Nitz, D. Sinclair, A. Borione, C. E. Covault, J. W. Cronin, B. E. Fick, K. G. Gibbs, H. A. Krimm, N. C. Mascarenhas, T. A. McKay, D. Müller, B. J. Newport, R. A. Ong and L. J. Rosenberg, 1991, *Proc. 22nd Int. Cosmic Ray Conf. (Dublin)*, **4**, 311.

Van Der Walt, D. J., 1988, *J. Phys. G*, **14**, 105.

Van Der Walt, D. J., B. C. Raubenheimer, O. C. De Jager, A. R. North, G. Van Urk and E. J. De Villiers, 1987, *Proc. 20th Int. Cosmic Ray Conf. (Moscow)*, **1**, 303.

Veigele, WM. J., 1973, *Atom. Data*, **5**(1), 52.

Völk, H. J. and P. L. Biermann, 1988, *Ap. J. Lett.*, **333**, L65.

Von Weizäcker, C., 1951, *Ap. J.*, **114**, 165.

Walborn, N. R., B. M. Lasker, V. G. Laidler and Y-H. Chu, 1987, *Ap. J. Lett.*, **321**, L41.

Wdowczyk, J., 1965, *Proc. 9th Int. Cosmic Ray Conf. (London)*, **2**, 691.

Wdowczyk, J. and A. W. Wolfendale, 1984, *J. Phys. G*, **10**, 1599.

———, 1984, *J. Phys. G*, **10**, 1453.

———, 1987, *J. Phys. G*, **13**, 411.

———, 1983, *Nature*, **306**, 347.

Webber, W. R., M. A. Lee and M. Gupta, 1992, *Ap. J.*, **390**, 96.

Westfall, G. D., L. W. Wilson, P. J. Lindstrom, H. J. Crawford, D. E. Greiner and H. H. Heckman, 1979, *Phys. Rev. C* , **19**(4), 1309.

White, G. L. and D. F. Malin, 1987, *Nature*, **327**, 36.

Wilson, J. R., R. Mayle, S. E. Woosley and T. Weaver, 1986, *Ann. N.Y. Acad. Sci*, **470**, 267.

Winn, M. M., J. Ulrichs, L. S. Peak, C. B. A. McCusker and L. Horton, 1986, *J. Phys. G*, **12**, 675.

———, 1986, *J. Phys. G*, **12**, 653.

Woosley, S. E., 1987, in *Proceedings of the Fourth George Mason Workshop: Supernova 1987A in the Large Magellanic Cloud*, ed. M. Kafatos and A. G. Michalitsianos, p. 289, Cambridge University Press.

———, 1988, *Ap. J.*, **330**, 218.

Woosley, S. E., P. A. Pinto, P. G. Martin and T. A. Weaver, 1987, *Ap. J.*, **318**, 664.

Woosley, S. E., P. A. Pinto and T. A. Weaver, 1988, *Proc. Astron. Soc. Aust*, **7**(4), 355.

Woosley, S. E., P. Pinto and D. Hartman, 1989, *Ap. J.*, **346**, 395.

Woosley, S. E., P. A. Pinto and L. Ensman, 1988, *Ap. J.*, **324**, 466.

Woosley, S. E. and T. A. Weaver, 1988, *Phys. Rep.*, **163**, 79.

Woosley, S. E. and T. A. Weaver, 1986, *Ann. Rev. Astron. Ap.*, **24**, 205.

Xu, Y., P. Sutherland and R. McCray, 1988, *Ap. J.*, **327**, 197.

Yamada, S. and K. Sato, 1991, *Ap. J.*, **382**, 594.

Yamada, Y., K. Kasahara and T. Nakamura, 1989, *Progr. Theoret. Phys.*, **81**(1), 93.

Yamada, Y., T. Nakamura and K-ichi Nomoto, 1990, *Progr. Theoret. Phys.*, **84** (3), 436.

Yamada, Y., T. Yoshida and M. Den, 1992, paper presented at KUNS 1085.

Yen, E., 1974, *Phys. Rev. D* , **10**(3), 836.

Yodh, G. B., J. A. Goodman, S. C. Tonwar and R. W. Ellsworth, 1984, *Phys. Rev. D* , **29**(5), 892.

Yodh, G. B., Y. Pal and J. S. Trefil, 1972, *Phys. Rev. Lett.*, **28**(15), 1005.

Zatsepin, G. T. and V. A. Kuz'min, 1966, *Soviet Phys. JETP Lett.*, **4**, 78.

Appendix A

Model 10HMM (ave)

This Appendix contains the elemental abundances for the 18 zone Model 10 HMM (ave). This has been adopted from the 69 zone model of the SN 1987A ejecta used by Pinto and Woosley (1988a).

Zone	^{1}H	^{2}He	^{12}C	^{14}N	^{16}O	^{20}Ne
1	3.61×10^{-3}	7.51×10^{-1}	6.71×10^{-3}	5.26×10^{-5}	3.89×10^{-2}	1.40×10^{-3}
2	3.18×10^{-2}	4.57×10^{-1}	4.51×10^{-2}	4.41×10^{-4}	3.18×10^{-1}	1.14×10^{-2}
3	3.85×10^{-2}	4.71×10^{-1}	4.37×10^{-2}	4.58×10^{-4}	3.04×10^{-1}	1.11×10^{-2}
4	5.40×10^{-2}	5.01×10^{-1}	4.06×10^{-2}	4.84×10^{-4}	2.76×10^{-1}	1.04×10^{-2}
5	8.42×10^{-2}	5.46×10^{-1}	3.49×10^{-2}	5.04×10^{-4}	2.28×10^{-1}	9.09×10^{-3}
6	1.30×10^{-1}	5.94×10^{-1}	2.74×10^{-2}	4.86×10^{-4}	1.69×10^{-1}	7.26×10^{-3}
7	1.81×10^{-1}	6.23×10^{-1}	2.04×10^{-2}	4.28×10^{-4}	1.19×10^{-1}	5.49×10^{-3}
8	2.40×10^{-1}	6.32×10^{-1}	1.40×10^{-2}	3.33×10^{-4}	7.73×10^{-2}	3.82×10^{-3}
9	3.03×10^{-1}	6.21×10^{-1}	8.66×10^{-3}	2.32×10^{-4}	4.55×10^{-2}	2.40×10^{-3}
10	3.70×10^{-1}	5.86×10^{-1}	5.15×10^{-3}	1.51×10^{-4}	2.59×10^{-2}	1.45×10^{-3}
11	4.48×10^{-1}	5.28×10^{-1}	2.94×10^{-3}	9.18×10^{-5}	1.43×10^{-2}	8.31×10^{-4}
12	5.21×10^{-1}	4.66×10^{-1}	1.64×10^{-3}	5.38×10^{-5}	7.75×10^{-3}	4.67×10^{-4}
13	5.57×10^{-1}	4.18×10^{-1}	1.01×10^{-3}	3.43×10^{-5}	4.69×10^{-3}	2.90×10^{-4}
14	6.18×10^{-1}	3.76×10^{-1}	6.95×10^{-4}	2.38×10^{-5}	3.20×10^{-3}	1.99×10^{-4}
15	6.42×10^{-1}	3.54×10^{-1}	5.40×10^{-4}	1.86×10^{-5}	2.48×10^{-3}	1.55×10^{-4}
16	6.51×10^{-1}	3.45×10^{-1}	4.76×10^{-4}	1.64×10^{-5}	2.18×10^{-3}	1.37×10^{-4}
17	6.51×10^{-1}	3.45×10^{-1}	4.76×10^{-4}	1.64×10^{-5}	2.18×10^{-3}	1.37×10^{-4}
18	6.55×10^{-1}	3.42×10^{-1}	4.60×10^{-4}	1.59×10^{-5}	2.15×10^{-3}	1.32×10^{-4}

Table A.1: Model 10 HMM (ave) Abundances by mass.

Zone	^{24}Mg	^{28}Si	^{32}S	^{36}Ar	^{40}Ca	^{44}Ti
1	4.55×10^{-4}	7.85×10^{-3}	5.47×10^{-3}	1.98×10^{-3}	5.61×10^{-3}	1.01×10^{-2}
2	3.64×10^{-3}	6.29×10^{-2}	4.02×10^{-2}	7.09×10^{-3}	4.34×10^{-3}	7.37×10^{-5}
3	3.49×10^{-3}	6.02×10^{-2}	3.85×10^{-2}	6.79×10^{-3}	4.15×10^{-3}	7.05×10^{-5}
4	3.18×10^{-3}	5.45×10^{-2}	3.48×10^{-2}	6.14×10^{-3}	3.76×10^{-3}	6.37×10^{-5}
5	2.64×10^{-3}	4.49×10^{-2}	2.87×10^{-2}	5.06×10^{-3}	3.10×10^{-3}	5.25×10^{-5}
6	1.98×10^{-3}	3.32×10^{-2}	2.12×10^{-2}	3.74×10^{-3}	2.29×10^{-3}	3.87×10^{-5}
7	1.47×10^{-3}	2.32×10^{-2}	1.48×10^{-2}	2.62×10^{-3}	1.61×10^{-3}	2.71×10^{-5}
8	9.25×10^{-4}	1.51×10^{-2}	9.64×10^{-3}	1.70×10^{-3}	1.04×10^{-3}	1.76×10^{-5}
9	5.51×10^{-4}	8.87×10^{-3}	5.66×10^{-3}	1.01×10^{-3}	6.13×10^{-4}	1.03×10^{-5}
10	3.17×10^{-4}	5.03×10^{-3}	3.21×10^{-3}	5.68×10^{-4}	3.48×10^{-4}	5.86×10^{-6}
11	1.76×10^{-4}	2.76×10^{-3}	1.76×10^{-3}	3.12×10^{-4}	1.91×10^{-4}	3.22×10^{-6}
12	9.61×10^{-5}	1.50×10^{-3}	9.56×10^{-4}	1.69×10^{-4}	1.04×10^{-4}	1.74×10^{-6}
13	5.84×10^{-5}	9.05×10^{-4}	5.77×10^{-4}	1.02×10^{-4}	6.26×10^{-5}	1.05×10^{-6}
14	4.00×10^{-5}	6.18×10^{-4}	3.94×10^{-4}	6.98×10^{-5}	4.28×10^{-5}	7.18×10^{-7}
15	3.09×10^{-5}	4.78×10^{-4}	3.05×10^{-4}	5.40×10^{-5}	3.31×10^{-5}	5.55×10^{-7}
16	2.72×10^{-5}	4.20×10^{-4}	2.68×10^{-4}	4.75×10^{-5}	2.91×10^{-5}	4.88×10^{-7}
17	2.72×10^{-5}	4.20×10^{-4}	2.68×10^{-4}	4.75×10^{-5}	2.91×10^{-5}	4.88×10^{-7}
18	2.63×10^{-5}	4.06×10^{-4}	2.59×10^{-4}	4.59×10^{-5}	2.81×10^{-5}	4.72×10^{-7}

Table A.2: Model 10 HMM (ave) Abundances by mass.

Zone	^{48}Cr	^{52}Fe	^{54}Fe	^{56}Ni
1	9.97×10^{-3}	1.71×10^{-2}	5.08×10^{-3}	1.35×10^{-1}
2	1.04×10^{-4}	1.61×10^{-3}	6.07×10^{-5}	1.62×10^{-2}
3	1.00×10^{-4}	1.55×10^{-3}	5.81×10^{-5}	1.55×10^{-2}
4	9.08×10^{-5}	1.44×10^{-3}	5.25×10^{-5}	1.41×10^{-2}
5	7.54×10^{-5}	1.23×10^{-3}	4.32×10^{-5}	1.18×10^{-2}
6	5.62×10^{-5}	9.52×10^{-4}	3.19×10^{-5}	8.84×10^{-3}
7	3.98×10^{-5}	7.02×10^{-4}	2.23×10^{-5}	6.28×10^{-3}
8	2.61×10^{-5}	4.77×10^{-4}	1.45×10^{-5}	4.12×10^{-3}
9	1.55×10^{-5}	2.94×10^{-4}	8.52×10^{-6}	2.44×10^{-3}
10	8.90×10^{-6}	1.74×10^{-4}	4.83×10^{-6}	1.39×10^{-3}
11	4.93×10^{-6}	9.88×10^{-5}	2.65×10^{-6}	7.66×10^{-4}
12	2.69×10^{-6}	5.50×10^{-5}	1.44×10^{-6}	4.15×10^{-4}
13	1.63×10^{-6}	3.39×10^{-5}	8.67×10^{-7}	2.51×10^{-4}
14	1.12×10^{-6}	2.33×10^{-5}	5.92×10^{-7}	1.71×10^{-4}
15	8.63×10^{-7}	1.81×10^{-5}	4.58×10^{-7}	1.33×10^{-4}
16	7.60×10^{-7}	1.59×10^{-5}	4.03×10^{-7}	1.17×10^{-4}
17	7.60×10^{-7}	1.59×10^{-5}	4.03×10^{-7}	1.17×10^{-4}
18	7.34×10^{-7}	1.54×10^{-5}	3.89×10^{-7}	1.13×10^{-4}

Table A.3: Model 10 HMM (ave) Abundances by mass.